Three Dimensional Monte Carlo Simulations of Ionized Nebulae

Barbara Ercolano

Thesis submitted for the Degree of Doctor of Philosophy
of the University of London

Department of Physics & Astronomy
UNIVERSITY COLLEGE LONDON

September 2002

To my family and my friends

"Gasping, dying,
But somehow still alive,
This is the fierce last stand
Of all I am..."

Steven Morrissey.

ABSTRACT

The study of photoionized environments is fundamental to many astrophysical problems. Up to the present most photoionization codes have numerically solved the equations of radiative transfer by making the extreme simplifying assumption of spherical symmetry. Unfortunately very few real astronomical nebulae satisfy this requirement. To remedy these shortcomings, a self-consistent, three-dimensional radiative transfer code has been developed using Monte Carlo techniques. The code, Mocassin, is designed to build realistic models of photoionized nebulae having arbitrary geometries and density distributions with both the stellar and diffuse radiation fields treated self-consistently. In addition, the code is capable of treating one or more exciting stars located at non-central locations.

The gaseous region is approximated by a cuboidal Cartesian grid composed of numerous cells. The physical conditions within each grid cell are determined by solving the thermal equilibrium and ionization balance equations. This requires a knowledge of the local primary and secondary radiation fields, which are calculated self-consistently by locally simulating the individual processes of ionization and recombination. The main structure and computational methods used in the Mocassin code are described in this thesis.

Mocassin has been benchmarked against established one-dimensional spherically symmetric codes for a number of standard cases, as defined by the Lexington/Meudon photoionization workshops (Péquignot, 1986; Ferland *et al.*, 1995; Péquignot *et al.*, 2001). The results obtained for the benchmark cases are satisfactory and are presented in this work. A performance analysis has also been carried out and is discussed here.

The code has been applied to construct a realistic model of the planetary nebula NGC 3918. Three different geometric models were tried, the first being the biconical density distribution already used by Clegg *et al.* (1987). In this model the nebula is approximated by a biconical structure of enhanced density, embedded in a lower density spherical region. Spindle-like density distributions were used for the other two models (models A

and B). Model A used a mass distribution slightly modified from one of Mellema's (1996) hydrodynamical models that had already been adopted by Corradi *et al.* (1999) for their observational analysis of NGC 3918. The spindle-like model B instead used an analytical expression to describe the shape of the inner shell of this object as consisting of an ellipsoid embedded in a sphere.

The effects of the interaction of the diffuse fields coming from two adjacent regions of different densities were investigated. These are found to be non-negligible, even for the relatively uncomplicated case of a biconical geometry. It was found that the ionization structure of low ionization species near the boundaries is particularly affected.

All three models provided acceptable matches to the integrated nebular optical and ultraviolet spectrum. Large discrepancies were found between all of the model predictions of infrared fine-structure line fluxes and *ISO SWS* measurements. This was found to be largely due to an offset of $\approx$14 arcsec from the centre of the nebula that affected all of the *ISO* observations of NGC 3918.

For each model, projected emission-line maps and position-velocity diagrams from synthetic long-slit spectra were also produced, which could be compared to recent *HST* images and ground-based long-slit echelle spectra. This comparison showed that spindle-like model B provided the best match to the observations. It was therefore shown that although the integrated emission line spectrum of NGC 3918 can be reproduced by all three of the three-dimensional models investigated in this work, the capability of creating projected emission-line maps and position-velocity diagrams from synthetic long-slit spectra was crucial in constraining the structure of this object.

A model of one of the hydrogen deficient knots (J3) of the *born-again* planetary nebula Abell 30 has also been constructed. Chemical and density inhomogeneities within the knots are included in order to reproduce the observed spectrum. The final model consists of a dense core of highly C-O-enriched material, surrounded by an optically thin envelope of hydrogen-deficient material with somewhat less enhanced C and O abundances. A simplified treatment of dust photoelectric heating was implemented for this model, and it was found that dust grains played a very important role in the energy balance of the knot, providing the dominant source of heating via their photoelectron emission in the optically thin outer layer. A dust-to-gas ratio of 0.05 by mass was sufficient to obtain a temperature structure in the knot, which was suitable for the observed spectroscopic features to be produced.

Contents

List of Figures

List of Tables

CHAPTER 1

Introduction

The interpretation of spectroscopic observations of photoionized plasmas can address many fundamental questions in astrophysics. For instance, planetary nebulae and H II regions can provide information on primordial abundances, which are fundamental to the theories of cosmological nucleosynthesis (Pagel, 1997). Moreover, since planetary nebulae represent the final stage of evolution for most stars in our Galaxy, the modelling of these objects is important for the study of the properties of their central stars, fundamental to understanding the processing and dredging occurring during the lifetime of the star (Clegg *et al.*, 1987; Boroson *et al.*, 1997; Hyung *et al.*, 1997). In addition, since the physical conditions in photoionized nebulae are governed by a number of atomic processes, they provide a *natural laboratory* to test atomic physics theories.

The modelling requires the determination of the primary and secondary radiation fields, e.g. the stellar and diffuse radiation fields in the case of planetary nebulae and H II regions. Generally, the photoionization codes presently used allow the determination of these radiation fields by solving the equations of radiative transfer numerically, under the simplifying assumption of spherical geometry. However, high spatial resolution images of these objects are easily obtainable with present instrumentation, and these have shown that in almost all cases the hypothesis of spherical geometry and/or homogeneity are far from reality (note the extremely aspherical shapes of many planetary nebulae, or the filaments and knots seen in the Hubble Space Telescope images of Orion). Knots of higher density cause the regions behind them to be protected from direct starlight, hence building up extended shadow zones. The ionization of such zones is dominated by the

diffuse radiation field, which is generally softer than the stellar component, causing an enhancement of the low ionization species. Classical codes normally resort to the use of filling factors to account for density enhancement, but these do not properly replicate the observed clumpiness in nebulae. Photoionization models of realistic objects including asymmetries and inhomogeneities require fully three-dimensional treatments, where the radiative transfer is solved properly for both components of the radiation field. In these cases the application of standard differential or integral techniques can give rise to very complicated codes, as the number of variables becomes very large.

The Monte Carlo approach to transfer problems provides a technique which can handle the radiation transport problem for arbitrary geometry and density distribution without the need to impose symmetries. The Monte Carlo method has already been successfully applied to astrophysical problems such as the penetration of ultraviolet radiation into the interiors of clumpy interstellar clouds (Boissé, 1990), resonance-like scattering in accretion disc winds (Knigge *et al.*, 1995) and polarization maps for the circumstellar envelopes of protostars (Fischer *et al.*, 1994).

As was noted by Lucy (1999), in most Monte Carlo transfer codes, including the examples above, the absorption and scattering coefficients are not coupled to the radiation field. In the paper referenced above, Lucy discusses the reason why Monte Carlo developers have, in the past, avoided problems requiring solution by iteration. This is because such problems are solved by applying corrections at each iteration and these corrections are derived from the residuals expressing the failure of the previous solution to satisfy the basic equations. The problem that arises when Monte Carlo techniques are applied is that these residuals might be dominated by sampling errors, hence preventing the convergence to a solution of the desired accuracy. However, today's computer power, together with more sophisticated Monte Carlo techniques, have made the solution of problems requiring iteration feasible. Och *et al.* (1998) implemented the technique to determine the temperature and ionization structure for a one-dimensional H II region of uniform density. They obtained good agreement with the predictions of conventional codes, hence reaffirming the validity of the Monte Carlo method. Another recent example of the application of the Monte Carlo technique to problems requiring solution by iteration is the work by Lucy (1999), who obtained the temperature stratification and emergent spectrum of a non-grey spherically extended stellar atmosphere in LTE. His results show good agreement with predictions of Castor (1974), once again re-affirming the validity of the

method. The above mentioned work by Och *et al.* (1998) and that by Lucy (1999) are both one-dimensional test problems; however, the Monte Carlo techniques and the associated temperature correction procedure are not restricted to one-dimensional stratification but can be generalized to treat realistic three-dimensional models of inhomogeneous nebulae.

The work presented here is concerned with the development of a fully three-dimensional photoionization code using Monte Carlo techniques. The code is designed for the study of asymmetric and/or inhomogeneous galactic nebulae (planetary nebulae and H II regions), however it is easily extendable to the study of any other photoionized environment. A detailed description of the code, including computational methods, input commands and output files is given in Chapter 2. In Chapter 3 the code is benchmarked against established one-dimensional photoionization codes for standard model nebulae. A detailed three-dimensional photoionization study of the planetary nebula NGC 3918 is carried out in Chapter 4. The code is then applied to the modelling of one of the hydrogen-deficient knots in the born-again planetary nebula Abell 30, which shows large ORL/CEL abundance discrepancies (Wesson et al., in preparation). The overall final conclusions are given in Chapter 6. The rest of this introductory chapter is dedicated to background knowledge relevant to the work carried out in this thesis, including some of the important aspects of stellar evolution leading to the formation of planetary nebulae and the physics of photoionized nebulae in general. A brief history of classical photoionization modelling is also given at the end of the chapter.

1.1 Post Main Sequence Evolution of Low and Intermediate Mass Stars

The post main sequence evolution of low and intermediate mass stars begins when all hydrogen is exhausted in the stellar cores and shell hydrogen burning starts. At this point these stars cross the Hertzsprung Gap and start ascending the Red Giant Branch (RGB). At the end of the first ascent on the RGB, helium core burning starts and the star moves onto the horizontal branch; this happens degenerately for low mass stars and non-degenerately, through the triple-α reaction, for intermediate mass stars. Both low and intermediate mass stars eventually end up with electron-degenerate carbon-oxygen (C/O) cores and start evolving along the asymptotic giant branch (AGB), while they burn helium in a shell around their degenerate C/O core. This is the phase where, for

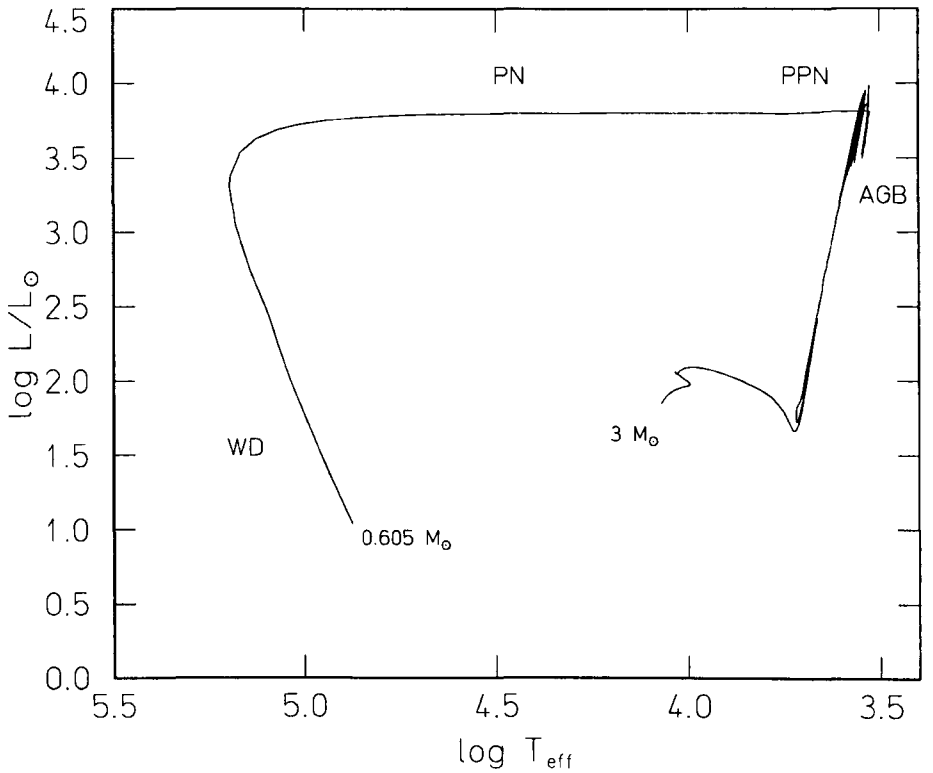

Figure 1.1: Evolutionary path for an initially 3 $M_\odot$ star from the main sequence to the white dwarf stage. Model by Bloecker (2001).

low-mass stars, the evolutionary track in the HR diagram approaches that of the first giant branch. Since planetary nebulae are descendants of AGB stars, it is essential to understand the evolution of the latter, in order to gain an insight into planetary nebula formation and hence understand the final structures of the nebulae we observe. The next few sections contain an overview of the theory of stellar evolution of low and intermediate mass stars from when they leave the main sequence to the planetary nebula phase.

1.1.1 From the Main Sequence to the Asymptotic Giant Branch

All stars spend most of their lives burning hydrogen on the main sequence. When hydrogen is exhausted in the core, however, a star will undergo some dramatic changes, in a fashion which is mainly determined by its main sequence mass. The post-main sequence evolution of a star with low or intermediate mass begins when it leaves the main sequence, having burnt all the hydrogen in its core. This is when it moves on to become a giant as the hydrogen is ignited in its envelope causing it to expand. The envelope is convective and it penetrates inwards, thus causing freshly processed nuclear material to be *dredged-up*

to the surface. The effect of this first dredge-up event is that the surface composition of the star will change. At this point the evolution of low and intermediate mass stars diverge slightly. The helium core of a low mass star is electron degenerate and therefore supported by degenerate electron pressure, which, unlike a perfect gas, depends on density and not on temperature. The core is heated by the hydrogen shell burning until it reaches a temperature of about $10^8\,K$ when helium burning starts in a *flash*. When part of the degenerate core is ignited, the increased temperature does *not* increase the pressure, hence the core does not expand, like it would in the case of a normal gas. The increased temperature, instead, increases the hydrogen burning rate, generating more energy, thus further increasing the temperature. When a temperature of about 3.5×10^8 K is reached, the electrons become non degenerate and the core expands and cools. This process is called a *helium flash* because the high thermal conductivity of a degenerate gas creates a thermal run-away, hence allowing helium burning to spread through the core in a few minutes. This does not occur for intermediate mass stars, where the helium core is not degenerate and helium burning occurs normally via the triple-α reaction. Both low and intermediate mass stars share the next stage of their evolution, their C/O core contracting and becoming electron degenerate, since their mass is not sufficient to ignite the next nuclear reaction non-degenerately. The segment of the evolutionary track which takes a star from the first giant branch to the beginning of the AGB is known as the zero-age horizontal branch, and it is shown in Figure 1.1.

1.1.2 The Asymptotic Giant Branch

The AGB track for stars with main sequence mass less than 1 $M_\odot$ approaches the first giant branch track for stars of the same mass, but slightly to the blue. For this reason this track is named *asymptotic giant branch*; this name, however, is not meaningful for higher mass stars, since they evolve along different tracks on the H-R diagram. AGB stars can be divided into early AGBs (E-AGBs) and thermally pulsating AGBs (TP-AGBs).

The second dredge-up phase occurs when core helium burning is exhausted; however only the more massive intermediate mass stars will experience an appreciable change in their surface composition as a result of this event; for a more quantitative analysis see Iben and Renzini (1983).

During the E-AGB phase, hydrogen shell burning has stopped and helium burning in a thin shell around the core provides most of the energy to the star. During this phase the

stellar luminosity increases monotonically, while the effective temperature slowly decreases, also monotonically. When a critical luminosity is reached, hydrogen is re-ignited in a thin shell and the star begins to pulsate. This marks the end of the E-AGB and the beginning of the TP-AGB.

Thermal pulses occur because the helium, which is burning non-degenerately in a shell around the C/O electron degenerate core, ignites and causes the star to expand. The expansion cools the star to the point where shell helium burning ceases; gravity will then cause the material to fall back towards the core. As the material falls inwards, the density increases and the gas heats up again until hydrogen is re-ignited. The mass of the helium shell increases until it causes helium at the base to re-ignite, thus starting another thermal pulse. The amplitude of the thermal pulses increases with each successive pulse very rapidly, at first, and then asymptotically approaching a maximum amplitude (Iben and Renzini, 1983). The TP-AGB phase is very important as it enriches the helium burning shell in carbon and neutron-rich isotopes, created by the triple-α reaction and the s-process respectively. This material can then be carried out towards the surface of the star, during the thermal pulses, in a phase known as the *third dredge-up*. All AGB stars ultimately eject their envelopes through a steady wind, and possibly a superwind, before becoming white dwarfs (and possibly forming planetary nebulae); in any case, however, the enriched material brought up to the envelope from the helium burning shell is ultimately dispersed into the interstellar medium.

Stars with initial main sequence masses $\geq$ 8-10 $M_{\odot}$ do not form a C/O degenerate core, since the core temperature is much higher, further element burning can occur, depending on the mass of the star, which goes through successive red giant phases between each nuclear burning stage. After each nuclear burning phase, the reaction continues in a shell around the core, until the star is left with an *onion-like* structure with concentric shells, each undergoing a different reaction. Nuclear burning continues until an iron core is formed, at which point the star collapses in a supernova explosion.

The next few paragraphs are concerned with the mass-loss and envelope ejection mechanisms, in particular with those leading to the formation of planetary nebulae.

1.1.3 Envelope Ejection Mechanisms

Red giants and red supergiants are observed to lose mass steadily through a stellar wind. The mechanisms responsible for these winds are still not well understood, although many

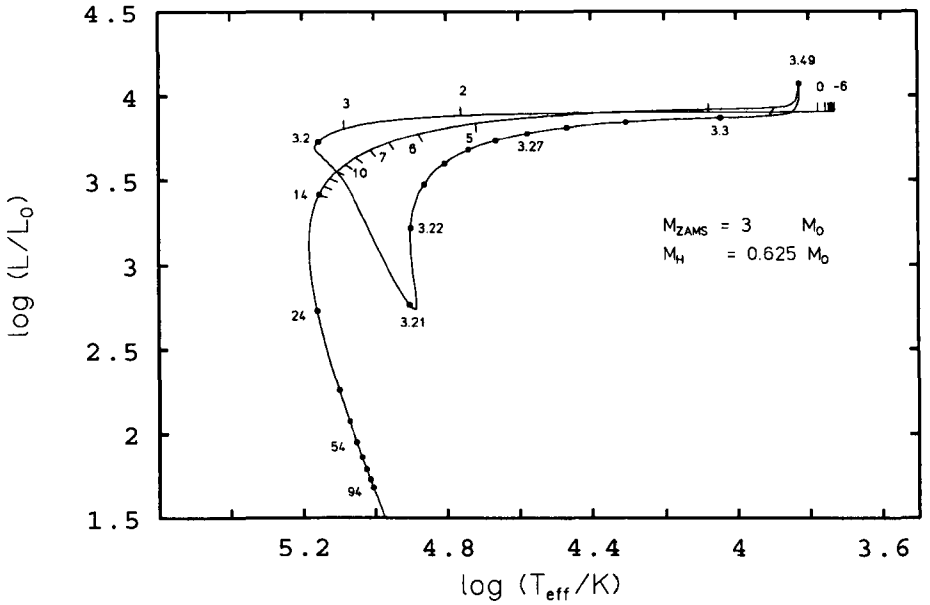

Figure 1.2: Evolution of a post-AGB model for a star with initial mass of 3 $M_\odot$ and remnant mass of 0.625 $M_\odot$ suffering from a LTP (Bloecker, 1995b). Time marks are in units of 10^3 yrs.

theoretical models have been proposed. The typical mass loss rates observed in AGB stars, of the order of about $10^{-8}\,M_\odot\,yr^{-1}$ to about $10^{-5}\,M_\odot\,yr^{-1}$, are, however, at least a a factor of ten lower then the several $10^{-5}\,M_\odot\,yr^{-1}$ required for the formation of planetary nebulae. A superwind, with average mass loss between about $10^{-5}\,M_\odot\,yr^{-1}$ and about $10^{-3}\ M_\odot\,yr^{-1}$, is believed to be responsible for the total ejection of the envelope within a timescale of about 1000 yrs, as required for the formation of planetary nebulae (see for instance Kwok, 1994; Iben and Renzini, 1983). This topic will be discussed in more details in Section 1.1.4.

In the case of more massive AGB stars, mass loss via a stellar wind might not be enough for the core to reach a mass lower than about 1.4 $M_\odot$, before the ignition of the carbon there. Several authors have shown that a thermal runaway would follow carbon ignition leading to the total disruption of the star. The final explosion has been called a supernova of type $I\frac{1}{2}$ by Iben and Renzini (1983). Since this topic is not directly related to the aim of this work, the discussion on supernovae of type $I\frac{1}{2}$ will not be taken any further.

1.1.4 The Formation of Planetary Nebulae

During the superwind phase the mass of the hydrogen envelope decreases very rapidly. The star eventually departs from the giant branch, as the stellar luminosity stays constant while the radius of the star starts decreasing, once the envelope mass becomes insufficient to maintain a red giant structure, thus causing the effective temperature to rise. The movement of the star on the H-R diagram has some definite effect on the superwind, which eventually stops, after the mass of the envelope has fallen below some critical value. At the end of the superwind phase the ejected envelope keeps expanding, while the temperature of the central star keeps rising. The envelope eventually begins to become ionized when the effective temperature of the source reaches about 30,000 K. There is the possibility for low mass cores, however, that the envelope will be completely dispersed before the star can become hot enough to ionize it. In fact, the time before nuclear burning is extinguished goes as $M_c^{-9.6}$, where M_c is the degenerate C/O core mass (Iben and Renzini, 1983). This is the case of the so-called *lazy PNs*, where a planetary nebula will never become observable. On the other hand, if the star evolves too quickly, then the nebula is illuminated only for a short length of time before nuclear burning is extinguished and the star becomes a white dwarf, with the planetary nebula's life then being too short to be detected. The evolution following the planetary nebula stage consists of the central star, which is sometimes called the PN nucleus (PNN), evolving along the horizontal PN path and approaching the appropriate white dwarf cooling sequence (see Figure 1.1) with the planetary nebula slowly dispersing. More quantitative descriptions are available from accurate stellar evolution models (see, for example, Herwig, 2000; Bloecker, 1995a,b), although the evolutionary models heavily depend on many uncertain quantities and the results are not always in agreement.

There is, however, the possibility that the star will experience a late thermal pulse at the end of the hydrogen-burning horizontal planetary nebula evolution phase, or even after the star has begun its descent along the white dwarf cooling track, causing it to return to the top of the AGB, with a new planetary nebula around it (Iben and Renzini, 1983; Iben, 1984). This is called the *born-again* scenario and it is often invoked in order to explain the existence of hydrogen deficient central stars of planetary nebulae (CSPNe) which are found to constitute approximately 20% of the whole CSPNe population (Mendez, 1991). Theoretical calculations (Iben *et al.*, 1983; Bloecker, 1995b; Herwig *et al.*, 1999) have shown

that during the final thermal pulse, most of the remaining hydrogen is incorporated into the helium burning convective shell and burned. The star then quickly evolves back to the AGB, starting the post-AGB evolution again as a helium burner. The evolutionary track of a star with initial mass of 3 $M_{\odot}$ experiencing a late thermal pulse is shown in Figure 1.2 (Bloecker, 1995b). The central stars of planetary nebulae Abell 30 (see chapter 5) and Abell 78 were identified by Iben *et al.* (1983) as being in the postpulse, quiescent helium burning phase.

1.1.5 The Shapes of Planetary Nebulae

Recent observations with various instruments, and in particular with the Hubble Space Telescope, have revealed an overwhelming variety in the shapes of planetary nebulae. These objects, which are amongst the most spectacular in the Galaxy, are very rarely circular in projection; a recent study inferred that about 50% of all known planetary nebulae are low eccentricity ellipticals, while only about 10% are circular in projection, with the remainder having more extreme elliptical or bipolar geometries (Soker, 1997, 2001). Some objects, for example the two young planetary nebulae He 2-47 and PN M1-37 (also dubbed the *starfish twins*, Sahai, 2000), show even more complicated geometries, with multiple lobes, while other planetary nebulae have FLIERs (fast, low ionization emitting regions; Balick *et al.*, 1993, 1994, 1998), BRETS (bipolar, rotating, episodic jets; Lopez *et al.*, 1997), ansae, knots, filaments, tails or multiple envelopes (see e.g. Perinotto, 2000; Corradi *et al.*, 1999; García-Segura, 1997). As has already been discussed in this chapter, planetary nebulae are descendants of AGB stars, the question then must be asked as to how can such objects, which have a largely spherical envelope, produce the observed variety of shapes. The mechanisms for shaping the planetary nebulae are still very poorly understood, although plenty of papers have been written on the subject. Hydrodynamical modelling based on the interacting-winds theory (Kwok *et al.*, 1978; Kahn, 1989; Mellema, 1996) can be quite successful in reproducing the overall shape of some planetary nebulae. Although several mechanisms have been proposed for the shaping of bipolars and high eccentricity ellipticals, currently the general consensus seems to agree at least on the need of a close orbiting stellar companion in order to trigger an axisymmetric mass loss which could result in the observed shapes (for example see Soker and Harpaz, 1999; Sahai, 2000). With regards to low eccentricity ellipticals, a different mechanism has been proposed by Soker (2001), which applies to single evolved stars with a planetary system.

1.2 The Physics of Ionized Gaseous Nebulae

In this section the fundamental concepts of photoionized systems are discussed. These are fairly well understood and explained in several textbooks. In this work the review by Osterbrock (1989) has been mostly used.

Gaseous nebulae, both H II regions and planetary nebulae, radiate energy thanks to the ultraviolet photons they receive from a nearby ionizing source. The atoms in the gaseous region absorb those stellar photons with energies above their ionization potentials and the photon energies in excess of the ion's ionization potential is transformed into the kinetic energy of the liberated electrons (*photoelectrons*). The photoelectrons are quickly thermalized through collisions with other electrons and ions and establish a Maxwellian energy distribution, with temperatures typically between 5,000 K and 20,000 K. This process provides heating to the nebula. The photoelectrons collide with the ions in the gas leaving the latter in excited states. The nebula is cooled by the downward radiative transitions of the collisionally excited ions, producing emission lines that can escape the nebula. Although the radiative transition probabilities of these downward transitions are very small, at the very low densities typical of ionized nebulae (e.g. $N_e \leq 10^5 cm^{-3}$), collisional de-excitation is even less probable. The electrons eventually recombine with the ions and the degree of ionization at each point in the nebula is determined by the equilibrium between ionizations and recombinations. The electron temperature in the envelope is fixed by the balance between heating and cooling. Emission lines from collisionally excited ions of common elements, such as [O III] $\lambda\lambda$ 4959, 5007, dominate the spectra of ionized nebulae and provide most of the cooling; however, recombination lines of H I, He I and, in the higher ionization cases, He II, are also present. The recombination lines are formed when an electron recombines to an excited level of a given ion and then cascades down to the ground level by radiative transitions. Figure 1.3 shows the energy level diagram for the [O III] transitions, including the aforementioned [O III] $\lambda\lambda$ 4959, 5007 doublet.

In the next few sections the key concepts of ionization equilibrium and thermal balance will be discussed in more detail, as well as other relevant physical processes, such as, for example, charge exchange and dielectronic recombination.

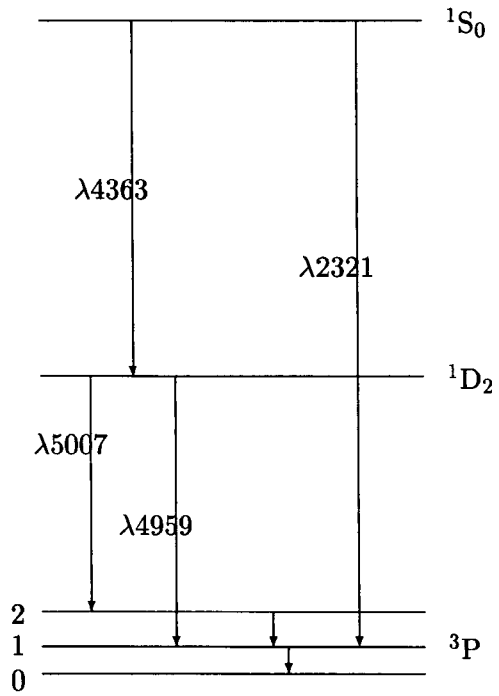

Figure 1.3: Energy-level diagram for the lowest terms of [OIII] from ground $2p^2$ configuration. The splitting of the ground ^3P term is enhanced for clarity. Only the strongest transitions are marked. The two unlabeled transitions in the ground term both occur in the infrared.

1.2.1 Ionization Equilibrium

The ionization degree at a given location in the nebula is fixed by the balance between the number of ionizations and the number of recombinations of electrons with the ions. For a pure hydrogen nebula, the ionization equilibrium can be written as

$$N_{H^0} \int_{\nu_{H^0}}^{\infty} \frac{4\pi J_\nu}{h\nu} a_\nu(H^0)\, d\nu = N_e\, N_p \alpha_A(H^0, T) \tag{1.1}$$

where N_{H^0}, N_e and N_p are the neutral hydrogen, electron and proton densities per unit volume, respectively; ν_{H^0} is the ionization frequency threshold of neutral hydrogen; J_ν is the frequency-dependent mean intensity of the radiation field; $a_\nu(H^0)$ is the frequency-dependent photoionization cross-section of neutral hydrogen; and $\alpha_A(H^0, T)$ is the temperature dependent effective recombination coefficient to all levels of H^0. J_ν has units of energy per unit area per unit solid angle per unit time per frequency interval, the quantity $4\pi\, J_\nu / h\nu$, therefore, represents the number of incident photons per unit area per unit time per frequency interval. Clearly, the right hand side of Equation 1.1 represents the total

number of recombinations and the left hand side the total number of ionizations. In order to simplify the calculations, all photoionizations are assumed to occur from the ground state. In general, the error introduced by this approximation is negligible, as the lifetime of neutral hydrogen in its excited levels is very short, compared to the mean lifetime of the same atom against photoionization. In this picture, photoionization from the ground level is balanced by recombination to any of the excited levels, followed by radiative cascades to the ground state. The recombination coefficient appearing on the right hand side of Equation 1.1 is the sum of the coefficients for recapture at all levels, which is generally written as

$$\begin{aligned} \alpha_A &= \sum_{n,L} \alpha_{n^2L}(H^0,T) \\ &= \sum_n \sum_L \alpha_{nL}(H^0,T) \\ &= \sum_n \alpha_n(H^0,T) \end{aligned} \tag{1.2}$$

where n is the principal quantum number and L is the orbital angular momentum quantum number.

Cascades from excited levels down to the ground state always occur via single photon radiative transitions, except in the case of transitions from the 2^2S level of H^0, which can only decay down to the 1^2S level via the emission of two photons. This is a continuum emission process, with the sum of the energies of the two photons of 10.2 eV. A similar situation occurs for the 2^1S excited level of He^0, which can only decay to the ground level, 1^1S, by two-photon emission, with the sum of the energies of the two photons being 20.6 eV. The same occurs again in the case of the He^+ $2^2S \rightarrow 1^2S$ two-photon transition, where the sum of the energies of the two photons here is equal to 40.8 eV.

Equations similar to Equation 1.1 are used to describe the ionization balance of all other species, and, in fact, Equation 1.1 can be applied to any species X^i, where i is the ionization stage of element X, by substituting N_{H^0} and N_p with N_{X^i} and $N_{X^{i+1}}$, respectively and using the appropriate photoionization cross-section, $a_\nu(X^i)$, frequency threshold, ν_{X^i} and total recombination coefficient, $\alpha_T(X^i,T)$.

Once emitted, the photoelectrons are quickly thermalised to a Maxwell-Boltzman energy distribution, since the cross-section for elastic collisions between the electrons is much larger than all the recombination cross-sections or the cross-section for any other nebular process involved. The local electron temperature is, therefore, determined by the elec-

trons' Maxwellian distribution function and all recombinations and collisional excitations can be assumed to occur at rates fixed by this temperature.

The total radiation field is the the sum of the stellar and the diffuse components. The stellar component consists of photons emitted directly by the ionizing source; the diffuse component is emitted by the gas in the nebula. It is easier to treat the two components separately such that

$$I_\nu = I_\nu^s + I_\nu^d \tag{1.3}$$

where I_ν, I_ν^s and I_ν^d are the specific intensities of the total, stellar and diffuse radiation fields, respectively. The stellar radiation field is attenuated by geometrical dilution and by absorption according to

$$4\,\pi\,J_\nu^s = \pi\,F_\nu^s(r) = \pi\,F_\nu^s(R)\frac{R^2 e^{-\tau_\nu(r)}}{r^2} \tag{1.4}$$

where R is the radius of the star, therefore $\pi\,F_\nu^s(R)$ and $\pi\,F_\nu^s(r)$ are the astrophysical fluxes at the stellar radius and at distance r from the centre of the nebula per unit area per unit time per unit frequency interval; $\tau_\nu(r)$ is the radial optical depth at r, which, in the case of a pure hydrogen nebula, is given by

$$\tau_\nu(r) = \int_0^r N_{H^0}(r')a_\nu(H^0)dr' \tag{1.5}$$

The diffuse radiation field is described by the equation of radiative transfer

$$\frac{dI_\nu^d}{ds} = -N_{H^0}a_\nu I_\nu^d + j_\nu \tag{1.6}$$

where j_ν is the local gas emissivity for ionizing radiation, in units of energy per unit volume per unit time per unit solid angle per unit frequency.

1.2.2 Charge Exchange

Charge exchange reactions with hydrogen can play an important role in the ionization structure of nebulae and must be taken into account in the ionization balance calculations of some ions. In particular, charge exchange of neutral oxygen in two-body recombination with hydrogen is very important; this reaction can be written as follows (Stancil *et al.*, 1999).

$$O^0(^3P_J) + H^+ \rightarrow O^+(^4S) + H^0(^2S) \tag{1.7}$$

The reaction rate per unit volume per unit time is given by $N_{O^0} N_p \delta(T)$, where $\delta(T)$ is an integral expression of the reaction cross-section (Osterbrock, 1989). The inverse reaction is also important, and the rate per unit volume per unit time can be written as $N_{O^+} N_{H^0} \delta'(T)$, where $\delta'(T)$ is related to $\delta(T)$ via the Milne relation

$$\delta'(T) = \frac{\omega_{O^0}}{\omega_{O^+}} e^{\frac{\Delta E}{kT}} \delta(T) = \frac{9}{8} e^{\frac{\Delta E}{kT}} \delta(T) \tag{1.8}$$

where ω_{O^0} and ω_{O^+} are the statistical weights of the ground levels of O^0 and O^+, respectively; $\Delta E = 0.019\,\mathrm{eV}$ is the difference in the ionization potentials of O^0 and H^0.

A similar reaction also occurs between nitrogen and hydrogen; however the rates for this are much smaller than in the case of oxygen and, apart from very high density environments, charge exchange does not affect the nitrogen ionization balance significantly.

Charge exchange reactions can also occur between other heavy ions and hydrogen. This can be written in the general case as

$$X^{+i} + H^0 \rightarrow X^{+(i-1)} + H^+ \tag{1.9}$$

and the rate per unit volume per unit time may then be written as $N_{X^{+i}} N_{H^0} \delta'(T)$. The $X^{+(i-1)}$ ions, however, are left in an excited state, therefore the inverse reaction does not occur at nebular temperatures, as, for example, in the case of (Osterbrock, 1989)

$$O^{+2}(2s^2 2p^2\,{}^3P) + H^0(1s\,{}^2S) \rightarrow O^+(2s2p^4\,{}^4P) + H^+ \tag{1.10}$$

Some charge exchange reaction rate coefficients for oxygen, nitrogen and other heavy ions are listed by Osterbrock (1989, pages 43 and 45). For a more complete and up to date listing of all hydrogen charge exchange reaction rate coefficients for the first thirty elements, see Kingdon and Ferland (1996); Stancil *et al.* (1999); Stancil (2001).

Although the density of neutral hydrogen is very low in most ionized nebulae, their large cross-sections mean that charge exchange reactions are as important, and sometimes even more important than standard recombination, for some of the ions involved. However, the effects of this process on the ionization structure of hydrogen are negligible.

Charge exchange reactions with helium can also occur in the same fashion. These can have non-negligible effects on the ionization structure of some planetary nebulae and should be taken into account (see for instance Swartz, 1994; Butler *et al.*, 1980; Butler and Dalgarno, 1980).

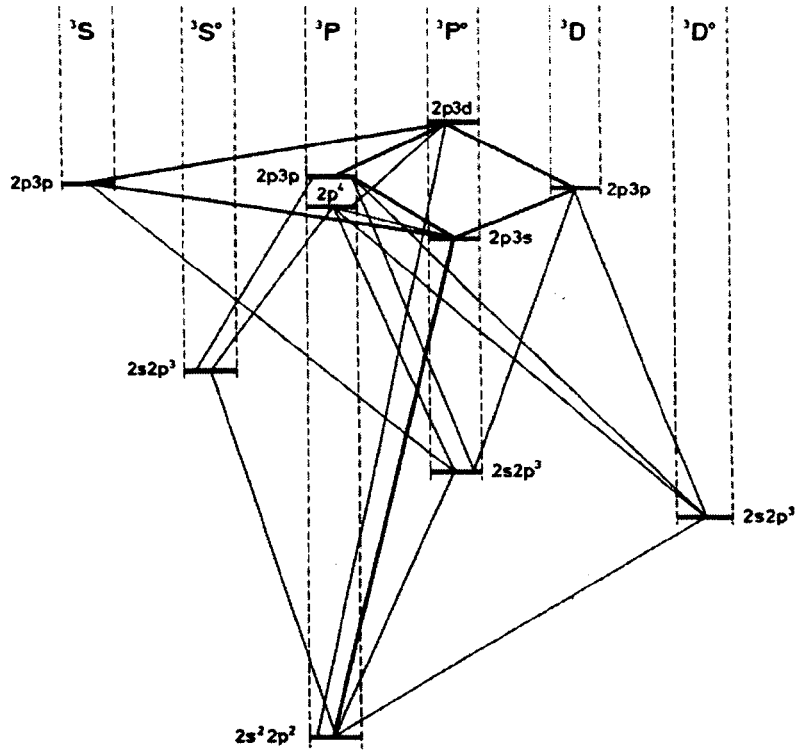

Figure 1.4: Transitions between O III multiplets which occur following excitation of O III 2p3d $^3P_2^0$ (Saraph and Seaton, 1980)

1.2.3 The Bowen Resonance-Fluorescence Mechanism

The Bowen resonance-fluorescence mechanism (Bowen, 1934) is caused by a coincidence between the wavelengths of the He II Lyα line at 303.78 Å and the O III $2p^2\ ^3P_2$ - $2p3d\ ^3P_2^0$ line at 303.80 Å. In most ionized nebula where helium is doubly ionized, the density of He II Lyα photons is quite high in the He^{2+} zone, due to the residual He^+, still existing in this zone, which causes these line photons to scatter several times before they can escape. Since O^{2+} is also present in the same zone, some of the He II Lyα line photons will be absorbed by it, populating the $3d\ ^3P_2^0$ level of O III. Figure 1.4 shows a diagram with the transitions between O III multiplets which occur following excitation of O III $3d\ ^3P_2^0$. This level decays most frequently to $2p^2\ ^3P_2$ by resonance scattering (probability 0.74; Osterbrock, 1989). The second most most likely route (probability 0.24; Osterbrock, 1989), is decay to $2p^2\ ^3P_1$ by emission of a line photon at 303.62 Å; this photon may then escape or be absorbed by another O^{2+} ion. However, as shown in Figure 1.4, the $3d\ ^3P_2^0$ level can also decay to a level in the 3p term (probability 0.02; Osterbrock, 1989), emitting one of six UV line photons (the strongest being the $3p\ ^3S_1$ - $3d\ ^3P_2^0$ line

at 3132.86 Å). These levels of 3p can then decay back to $2p^2\ ^3P$ via the 3s term or via the $2p^3$ term. In general, the pumping of the the $3d\ ^3P_2^0$ level of O III by He II Lyα line photons is known as the Bowen resonance-fluorescence mechanism.

Not all He II Lyα photons are, of course, absorbed by O^{2+}; a large fraction of these is actually absorbed by H^0 or He^0 photoionization. The fraction of He II Lyα photons caught in the Bowen fluorescence mechanism constitutes the Bowen efficiency. Several observational studies have been carried out of the UV fluorescence lines and of the Bowen efficiency in several types of objects, including symbiotic stars, AGNs (e.g. Kastner and Bhatia, 1996) and planetary nebulae (e.g. Liu, 1993). Even amongst the same type of object (e.g. the planetary nebulae sample used by Liu, 1993) large variations are measured from object to object for the values of the observed Bowen efficiencies . The average value obtained for the planetary nebulae considered by Liu (1993) is 0.42.

Finally, a wavelength coincidence, similar to the one which causes the Bowen resonance-fluorescence mechanism for O III, also occurs between the $2p^2\ ^3P_2$ – $2p3s\ ^3P_1^0$ line of O^{2+} at 374.436 Å and the $2p\ ^2P_{3/2}^0$–$3d\ ^2D$ lines of N^{2+}, giving rise to three emission lines between 4365 Å and 4643 Å and two more lines in the optical region (at 4097.3 Å and 4103.4 Å). More details about the N III fluorescence lines can be found in Liu (1993).

1.2.4 Dielectronic Recombination

Dielectronic recombination involves the capture of a free electron along with the emission of a photon (Burgess, 1964). In a recent review, Badnell (2001) describes dielectronic recombination as a *two-step* process and, unlike radiative recombination, which is described as a *one-step process* involving a continuum distribution of free electron energies, dielectronic recombination can only take place at certain free electron energies. As an example of radiative recombination, a He-like ion recombining with an electron is considered, which, schematically, can be written as

$$1s^2 + e^- \rightarrow 1s^2nl + \gamma, \tag{1.11}$$

where n and l are the principal and orbital quantum numbers. Clearly a one step process. Using the same example, the two steps of the dielectronic recombination process can be written as

$$1s^2 + e^- \rightleftharpoons 1s2pnl, \tag{1.12}$$

where ($\rightarrow$) is dielectronic capture and ($\leftarrow$) is autoionization; followed by

$$1s2pnl \rightarrow 1s^2nl + \gamma, \tag{1.13}$$

For astrophysical elements, radiative stabilization is achieved when the final state lies below the ionization limit of the recombined ion, since this would most probably autoionize (i.e. no contribution to recombination) should the final state lie above its ionization limit.

Gorczyca and Korista (2001) provide access to recent dielectronic recombination data and to basic routines, which can be used to incorporate this data into a photoionization model, through the Atomic Data for Astrophysics (ADfA) web-site:

http://www.pa.uky.edu/ verner/atom.html.

These include fits to high temperature (Aldrovandi and Péquignot, 1973; Shull and van Steenberg, 1982*a*,*b*; Arnaud and Rothenflug, 1985) and low temperature dielectronic recombination data (Nussbaumer and Storey, 1983, 1986, 1987).

1.2.5 Thermal Balance

For a nebula to be in thermal equilibrium, the total heating energy must equal the total cooling at every point in the ionized region. In the next few paragraphs all the heating and the cooling channels which must be taken into account will be discussed.

The heating is provided by the kinetic energy of the liberated photoelectrons. As has already been mentioned, when a photon of energy $h\nu$ ionizes a given ion, X^i, which has an ionization potential equal to $h\nu_{X^i}$, where ν_{X^i} is the ionization threshold frequency, the difference between the energy of the absorbed photon and the ionization potential of the ion, $h(\nu - \nu_{X^i})$, is transferred as kinetic energy to the photoelectron; the electrons are quickly thermalised through elastic collisions with other electrons and with ions, therefore their initial energy effectively contributes to the local heating. As an example, we consider the simple case of a pure hydrogen nebula, the energy input by photoionization at a given location can be written as

$$G_{phot}(H) = N_{H^0} \int_{\nu_{H^0}}^{\infty} \frac{4\pi J_\nu}{h\nu} h(\nu - \nu_{H^0}) a_\nu(H^0) d\nu \tag{1.14}$$

where N_{H^0} is the local density of neutral hydrogen, $\frac{4\pi J_\nu}{h\nu}$ is the number of photons per unit area per unit time with frequency in the interval $(\nu, \nu+\delta\nu)$, and $a_\nu(H^0)$ is the neutral hydrogen photoionization cross-section at frequency ν, therefore $\frac{4\pi J_\nu}{h\nu} a_\nu(H^0)$ is the total number of photons absorbed by neutral hydrogen per unit time.

The heating due to photoionizations at each location in the nebula must be balanced by the total cooling at the same location. Several channels contribute to the cooling; the most effective mechanism is the emission of collisionally excited lines from common ions, such as O^+, O^{2+} and N^+. These lines are emitted when the ions, which are collisionally excited by the electrons, cascade back down to the ground level via radiative transitions; most of these transitions are forbidden by electric dipole selection rules, however, at the typically very low nebular densities, collisional de-excitation is even less probable, and, therefore, forbidden radiative transitions become the preferred de-excitation mechanism. The collisional lines are emitted at wavelengths longward of the Lyman limit and they can, therefore, escape the nebula without any further interactions. This means that they cool the gas by removing energy from it. Recombination lines from H I, He I and He II also contribute to the cooling, but much less than the forbidden lines. However, the He I and He II Lyman lines do not easily escape the nebula, since the He I Lyman lines have energies greater than 13.6 eV, the neutral hydrogen ionization potential, and, therefore, they are easily absorbed by H^0, while the He II Lyman lines, with energies greater than 24.6 eV, the neutral helium ionization potential, can ionize both H^0 and He^0.

The energy loss by recombination is not the dominant coolant when heavy elements are present; however, in the case of a pure hydrogen nebula, this, together with free-free radiation, discussed below, constitute the only cooling channels. The kinetic energy lost by the gas per unit volume per unit time through hydrogen recombination can be expressed as

$$L_r(H) = N_e N_p k T_e \beta_A(H^0, T) \tag{1.15}$$

where N_e and N_p are the local electron and proton densities , k is the Boltzmann constant, T_e is the local electron temperature, and $\beta_A(H^0, T)$ is the kinetic energy averaged hydrogen recombination coefficient to all levels. For a more detailed description of β_A see Osterbrock (1989, page 50).

Another, less important, energy loss channel is the free-free continuum radiation, or bremsstrahlung. The effects of this process on the thermal equilibrium of the nebula are, in general, very small, when cooling by collisionally excited lines is available. However this process is still important, and should be considered when making photoionization calculations, as it provides cooling even in the case of a pure hydrogen nebula. For the formulae used to calculate the contribution due to this process see Osterbrock (1989, page

53).

Finally the thermal balance equation, including all cooling channels as described above, can be simply written as:

$$G_{phot} = L_c + L_r + L_{ff} \tag{1.16}$$

where L_c is the contribution due to collisional excited radiative cooling and L_r and L_{ff} are the contributions due recombination and free-free radiation, respectively.

1.3 Classical Photoionization Modelling

In this section a brief history of photoionization modelling will be given together with a description of the standard characteristics of classical photoionization codes for ionized nebulae. The basic physics behind these models has already been discussed in the previous section, therefore this section will now mainly focus on a description of the major steps in the evolution of this field. Note that the development of tools for the modelling of X-ray sources and Active Galactic Nuclei (AGNs) also started around the same time as the nebular work (e.g. Tarter *et al.*, 1969), and the basic characteristics of the codes are the same. However in the case of X-ray sources the entire range of ionization stages of abundant metals must be treated, even though not all of them are included in the thermal balance of most codes. Moreover, high energy processes, such as Compton heating and inner-shell ionization, must also be taken into account. In the following discussion we will concentrate on the history and evolution of codes for the treatment of galactic nebulae, although many modern codes, such as Cloudy (Ferland, 1994) and Nebu (Petitjean *et al.*, 1990), can be successfully applied to a range of astrophysical environments.

Amongst the first numerical models for photoionized nebulae were those calculated by Flower (1968), Harrington (1968) and Rubin (1968). These early models included the basic physical processes of ionization and recombination of hydrogen and helium, thermal balance and escape of the emitted photons from the nebula. However, the lack of reliable atomic data heavily limited the success of these models as well as the fact that a number of important physical processes, such as charge exchange and dielectronic recombination (Aldrovandi and Péquignot, 1973; Péquignot *et al.*, 1978; Storey, 1981), were not known at the time. The evolution of photoionization modelling has gone hand in hand with advances made in atomic physics and computer technology. The application

of photoionization models to a wider range of ions has been aided by the photoionization cross-section calculations by Reilman and Manson (1979) and, more recently, the Opacity Project (Hummer *et al.*, 1993). Compilations based on the latter's data (e.g. Verner and Yakovlev, 1995), have made possible the inclusion of accurate photoionization cross-sections for more ions in the calculations. Mendoza (1983) presented a compilation of radiative and collisional data for collisionally excited ultraviolet, optical and infrared lines which was widely adopted, with some of these data still in use today, though most have been superseded by more recent calculations, such as the R-matrix calculations of the Iron Project (Hummer *et al.*, 1993) and the Belfast group (e.g. McLaughlin and Bell, 1998; Ramsbottom *et al.*, 1998). Currently, radiative and dielectronic recombination rates are still highly uncertain or unavailable for some ions; recent efforts to improve the situation have been reviewed by Nahar and Pradhan (1999) and Nahar (2000). Most photoionization models include temperature dependent analytical fits to these recombination rates, such as those of Aldrovandi and Péquignot (1973) for radiative and high temperature dielectronic recombination, and those of Nussbaumer and Storey (1983) for low temperature dielectronic recombination.

Several authors have developed photoionization codes to treat a variety of astrophysical systems. It follows, from the discussion above, that the construction of such codes involves a number of choices regarding atomic data, physical assumptions and numerical algorithms; this results in the various codes having many differences, and therefore sometimes returning slightly different answers to the same problems. With the advancing of the field and with numerous photoionization codes being active at the moment, benchmarking is a necessity in order to guarantee a certain standard of results. For this reason, a series of workshops have been held (Péquignot *et al.*, 2001; Ferland *et al.*, 1995; Péquignot, 1986) and a number of benchmarking problems devised. The aim of these workshops has been to provide a platform for atomic physicists, modellers and observers to collaborate and establish good lines of communication between all fields which contribute to the understanding of photoionized gas. Table 1.1 lists the one-dimensional classical photoionization codes which were benchmarked at the last workshop, held in Lexington in November 2000. Chapter 3 in this work contains a description of the benchmarking, together with tables showing Mocassin's and the other codes' performances in the various problems.

Available computer power has increased enormously since the dawn of photoionization modelling. Moore's law predicts an increase in processor speeds of a factor of two every

Table 1.1: Classical photoionization codes benchmarked at the Lexington 2000 meeting.

Code	Author	Ref
Cloudy	Ferland	a
Ion	Netzer	b
Nebu	Péquignot	c
Xstar2	Kallman	d
Harrington	Harrington	e
MappingsII	Sutherland	f
Nebula	Rubin	g

a: Ferland (1994)

b: Netzer (1993)

c: Petitjean *et al.* (1990)

d: Kallman and McCray (1982)

e: Harrington (1968); Harrington *et al.* (1982)

f: Sutherland and Dopita (1993)

g: Rubin (1968)

eighteen months, thus giving a total increase of $\geq 10^7$ in the past 34 years. This has allowed more complex models to be built, including more ions, more frequency points, more lines and more atomic levels. However the fundamental assumption of spherical symmetry has, in general, been retained. A glance at an image of any Galactic H II region will immediately demonstrate that these objects are neither spherically symmetric nor homogeneous. In addition, they usually have multiple exciting stars, located at non-central positions in the nebula. By contrast, planetary nebulae have only a single, centrally located, exciting star. However, even for planetary nebulae, spherical symmetry is not a realistic assumption, as discussed in Section 1.1.5. Moreover, the continuous increase in computer hardware technology may mean that, in the future, photoionization models might be built to incorporate time dependent effects, or to be incorporated in the hydrodynamical models. In order to do this, the photoionization models must abandon

their assumption of spherical geometry, which, as we have already discussed, is not correct for most cases, and adopt a fully three-dimensional approach.

CHAPTER 2

Description of the Monte Carlo code

2.1 Introduction

The first application of Monte Carlo methods dates back to the 1940's, with the work of Metropolis and Ulam (1949). This is when the term *Monte Carlo* first appeared and when systematic development of techniques really began. However, Hammersley and Handscomb (1964) identified a number of isolated and undeveloped instances as early as the second half of the nineteenth century. As discussed later, the successful application of this method to solve complex problems relies heavily on the computer power available. For this reason, although Monte Carlo techniques have been developed for over fifty years, it is only in the past fifteen years or so that their application has been made particularly attractive by the fast advance of computer hardware technology.

In general, the term *Monte Carlo* is used for all those techniques which allow us to find the solutions to various problems in computational mathematics and physics *by constructing for each problem a random process with parameters equal to the required quantities of that problem. The unknowns are determined approximately by carrying out observations on the random process, and by computing its statistical characteristics which are approximately equal to the required parameters* (Shreider, 1964). The fundamental idea is that if a physical process allows the conceptual construction of a model characterised by quantities which can be represented by continuous distributions in the interval [0,1], then it can be simulated with a pseudo-random number generator. Schematically:

Physical Quantities $\Rightarrow$ Random Numbers

Random Numbers ⇒ Physical Quantities

The term *simulation* is perhaps suggestive of lack of rigour; in fact Monte Carlo methods are as valid as standard numerical procedures. In general, for standard numerical procedures we need to use a discrete representation of continuous quantities such as space and time variables, say Δx and Δt, meaning that convergence will only be achieved in the limit when Δx and Δt approach zero. Similarly, in Monte Carlo simulations, convergence is reached as N, the number of Monte Carlo quanta used in the experiment, approaches infinity. It can be easily shown (e.g. Shreider, 1964) that $\delta \sim \frac{1}{\sqrt{N}}$, where δ is the error of the Monte Carlo simulation.

The next section of this chapter covers the main concepts behind the Monte Carlo methods applied to photoionization modelling. The general architecture and the computational methods used in this work are described in Section 2.3. The final section of this chapter contains a description of IDL routines written by Christophe Morisset (Morisset *et al.*, 2000) and used as visualization tools for our models.

2.2 The Monte Carlo Method Applied to Photoionization Modelling

2.2.1 Background

It has already been mentioned in Chapter 1 that the Monte Carlo method has been applied to a variety of astrophysical processes, with several different techniques having been developed. In addition, Monte Carlo techniques have also been used in dust radiative transfer codes for some time, examples include Lefevre *et al.* (1982), Lefevre *et al.* (1983) and, more recently, Wolf *et al.* (1999). These authors use a technique in which stellar and diffuse photon packets are emitted separately; the number of diffuse photon packets (i.e. packets emitted by the dust) is determined by the dust grain temperature, while the grain temperature is determined by the balance between the number of absorbed and emitted photons packets. An initial guess for the dust grain temperature is provided by the number of packets absorbed, and the iteration continues until the grain temperatures converge. Using this method the stellar luminosity is not automatically conserved during the Monte Carlo simulation; only after the grain temperatures have reached convergence is the stellar luminosity approximately conserved. The convergence of such codes is often

very slow and requires a large number of iterations and simulation quanta in order to reach the required accuracy.

Bjorkman and Wood (2001) have described a general radiative equilibrium and temperature correction procedure for use in Monte Carlo radiative transfer codes having sources of temperature-independent opacity, such as dust. Their technique makes use of information naturally given by the Monte Carlo method, which, by tracking every photon/energy packet, makes it easy to determine where in the simulation grid energy is being absorbed. When energy is deposited at a given location, following a packet's absorption, the local medium is heated. Whenever this occurs the new local temperature is calculated and the packet is then re-emitted accordingly. The packets are followed in their path through the region, as they undergo scatterings and absorptions followed by re-emissions, with the temperatures being updated after each event, until the packets reach the edge of the nebula and escape to infinity, hence contributing to the emergent spectrum. Once all the stellar photon packets have escaped, the resulting envelope temperature and the emergent spectrum are correct without the need of any further iterations.

A great limitation of Bjorkman & Wood's method is that it cannot be applied to situations where the opacities are temperature-dependent, as is the case in photoionized gaseous nebulae. There are two reasons for the failure of this method when the opacity varies with the local temperature: firstly, the number of photon packets absorbed by the cell prior to the temperature update, would be either too small or too large, and, secondly, a change in temperature would also imply a change of the interaction locations of previous packets, signifying that the paths of the previous photon packets should have been different. While it is clear that, when dealing with photoionized gas, Bjorkman & Wood's technique is not applicable, their work is nevertheless very enlightening and should be taken into account for further developments of the code when a treatment for dust grains will be introduced in the models.

In the current work the approaches described above will not be followed, instead a strategy will be followed similar to that used in the one-dimensional code developed by Och *et al.* (1998). They employed a different Monte Carlo treatment of the radiative transfer which allowed them to iteratively determine the temperature and ionization stratification for a spherically symmetric H II region of uniform density. Some of the techniques that they used are also described in detail by Lucy (1999, 2001, 2002). The basic concept is that, when calculating radiative equilibrium temperatures, conservation of stellar lumi-

nosity is more important than the details of the spectral energy distribution. With this in mind conservation of stellar luminosity is enforced by using energy packets of constant energy throughout the simulations. Moreover, all absorbed packets are re-emitted immediately after every absorption event. The frequencies of the re-emitted energy packets are determined by the local gas emissivities. Although the frequency distribution of the re-emitted packets will not be correct until the nebular temperatures have converged, this method naturally enforces radiative equilibrium at each point in the nebula and so naturally provides conservation of energy. This not only results in a simpler code but also makes the convergence of the nebular temperatures easier (Lucy, 1999, 2001). Energy packets will be discussed in more detail in Section 2.2.2.

2.2.2 Energy Packets

The main principle of the treatment of a photoionized gaseous nebula consists of locally simulating the individual processes of ionization and recombination. The radiation field is therefore expressed in terms of energy packets, $\varepsilon(\nu)$, which are the calculation's quanta. $\varepsilon(\nu)$ is a packet consisting of n photons of frequency ν such that

$$\varepsilon(\nu) = nh\nu \tag{2.1}$$

In addition, we take all packets to have constant energy ε_0. There are several reasons for choosing to work with monochromatic, indivisible packets of radiant energy instead of photons. First of all, energy packets are more computationally economic and, also, since they all have the same energy, then those packets emitted in the infrared will contain a larger number of photons which, as a consequence, will not have to be followed individually (Abbott and Lucy, 1985). Also, as the total stellar luminosity, L_*, is evenly split amongst the stellar energy packets, the energy carried by a single packet in the time interval Δt, which represents the duration of the Monte Carlo experiment, is given by

$$\frac{L_*}{N} = \frac{\varepsilon_0}{\Delta t} \tag{2.2}$$

where N is the number of energy packets used in the simulation (Och *et al.*, 1998). Most importantly, the use of constant energy packets is a natural way of imposing strict energy conservation at any point in the nebula (Lucy, 1999). So, when a packet of energy $\varepsilon(\nu_a) = \varepsilon_0$ is absorbed, it is immediately re-emitted with a frequency ν_e, which is determined according to a frequency distribution set by the gas emissivity of the current cell.

The packet emitted, $\varepsilon(\nu_e)$, will then have the same energy as the absorbed packet, $\varepsilon(\nu_a)$, meaning that only the number, n, of photons contained in the packet is changed.

2.2.3 Initiation

The gaseous region is approximated by a three-dimensional Cartesian grid, where the ionizing source can be placed at the centre of the grid or in one corner. This feature is very useful when dealing with axisymmetric nebulae, since, by placing the source in a corner of the grid, we need only consider one eighth of the nebula, which can then be reconstructed in full at the end of the simulation. This allows the running of models with much higher spatial resolution than those which would be possible if a full nebula had to be considered (i.e. by putting the source in the centre and, therefore not making use of any symmetry properties of the object). Switches built inside the code allow the user to specify whether the nebula has some degree of symmetry and, if so, whether the symmetry is to be used. These switches can be set at the start of the simulation by including the *symmetricXYZ* command in the input file (see Section 2.3.3).

Inside each grid cell all nebular properties, such as the mass density of the gas, ρ, the electron temperature and density, T_e and N_e, and the frequency dependent gas opacity and emissivity, κ_ν and j_ν, are constant by definition. Thermal balance and ionization equilibrium are imposed in each grid cell in order to obtain the physical conditions in the local gas.

The energy packets are created at the position of the ionizing source and they all carry the same energy ε_0, as discussed in the previous section. The frequency, ν, of each individual packet emitted is derived from the input spectrum of the ionizing source according to the probability density function

$$p(\nu) = \frac{F_\nu d\nu}{\int_{\nu_{min}}^{\nu_{max}} F_{\nu'} d\nu'} = \frac{F_\nu d\nu}{L_*/(4\pi R_*^2)} \tag{2.3}$$

where F_ν is the stellar flux and R_* is the stellar radius. This is then the probability of an energy packet being emitted with a frequency lying in the interval $(\nu, \nu + d\nu)$. The upper and lower integration limits, ν_{min} and ν_{max} , have to be chosen properly, depending on the input spectrum, in order to ensure that the bulk of the radiation is included in the frequency range. As the source emits energy isotropically, the direction of travel of every energy packet emitted is chosen randomly. This is done by choosing two random numbers,

α and β, in the interval $[0, 1]$, and calculating the following quantities:

$$\begin{aligned} w &= 2\alpha - 1 \\ t &= \sqrt{1 - w^2} \\ \theta &= \pi(2\beta - 1) \\ u &= t cos\theta \\ v &= t sin\theta \end{aligned} \tag{2.4}$$

The random unit vector in Cartesian coordinates is then (u, v, w) (Harries and Howarth, 1997).

2.2.4 Trajectories

Once a stellar packet is created at the source and launched into the nebula, its trajectory must be computed as it undergoes absorptions followed by re-emissions due to bound-free and free-free processes. The trajectory ends when the packet reaches the edge of the nebula, where it escapes to infinity and contributes to the emergent spectrum.

There are two methods to track the packets and determine the locations of the absorption events. Consider a packet of frequency ν_p, emitted in the direction $\hat{u}$. The first of these methods consists of calculating the run of optical depth, τ_{ν_p}, at the energy packets frequency ν_p, from the location at which the packet is emitted to the edge of the ionized region along the direction of travel, $\hat{u}$. The probability of absorption along that path is then given by

$$p(\tau_{\nu_p}) = 1 - e^{-\tau_{\nu_p}} \tag{2.5}$$

and the normalised cumulative probability function is given by

$$\begin{aligned} P(l) &= \frac{\int_0^{\tau_{\nu_p}(l)} e^{-\tau_{\nu_p}} d\tau_{\nu_p}}{\int_0^{\infty} e^{-\tau_{\nu_p}} d\tau_{\nu_p}} \\ &= 1 - e^{-\tau_{\nu_p}(l)} \end{aligned} \tag{2.6}$$

where $\tau_{\nu_p}(l)$ is the optical depth to the absorption event and l is the path length. The position at which the energy packet will be absorbed will then be determined by choosing a random number in the interval $[0, 1]$ and comparing it against $P(l)$. In reality, it is more convenient to use the inverse approach, where the optical depth from the energy packet source to the event can be derived from the inverse of Equation 2.5

$$\tau_{\nu_p}(l) = -ln(1 - U_R) \tag{2.7}$$

where U_R is a random number in the interval $[0, 1]$. Once $\tau_{\nu_p}(l)$ has been calculated then the path length can be directly derived (Harries and Howarth, 1997).

The second method was suggested by Lucy (1999) and it consists of testing whether an absorption event occurs on a cell by cell basis. In other words, assume that within each uniform cell the random path of a packet between events is given by Equation 2.7, which corresponds to a physical displacement, l, given by

$$\tau_{\nu_p} = \kappa_\nu \rho l \tag{2.8}$$

where κ_ν and ρ are the frequency dependent absorption coefficients and the density of the current cell respectively. The method then consists of checking whether the displacement l is large enough to carry the packet out of its current cell. If this is the case, the packet is moved along its direction of travel, $\hat{u}$, up to the boundary with the adjacent cell, where a new value for U_R is cast, giving a new value of τ_{ν_p}, and any further movement of the packet in this new cell is to be followed. Alternatively, if the displacement l is not large enough to carry the energy packet across the next boundary, the packet will be absorbed and then re-emitted at the end-point of the displacement. Lucy also clarifies in his paper that the selection of a new τ_{ν_p} at the crossing of a boundary does not introduce a bias, since a photon always has an expected path length to its next event corresponding to $\tau_\nu = 1$, regardless of the distance it might already have travelled.

In this work both methods were implemented in the code, in turn, in order to test their respective performances. The first method proved to be much more computationally expensive then the second. This is due to the fact that, in order to track down the position at which an energy packet is absorbed, using our knowledge of $\tau_{\nu_p}(l)$, an array searching routine has to be used to locate the index of $\tau_{\nu_p}(l)$ within the array of optical depths calculated from the packet's source to the edge of the nebula. Although the searching procedure employs a bisection technique, which makes it quite efficient, the large number of calls to it, due to the large number of energy packet interactions within a simulation, meant that nearly 60% of the run time was spent carrying out these searches. The second method does not require any calls to the array searching routine, as the packets are followed step by step through the nebula, this results in the run time being considerably reduced. The current version of Mocassin therefore uses Lucy's approach to track the energy packets throughout the nebula.

Finally, the direction of travel of the newly emitted diffuse energy packets (i.e. those

packets re-emitted immediately after an absorption event) needs to be determined every time. Since absorption and re-emission are two independent events, the diffuse packets are emitted isotropically and therefore their direction of travel is chosen randomly using Equations 2.4

2.2.5 The Mean Intensity

The success of a Monte Carlo model often relies on the careful choice of appropriate *estimators*. Monte Carlo estimators provide the means to relate the quantities we *observe* during our Monte Carlo experiment to the physical quantities we want to determine. In a photoionization model, a measure of the radiation field is needed, namely the mean intensity, J_ν.

In the work of Och *et al.* (1998), the Monte Carlo estimator of J_ν is constructed by using the definition of the specific intensity, I_ν, in spherical coordinates, (r, θ), as a starting point:

$$\Delta E = I_\nu(r,\theta)\Delta A \mid cos\theta \mid \Delta\nu\Delta\omega\Delta t \tag{2.9}$$

where ΔA is the reference surface element, θ the polar angle and $\Delta\omega$ is the solid angle. The mean intensity can then be obtained by calculating the zero order moment of I_ν, which gives

$$4\pi J_\nu(r) = \int_\Omega I_\nu \, d\omega = \frac{\Delta E}{\Delta t} \sum_{i=1}^{N_k} \frac{1}{cos\theta_i} \frac{1}{\Delta A} \frac{1}{\Delta\nu} \tag{2.10}$$

by comparison with Equation 2.9. The sum is over all packets N_k with frequency lying in the interval $(\nu, \nu + d\nu)$, crossing ΔA at an angle θ. As discussed above, $\Delta E/\Delta t$ represents the energy carried by a single packet in the time interval Δt, since $\Delta E = \varepsilon_0$, and is given by equation 2.2 . Equation 2.10 then provides a relation between the Monte Carlo *observables* (i.e. the number of energy packets with frequency lying in the interval $(\nu, \nu + d\nu)$, crossing ΔA at the angle θ) and the mean intensity of the radiation field, which is the required physical quantity.

The use of Och *et al.*'s estimators for J_ν, however, becomes problematic in the non-spherically symmetric case, since the reference surface for the volume elements in an arbitrary two- or three-dimensional coordinate system might not be unique or as obvious as in the one-dimensional case. In this work, we seek a more general expression for the estimator of J_ν and, therefore, following Lucy's argument (Lucy, 1999), we construct an

estimator for J_ν starting from the result that the energy density of the radiation field in the frequency interval $(\nu, \nu + d\nu)$ is $4\pi J_\nu d\nu/c$. At any given time, a packet contributes energy $\varepsilon(\nu) = \varepsilon_0$ to the volume element which contains it. Let l be a packet's path length between successive *events* where the crossing of cell boundaries is also considered an event; the contribution to the time averaged energy content of a volume element, due to the l fragments of trajectory, is $\varepsilon_0 \delta t/\Delta t$, where $\delta t = l/c$. From this argument it follows that the estimator for the volume element's energy density can be written as

$$\frac{4\pi J_\nu d\nu}{c} = \frac{\varepsilon_0}{\Delta t}\frac{1}{V}\sum_{d\nu}\frac{l}{c} \tag{2.11}$$

where V is the volume of the current grid cell and the summation is over all the fragments of trajectory, l, in V, for packets with frequencies lying in the interval $(\nu, \nu + d\nu)$. Again, a relation between Monte Carlo observables (i.e. the flight segments, l) and the mean intensity of the radiation field, J_ν has been obtained. Moreover, Equation 2.11 is completely independent of the coordinate system used and, indeed, of the shapes of the volume elements, V. Another important aspect of this approach is that all packets passing through a given grid cell contribute to the local radiation field, even without being absorbed; this means that Equation 2.11 returns estimators of the radiation field even in the extremely optically thin case, when all packets pass through the nebula without any absorption events. From this argument it follows that this technique allows a much better sampling and, hence, in general, much less noisy results compared to other techniques based on estimators for which only packets *absorbed* within a given volume element count.

2.2.6 Gas emissivity and the diffusion of energy packets

As we have already discussed in previous sections, after an energy packet is absorbed, a new packet is re-emitted from the same location in a random direction. The frequency of the re-emitted packet is calculated by sampling the spectral distribution of the total local emissivity, j_ν^{tot}. In order to satisfy the thermal balance implied by the Monte Carlo model, all major emission processes have to be taken into account, including the complete non-ionizing nebular continuum and line emission, since they are part of the energy budget. The non-ionizing radiation generated in the nebula is assumed to escape without further interaction and constitutes the *observable spectrum* which can then be compared with observations. The following paragraphs are concerned with the description of the individual contributions to the total emissivity.

The continuum emission due to H I, He I, He II and to heavier ions is included. The H I continuum can be divided into the Lyman continuum, which is capable of ionizing H, and the Balmer, Paschen, etc. continua, which are not capable of ionizing H. The emissivity in the Lyman continuum is calculated directly from a combination of the Saha and Milne relations:

$$j_\nu = \frac{h\nu^3}{c^2}\frac{\omega_i}{\omega_{i+1}}\left(\frac{h^2}{2\pi mkT_e}\right)^{3/2} a_\nu(\mathrm{X}^i) e^{-h(\nu-\nu_0)/kT_e} \mathrm{X}^{i+1} N_e \qquad (2.12)$$

where ω_i and ω_{i+1} are the ground state statistical weight of the ions involved, X^{i+1} is the abundance of the recombining ion, $a_\nu(X^i)$ is the photoionization cross section and ν_0 is the photoionization threshold. The emissivity of the other series continua are obtained by interpolation of published data (Ferland, 1980). A similar approach is used for the He I and He II continua, where for frequencies greater than 1.8 Ryd and 4 Ryd, respectively, Equation 2.12 is used, and the emissivities at lower frequencies are obtained by interpolation of the data published by Brown and Matthews (1970) for the He I series and by Ferland (1980) for the He II series. The continuum emissivity due to heavy elements is also calculated using Equation 2.12. In the hydrogenic case (i.e. H I and He II) the two-photon continuum is calculated using the formalism described by Nussbaumer and Schmutz (1984); the data of Drake *et al.* (1969) are used for He I.

Recombination lines between lower levels n=2 through n=8 and upper levels n=3 through n=15, for H I, and lower levels n=2 through n=16 and upper levels n=3 through n=30 for He II, are calculated as a function of temperature according to the Case B data published by Storey and Hummer (1995). The He I recombination lines are calculated as a function of temperature using the data of Benjamin *et al.* (1999). In general, He I singlet lines follow Case B whereas triplet lines follow Case A (as there is no n = 1 level for the triplets). Transitions to the 1^1S ground state of He I produce lines which are capable of ionizing H and low ionization stages of higher elements. In particular, the emissivities of the He I Lyman lines from n=2 through n=5 (Brocklehurst, 1972) and the intercombination lines corresponding to the transitions 2^3S-1^1S and 2^3P-1^1S are estimated as a function of temperature using the data of Robbins (1968). The contributions due to these lines to the total energy distribution, from which the probability density functions are derived, are added to the respective energy bins. Similarly, He II Lyman lines can ionize both neutral hydrogen and neutral helium, as well as some of the low ions of heavier elements. Therefore the emissivities of the He II Lyman lines from n=2 through n=5 (from Storey

and Hummer, 1995) are also estimated as a function of temperature and their contributions to the total energy distribution added into the respective frequency bin, as for the He I lines. This method is based on the fact that all emission profiles are currently treated as δ functions and the line opacity is assumed to be zero.

It is worth noting at this point that, in reality, not all He II Lyα line photons will be available to photoionize H^0 and He^0, a fraction of these will, in fact, be absorbed by O^{2+} exciting the 3d $^2P^0_2$ level of O III, via the Bowen resonance-fluorescence mechanism (see Section 1.2.3). Most of the lines produced from the downward cascades to the ground term $2p^2$ of O III are emitted in the UV, and are therefore assumed to simply escape from the nebula without further interaction. However, some of the lines produced by this process are emitted shortward of 504 Å and can, therefore, be absorbed by H^0 and He^0. These include the two direct transitions $2p^2\ ^3P$–$3d\ ^3P^0_2$, and the $2p^2\ ^3P$–$2p3s\ ^3P$ lines (the strongest of which being the $2p^2\ ^3P_2$–$2p3s\ ^3P^0_1$ at 374.436 Å). For all the downwards routes mentioned so far, however, *one* H^0 and He^0 ionizing He II Lyα photon is simply exchanged with *one* other H^0 and He^0 ionizing photon at a slightly different wavelength. The O III 2p3p term, however, can also decay to the ground $2p^2$ term via the $2p^3$ term, hence emitting *two* H^0 ionizing photons, with wavelengths between 660 Å and 550 Å, for the first photon and 700 Å and 830 Å, for the second photon. This finally means that a certain fraction of He II Lyα photons captured by O^{2+} will actually be converted into *two* H^0 ionizing photons, hence increasing the number of secondary photons –extra ionizing photons– available, and possibly resulting in a slightly larger Hβ flux. The exact treatment of this process is, however, very complicated and most of the currently active photoionization codes use some sort of approximation to estimate the number of extra ionizing photon produced by each primary ionization of He^+ (including the production of the He II Ly lines and of the Bowen lines mentioned above). As described in the previous paragraph, Mocassin already takes into account the production of secondary ionizing He II Ly photons, although the capture of these line photons by O^{2+} ions and the possible subsequent line emission is not taken into account. However, the following simple calculation shows that the effect of the Bowen mechanism *alone* on the final Hβ flux is actually very small and probably within the uncertainty introduced by the use of an approximation. If a Bowen efficiency of 0.40 is assumed for a given object and, since there is approximately 50% probability that the 3p term will decay to the ground $2p^2$ through the $2p^3$ term (hence emitting two H^0 ionizing photons), then this means that 1.2

extra H^0 ionizing photons are introduced by the Bowen fluorenscence mechanism for each He II Lyα line photon. In general, the recombination of He^{2+} and all subsequent processes (including the Bowen resonance-fluorescence mechanism) can generate approximately 1.5-1.8 H^0 ionizing photons for each primary ioniztion of He^+, possibly increasing the Hβ flux by a factor of $\approx$1.3 (Péquignot, private communication). From this it follows that, since 1.2 extra secondary photons are created for each He^{2+} recombination, approximately 1.10-1.15 extra ionizing photons are created for each primary ionization of He^+ by the Bowen resonance-fluorescence mechanism *alone*. This could then result in the Hβ flux being increased by approximately 6%. This is a very rough estimate and should, in fact, be taken as an upper limit to the real increase, since the N III resonance-fluorescence mechanism, mentioned in Section 1.2.3 and discussed by Liu (1993) has not been taken into account. This mechanism would, in fact reduce the number of extra H^0 ionizing photons by the resonant absorption of the O III $2p^2\ ^3P_2$–$2p3s\ ^3P^0_1$ line at 374.436 Å by N^{2+} ions. Given the very small magnitude estimated for the effects of the Bowen resonance-fluorescence mechanism alone on the final flux of Hβ, and, after taking into consideration the high level of uncertainty introduced by an approximate treatment of this process, which involves the knowledge of the Bowen efficiency (different for every object), it was decided to neglect this process altogether in the current version of Mocassin. It is clear from the benchmarking carried out in the next Chapter that the exclusion of this effect does not make any appreciable difference to the final results.

Finally, the emissivities of the collisional lines of the heavier ions are calculated. This is done by using matrix inversion procedures in order to calculate the level populations of the ions. Appendix A contains references for the atomic data used for each ion.

The energy distribution is derived from the total emissivity, summing over all the contributions in a particular frequency interval. The non-ionizing line emission is treated separately, since, whenever such line packets are created, they escape without further interaction [1].

Once the line and continuum emissivities have been calculated, the probability that the absorption of an ionizing energy packet will be followed by the emission of a non-ionizing

[1]Resonance lines longward of 912 Å (e.g. C IV$\lambda\lambda$1548, 1550) may, in fact, diffuse out of the nebula via resonant scattering and may also be absorbed by dust during such diffusion. A treatment of dust grains will be included in future developments of the Mocassin code, and such effects may then be accounted for.

packet is given by:

$$P_{esc} = \frac{\sum_i j^l_{X^i} + \int_0^{\nu_H} j^c_\nu d\nu}{\sum_i j^l_{X^i} + \sum j^l_{\rm HeI} + \sum j^l_{\rm HeII} + \int_0^{\nu_{max}} j^c_\nu d\nu} \tag{2.13}$$

where ν_{max} is the higher limit of the frequency grid; the $j^l_{X^i}$ are the emissivities of the non-ionizing recombination lines of all species considered; j^c_ν is the frequency dependent continuum emissivity; $j^l_{\rm HeI}$ and $j^l_{\rm HeII}$ are the contributions due to those recombination lines of He I and He II which are capable of ionizing neutral hydrogen and neutral helium. The choice between the re-emission of an ionizing packet or a non-ionizing packet is made at this point in the code.

If an ionizing energy packet is to be re-emitted, then the new frequency will be calculated according to the normalized cumulative probability density function for the ionizing radiation, given by

$$p(\nu) = \frac{\int_{\nu_{\rm H}}^{\nu} j^c_{\nu'} d\nu' + \sum j^l_{\rm HeI} + \sum j^l_{\rm HeII}}{\int_{\nu_{\rm H}}^{\nu_{max}} j^c_{\nu'} d\nu' + \sum j^l_{\rm HeI} + \sum j^l_{\rm HeII}} \tag{2.14}$$

where, as usual, the contributions due to the He I and He II lines are added in the corresponding frequency bins. If a non-ionizing energy packet is to be re-emitted, then its frequency can be determined from the probability density function for non-ionizing radiative energy, which is analogous to Equation 2.14.

2.2.7 The Iterative Procedure

An initial guess of the physical conditions in the nebular cells, such as the ionization structure, electron temperature and electron density, needs to be specified before the simulation can begin. Procedures in Mocassin have been constructed such that only an initial guess at the electron temperature (which is initially set to a constant value throughout the nebula) must be included in the input file. Mocassin can then guess an initial ionization structure and, hence, the electron density. Alternatively, Mocassin can be run in its one-dimensional mode (see Section 2.2.9) to generate one or more one-dimensional solutions, which can then be mapped onto the three-dimensional Cartesian grid, using the simple built-in interpolation procedures. Several tests have shown that the choice of the initial conditions has no influence on the final result of the simulation, but it can, however, have a small impact on the number of iterations required to reach convergence.

Once the initial conditions are specified, the frequency dependent total emissivities are calculated in each grid cell in order to set up the probability density functions for

re-emitted radiation, which are used for the determination of the frequency distribution of the re-emitted energy packets during the Monte Carlo simulation. The energy packets are then fired through the grid and their trajectories computed. Once all the energy packets trajectories have been computed, the Monte Carlo estimators for the mean intensity of the stellar and the diffuse radiation fields can be obtained, as described in Section 2.2.5. The ionization fraction and the electron temperatures and densities must now be updated to be self-consistent with the current estimates of the radiation field at each grid point. This means solving the local ionization balance and thermal equilibrium equations simultaneously. The entire procedure is repeated until convergence is achieved. The convergence criterion used in most of this work is based on the change of the hydrogen ionization structure between successive iterations. In some cases, however, this is not a suitable convergence criterion (e.g. in hydrogen-deficient environments), for this reason, other criteria are also implemented in the code (e.g. based on the change of the local helium ionization structure, or of the local electron temperature between successive iterations), and these can be easily selected by using the appropriate switches in the input file.

2.2.8 The Adaptive Grid

Adaptive grid routines are implemented in order to ensure an adequate spatial sampling throughout the duration of the simulation, as the local physical conditions in the ionized region change. First of all, as the model develops, the original estimate for the Stroemgren radius of the nebula, whether provided by the user or calculated by Mocassin at the start, might become inappropriate if the hydrogen ionization front moves. The procedure *adjustOuterRadius*, is designed to check the abundances of neutral hydrogen at the edges of the nebula in the three axial directions independently. If it is found that hydrogen does not recombine within the Cartesian grid in a given direction, then the outer radius of the nebula is increased by a factor, *grow*, specified by the user in the input file. If, on the other hand, hydrogen recombines too far from the outer edge inside the nebula, the outer radius is then decreased by the same factor *grow*. Note that the above is only valid in the case when the nebula is radiation bounded, in the case when we want to construct a matter bounded model, the *adjustOuterRadius* procedure must be disabled and the outer radius of the nebula must be decided upon before the start of the simulation.

As the simulation progresses, the need might also arise for better spatial resolution in particular regions of the grid inside the ionized region. If, for example, the optical depths

at a given significant frequency vary too rapidly from one cell to the next, then more grid points must be introduced in this region. The procedure *adjustGrid* checks the gradients of the optical depths from one cell to the next in the three axial directions. If at a given location the gradient is greater than the limit set by the user in the input file, a new axis point will be introduced at that position. Both the *adjustOuterRadius* and the *adjustGrid* routines write the modified grid axis out to a file before going out of scope, and the new grids are then created and set up by separate procedures, which are discussed next. As we have already mentioned elsewhere, most three-dimensional simulations are very expensive in terms of memory usage and computational time, this is due to the volume of data comprised within such grids. The easiest and most natural way to map an existing grid onto a new larger or smaller one would be to create a new grid, defined spatially in the *adjustOuterRadius* and the *adjustGrid* routines' output files, and to map the old grid onto it. This, however, implies that both grids must exist in the computer memory at the same time, which, of course, is prohibitively expensive. The other solution, which was adopted in this work, is for the old grid to be written out to disc, and then only when all its memory has been deallocated, the new grid to be created. The old grid arrays are then read into memory and mapped onto the new grid, one by one, deallocating their memory as soon as they are no longer needed. The reading and mapping of the old grid onto the new one is performed by a subroutine called *refillGrid*, which, like all the other adaptive grid routines, is included in the *grid_mod* module (see Section 2.3.1).

2.2.9 The One-Dimensional Mode

A one-dimensional mode was also implemented in order to allow Mocassin to treat spherically symmetric problems more efficiently. There are several instances when a faster one-dimensional computation may be preferable to a fully three-dimensional one. First of all, in the case of benchmarking the code with other one-dimensional codes, as will be discussed in the next chapter, and also when modelling objects which are not spatially resolved in the observation. In these cases spherical symmetry is generally assumed, and a fully three-dimensional treatment is not necessary. Finally, as discussed in Section 2.2.7, the output from one or several one-dimensional runs can be fed into the full version of Mocassin to be mapped onto the three-dimensional grid and used as starting conditions.

When the one-dimensional mode is enabled, Mocassin will work on a *strip* of cells, by creating a $(n \times 1 \times 1)$ grid. The transport of the energy packets is then carried out

on a *virtual* three-dimensional grid (which does not require any memory) with all the packets' contributions to the radiation field being added to the cells at the appropriate radial positions on the strip. There is, in practice, a switch from Cartesian coordinates to polar coordinates and the volume of each cell in the strip is assumed to be that of a spherical shell having the same thickness as the x-dimension of the corresponding cell. It is clear from the above that the treatment of the radiative transfer is the same when the one-dimensional mode is enabled and therefore self-consistent for both components of the radiation field. This gives the one-dimensional version of Mocassin an advantage over most classical spherically symmetric codes, where various approximations for the transport of the diffuse component of the radiation field are normally used.

2.2.10 Comparison of the Model with Observations

When the model has converged to its final solution, the output spectrum can be computed and compared with the results obtained from other models or with observational data. The total luminosity of the nebula in various emission lines longward of the Lyman limit can be obtained by using two methods. The first method, which is only available to Monte Carlo codes, consists of summing up the number of energy packets in the given line, N_{line}, over all the grid cells. Hence, the power emitted in that line is given by

$$L_{line} = \frac{\varepsilon_0}{\Delta t} \sum_{i=1}^{i_{max}} \sum_{j=1}^{j_{max}} \sum_{k=1}^{k_{max}} N_{line}(x_i, y_j, z_k) \tag{2.15}$$

where $\frac{\varepsilon_0}{\Delta t}$ is given by Equation 2.2, i_{max}, j_{max} and k_{max} are just the upper limits of the grid extent. The second method consists of using the values of the local electron temperatures and ionic abundances given by the final model solution to obtain the line emissivities for each grid cell. The luminosity of the nebula in any given line can then be calculated easily by integrating the emissivity of the required line over the volume of the nebula.

A comparison of the results obtained using the two methods described above, provides an indication of the level of accuracy achieved during the simulation, as the two methods will give consistent results only if enough energy packets are used in order to yield good statistics for every line. However, in general, the second method (formal solution) yields the most accurate results, particularly for weak lines, which only emit a few photons.

In addition to the integrated emergent spectrum, other useful comparisons with the observations can be carried out; e.g. projected images of the final model nebula in a given line or at a given continuum frequency can be produced for arbitrary viewing an-

gles. These can be compared directly with real images obtained in an appropriate filter. Mocassin computes and stores the physical properties of the nebula as well as the emissivities of the gas at each grid point; these can be fed into IDL plotting routines in order to produce maps (Morisset *et al.*, 2000). Also, by assuming a velocity field, line spectral profiles can be produced, together with position-velocity diagrams. These can be compared with observations, if available, to deduce spatio-kinematic information of the object being studied. A more detailed description of the IDL visualization routines is given in Section 2.4 and in Morisset *et al.* (2000) and Monteiro *et al.* (2000).

2.3 Mocassin Architecture

The Fortran 90 programming language was used to write the Mocassin code. Several considerations are behind this choice, however there are two main reasons. Firstly, the need for a language which can provide some higher level features, such as dynamic allocation of memory and modularity, and, secondly, the need for backward compatibility with Fortran 77. Dynamic allocation and deallocation of memory is very important in terms of writing efficient code, especially in those cases where the manipulation of large arrays of data is required and memory usage, therefore, becomes a fundamental issue. The pointer facilities provided by Fortran 90 are extremely useful for the efficient manipulation of the several multi-dimensional arrays used in the code. Another important feature offered by Fortran 90, which did not exist in Fortran 77, is the *module* program unit. In simple words, the main reason for constructing a module is to make some or all the entities declared within it accessible by other parts of the code, but in a safer and more controlled manner than by using common blocks. Modules that share each other's public entities are said to be *use-associated.* The segmentation of a large code into self-contained modules, which can interact with each other only through specific interfaces, has several advantages as it improves clarity, thus facilitating future development and maintenance of the code. *Derived types* allow the creation of user defined variable *types*, which are very useful when writing complex programs as they allow information to be stored in a more compact and logical manner. Derived type variables have, in general several components, intrinsic types or other derived types, which can be easily accessed individually or as a group, hence aiding the clarity of the referencing in the various procedures' argument lists. Examples of the derived variable types constructed in this work are contained in the common_mod module,

which is described in Section 2.3.1. More information about the general characteristics of the Fortran 90 programming language and its differences from Fortran 77 can be found, for example, in Ellis *et al.* (1994).

Many of these features, in fact all of them, are available in other programming languages such as C and C++, with functions such as, for example, *malloc* and *calloc* for the dynamical allocation and *free* for deallocation of memory, and with *structures* and *unions* which are analogous to the Fortran 90's derived variable types. The final choice of Fortran 90 over the other languages was ultimately due to the backward compatibility issues with Fortran 77, since, over the years, a great deal of astrophysical research has been carried out using this language.

Mocassin was developed and run initially on a Compaq(Dec) XP1000 with a 500 MHz CPU and 1 Gb of memory and a preliminary serial version of the code still exists. A fully parallel version of the code has since been developed using Message Passing Interface (MPI) routines and it currently runs on a Silicon Graphics Origin 2000 machine with 24 processors and 6 Gb of memory and a SUN Microsystems Sunfire V880 machine with 16 processors and 64 Gb of memory. In general, Monte Carlo simulations are, by their own nature, very parallelizable problems and, indeed, Mocassin can achieve a linear *speed-up*, i.e. a speed-up that is directly proportional to the number of processors used. A more detailed description of the parallel logic used is given in Section 2.3.1.

2.3.1 Computational Methods

As we have already mentioned, Mocassin has a modular design in aid of flexibility, which is fundamental to future development and maintenance. With regards to this issue, every effort has been made to ensure that appropriate referencing and comments are available throughout the code, with descriptions of every module and most procedure within them. The next few paragraphs contain brief descriptions of all of Mocassin's modules and their role within the model, as well as a brief description of the three main simulation drivers. The following paragraphs are ordered alphabetically, by the name of the module unit described.

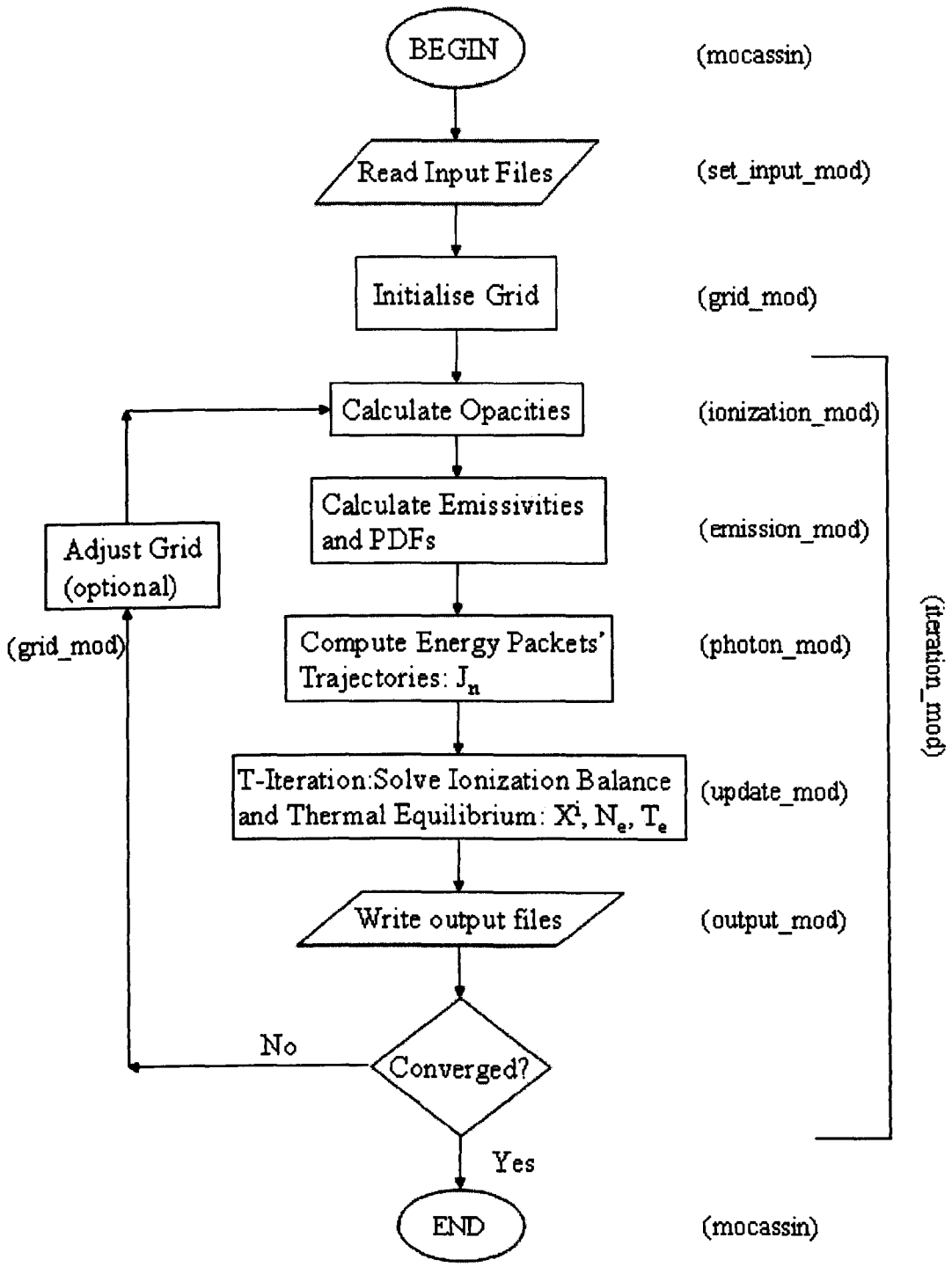

Figure 2.1: Mocassin flow-chart. The modules in scope at each stage are given in parentheses.

2.3.1.1 The common variables module

Common_mod contains the declaration of all public [2] variables used by most modules and it also contains the declaration of the two main derived types: *grid_type* and *energy_packet_type*. These are the two fundamental objects of the simulation. A grid_type variable consists of several multi-dimensional arrays of real, integer and logical variables, which completely define the physical conditions throughout the nebula. They include gas densities, electron densities, temperatures, ionization structure, opacities, radiation fields etc. The energy_packet type completely characterises an energy packet by carrying information about its frequency, type (stellar or diffuse, line or continuum), position and direction vectors. Some other global entities included in this module are the frequency grid, with all its pointers, and the photoionization cross-section array for all the elements. Note that this module only contains the variables declarations but no hard data, which are either stored into separate external files (as in the case of photoionization cross-sections data) or calculated elsewhere in the code (as in the case of the frequency grid). The initialization of the variables declared in the common_mod module will then be carried out by the relevant procedures at the appropriate time during the simulation.

2.3.1.2 The composition module

Composition_mod sets up the chemical composition of the nebula. This module contains the procedures to read from the appropriate external file according to the 'composition' field in the grid_type variable. This field is set by the user with the input command *nebComposition* (e.g. 'solar' etc). The first thirty elements can all be included in the simulation, although the atomic data, when available at all, for some of the less frequently used elements are patchy. However, only a fraction of these will be needed for the modelling of most nebulae. There are several switches throughout the code to ensure that no memory is allocated and no loop time wasted on absent elements. This module only needs to be called once at the beginning of the model and it is at this time that the elements' on/off switches are set, so when a given element's abundance is set to zero in the composition data file, this element will automatically be switched off. The references for all the atomic data currently used in the code are given in Appendix A.

[2] The variables declared in common_mod are only accessible to those modules which are use-associated to it (see Section 2.3).

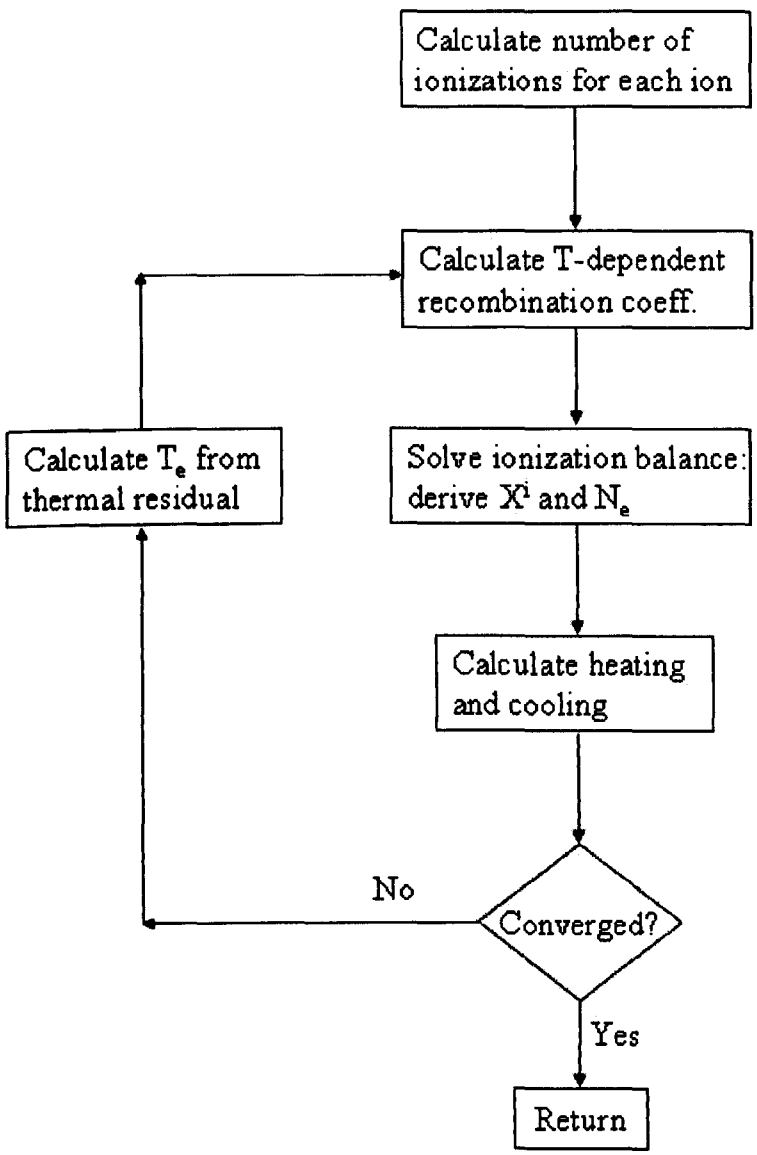

Figure 2.2: Temperature iteration flow-chart.

2.3.1.3 The physical constants module

Constants_mod contains all the public physical and mathematical constants which are used by various other modules throughout the code. Unlike the items included in common_mod, all variables in this module are declared with the keyword *parameter*, which means that their value cannot be changed during the simulation, and are initialized within the module.

2.3.1.4 The incident continuum module

Continuum_mod deals with the calculation of the intensity of the incident continuum. The global variable *contShape*, set up by the user in the input file, can either specify the name of an external model atmosphere data file or can be set to the keyword *blackBody*, if a black body ionizing continuum is required. So this module contains the procedures to read the data from a file or calculate the black body spectral distribution for the given stellar temperature. The frequency distribution of the emitted stellar energy packets is derived from the incident spectrum through the probability density functions, (see Section 2.2.3), which are also calculated here. This module is called only once before the first iteration and only the probability density functions are stored for the duration of the experiment.

2.3.1.5 The gas emission module

Emission_mod contains all the procedures to deal with the redistribution of radiation during the Monte Carlo run. The physical processes included have already been described in detail (see Section 2.5). The frequency dependent emission from the continuum and from all emission lines is calculated first. The probability density functions are then derived from these, according to Equation 2.14 and its analogue for line emission, and used to determine the frequency distribution of the re-emitted diffuse energy packets. This module is central to the code and most of its procedures need to be called after each iteration in order to re-calculate emissivities and update the probability density functions at each grid cell.

2.3.1.6 The atomic data module

Elements_mod contains the procedures to set up some of the atomic data for hydrogen, helium and the other elements. The data sets are statistical weights, level energies etc. The collisional strengths and the transition rates for the heavy ions' collisional lines are

not set up at this point. They are stored into individual external files for each ion and read into memory only when needed by the matrix inversion procedures in *emission_mod*, which calculate the level populations and the line emissivities. This module only needs to be called once at the beginning of the simulation.

2.3.1.7 The grid module

Grid_mod contains all the procedures for the initialization and the manipulation of the three-dimensional Cartesian grid, including procedures needed to map the results from one or more spherical symmetric models onto it, if desired. However, it was not necessary for any of the simulations carried out in this work to utilise the results of a one-dimensional code as initial conditions, as Mocassin succeeded in reaching convergence within an acceptable number of iterations by using its own guesses at the initial electron temperature distribution and ionization state of the nebulae.

The adaptive grid procedures are also contained in this module. The user can decide whether to use the adaptive logic or to define an adequate grid according to the available memory. As described in Section 2.2.8, a feature of the adaptive logic is that the grid axes are independent of each other, therefore the user can decide to modify the grid at any chosen time in any of the six directions($\pm$x, $\pm$y, $\pm$z) according to the geometrical nature of their problem. It is worth noting at this point that the *adjustGrid* and the *adjustOuterRadius* routine will increase the total number of grid cells by introducing new axis points where needed. The memory usage will therefore increase as the arrays' dimensions increase; this should be taken into account when running Mocassin through a restricted memory queuing system. When a program deals with three-dimensional problems the size of the data is, in most cases, very large, and memory usage has been a fundamental issue throughout the development of the Mocassin code. Although an adaptive grid is very useful and a photoionization code would not be complete without such a feature being implemented, we have found that it is more economic in terms of CPU time and memory to decide on a suitable grid beforehand, perhaps by doing some mock runs, and then disabling the adaptive grid. A more detailed description of the adaptive grid procedures is given in Section 2.2.8.

2.3.1.8 The interpolating routines

Interpolation_mod contains all the procedures used for the interpolation of data throughout

the code. These include a *locate* subroutine, which uses the method of bisection in order to locate the position of a variable within a given array. Subroutines for polynomial and cubic spline interpolation are also included, together with a subroutine to perform three-dimensional linear interpolations. Note that one-dimensional linear interpolation, in logarithmic or linear scales, is widely used throughout the code. This is, however, a trivial task and it can be embedded in the code without the need for an external procedure to be written. Note also, that polynomial interpolation is not actually used anywhere in the code on a regular basis, however the routine is still included for testing and debugging purposes.

2.3.1.9 The ionization module

Ionization_mod is another central module in the code. It contains the procedures to calculate the frequency-dependent absorption opacities in any given grid cell, as well as subroutines to calculate Boltzmann and Gaunt factors and other continuum-related variables. As for the emission module, the *ionization_mod* driver also needs to be called after each iteration in order to update the opacities in each grid cell, as the ionization structure of the nebula changes.

2.3.1.10 The main drivers

Three main drivers have been developed to run Mocassin. Each driver can be selected by including it into the *make* command when compiling the program. All the modules are designed to work with any of the drivers described below without the need for any modifications.

Mocassin is the main driver of the Monte Carlo simulation. It contains a set of instructions to call the grid and continuum initializing modules at the start, and then a call to the main Monte Carlo iteration driver, which is where most of the computational time will then be spent, before returning back to *Mocassin*, when convergence is reached, to perform the final operations of freeing all the memory allocated to the grid arrays and finalizing the MPI routines.

MocassinWarm is the *warm start* version of Mocassin. Here the grid is initialised with the results computed by a previous *Mocassin* simulation and stored into three grid files. After the initialization the simulation then proceeds as usual. *MocassinWarm* starts off with a call to the *resetGridRoutine*, defined within the *set_input_mod* module, which

reads the physical properties of the nebula from external files and assigns them to the Cartesian grid. Continuum initialization routines then follow and then the call to the main Monte Carlo iteration driver. Just as for the standard *Mocassin* main function, the program returns to it when convergence is achieved and the final deallocation of memory and finalizing of the MPI routines is performed.

MocassinPlot is used as a driver when the luminosity of each individual volume element in a given set of lines or at a given set of continuum frequencies is required for plotting. The plots specifications must be listed in the *plot.dat* file, which is a text file composed by two columns: the first containing the *line* or *continuum* specifier; the second containing either the required emission line code number (obtainable from the *lineFlux.out* file), or the continuum frequency in units of [Ryd] and the width of the range. In this work only the emission line plotting device has been used in the models. This version of the program uses the same input files as the *warm start* version to initialise the Cartesian grid. The gas continuum or line emissivities, and hence the line or continuum luminosities required, can be calculated analytically from the physical properties of each volume element, which are known from a previous simulation. This is the fastest route to obtaining an accurate solution, and it is selected by setting the *lgAnalytical* switch in the driver to *.true.* . Another method consists of computing the trajectories of a large set of energy packets, and calculating the line or continuum luminosities of each grid cell according to Equation 2.15. This second method is much more time consuming as a very large number of energy packets must be employed in order to achieve an adequate accuracy for the weaker lines.

2.3.1.11 The Monte Carlo iteration driver

The *iteration_mod* module is the driver for the main Monte Carlo iteration. As shown in the scheme given in Figure 2.1, the first step of the iteration is to calculate the frequency-dependent opacities in each grid cell according to the current estimates of the ionic abundances. These will be needed later in order to compute the energy packets' trajectories. The gas emissivities at each grid cell are then calculated using the current estimates of the physical properties of the nebula. At this point, the energy packets' histories can be computed and, from these, estimates for the local frequency-dependent mean intensities of the stellar and diffuse radiation fields can be derived. The next step involves the solution of the ionization balance and of the thermal equilibrium equations simultaneously, in order to obtain new estimates for the electron temperatures, ionic fractions and electron densi-

ties. A more detailed description of the temperature iteration is given in Section 2.3.1.17. Regardless of whether the module is fully converged, the results obtained at the end of each iteration are written out to files (see Section 2.3.1.12) for the reasons discussed in the next paragraph.

2.3.1.12 The output module

The *output_mod* module contains all the procedures to calculate line luminosities, weighted mean electron temperatures and whatever output is required for the current model. The files produced by this module are listed and described in more detail in Section 2.3.3. The output is calculated and written out to files at the end of each iteration, together with all the physical properties of the nebula at each grid cell. The main reason for choosing to write the grid physical properties out to disc after each iteration is to allow the implementation of a *warm start* facility. This is a very powerful tool in long simulations as it allows the simulation to be interrupted at any time and restarted from the last iteration. The reasons for wanting to stop a simulation could be many, for example, one might decide to run a particular simulation only at night when the computer usage is reduced, or one might want to increase the number of energy packets used, or even change some of the input parameters and use the last iteration as the starting point for the new simulation. The advantage of computing and writing out results after each iteration also lies in the fact that users can then keep track of the progress made by their model as it is computed, hence decide whether they want to carry on with it, without having to wait until convergence is achieved in all grid cells. The *warm start* routine is described in more detail in Section 2.3.1.10.

2.3.1.13 The opacity path integration module

PathIntegration_mod performs the integration of opacities along an arbitrary path through the nebula. This module is called whenever the optical depth from a given position to the edge of the nebula along a given direction is required. As discussed in Section 2.2.4, when computing the energy packets' trajectories using the method outlined by Harries and Howarth (1997), the run of the optical depths from the location of the emission of an energy packet to the edge of the nebula along the packets' direction of travel is required, in order to calculate the path length to the next absorption event. In this scheme, the *pathIntegration_mod* module is central to the program and needs to be called many times

during a simulation. However, in the strategy adopted in this work (Lucy, 1999), this module does not need to be used as much anymore, since only the optical depth to the crossing of the next cell boundary is required, and this is simply given by Equation 2.8. The procedures for the integration of the opacity along a given path are still used in the code, as the run of the optical depths from the centre of the grid to the edge of the nebula, along the three axis directions, is calculated and given as output in the file *tau.out*. The gradient of the optical depth at an energy of 1 Rydberg from one cell to the next is used by the adaptive grid routines as a criterion to check the spatial sampling, this module is therefore called once again when the adaptive logic is active (see sections §2.2.8 and §2.3.3).

2.3.1.14 The energy packet diffusion module

Photon_mod contains all the procedures for *creating* (i.e. initializing) and managing the energy packets throughout the simulation. This module can be considered as the heart of the Moccasin code and it contains most of the Monte Carlo logic. The energy packets' trajectories are computed here and the estimators of the mean intensity of the radiation field, J_ν^{ste}, for the stellar, and J_ν^{dif} for the diffuse component, are evaluated before the module goes out of scope. Only one packet at a time is followed by each processor by means of the recursive subroutine *energyPacketRun*; this procedure will keep calling itself until the history of the current packet is concluded, which is when the energy packet escapes the nebula by either reaching the outer edge or by being transformed into a line packet with energy below the ionization potential for any ions, in which case it escapes the nebula without further interaction.

2.3.1.15 The initialization module

Set_input_mod contains the subroutines to read the input files and set up the specifications of the current simulation. A more detailed description of the possible commands which can be included into the input file is given Section 2.3.3. As discussed in Section 2.2.7, the initial conditions of a simulation can be obtained by running Mocassin in its one-dimensional mode, to generate one or more one-dimensional solutions. The grid files produced can then be used by the grid procedures which will map the results onto the three-dimensional grid according to the particular geometry of the problem. As discussed earlier, however, Mocassin can also use its own guesses of the initial conditions to begin a

three-dimensional (or a one-dimensional) simulation with, and, therefore, the utilization of results from the one-dimensional mode is not essential at all.

2.3.1.16 The vector mathematics module

In a three-dimensional Cartesian grid the use of vectors is necessary on many occasions. The definition of the derived vector type and all the procedures needed to perform mathematical operations on vectors are contained in the *vector_mod* module. This module also includes procedure to obtain random unit vectors, using Equations 2.4, which are used to assign a direction of travel to newly created stellar or diffuse energy packets.

2.3.1.17 The ionization balance and thermal equilibrium module

The ionization balance and thermal equilibrium are enforced in each grid cell in order to derive local ionic fractions, as well as electron densities and temperatures. Figure 2.2 shows a schematic representation of the temperature iteration which is carried out at each grid cell by the procedures contained in the *update_mod* module. First of all, the number of stellar radiation fields and diffuse field photoionizations are derived for each ion from the Monte Carlo estimators of the radiation field, J_ν^{ste} and J_ν^{dif}, according to

$$N_{phot}^{ste} = N(X^i) \int_{\nu_{X^i}}^{\infty} \frac{4\pi J_\nu^{ste}\, a_\nu(X^i)}{h\nu} d\nu \tag{2.16}$$

where $N(X^i)$ is the density of the ion X^i, $J_\nu^{ste}\, d\nu$ is the Monte Carlo estimator of the radiation field in the frequency interval $(\nu, \nu + d\nu)$, calculated according to Equation 2.11; $a_\nu(X^i)$ is the frequency dependent photoionization cross-section of the ion X^i, and ν_{X^i} is the ionization threshold frequency of the ion X^i. Another equation, analogous to Equation 2.16, exists to calculate the number of diffuse photoionizations of the same ion. The next stage of the temperature iteration is the calculation of the temperature-dependent recombination coefficients. Both radiative and dielectronic contributions are included where available. The references for the atomic data used are given in Appendix A. It is worth noting that the recombination coefficients are calculated using the current estimates of the electron temperature. At this point all the elements to solve the photoionization equilibrium equations for each ion have been obtained. These equations are coupled and, therefore, they must be solved simultaneously; this is achieved by making the ionization equilibrium routine a recursive one, which keeps calling itself until convergence of the main ionic fractions is reached. Incidentally, the temperature iteration is also carried out

in the same fashion, by using a recursive temperature iteration driver. Using the new estimates for the ionic fractions and electron density, the total heating due to photoionization and the total cooling due to recombination, free-free radiation and collisional excitation of heavy element ions can be calculated. If the thermal residual is below the limit set for convergence, the temperature iteration is concluded and the current estimates of the physical conditions in the nebula returned to the grid in the main Monte Carlo iteration driver. On the other hand, if the condition for convergence is not satisfied, a new correction for the electron temperature is derived by setting the thermal residual to zero. The convergence limit can be adjusted by modifying the variable *thLimit* in the *update_mod* module.

2.3.1.18 The Opacity Module

The *xSec_mod* module contains all the procedures to initialise the opacities array. The cross-sections for all opacity sources are stored in the same one-dimensional array, *xSecArray* and accessed using a system of pointers. The cross-section array is created by the *initXSecArray* routine, which also sets up all the relevant pointers. Most of the data used in this module was taken from the Opacity Project (Verner *et al.*, 1996); full references for all the atomic data used are available in Appendix 1

2.3.2 The Message Passing Interface (MPI) Routines

MPI is a standard specification for *Message Passing Interface*, providing message passing programs for Fortran and C languages. When running a simulation on multiple processors there will be parts of the code which will be run by all processors, in fact, in the parallel version of Mocassin, every processor has its own copy of the three-dimensional grid, whereas, in other parts, particularly loops, the workload can be shared amongst all the processors in use, hence decreasing the time of the computation. For example, if the trajectories of 10^6 energy packets have to be computed and there are 10 processors available, then each of them will only need to compute the trajectories of 10^5 packets. However, after all the packets' trajectories have been calculated, the information about the radiation field at each grid point obtained by each individual processor must be shared with all the others before the next step of the simulation can be carried out, with the processors, again, sharing the workload between them. It is in this exchange of information amongst the processors that the MPI functions are applied. A number of message passing functions

Table 2.1: Mocassin's input commands and default values.

Keyword	Default	Keyword	Default
autogrid	.true.	nPhotons*	NA
autoInitialize	.true.	nuMax	24.
contShape	'blackbody'	nuMin	1.001e-5
convLimit	0.05	nx	30
densityFile	'none'	ny	30
densityLaw[b]	0.	nz	30
grow	1.05	oneD	.false.
Hdensity[b]	0.	Rin	0.
LPhot[a]	NA	Rout[c]	0.
LStar[a]	NA	symmetrixXYZ	.false.
maxIterateMC	30	talk	.false.
mu	0.5	tauRatio	100.
nbins	300	TeStart	10000.
nebCombosition	'solar'	TStellar*	NA

* this field is essential and must be included in the input file.

[a] either Lphot or LStar must be defined (see text).

[b] either Hdensity, densityLaw or densityFile must be defined (see text).

[c] if Rout is not entered Mocassin will use its own estimate of the Stroemgren radius.

were employed throughout the code and very extensive testing was carried out to ensure that no bias was introduced by the parallelization process. More information about MPI functions and constants can be found at *http://www-unix.mcs.anl.gov/mpi/mpich/*.

2.3.3 Input Commands

The input parameters of a Mocassin simulation are defined by the user in the input file using a set of keywords. Not all the parameters described in this section are needed for each simulation; in fact, with the exception of a few essential ones, most of the keywords can be omitted, in which case Mocassin will set the corresponding parameter to its default value. Table 2.1 contains a list of all possible keywords that can be included in the input

file and their default values. The asterisks mark those fields for which default values are not available and which must, therefore, be specified in the input file. Note that the logical variables are set to *.true.* by including the respective keyword in the input file, and they are set to *.false.* by omitting it. The order in which the keywords are given in the input file is irrelevant. A brief description of all the input commands is given in the next few paragraphs.

autogrid If this keyword is included, Mocassin will automatically create a *nx* by *ny* by *nz* Cartesian grid with the source at the centre or in a corner, according to whether the keyword *symmetricXYZ* is specified or not. All grid cells have the same volume and they are specified by the coordinates of their centres. If, on the other hand, this keyword is omitted, the program will look for an external file containing the Cartesian grid axis specifications. This file must contain a list of the x-, y- and z-axis points, in this order, in units of [*cm*].

autoInitialize This keyword must be included if the initial conditions of the nebula are to be guessed by the program. If it is omitted Mocassin will ask for the path of the input one-dimensional files to be mapped onto the three-dimensional grid.

contShape The shape of the ionizing continuum can be specified in the *contShape* field. The default value is 'blackbody', in which case the ionizing stellar continuum is approximated by the Planck function for the stellar temperature defined by *TStellar*. If a stellar atmosphere data file is to be used, the *contShape* keyword must specify the path of the external file containing the data. For example `contShape nLTe140lg65` tells the program to look for the nLTe140lg65 data file in the current directory. The stellar atmosphere files must be in a format consisting of two columns: the first containing the frequency points in units of [Hz] and the second containing the corresponding frequency-dependent stellar Eddington fluxes in units of [erg cm^{-2} s^{-1} Hz^{-1} sr^{-1}]. The file names used in this work are in the format *nLTexlgy* for non-LTe stellar atmospheres and *LTexlgy* for LTe stellar atmospheres, although the latter have not been used in any of the simulations run in this work. The letter x is the stellar effective temperature divided by 10^3 and the letter y is the value of *log g* multiplied by 10. So, for instance, the file nLTe140lg65 contains the data for a non-LTe stellar atmosphere for an effective temperature of 140,000 K and *log g* equal to 6.5. It is clear, however, that any other filename system may be used.

convLimit This is the convergence limit for the variation of the fractional abundance of neutral hydrogen, $X(H^0)$, in each grid cell from one Monte Carlo iteration to the next. In other words, a given grid cell is assumed to have converged if $\frac{|X(H^0)-X(H^0)_{old}|}{X(H^0)_{old}} \leq convLimit$, where $X(H^0)_{old}$ is the fractional abundance of neutral hydrogen from the previous iteration. As discussed earlier other convergence criteria can also be used.

densityFile The density structure of the nebula can be defined cell by cell by using an external density file. Mocassin knows that a density file is to be used when the *densityFile* keyword is included in the input file followed by the name and path of the file where the data is stored. This file must be structured in four columns, with the first three columns containing the x-, y-, and z- coordinates of the grid cell in [cm] and the last columns containing the value of the hydrogen density by number in [cm^{-3}] at the particular grid cell.

densityLaw This keyword is usually followed by a set of parameters which are to be fed into the density law routine, included in the *grid_mod* module. Any density law can be specified by editing the code in the *setGrid* subroutine. If the nebula is homogeneous, this keyword must be omitted and the *Hdensity* keyword included instead. Note that if neither of the two keywords is included, and an external density file is not specified with the *densityFile* keyword, the nebular density distribution is then left undefined and the simulation halted with an error message being produced.

grow This is the factor by which the outer radius of the Cartesian grid must be enlarged or reduced, in the *adjustOuterRadius* routine, if necessary (see Section 2.2.8). This parameter is therefore only relevant if the *adjustOuterRadius* procedure is enabled.

Hdensity This keyword specifies the constant hydrogen density, by number, in the two regions of a bipolar nebula of the type shown in figures 2.3 and 2.4. The command `Hdensity 300 600` will then set the hydrogen density, by number, to the constant value of 300 cm^{-3} in region I and to 600 cm^{-3} in region II. A spherically symmetric homogeneous nebula can, of course, be reproduced by simply setting the same hydrogen density in both region I and region II. If a different geometry is used then the density distribution can be specified using the *densityLaw* or the *densityFile* keyword and the *Hdensity* keyword must be omitted.

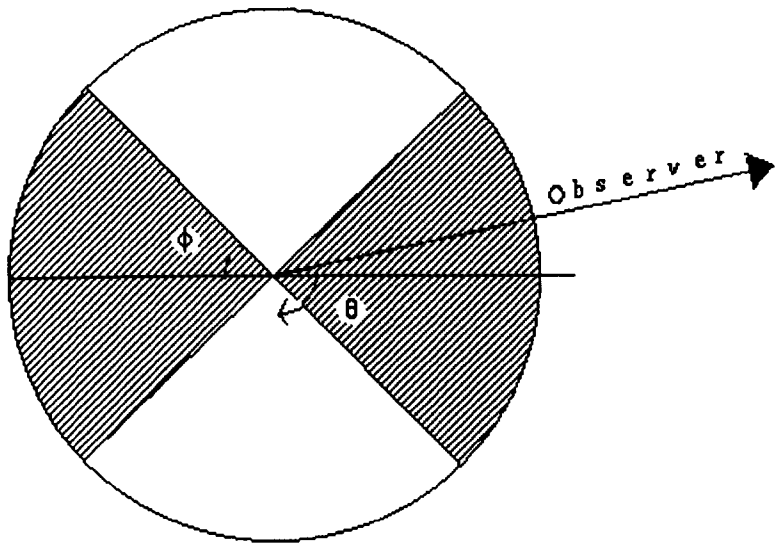

Figure 2.3: Two dimensional representation of a bipolar density distribution. In this case, front and rear cones (shaded) form region I which have a density distribution different from region II (clear). The nebula polar axis can be tilted with respect to the observer by any angle.

LPhot This is the number of hydrogen-ionizing photons emitted by the source per unit time, which is generally referred to as $Q(H^0)$, with units of $[sec^{-1}]$. If this is given then the stellar luminosity, *LStar* is automatically derived from it.

LStar This is the stellar luminosity in units of $[erg\ sec^{-1}]$. If this is given as an input, then the number of hydrogen-ionizing photons, $Q(H^0)$, is automatically derived from it and from the input spectrum.

maxIterateMC This is the maximum number of Monte Carlo iterations to be performed in the simulation. Even if the desired level of accuracy is not reached within the number of iterations set here, the program will terminate after *maxIterateMC* number of Monte Carlo iterations have been performed.

mu This is the cosine of the opening angle for a bipolar density distribution, as shown in figures 2.3 and 2.4.

nbins The total number of points to be used in the frequency mesh.

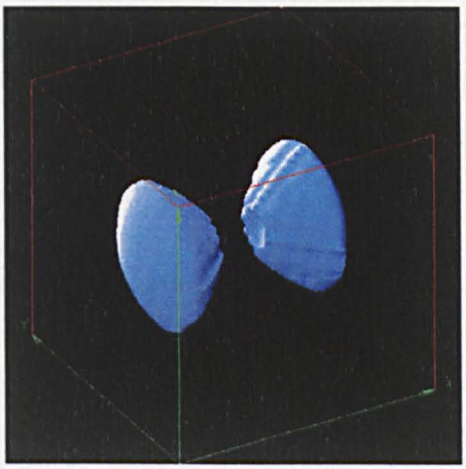

Figure 2.4: Three-dimensional representation of a bipolar density distribution. Only region I is shown.

nebComposition This keyword specifies the path of the nebular composition data file. If the default 'solar' composition is to be used, this keyword can be omitted, otherwise the command `nebComposition meudonPN.dat`, for example, means that the nebular composition is specified in the *meudonPN.dat* file to be found in the current directory. All composition input files must be in a format consisting of one column containing the abundances by number and relative to hydrogen for the first thirty elements in order of ascending atomic number. The abundances of elements which are not to be included in the simulations must be set to zero.

nPhotons This is the number of energy packets to be used in the Monte Carlo simulation and it has to be specified for each model.

nuMax and nuMin *nuMax* and *nuMin* set the high and low limits of the frequency mesh in units of [*Ryd*]. Note that the value of *nuMin* must not be set to zero.

nx, ny and nz These are the number of axial points in the x- y- and z-direction, respectively. Note that the three directions are independent of each other, therefore any kind of cuboidal shape can be obtained.

oneD When this keyword is included in the input file, Mocassin will revert to its one-dimensional mode. The number of radial points to be used in the simulation must be entered via the *nx* specifier. Any values given to the *ny* and *nz* specifiers will be ignored

as these are automatically given value of unity. Note also that when the one-dimensional mode is enabled the *symmetricXYZ* (see below) is automatically switched off. If both the *oneD* and the *symmetricXYZ* keywords are included in the input file *oneD* overrides *symmetricXYZ*.

Rin This is the inner radius of the ionized region, in units of $[cm]$.

Rout This is the outer radius of the ionized region in units of $[cm]$. If no value is specified for this field in the input file, the program will automatically estimate the Stroemgren radius, R_{str}, according to

$$\frac{4\pi}{3} R_{str}^3 N_H^2 \alpha_B = Q(H^0) \tag{2.17}$$

where N_H is the hydrogen density, α_B is the Case B hydrogen recombination coefficient and $Q(H^0)$ is the number of hydrogen-ionizing photons emitted by the source per unit time (see Osterbrock, 1989, page 21).

symmetricXYZ When the nebula to be modelled shows axial symmetry in the x- y- and z-directions, this keyword can be used to enable the symmetric grid procedures. This will result in the ionizing source being put in a corner of the grid, instead of being put in the centre, meaning that only one eighth of the nebula will have to be computed.

talk This is the toggle switch to enable the verbose version of the program.

tauRatio This is the limit to the optical depth gradient from one cell to the next which is used by the *adjustGrid* procedure in order to verify the spatial sampling through the grid. This field is only relevant when the adaptive grid procedures are enabled,

TeStart This is the initial guess for the nebular temperature. Two values of the temperature in units of $[K]$ must be specified for region I and region II in the case of a bipolar nebula, as shown in figures 2.3 and 2.3. Only one value is needed, instead, in the case of any other geometry, specified using an external file or a density law. When the output from one or more 1-D models are used as initial conditions of the Monte Carlo simulation, this field does not need to be specified at all.

TStellar This is the temperature in $[K]$ of the ionizing stellar source

2.3.4 Output Files

Mocassin produces several output files at various times during the simulation. The files *ionratio.out*, *lineFlux.out*, *temperature.out*, *tau.out* and *ionDen.out* are all produced by the *output_mod* module. *Ionratio.out* contains the volume weighted ionic fractions. Different authors is the past have used slightly different definitions of this quantity in their models. Harrington *et al.* (1982) defined the average density of an ion over the nebular volume as

$$< N_{ij} >= \frac{\int N_e N_{ij}\, dV}{\int N_e\, dV} \tag{2.18}$$

where N_{ij} is the density of the ion j of element i, N_e is the electron density and dV is the volume element. From this they calculated the fractions of atoms in the various ionization stages, $f(N_{ij})$, as,

$$f(N_{ij}) = \frac{< N_{ij} >}{\sum_k N_{ik}} \tag{2.19}$$

Ferland *et al.* (1995), instead, calculated the quantity $< N_{ij} > / < H^+ >$, according to

$$\frac{< N_{ij} >}{< H^+ >} = \frac{n(H)}{n(He)} \frac{\int N_e N_{ij}\, dV}{\int N_e N_p\, dV} \tag{2.20}$$

where $n(H)$ and $n(He)$ are the total hydrogen and helium densities, and N_p is the proton density. The choice of which quantities one should use when producing a model very much depends on the need for comparison with other model results. The quantity $< N_{ij} > / < H^+ >$, as described by Ferland *et al.* (1995), was used for the computation of the benchmark models, since all other modelers had used it for comparison. However, when computing the models for NGC 3918 (see chapter 4), $f(N_{ij})$ was chosen instead, since it had already been used in previous work carried out by Clegg *et al.* (1987). The code to calculate either of these two quantities is well commented and included in the *output_mod* module and it is very simple to select which of the two should finally be evaluated. In general, the first two columns of the *ionratio.out* file give the atomic number of the element and its ionization stage (1 for neutral, 2 for singly ionized etc.), and the third and fourth columns give the required quantity calculated for regions I and II of a bipolar nebula of the type shown in figures 2.3 and 2.4. If a different geometry is used or one of the two columns will contain the values, which would then have been integrated over the entire nebular volume.

The file *lineFlux.out* contains the volume integrated intensities of all the emission lines calculated by Mocassin. These are all given relative to $H\beta$, which is in absolute units.

In the case of a bipolar geometry of the type shown in Figures 2.3 and 2.4, the results given are integrated over the volume of each of the two regions. In the case of any other geometry, the results are integrated over the entire nebular volume instead. The first two columns give the code numbers for the higher and lower levels of the transition. The levels corresponding to each code number can be found in the atomic data file of the relevant ion. The third and fourth columns give the analytical and Monte Carlo line intensities relative to $H\beta$ (see Section 2.2.10). Finally the last column gives the ratio of the two previous columns. An indication that good accuracy has been achieved is when the ratio between the two columns approaches unity.

Following the definition given by Ferland *et al.* (1995), the file *temperature.out* contains the mean electronic temperatures weighted by the ionic species, as given by

$$T(N_{ij}) = \frac{\int N_e N_{ij} T_e \, dV}{\int N_e N_{ij} \, dV} \tag{2.21}$$

Harrington *et al.* (1982) and, later, Clegg *et al.* (1987) used a different definition for the mean temperatures, namely

$$T(N_{ij}) = \frac{\int N_e N_{ij} T_e r^2 \, dr}{\int N_e N_{ij} r^2 \, dr} \tag{2.22}$$

where r is the distance from the centre of the nebula. However, this definition is more suitable for spherically symmetric codes and, therefore, it was not implemented in this work.

The output file *tau.out* contains the run of the optical depth from the centre of the nebula to the outer edge along the three axial directions. The optical depths are calculated at the neutral hydrogen ionization threshold, $\nu = 1.0$ *Ryd*, at the neutral Helium ionization threshold, $\nu = 1.8$ *Ryd*, and at the singly ionized Helium ionization threshold, $\nu = 4.0$ *Ryd*. The first column of the file gives the distance in [*cm*] from the centre of the nebula and the second column gives the optical depth from the centre to that point.

The file *ionDen.out* contains the ionic fractions at each grid cell. The first three columns give the x-, y- and z-axis indices of the cell, the fourth and fifth columns give the atomic number and the ionization stage of the element (as above, 1 for atom, 2 for singly ionized etc.) and, finally, the sixth column gives the corresponding ionic fraction.

All the contributions to the heating and to the cooling of the nebula are calculated at each grid cell and stored in files named *fort.X*. These files are produced by each processor used in the simulation during the *update_mod* module as the local thermal balance

equations are solved by iteration (see Figure 2.2). The files extensions, X, are given by $10 + N_{proc}$, where N_{proc} is the processor MPI identification number. Since the files are written out dynamically, they record all the steps of the temperature-iteration. For each grid cell, the x-, y- and z-axis indices are first written out, followed by the local electron temperature and electron density. The contributions to the cooling due to free-free radiation of H^+, He^+ and He^{2+} are then stored, as well as those due to recombination of H^+, He^+ and He^{2+} and to collisional excitation of the heavy ions and hydrogen. Finally the stellar and the diffuse contributions to the heating of the nebula are recorded. These files are extremely useful to investigate the heating and the cooling contributions in play at each location in the nebula.

As we have already mentioned elsewhere, three grid files are also written out after each iteration by routines contained in the *grid_mod* module. These files, *grid1.out*, *grid2.out* and *grid3.out*, are needed by the *warm start* driver to re-initialise an interrupted simulation. These files are formatted such that they can be written out and read back in quickly and therefore they may not be very clear to the human eye. However, most of the information they contain is also given in a more intelligible form in the other output files listed above. The first line of the *grid1.out* file gives the number of x-, y- and z-axes points in the grid, followed by the Stroemgren radius in [*cm*]. The next few lines list the x-axis points, then the y-axis points and, finally, the z-axis points. The rest of the file contains electron temperatures, electron densities, hydrogen densities and two logical values which are used to identify whether the current cell is within the ionized region. This information is given for each grid cell, with the last index varying the fastest (i.e. (1,1,1), (1,1,2), etc.) . The file *grid2.out* contains the ionic fractions at each grid cell for the ions included in the simulation. These are given in order of increasing atomic number and ionization stage, with each element occupying one line. The grid cell indices vary in the same fashion as in the *grid1.out* file. Finally the file *grid3.out* contains a list of the specified simulation parameters, that is, in this order, *SymmetricXYZ*, *talk*, *contShape*, *nebComposition*, *nPhotons*, *nbins*, *grow*, *nuMax*, *nuMin*, *Rin*, *tauRatio*, *TStellar*, *XHIlimit*, *maxIterateMC*, *LStar*, *mu*.

The *MocassinPlot* driver produces also an output file, containing the luminosities of each individual grid volume element in the required emission lines. This file, named *plot.out*, is written in a format which is readable by the IDL visualization routines (see Section 2.4).

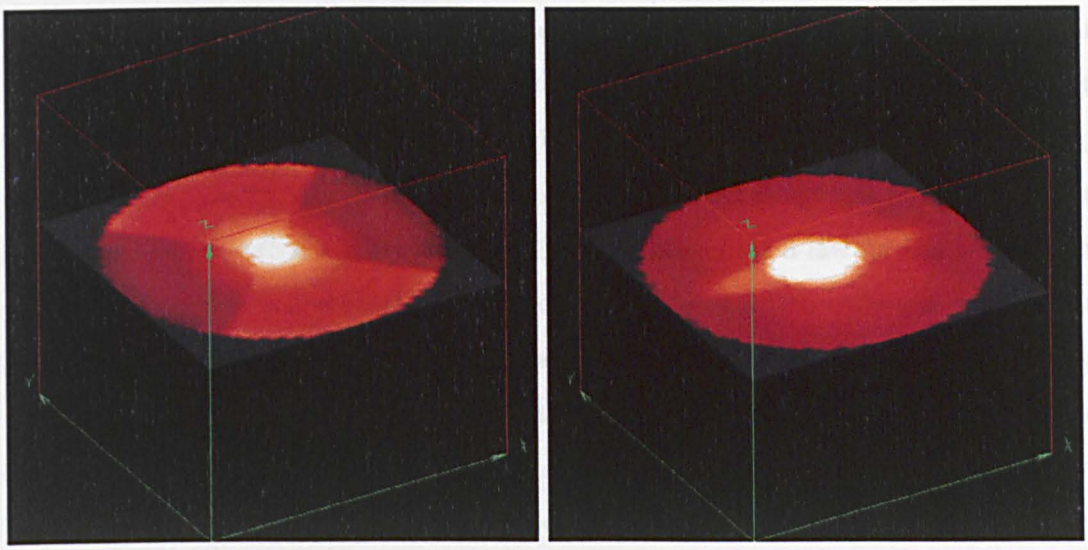

Figure 2.5: Slice temperature plots for the biconical (lefthand panel) and the spindle-like model A (righthand panel) of the planetary nebula NGC 3918. A detailed description of these models is given Chapter 4

2.4 Visualization Tools

It has already been mentioned in Section 2.2.10 that projected maps and other visual aids provide a very powerful tool for the comparison of model results with the observation. In order to obtain images in a given emission line, the sum of the line intensities along the line of sight must be computed. Therefore, a three-dimensional photoionization model, such as Mocassin, is needed as it naturally calculates the ionization distribution at each grid cell in the nebula. The driver *MocassinPlot*, described in the previous section, was designed to work on a a converged model grid to produce a set of line intensities suitable for plotting. IDL procedures written by Christophe Morisset (Morisset *et al.*, 2000) and modified for use with Mocassin's output files, were used.

The viewing angle of the nebula can be set in the IDL code so that the nebula can be rotated and projected images in any emission line or at any continuum frequency can be produced. If the nebula is defined in an XYZ-coordinate system, and the rotation and projections operate in an xyz-coordinate system, then before any rotation is carried out the XYZ- and the xyz-coordinate systems must coincide. The rotations of the data cube are performed in the xyz-space, plane by plane, and, if necessary, up to three rotations around the three axes can be performed. Only the minimum number of rotations required to obtain a given viewing angle should, however, be performed, since noise is introduced

with each rotation. Projected images on the plane of the sky in any given emission line, or continuum frequency, are obtained by integrating the emissivities of the cell along the line of sight, taken perpendicular to one of the cube faces. The intensity corresponding to a given aperture placed at a given position on the projected image can then be calculated and also compared with the observations. Moreover, assuming a law for the velocity field, which can, of course be modified to fit the observations, the IDL code can also calculate and produce plots of the emission line spectral profiles as well as position-velocity diagrams (echellograms). Mocassin also produces and stores to files the electron temperatures and densities as well as the ionization fractions at each grid cell, so standard IDL three-dimensional plotting devices can be used to visualize the spatial distribution of any of these physical quantities. Three-dimensional *slice*[3] plots of the ionization distribution of some given species, for example, are very useful in order to quickly visualize the position of the various ionization fronts in the nebula. Also *slice* plots of the electron temperature distribution of a nebula can be very informative; Figure 2.5 shows two such plots obtained for the biconical (lefthand panel) and spindle-like (righthand panel) density distribution models of the planetary nebula NGC 3918 (see Chapter 4 for a description of the model). Examples of the other types of plots described in this section are available in Section 4.5.

2.5 Limitations and Possible Developments

Mocassin's main limitation is imposed by the computer power available. The great volume of data which has to be handled in a three-dimensional simulation, implies the need for a system with multi-processing capabilities in order to accelerate the computational time. However, the fast development of Beowulf Linux clusters is making parallel computing more affordable, and this is also a reason why the MPI formalism was chosen, as this allows information to be passed from one processor to another and, therefore, it does not necessarily require a system with shared memory facilities. Such systems, which include the Silicon Graphics Origin 2000 machine used for this work, are generally much more expensive than Beowulf clusters.

Mocassin was designed for the modelling of planetary nebulae and H II regions and

[3]IDL slice plots show cross-sections of a three-dimensional object cut across at any position, interactively chosen at the time of the plot. The viewing angle of the nebula can also the changed interactively at any time. The slice plot device is available in the standard IDL *slicer3* package

it does not, at present, include the high energy physical processes which are needed, for example, for the modeling of AGNs. However the inclusion of processes such as inner shell photoionization and Compton heating is straightforward and this is intended to be one of the developments of the near future. Moreover, plans also exist to include a treatment of dust in the code. This is necessary for the modelling of dusty objects where dust grains may be one of the main sources of opacity. Finally, the extension of the code to include the facility to model the photodissociation regions (PDRs) and the molecular regions of nebulae is also possible and is one of the longer term goals. More details on the future development plans for Mocassin are given in Chapter 6.

CHAPTER 3

Application to benchmark cases

3.1 Introduction

Numerical simulations of photoionized nebulae are very complex and a number of factors, such as numerical approximations, assumptions and the complexity of the calculation itself introduce a degree of uncertainty into the results. For this reason, it is very important for modelers to have certain standards of comparison, in order to identify problems in their codes and to reach an adequate accuracy in their calculation. A series of meeting were held in Meudon, France, in 1985 (Péquignot, 1986) and in Lexington, KY, in 1995 (Ferland *et al.*, 1995) and in the year 2000 (Péquignot *et al.*, 2001), in order to define a set of benchmark cases which could be used by all modelers to test their codes against. The benchmark cases which resulted from these meetings include H II regions, planetary nebulae, narrow line regions (NLRs) of AGNs and X-ray slabs. Mocassin, however, does not have, at present, the capability to treat NLRs and X-ray slabs, as some relevant physical processes, such as Compton heating/cooling and inner shell ionization, are not yet included. For this reason, only the H II region and the planetary nebula benchmarks are performed in this work. Nevertheless, the expansion of the code to include high energy processes is planned in the future.

Results from several other codes are available for comparison; these are all one-dimensional codes and, apart from differences in the atomic data set used by each one of them, their main differences lie in the treatment of the diffuse radiation field transfer. A brief description of each of these codes is given in Ferland *et al.* (1995). Although most of these codes have evolved somewhat since the 1995 Lexington meeting, mostly via

Table 3.1: Lexington 2000 benchmark model input parameters.

Parameter	HII40	HII20	PN150	PN75
L(BB)/10^{37}(erg sec^{-1})	308.2	600.5	3.607	1.913
T(BB)/10^3K	40	20	150	75
$R_{in}/10^{17}$cm	30	30	1	1.5
n_H/cm^{-3}	100	100	3000	500
He	0.10	0.10	0.10	0.10
C$\times$ 10^5	22.	22.	30.	20.
N$\times$ 10^5	4.	4.	10.	6.
O$\times$ 10^5	33.	33.	60.	30.
Ne$\times$ 10^5	5.	5.	15.	6.
Mg$\times$ 10^5	-	-	3.	1.
Si$\times$ 10^5	-	-	3.	1.
S$\times$ 10^5	0.9	0.9	1.5	1.

Elemental abundances are by number with respect to H.

the updating of the atomic data sets and the inclusion of more and specialised physical processes, their basic structure has stayed the same. The seven codes included for comparison are G. Ferland's *Cloudy* (GF), J.P. Harrington's code (PH), D. Péquignot's *Nebu* (DP), T. Kallman's *XStar* (TK), H. Netzer's *Ion* (HN), R. Sutherland's *Mappings* (RS) and R. Rubin's *Nebula* (RR). Only two of these codes, the Harrington code and Rubin's *Nebula*, treat the diffuse radiative transfer exactly. The others use some versions of the *outward-only approximation* of varying sophistication. In this approximation all diffuse radiation is assumed to be emitted isotropically into the outward half of the space.

The predicted line fluxes from each code for each of the benchmark codes are listed in Table 3.3 to Table 3.6, together with mean electron temperatures weighted by N_pN_e, $< T[N_pN_e] >$, the electron temperature at the inner edge of the nebula, T_{inner}, and the mean $\frac{<He^+>}{<H+>}$, which represents the fraction of helium in the H^+ region which is singly ionized. $< T[N_pN_e] >$ and $\frac{<He^+>}{<H+>}$ are calculated according to equations 2.21 and 2.20 respectively. Table 3.1 contains the input parameters for all the benchmark models discussed here.

Four benchmark model nebulae were computed, two H II regions and two planetary nebulae. These benchmarks were designed to be uncomplicated yet to test different aspects of the modelling (Ferland *et al.*, 1995). The nebulae are homogeneous and blackbodies are used as ionizing sources instead of stellar atmospheres.

All the benchmark cases described in Table 3.1 were performed using both the three-dimensional and the one-dimensional mode of Mocassin and both sets of results are included here for comparison. It is clear from the results listed in Table 3.3 to Table 3.6, that the results of the three-dimensional and one-dimensional modes are consistent with each other. The small differences that do exist can be entirely attributed to the coarseness of the grid used for the three-dimensional calculations. The aim of the benchmarking described in this chapter is to assess the reliability of Mocassin in its fully *three-dimensional* mode, for this reason the one-dimensional mode results will not be included in the following performance analysis, moreover the inclusion of two sets of results from what is, essentially, the same code would introduce a bias in the median and isolation factors calculations described below. Finally, to avoid any confusion, any mention of Mocassin throughout the contents of this thesis refers to the fully three-dimensional version of the code, unless otherwise stated.

Figures 3.1 to 3.4 show the fractional ionic abundances of oxygen (top panels) and carbon (bottom panels) obtained by Mocassin for the four benchmark cases analysed. The ionic abundances of every cell in the ionized regions are plotted against their radial distance from the star. These plots are interesting not only because they provide a clear picture of the overall ionization structure of each model, but also because from the scatter of the data points, one can estimate the accuracy of the final results (Note that such plots are only meaningful for spherically symmetric cases).

Following the analysis of Péquignot *et al.* (2001), isolation factors, if's were computed for each result in each case study. These are defined as the ratio of the largest to the penultimate largest value of a given output quantity and the ratio of the penultimate smallest value to the smallest value. These ratios are computed with the intention to identify aberrant values. A large if can be attributed to a number of factors, but often these can be assigned to a difference in the atomic data set used in the code by each modeler. A list of the number of if's larger than the values 1.01, 1.03, 1.10, 1.30 and 2.00 is given in Table 3.7, for each benchmark. After analysing the benchmark results obtained by all the modelers who participated in the Lexington workshop, Péquignot *et al.* (2001)

Table 3.2: Summary of the number of energy packets needed for >50% and >95% convergence (see text for explanation) for each of the benchmark cases

Case	τ_{edge}			$n_x \times n_y \times n_z$	N_{packets}	
	H^0	He^0	He^+		>50%	>95%
HII40	4.79	1.15	177.8	13×13×13	$5{\cdot}10^5$	$5{\cdot}10^6$
HII20	2.95	1.13	91.2	13×13×13	$5{\cdot}10^6$	$5{\cdot}10^7$
PN150	34.0	6.87	57.9	13×13×13	$3{\cdot}10^5$	$3{\cdot}10^6$
PN75	1.16	0.24	31.5	13×13×13	$4{\cdot}10^5$	$4{\cdot}10^6$

suggested that an isolation factor larger than 1.30 is indicative of a significant departure and a possible problem. A large number of occurrences of $if > 1.30$ should either have an acceptable explanation or lead to corrections to the code.

The number of results not predicted by any given code is listed in the *No prediction* row of Table 3.7. Péquignot *et al.* (2001) also argued, in the proceedings of the November 2000 Lexington meeting, that the lack of a prediction for a particular observable may simply reflect a lack of interest by the modeller in it; on the other hand, a frequent occurrence of *No predictions* may also indicate limitations in the predictive power of a given code.

As argued by Péquignot *et al.* (2001), a large error can be introduced when the average over a small sample containing a number of aberrant values is taken. In order to minimise this error, median values are calculated instead of averages and these are given for each observable listed in Tables 3.3 to 3.6 in the column *Med.* Table 3.8 contains the number of median values scored by each code in each case study. When a median value is shared by two or more codes a score of one is given to each one, therefore the sum of the median values scored by all the codes is higher than the number of the observables in each case study (column *Total* in Table 3.8). It is worth noting that this is slightly different from the approach used in the Péquignot *et al.* (2001) paper, where fractional values are used for shared medians.

3.2 Sampling Requirements

As described in Chapter 2, the *MocassinWarm* driver allows to resume an interrupted run by starting the model from the end of the last Monte Carlo iteration. By modifying the file

grid3.out (see Section 2.3.4) the number of energy packets to be used can be adjusted before the simulation is restarted. This feature can be used to speed up the simulations by using the following approach. The first few iterations are run using a lower number of energy packets than actually needed; so, for example, if the optimum number of energy packets for a given model is 10^6, then the first few iterations can be carried out using only 10^5 packets, hence reducing the run time for these by a factor of ten. This will result in about 50%-60% of the grid cells converging; in general, the inner cells converge more quickly, due to the larger number of sampling units available there (due mainly to geometrical dilution and to the reprocessing of energy packets to non-ionizing energy packets). At this point the simulation is interrupted and then resumed, after having adjusted the number of energy packets to the final required value (i.e. 10^6, in the previous example). Final convergence will then be achieved, in most cases, within four or five further iterations. The actual number of iterations required depends on the number of energy packets used: the larger the number of sampling quanta available at each cell, the quicker the cells will converge to a solution. The numbers quoted above, however, also depend on each particular model's geometry and optical thickness. Optically thin models require a larger number of iterations and/or energy packets. This is due to the fact that the packets can escape the ionized region more easily and, therefore, they spend less time within the grid. This is the case, for example, of the optically thin H II region benchmark case, HII20. Table 3.2 lists the optical depths at the ionization threshold frequencies for H^0, He^0 and He^+, at the outer edge of the grids, for the four benchmark models analyzed here. For each model, the number of grid points is also given (column 5), together with the number of energy packets used, $N_{\rm packets}$, according to the two-step stategy described above, first to achieve convergence in 50%-60% of the total number of grid cells ((> 50%), column 6) and then to achieve total convergence ((> 95%), column 7). The aim of Table 3.2 is merely to provide some general guidelines for selecting the appropriate number of energy packets for a particular simulation; however, as stated before, the optimum number should be determined for each given model, particularly in non-spherically symmetric cases.

3.3 Benchmark Results

The Lexington/Meudon Standard H II region model (HII40) was the first benchmark to be run and some preliminary results have already been presented at the November

2000 Lexington meeting. However, those results, which were also included in the same conference proceedings (Ercolano, 2001; Péquignot *et al.*, 2001), were produced when Mocassin was still under development and, therefore, they should only be considered as a *snapshot* of that particular stage. The code has evolved considerably since the November 2000 Lexington meeting and the new, improved results are presented in this section (see Table 3.3).

3.3.1 The Standard H II Region Benchmark (HII40)

Mocassin scored eight *if*s > 1.01 for the HII40 benchmark model (Table 3.7); only three of these, however, had values greater than 1.3. Amongst these, *if*s > 1.10 are obtained for the [O III] 5007+4959 ($if = 1.18$) and for [O III] 4363 ($if = 1.45$); the ratio of these lines is often used as a temperature diagnostic (see, for example, Osterbrock, 1989, pages 119-125). Mocassin predicts $\frac{j_{\lambda 4959}+j_{\lambda 5007}}{j_{\lambda 4363}} = 745.4$, this value is higher than the value obtained by the other codes, in fact median value obtained for the ratio of these line fluxes by the other codes is equal to 589.2. This is fully consistent with Mocassin predicting a slightly lower temperature ($if = 1.027$) for this benchmark than do the other codes.

Finally, the number of median values obtained for this benchmark case is ten, which compares very well with the other codes' median scores, ranging from three to ten (see Table 3.8).

3.3.2 The Low Excitation H II Region Benchmark (HII20)

Mocassin scored seven *if*s for the low excitation H II region (HII20) benchmark model. None of these, however, has a value greater than 1.3. As in the HII40 nechmark case, the mean temperature, weighted by $N_{\rm p}N_{\rm e}$, predicted by Mocassin for this model is also slightly lower ($if = 1.034$) than the other models' predictions.

Five median values were obtained by Mocassin for this benchmark case, while the other codes scored between three and eleven (see Table 3.8).

3.3.3 The Optically Thick Planetary Nebula Benchmark (PN150)

The optically thick, high excitation planetary nebula (PN150) is the most demanding of the benchmark cases in terms of physical processes and atomic data required. Mocassin's score for this model was very good (Table 3.7), obtaining only six *if*s, with none of those

Table 3.3: Lexington 2000 Standard H II region (HII40) benchmark case results.

Line	Median	GF	HN	DP	TK	PH	RS	RR	BE	
									3-D	1-D
$H\beta/10^{37}$ erg/s	2.05	2.06	2.02	2.02	2.10	2.05	2.07	2.05	2.02	2.1(
$H\beta$ 4861	-	1.00	1.00	1.00	1.00	1.00	1.00	1.00	1.00	1.0(
He I 5876	0.116	0.119	0.112	0.113	0.116	0.118	0.116	-	0.114	0.11
C II] 2325+	0.144	0.157	0.141	0.139	0.110	0.166	0.096	0.178	0.148	0.12
C II 1335	0.082	0.100	0.078	0.094	0.004	0.085	0.010	-	0.082	0.08
C III] 1907+1909	0.070	0.071	0.076	0.069	0.091	0.060	0.066	0.074	0.041	0.04
[N II] 122.μm	0.034	0.027	0.037	0.034	-	0.032	0.035	0.030	0.036	0.03
[N II] 6584+6548	0.730	0.669	0.817	0.725	0.69	0.736	0.723	0.807	0.852	0.78
[N II] 5755	.0054	.0050	.0054	.0050	-	.0064	.0050	.0068	.0061	.005
[N III] 57.3 μm	0.292	0.306	0.261	0.311	-	0.292	0.273	0.301	0.223	0.22
[O I] 6300+6363	.0086	.0094	.0086	.0088	.012	.0059	.0070	-	.0065	.008
[O II] 7320+7330	0.029	0.029	0.030	0.031	0.023	0.032	0.024	0.036	0.025	0.02
[O II] 3726+3729	2.03	1.94	2.17	2.12	1.6	2.19	1.88	2.26	1.92	1.7
[O III] 51.8 μm	1.06	1.23	1.04	1.03	0.99	1.09	1.06	1.08	1.06	1.0
[O III] 88.3 μm	1.22	1.12	1.06	1.23	1.18	1.25	1.23	1.25	1.22	1.2(
[O III] 5007+4959	2.18	2.21	2.38	2.20	3.27	1.93	2.17	2.08	1.64	1.7(
[O III] 4363	.0037	.0035	.0046	.0041	.0070	.0032	.0040	.0035	.0022	.002
[O IV] 25.9 μm	.0010	.0010	.0010	.0010	.0013	.0013	.0010	-	.0010	.001
[Ne II] 12.8 μm	0.195	0.177	0.195	0.192	-	0.181	0.217	0.196	0.212	0.2(
[Ne III] 15.5 μm	0.322	0.294	0.264	0.270	0.35	0.429	0.350	0.417	0.267	0.26
[Ne III] 3869+3968	0.085	0.084	0.087	0.071	0.092	0.087	0.083	0.086	0.053	0.05
[S II] 6716+6731	0.147	0.137	0.166	0.153	0.315	0.155	0.133	0.130	0.141	0.13
[S II] 4068+4076	.0080	.0093	.0090	.0100	.026	.0070	.005	.0060	.0060	.005
[S III] 18.7 μm	0.577	0.627	0.750	0.726	0.535	0.556	0.567	0.580	0.574	0.56
[S III] 33.6 μm	0.937	1.24	1.43	1.36	0.86	0.892	0.910	0.936	0.938	0.93
[S III] 9532+9069	1.22	1.13	1.19	1.16	1.25	1.23	1.25	1.28	1.21	1.1
[S IV] 10.5 μm	0.359	0.176	0.152	0.185	0.56	0.416	0.388	0.330	0.533	0.53
$10^3 \times \Delta$(BC 3645)/$\AA$	5.00	4.88	-	4.95	-	5.00	5.70	-	5.47	5.4
$T_{\rm inner}$/ K	7653	7719	7668	7663	8318	7440	7644	7399	7370	748
$<T[N_pN_e]>$/K	8026	7940	7936	8082	8199	8030	8022	8060	7720	772
$R_{\rm out}/10^{19}$cm	1.46	1.46	1.46	1.46	1.45	1.46	1.47	1.46	1.46	1.4
$<He^+>$ / $<H^+>$	0.767	0.787	0.727	0.754	0.77	0.764	0.804	0.829	0.715	0.68

GF: G. Ferland's *Cloudy*; PH: J.P Harrington code; DP: D. Péquignot's *Nebu*; TK: T. Kallman's *XStar*; HN: H. Netzer's *Ion*; RS: R. Sutherland's *Mappings*; RR: R. Rubin's *Nebula*; BE: B. Ercolano's *Mocassin*.

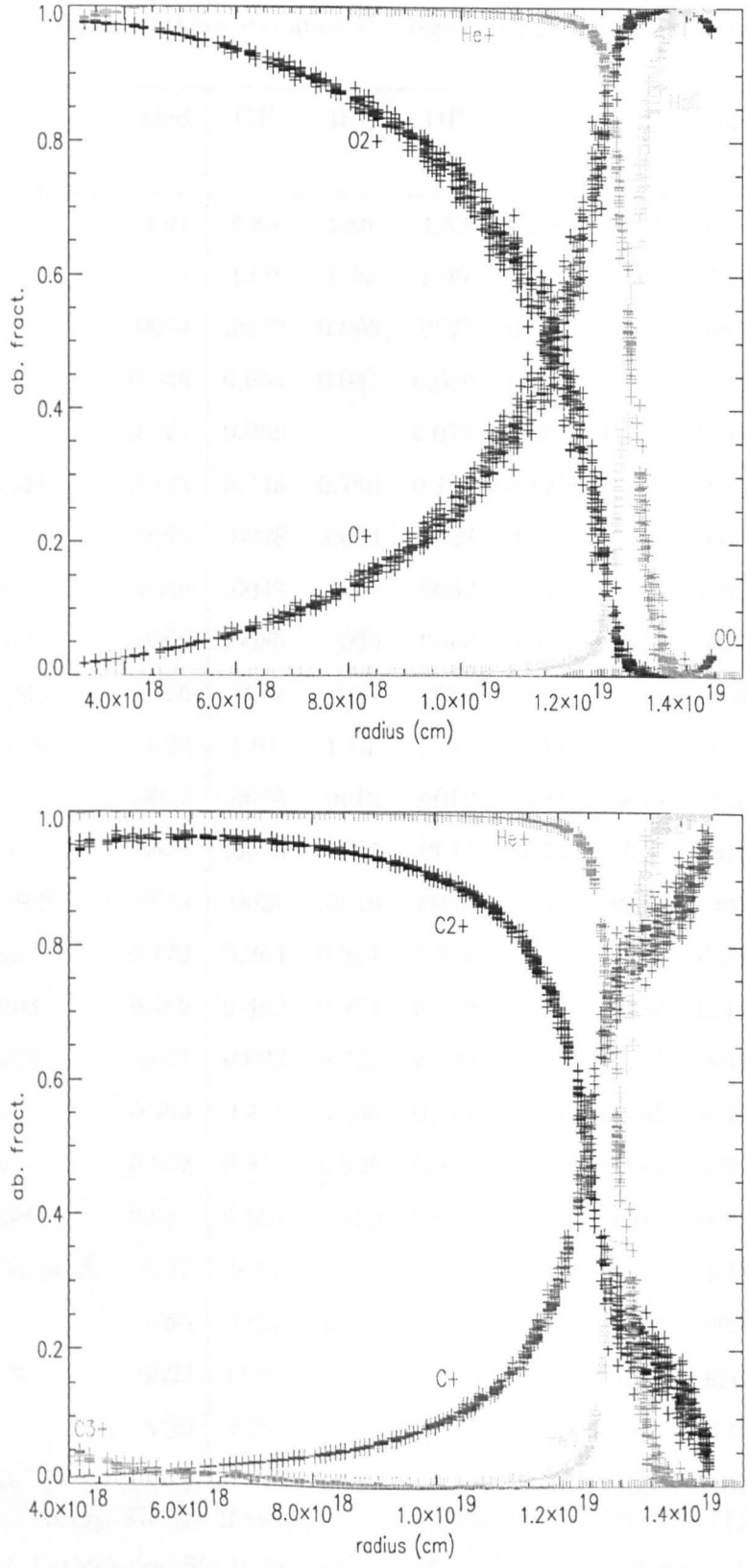

Figure 3.1: Fractional ionic abundances of oxygen (top panel) and carbon (bottom panel), as a function of radius, for the standard H II region benchmark case (HII40).

Table 3.4: Lexington 2000 low excitation H II region (HII20) benchmark case results.

Line	Med	GF	HN	DP	TK	PH	RS	RR	BE	
									3-D	1-D
$H\beta/10^{36}$ erg/s	4.91	4.85	4.85	4.83	4.9	4.93	5.04	4.89	4.97	5.09
$H\beta$ 4861	-	1.00	1.00	1.00	1.00	1.00	1.00	1.00	1.00	1.00
He I 5876	.0074	.0072	0.008	.0073	0.008	.0074	.0110	-	.0065	.0074
C II] 2325+	0.046	0.054	0.047	0.046	0.040	0.060	0.038	0.063	0.042	0.031
[N II] 122.μm	0.071	0.068	-	0.072	0.007	0.072	0.071	0.071	0.071	0.070
[N II] 6584+6548	0.823	0.745	0.786	0.785	0.925	0.843	0.803	0.915	0.846	0.771
[N II] 5755	.0028	.0028	.0024	.0023	.0029	.0033	.0030	.0033	.0025	.0021
[N III] 57.3 μm	.0030	.0040	.0030	.0032	.0047	.0031	.0020	.0022	.0019	.0032
[O I] 6300+6363	.0060	.0080	.0060	.0063	.0059	.0047	.0050	-	.0088	.0015
[O II] 7320+7330	.0086	.0087	.0085	.0089	.0037	.0103	.0080	.0100	.0064	.0051
[O II] 3726+3729	1.09	1.01	1.13	1.10	1.04	1.22	1.08	1.17	0.909	0.801
[O III] 51.8 μm	.0012	.0014	.0012	.0012	.0016	.0013	.0010	.0008	.0010	.0011
[O III] 88.3 μm	.0014	.0016	.0014	.0014	.0024	.0014	.0010	.0009	.0012	.0013
[O III] 5007+4959	.0014	.0021	.0016	.0015	.0024	.0014	.0010	.0010	.0011	.0012
[Ne II] 12.8 μm	0.273	0.264	0.267	0.276	0.27	0.271	0.286	0.290	0.295	0.296
[S II] 6716+6731	0.489	0.499	0.473	0.459	1.02	0.555	0.435	0.492	0.486	0.345
[S II] 4068+4076	0.017	0.022	0.017	0.020	0.052	0.017	0.012	0.015	0.013	.0082
[S III] 18.7 μm	0.386	0.445	0.460	0.441	0.34	0.365	0.398	0.374	0.371	0.413
[S III] 33.6 μm	0.658	0.912	0.928	0.845	0.58	0.601	0.655	0.622	0.630	0.702
[S III] 9532+9069	0.537	0.501	0.480	0.465	0.56	0.549	0.604	0.551	0.526	.582
$10^3 \times \Delta$(BC 3645)/$\AA$	5.57	5.54	-	5.62	-	5.57	5.50	-	6.18	6.15
$T_{\rm inner}$/ K	6765	7224	6815	6789	6607	6742	6900	6708	6562	6662
$<T[N_pN_e]>$/K	6662	6680	6650	6626	6662	6749	6663	6679	6402	6287
$R_{\rm out}/10^{18}$cm	8.89	8.89	8.88	8.88	8.7	8.95	9.01	8.92	8.89	8.92
$<He^+>$ / $<H^+>$	0.048	0.048	0.051	0.049	0.048	0.044	0.077	0.034	0.041	0.048

GF: G. Ferland's *Cloudy*; PH: J.P Harrington code; DP: D. Péquignot's *Nebu*; TK: T. Kallman's *XStar*; HN: H. Netzer's *Ion*; RS: R. Sutherland's *Mappings*; RR: R. Rubin's *Nebula*; BE: B. Ercolano's *Mocassin*.

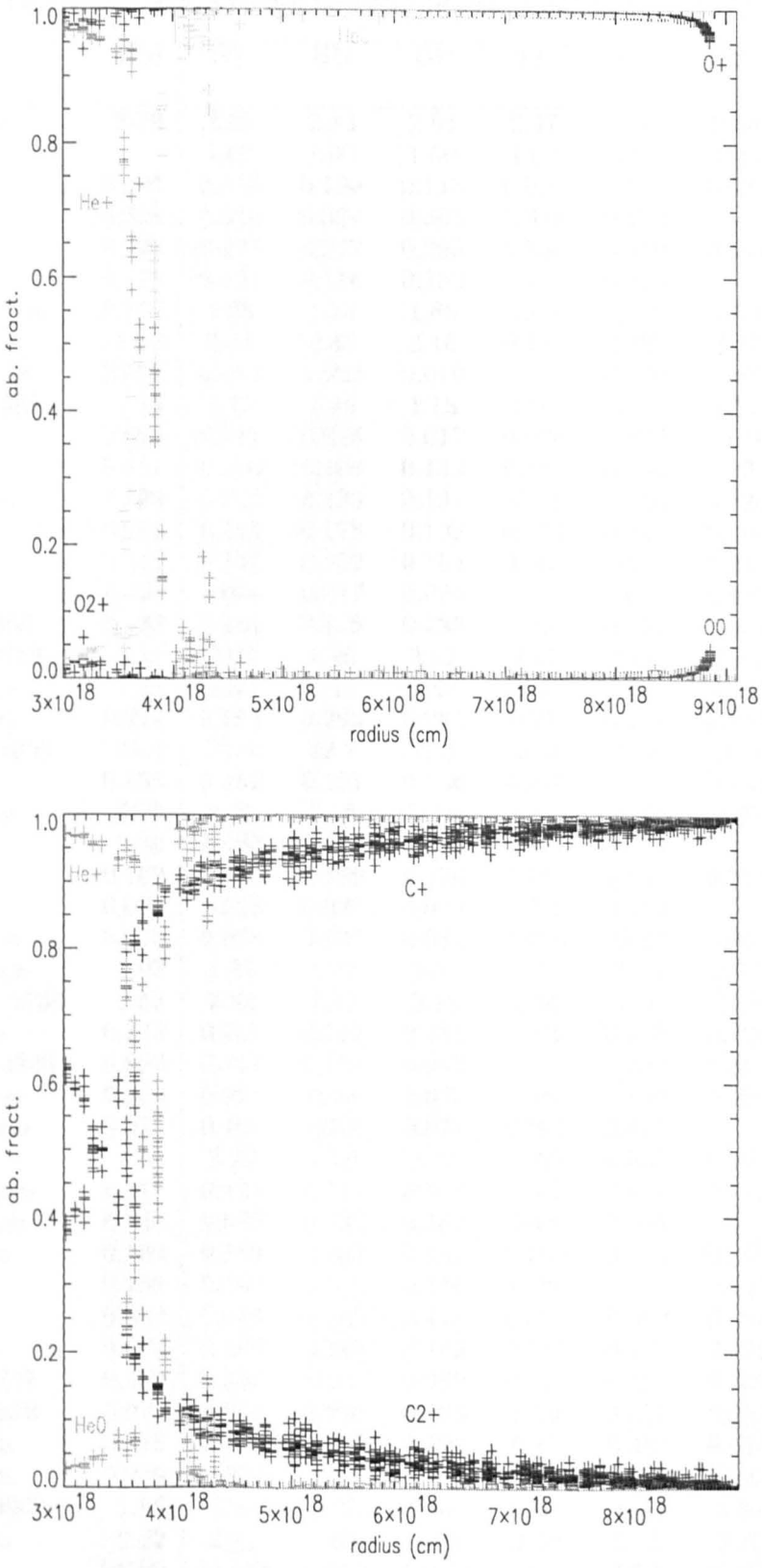

Figure 3.2: Fractional ionic abundances of oxygen (top panel) and carbon (bottom panel), as a function of radius, for the standard H II region benchmark case (HII20).

Table 3.5: Lexington 2000 optically thick planetary nebula (PN150) benchmark case results.

Line	Med	GF	HN	DP	TK	PH	RS	BE	
								3-D	1-D
$H_\beta/10^{35}$ erg/s	2.79	2.86	2.83	2.84	2.47	2.68	2.64	2.79	2.89
H_β 4861	-	1.00	1.00	1.00	1.00	1.00	1.00	1.00	1.00
He I 5876	0.104	0.110	0.129	0.118	0.096	0.096	0.095	0.104	1.06
He II 4686	0.328	0.324	0.304	0.305	0.341	0.333	-	0.333	0.320
C II] 2325+	0.293	0.277	0.277	0.293	0.346	0.450	0.141	0.339	0.330
C II 1335	0.119	0.121	0.116	0.130	-	0.119	-	0.103	0.104
C III] 1907+1909	0.174	1.68	1.74	1.86	1.69	1.74	1.89	1.72	1.71
C IV 1549+	2.16	2.14	2.43	2.16	0.154	2.09	3.12	2.71	2.65
[N I] 5200+5198	0.012	0.013	0.022	0.010	-	0.020	0.005	.0067	0.012
[N II] 6584+6548	1.17	1.15	1.16	1.18	1.01	1.35	1.17	1.43	1.37
[N II] 5755	0.017	0.017	0.016	0.017	0.020	0.023	0.016	0.022	.0021
N III] 1749+	0.111	0.106	0.109	0.132	0.184	0.139	0.091	0.111	0.110
[N III] 57.3 μm	0.129	0.129	0.133	0.134	0.12	0.135	0.126	0.120	0.122
N IV] 1487+	0.168	0.199	0.178	0.192	0.154	0.141	0.168	0.162	0.159
N V 1240+	0.147	0.147	0.159	0.154	0.055	0.107	0.248	0.147	0.145
[O I] 63.1 μm	0.020	0.024	0.017	0.025	-	.0072	0.049	0.010	0.011
[O I] 6300+6363	0.135	0.144	0.126	0.135	0.245	0.104	0.101	0.163	0.153
[O II] 3726+3729	2.11	2.03	1.96	2.32	2.11	2.66	1.75	2.24	2.25
[O III] 51.8 μm	1.39	1.30	1.45	1.42	0.954	1.39	1.28	1.50	1.52
[O III] 88.3 μm	0.274	0.261	0.292	0.291	0.27	0.274	0.252	0.296	0.299
[O III] 5007+4959	21.4	21.4	22.2	21.1	26.0	20.8	16.8	22.63	22.52
[O III] 4363	0.155	0.152	0.151	0.156	0.249	0.155	0.109	0.169	0.166
[O IV] 25.9 μm	3.78	3.45	3.16	3.78	3.95	4.20	4.05	3.68	3.60
O IV] 1403+	2.30	0.183	0.236	0.324	0.357	0.225	-	0.203	0.201
O V] 1218+	0.169	0.165	0.189	0.170	0.142	0.097	0.213	0.169	0.168
O VI 1034+	0.025	0.028	0.026	0.022	0.026	0.014	-	0.025	0.026
[Ne II] 12.8 μm	0.030	0.028	0.032	0.030	0.020	0.027	0.043	0.030	0.031
[Ne III] 15.5 μm	1.97	1.88	1.97	1.92	1.73	2.76	2.71	2.02	2.03
[Ne III] 3869+3968	2.63	2.64	2.32	2.25	2.86	3.04	2.56	2.63	2.61
[Ne IV] 2423+	0.723	0.707	0.712	0.785	1.13	0.723	0.832	0.749	0.741
[Ne V] 3426+3346	0.692	0.721	0.706	0.661	1.07	0.583	0.591	0.692	0.687
[Ne V] 24.2 μm	0.980	0.997	0.98	0.928	1.96	0.936	0.195	1.007	0.997
[Ne VI] 7.63 μm	0.076	0.107	0.075	0.077	0.692	0.011	-	0.050	0.051
Mg II 2798+	1.22	2.22	2.10	1.22	0.023	0.555	0.863	2.32	2.32
[Mg IV] 4.49 μm	0.111	0.121	0.111	0.107	0.13	0.042	0.115	0.111	0.109
[Mg V] 5.61 μm	0.144	0.070	0.132	0.162	0.18	0.066	-	0.156	0.156
[Si II] 34.8 μm	0.168	0.155	0.168	0.159	0.263	0.253	0.130	0.250	0.263
Si II] 2335+	0.159	0.160	0.155	0.158	0.20	-	0.127	0.160	0.164
Si III] 1892+	0.382	0.446	0.547	0.475	0.321	0.382	0.083	0.325	0.316
Si IV 1397+	0.172	0.183	0.218	0.169	0.015	0.172	0.122	0.214	0.207
[S II] 6716+6731	0.370	0.359	0.37	0.399	0.415	0.451	0.322	0.357	0.370
[S II] 4069+4076	0.077	0.073	0.078	0.086	0.19	0.077	0.050	0.064	0.063
[S III] 18.7 μm	0.578	0.713	0.788	0.728	0.15	0.488	0.578	0.495	0.505
[S III] 33.6 μm	0.240	0.281	0.289	0.268	0.06	0.206	0.240	0.210	0.214
[S III] 9532+9069	1.96	2.07	2.07	1.96	0.61	1.90	2.04	1.89	1.92
[S IV] 10.5 μm	2.22	2.09	1.65	1.76	2.59	2.22	2.25	2.25	2.22
T_{inner}/ K	18100	18120	17950	18100	19050	17360	19100	16670	17703
$< T[N_pN_e] >$/K	12110	12080	13410	12060	13420	12110	11890	12150	12108
$R_{out}/10^{17}$cm	4.04	4.04	3.90	4.11	4.07	4.04	3.98	4.11	4.19
$\frac{<He^+>}{<H^+>}$	0.704	0.702	0.726	0.714	0.79	0.696	0.652	0.702	0.711

GF: G. Ferland's *Cloudy*; PH: J.P Harrington code; DP: D. Péquignot's *Nebu*; TK: T. Kallman's *XStar*; HN: H. Netzer's *Ion*; RS: R. Sutherland's *Mappings*; BE: B. Ercolano's *Mocassin*.

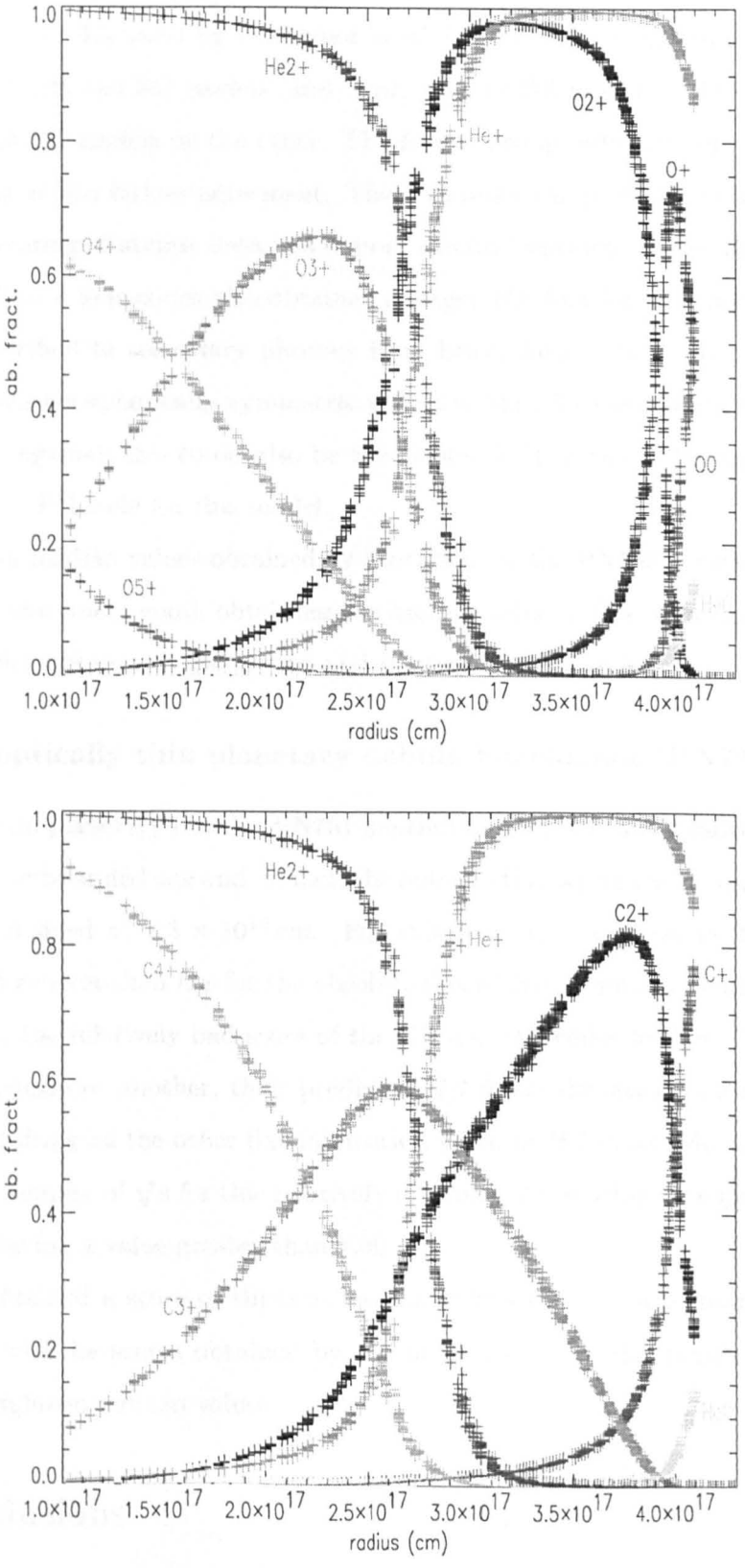

Figure 3.3: Fractional ionic abundances of oxygen (top panel) and carbon (bottom panel), as a function of radius, for the optically thick planetary nebula benchmark case (PN150).

being higher than 1.3 and only one being slightly higher than 1.1 (C II λ1335, $if = 1.13$). As has already been discussed by Péquignot *et al.* (2001), there seems to be a dichotomy between the GF, HN and DP models (and, now, also the BE model on the one hand) and the TK, PH and RS models on the other. The former group obtained very few *if*s larger than 1.1, indicative of a tighter agreement. This coherence can probably be attributed to a more recent updating of atomic data and a more careful treatment of the diffuse radiation field transfer. These four codes also obtained a larger $H\beta$ flux for this model, which can probably be ascribed to secondary photons from heavy ions. PH is the only code here with a fully iterative spherically symmetric radiative transfer treatment (since RR only computed H II regions); this could also be the reason for the relatively larger number of *if*s scored by the PH code for this model.

The score for median values obtained by Mocassin for the PN150 optically thick planetary nebula is extremely good, obtaining the highest value of fifteen medians, above the other codes which obtained between two and thirteen (see Table 3.8).

3.3.4 The optically thin planetary nebula benchmark (PN75)

The optically thin planetary nebula (PN75) benchmark model is not a radiation bounded case, but a matter bounded one and, in fact, the outer radius is given as an input parameter to all codes and fixed at 7.5×10^{19} cm. For this reason, in this model there is not a straightforward *conservation law* for the absolute flux of $H\beta$. This can be used to explain, in part at least, the relatively bad score of the GF and HN codes for low *if*s (Table 3.7), since, for one reason or another, their predicted $H\beta$ fluxes deviated somewhat from the average, thus shifting all the other line intensities, given in $H\beta$ units. Mocassin, however, obtained a low number of *if*s for this relatively difficult case, scoring nine *if*s in total, with none of those having a value greater than 1.30.

Mocassin obtained a score of thirteen median values for this benchmark case, which compares well with he scores obtained by the other codes for this benchmark, ranging from eight to eighteen median values.

3.4 Conclusions

The overall performance of Mocassin for the four benchmarks was very satisfactory, as shown by Table 3.7. The results obtained from the one-dimensional mode of Mocassin are,

Table 3.6: Lexington 2000 optically thin planetary nebula (PN75) benchmark case results.

Line	Med	GF	HN	DP	PH	RS	BE	
							3-D	1-D
$H_\beta/10^{34}$ erg/s	5.71	6.08	5.56	5.74	5.96	5.69	5.65	5.63
H_β 4861	-	1.00	1.00	1.00	1.00	1.00	1.00	1.00
He I 5876	0.131	0.130	0.144	0.132	0.126	0.125	0.132	0.132
He II 4686	0.087	0.085	0.089	0.087	0.087	-	0.093	0.094
C II] 2325+	0.039	0.023	0.047	0.040	0.044	0.034	0.038	0.043
C II 1335	0.089	0.096	0.089	0.101	0.085	-	0.086	0.085
C III] 1907+1909	0.790	0.584	0.96	0.882	0.602	1.00	0.698	0.709
C IV 1549+	0.354	0.298	0.480	0.393	0.291	0.315	0.414	0.463
[N II] 6584+6548	0.098	0.069	0.097	0.089	0.108	0.119	0.100	0.087
[N II] 5755	.0012	-	.0011	.0012	.0013	.0020	.0011	.0010
N III] 1749+	0.043	0.029	0.059	0.056	0.038	0.048	0.038	0.039
[N III] 57.3 μm	0.397	0.371	0.405	0.404	0.390	0.405	0.336	0.334
N IV] 1487+	0.018	0.019	0.024	0.020	0.012	0.011	0.017	0.020
[O II] 3726+3729	0.262	0.178	0.262	0.266	0.262	0.311	0.234	0.205
[O III] 5007+4959	11.35	10.1	13.2	11.7	10.1	11.8	11.0	11.1
[O III] 4363	0.060	0.046	0.077	0.066	0.048	0.065	0.056	0.057
[O III] 51.8 μm	1.98	1.94	2.09	1.94	1.95	2.02	2.07	2.07
[O III] 88.3 μm	1.12	0.986	1.13	1.12	1.07	1.12	1.14	1.14
[O IV] 25.9 μm	0.814	0.767	0.741	0.859	0.821	0.807	0.894	0.942
O IV] 1403+	0.013	0.009	0.015	0.014	.093	-	0.013	0.015
[Ne II] 12.8 μm	0.012	0.012	0.012	0.012	0.012	0.017	0.013	0.012
[Ne III] 15.5 μm	0.948	0.883	0.95	0.902	1.32	1.35	0.946	0.949
[Ne III] 3869+3968	0.872	0.784	0.948	0.818	0.919	1.10	0.826	0.838
[Ne IV] 2423+	0.030	0.028	0.032	0.036	0.027	0.020	0.034	0.039
Mg II 2798+	0.102	0.086	0.14	0.111	0.071	0.093	0.114	0.106
[Mg IV] 4.49 μm	.0062	.0021	.006	.0075	.0065	.0050	.0068	.0072
[Si II] 34.8 μm	0.029	0.025	0.034	0.025	0.060	0.004	0.061	0.052
Si II] 2335+	.0057	.0037	.0078	.0054	-	.0010	.0062	.0052
Si III] 1892+	0.104	0.087	0.16	0.136	0.101	0.019	0.107	0.110
Si IV 1397+	0.017	0.017	0.023	0.018	0.013	0.023	0.016	0.018
[S II] 6716+6731	.0020	0.023	0.036	0.029	0.013	0.016	0.017	0.013
[S II] 4069+4076	.0017	.0022	.0034	.0030	.0013	.0010	.0012	.0010
[S III] 18.7 μm	0.486	0.619	0.715	0.631	0.316	0.357	0.285	0.266
[S III] 33.6 μm	0.533	0.702	0.768	0.684	0.339	0.383	0.306	0.285
[S III] 9532+9069	1.20	1.31	1.51	1.33	0.915	1.09	0.831	0.777
[S IV] 10.5 μm	1.94	1.71	1.57	1.72	2.17	2.33	2.79	2.87
$10^3 \times \Delta$(BC 3645)/Å	4.35	4.25	-	4.25	4.35	4.90	4.54	4.56
T_{inner}/ K	14300	14450	14640	14680	14150	13620	14100	14990
$< T[N_pN_e] >$/K	10425	9885	11260	10510	10340	10510	10220	10263
$R_{out}/10^{17}$cm	-	7.50	7.50	7.50	7.50	7.50	7.50	7.50
$\frac{<He^+>}{<H^+>}$	0.913	0.912	0.92	0.914	0.920	0.913	0.911	0.908
τ(1Ryd)	1.47	1.35	1.64	1.61	1.47	-	1.15	1.29

GF: G. Ferland's *Cloudy*; PH: J.P Harrington code; DP: D. Péquignot's *Nebu*; HN: H. Netzer's *Ion*; RS: R. Sutherland's *Mappings*; BE: B. Ercolano's *Mocassin*.

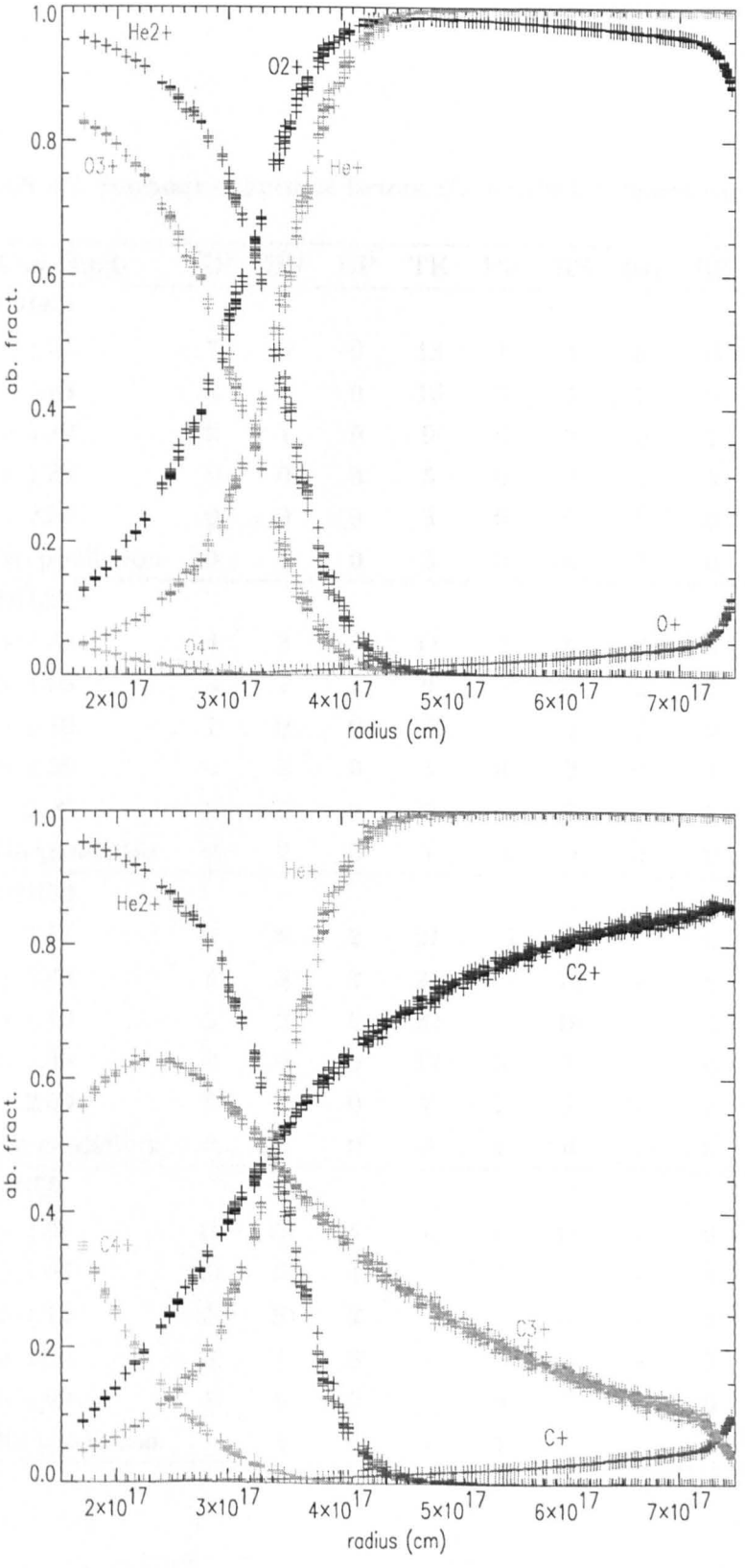

Figure 3.4: Fractional ionic abundances of oxygen (top panel) and carbon (bottom panel), as a function of radius, for the optically thin planetary nebula benchmark case (PN75).

Table 3.7: Summary of isolation factors, *if*s, for the benchmark cases

Case Study	GF	HN	DP	TK	PH	RS	RR	BE
HII40								
> 1.01	7	6	0	18	1	4	6	11
> 1.03	4	5	0	16	0	3	5	9
> 1.10	2	1	0	9	0	2	2	7
> 1.30	0	0	0	5	0	0	1	3
> 2.00	0	0	0	3	0	0	0	0
No prediction	0	1	0	5	0	0	5	0
HII20								
> 1.01	4	2	1	11	3	6	2	8
> 1.03	3	1	1	9	3	5	2	7
> 1.10	1	0	0	8	0	3	2	2
> 1.30	0	0	0	5	0	2	0	1
> 2.00	0	0	0	2	0	0	0	1
No prediction	0	2	0	1	0	0	3	0
PN150								
> 1.01	4	8	2	27	15	23	-	6
> 1.03	4	6	2	26	13	19	-	5
> 1.10	1	2	0	22	7	16	-	1
> 1.30	0	0	0	17	6	7	-	0
> 2.00	0	0	0	7	2	2	-	0
No prediction	0	0	0	3	1	6	-	0
PN75								
> 1.01	14	20	4	-	5	14	-	9
> 1.03	11	18	4	-	4	13	-	8
> 1.10	5	10	2	-	4	10	-	6
> 1.30	4	1	0	-	0	3	-	0
> 2.00	1	0	0	-	0	3	-	0
No prediction	1	1	0	-	1	4	-	0

Table 3.8: Summary of median values for the benchmark cases

Case Study	Total	GF	HN	DP	TK	PH	RS	RR	BE
HII40	31	9	8	10	3	10	10	7	10
HII20	24	2	7	8	5	7	6	3	6
Subtot HII	55	11	15	18	8	17	16	10	16
PN150	49	9	11	12	2	13	4	-	15
PN75	40	10	8	19	-	16	13	-	13
Subtot PN	89	20	19	31	(2)	29	17	-	28

in general, in very good agreement with those obtained using the fully three-dimensional Mocassin models. One noticeable difference, common to all four benchmarks, is that the kinetic temperature at the illuminated inner edge of the nebula, T_{inner}, is higher for the one-dimensional Mocassin results and closer to the values obtained by the other one-dimensional codes included in the comparison. This is an obvious effect caused by the coarseness of the three-dimensional grid: since all the physical properties of the gas are constant within each volume element, then the electron temperature of a given cell will be mainly representative of the kinetic temperature at its centre. From this, it naturally follows that the coarser the grid is, and the larger the cells, then the further the kinetic temperature at the centres of the cells adjacent to the inner radius will be from the true value at the inner radius.

The electron temperatures, $< T[N_{\rm p}N_{\rm e}] >$ and $T_{\rm inner}$, predicted by Mocassin for the Lexington benchmark models tend, in particular in the H II region cases, towards the lower limit of the scatter. In the case of $T_{\rm inner}$, this seems to be a characteristic of all codes using an exact treatment for the radiative transfer. As noted by Péquignot *et al.* (2001), the kinetic temperatures calculated by codes with exact transfer tend to be lower in the innermost layers of the nebula, as the ionizing radiation field there is softer. Only two codes in the Lexington benchmarks treated the radiative transfer exactly, namely Rubin's *Nebula* (RR) and the Harrington code (PH) and, in fact, Mocassin's results for the kinetic temperatures generally agree better with those two codes' predictions. For the standard H II region benchmark (HII40), Mocassin's kinetic temperature at the inner edge of the nebula, T_{inner}, agrees extremely well with the predictions of the RR and PH codes. Similar

results are obtained for the low excitation H II region benchmark (HII20), where, again, Mocassin's T_{inner} agrees with the results of PH and RR. In both H II regions benchmark cases, however, Mocassin predicted a value which was about 250 K lower than the median for $< T[N_pN_e] >$, obtaining an $if = 1.027$ for the HII40 case and $if = 1.034$ for the HII20 case. The cause of this small discrepancy is not clear to us.

Unfortunately, R. Rubin's code, *Nebula*, was not designed to treat planetary nebulae and, therefore, the only exact one-dimensional radiative transfer code available for the optically thick planetary nebula (PN150) and the optically thin planetary nebula (PN75) benchmarks is the Harrington code (PH). For PN150, Mocassin's T_{inner} is in reasonable agreement with PH's prediction, particularly if the prediction from the one-dimensional Mocassin run is considered, since, as discussed earlier, this represents a measurement of the temperature taken closer to the inner edge of the nebula. The Mocassin result for $< T[N_pN_e] >$ is within the scatter and, in particular, BE and PH agree very well for this observable. Note that only HN and TK obtain higher temperatures for this model; moreover, the TK computation was carried out with a new code, still under development, primarily designed for X-ray studies. That code could not treat the diffuse radiation field, leading to problems for the hard radiation field cases, such as PN150. Finally, for the PN75 benchmark planetary nebula, Mocassin's T_{inner} is within the scatter (the prediction from the one-dimensional model is actually at the higher limit of it) and in reasonable agreement with PH's prediction; the result for $< T[N_pN_e] >$ is also within the scatter and is in very good agreement with the prediction of the PH code. Once again, only HN predicts a higher value for this quantity, while TK's results for this model are not available.

The models presented in this chapter were all run using a 13×13×13 grid and, since they are all spherically symmetric, the ionizing source was placed in a corner of the grid. The number of energy packets used to sample the grids and bring them to convergence varied from three to five million. As has already been discussed, the accuracy of the results depends both on the spatial sampling (i.e. the number of grid cells) and on the number of energy packets used. It is clear, however, that the latter also depends on the number of points to be sampled, so if, for example, in a given simulation the number of grid cells is increased from $n_x \times n_y \times n_z$ to $n'_x \times n'_y \times n'_z$, then the number of energy packets used must also be increased from $N_{\rm packets}$ to $N'_{\rm packets} = \frac{n'_x \times n'_y \times n'_z}{n_x \times n_y \times n_z} \cdot N_{\rm packets}$. However for these relatively simple cases the three-dimensional grid specified above was found to be sufficient to produce acceptable results. In fact, since the benchmark models are spherically

symmetric then, although the number of sampling points along each orthogonal axis is only 13, this is the equivalent of a one-dimensional code with 273 radial points, which is the number of different values of r given by all the (x,y,z) combinations. This is clearly demonstated in figures ?? to ??, where the number of data points and the spacing between them shows that the spatial sampling is indeed appropriate. The plots also show that the number of energy packets used in the simulations was sufficient, since the scatter of the ordinate values for a given r, which is essentially a measure of the error bars, is very small. The largest scatter was obtained in the plots for the HII20 benchmark (Figure ??); this is a very soft ionizing radiation field case and a larger number of energy packets is probably required in order to reduce the scatter shown and increase the accuracy of the results. For the purpose of this benchmark exercise, however, the accuracy achieved for HII20 is sufficient to produce satisfactory results.

CHAPTER 4

Modelling of NGC 3918

4.1 Introduction

The southern planetary nebula NGC 3918 (PN G294.6+04.7) is a very well known and widely studied object. A detailed study, based on UV, optical and radio observations, was presented by Clegg *et al.* (1987). The morphological and kinematical information available at the time of their work, was, however, very limited, and, based on this, they constructed a photoionization model, using the Harrington code, having assumed a biconical geometry for a nebula which is then seen almost *pole-on*. A two-dimensional representation of their model is shown in Figure 2.3. They had first tried a spherical model, deriving the radial hydrogen density distribution from the average radial intensity profile in the $H\beta$ map they used, which had been obtained at the Boyden Observatory, South Africa, in 1973 by Drs. K. Reay and S. P. Worswick. The Zanstra temperature they derived for the central star was $117,000\,K$, corresponding to a luminosity of $4900\,L_{\odot}$; this model, however, did not succeed in reproducing the line strength of some of the high ionization species observed, such as, for example, Ne V, O V and O IV. They interpreted this as an indication that the nebula could be optically thin in some directions as seen from the star; this led to the formulation of the biconical model seen in Figure 2.3. The presence of an optically thin phase allowed an upward correction to the original Zanstra temperature and, in the final model, they adopted the ionizing spectrum described by a non-LTE model atmosphere for a central star having an effective temperature of $140,000\ K$, $log\ g\ =\ 6.5$ and a photospheric $He/H\ =\ 0.10$ by number. The resulting nebular model atmosphere was

calculated by Clegg *et al.* (1987) using the program of Mihalas and Auer (1975). This model seemed to reproduce the main spectroscopic features observed.

Present observational data, such as for example the images of NGC 3918 taken by the *HST* (see Figure 4.12) and the echellograms obtained in several emission lines by Corradi *et al.* (1999) (Figure 4.15), show, however, that a biconical model is inconsistent with the spatio-kinematical structure observed for this planetary nebula. Corradi *et al.* (1999) presented an analysis of optical images and high resolution long slit spectra of three planetary nebulae, including NGC 3918. They concluded that the large scale structure of this object consists of a bright inner shell of roughly elliptical shape, from which two fainter protrusions extend in the polar direction, giving what was described in their paper as an overall spindle-like appearance. This inner shell, which has a size of $12'' \times 20''$, measured along its major and minor axes, is surrounded by an elliptical shell with a diameter of $16''$. From the images and from the long slit spectra they obtained the basic kinematical, geometrical and the orientation parameters of the inner shell. They adopted a hydrodynamical model by G. Mellema (1996) to reproduce, at least qualitatively, the observations. The model which gave the best fit was one, from Mellema's set, which posits an initial mass distribution strongly enhanced in the equatorial region, with a density contrast between the equatorial and the polar regions as large as 10 (see Figure:4.2). The effects of an expanding shock driven by a strong wind would give a spindle-like structure similar to the one observed in the inner shell of NGC 3918. Corradi *et al.* (1999) derived the inclination and the kinematical parameters of the inner shell by using the spatio-kinematical model of Solf and Ulrich (1985) (which was also used to obtain $H\alpha$ position-velocity diagrams, as well as the shape of the inner shell), to match the observational data. Their final model still showed some deviation from the observations, particularly in the long-axis position-velocity plot, which they attributed to simplified assumptions in the spatio-kinematical model. Photoionization calculations, however, were not carried out in their work, and therefore no comparison with the observed spectrum was available to them.

Given the vast amount of observational data available for this object and the existence of the two different models described above, NGC 3918 seemed an excellent candidate for Mocassin's first application to a real astrophysical object. Three photoionization models were constructed, using different density distribution descriptions, in order to try to reproduce the main spectroscopic features, as well as the projected maps published by Corradi

et al. (1999). Velocity fields were then applied to the final converged grids in order to produce position-velocity diagrams to compare with the observations.

In Section 4.2 the biconical density distribution model of Clegg *et al.* (1987) is described and the results obtained for it with Mocassin are presented and compared with those of Clegg *et al.* (1987), who used the one-dimensional Harrington code. A consistency test for the diffuse radiation field is also carried out in this section, in order to investigate the effects of discontinuities in the diffuse field transport in one-dimensional codes. The results obtained from the spindle-like models of NGC 3918 are presented in Section 4.3. Discrepancies were found between the predictions of all the models and the *ISO SWS* measurements of the infrared fine-structure lines; the possible reasons of these discrepancies are discussed in Section 4.4. Section 4.5 is concerned with the visualization of the models' results and comparison with the observations. Finally, the conclusions are summarised in Section 4.6.

4.2 The Biconical Density Distribution Model

The first nebular model to be run was the pole-on biconical distribution described by Clegg *et al.* (1987). This consisted of an optically thick biconical structure embedded into an optically thin sphere. The bicones are aligned along the polar axis of the nebula which described an angle of 15° with the line of sight. Exactly the same parameters were used for the central star and, apart from helium, argon and iron, the same nebular abundances as in their model; these are summarised in Table 4.1. The main reason for using exactly the same parameters is to be able to distinguish between the causes of any discrepancies between this model's results and the original Clegg *et al.* (1987) model results. However, in the case of helium the empirical value derived by Clegg *et al.* (1987) was used instead of their model value, since they comment in their paper that this is more reliable. In the case of argon and iron the empirical abundance also had to be used, since these elements were not included in their code (that of J.P. Harrington) and, therefore, model results for these do not exist. The radial density law that was adopted by Clegg *et al.* (1987), and mapped onto the three-dimensional Cartesian grid used in the current model, was constructed by them by deconvolving the observed nebular surface brightness, using the formalism of Harrington and Feibelman (1983), and has the form

$$N_H(R) = N_0 \, (R/R_1)^n \, exp[-0.5(R/R_1)^2] \tag{4.1}$$

where $N_H(R)$ is the hydrogen number density at distance R from the centre of the nebula, N_0 is a normalization constant and R_1 and n are parameters which may be varied. The values used for these parameters are also given in Table 4.1, together with Φ, the half angle of the density enhanced cones, f, the density enhancement factor between the two regions, and the axial ratio, a/b.

Table 4.1: Input parameters for Mocassin's biconical model of NGC 3918.

L_*	6900 $L_\odot$	He/H	0.107
R_{in}	0. pc	C/H	8.e-4
R_{out}	0.106 pc	N/H	1.5e-4
T_{eff}	140,000 K	O/H	5.e-4
R_1	0.0333 pc	Ne/H	1.2e-4
n	2.3	Mg/H	1.4e-5
f	3	Si/H	1.e-5
Φ	45°	S/H	1.6e-5
N_0	2381 cm^{-3}	Ar/H	2.e-6
a/b	1	Fe/H	3.7e-7

The abundances are given by number, relative to H

4.2.1 The Biconical Density Distribution Model: Results

Following the analysis of Clegg *et al.* (1987), emission line fluxes are given relative to the total dereddened $H\beta$ flux integrated over the entire nebula, on a scale where $H\beta$ is equal to 100. The contributions from each sector and the total relative fluxes are listed in Table 4.2, together with Clegg et al.'s results for both sectors and the total observed values. The last column of the table contains the references for the observational data used. The fractional ionic abundances were also calculated for the thin and the thick regions and are given in Table 4.5. As has already been mentioned in Section 2.3.4, different definitions of this quantity are found in the literature; for the sake of consistency with Clegg *et al.* (1987) work, the definition given by Harrington *et al.* (1982) and expressed by Equation 2.19 will be used in this case. The mean temperatures weighted by the ionic abundances are calculated and given in Table 4.7. The definition of these given by Harrington *et al.* (1982)

Table 4.2: Observed emission lines fluxes for NGC 3918 and predictions of the biconical model.

Line	This Work			Clegg et al.			Observed	Ref
	Thin	Thick	Total	Thin	Thick	Total		
$H\beta/10^{-10}\frac{erg}{cm^2 s}$	0.45	1.88	2.33	0.45	1.86	2.32	2.29	b
$H\beta$ 4861	100	100	100	100	100	100	100	-
He I 5876	0.08	8.5	8.5	0.06	7.7	7.8	10.81	a
He II 4686	24	30	54	22	26	48	41.65	a
C II] 2326	0.21	57	57	0.72	81	82	31.24	a
C II 4267	0.004	0.32	0.32	0.006	0.32	0.32	0.50	a
[C II] 157.74μm	0.0	0.35	0.35	-	-	-	0.21	c
C III] 1908	33	577	610	58.7	577	637	492.5	a
C III 4648	0.10	0.50	0.61	0.10	0.42	0.52	0.42	a
C III] 2297	1.11	5.9	7.0	1.0	4.9	5.9	5:	e
C IV 1550*	596	964	1560	659	779	1439	457.6	a
C IV 4658	0.25	0.16	0.40	0.24	0.16	0.40	0.33	a
[N I] 5199	0.0	0.21	0.21	-	-	-	0.63	a
[N II] 6584	0.06	73	73	0.2	73	73	84	a
[N III] 1751	2.0	22	24	4.6	25	29	26.7	a
[N III] 57.3 μm	0.64	12	13	1.0	12	13	13.5	c
N IV] 1486	19	26	45	31	26	57	46.4	a
N V 1240*	42	22	64	47	19	66	41.4	a
[O I] 6300	0.0	2.7	2.7	0.0	0.56	0.56	5.24	a
[O I] 63.12 μm	0.0	0.23	0.23	-	-	-	6.72	c
[O I] 145.5 μm	0.0	0.018	0.018	-	-	-	0.23	c
[O II] 3727	0.08	104	104	0.2	89	89	94.5	a
[O III] 51.8 μm	2.8	90	93	4.0	94	98	88.6	c
[O III] 88.4 μm	0.91	16	17	1.3	17	19	27.51	c
[O III] 5007	40	1543	1583	63	1539	1602	1657	a
[O III] 4363	0.85	19	20	1.4	18.9	20	21.6	a
[O IV] 25.9 μm	190	161	352	274	177	451	89	d
O IV] 1402	16	14	30	28	16	43	48.9	a
O IV 1342	1.4	0.83	2.2	1.0	0.6	1.6	2:	e
[Ne II] 12.8 μm	0.001	0.94	0.94	0.0	0.77	0.77	12:	f
[Ne III] 15.6 μm	1.8	130	132	1.3	167	168	46.3	d
[Ne III] 3869	4.1	161	165	3	172	175	135.5	a
[Ne IV] 2423	35	42	77	50	52	102	132	e
[Ne V] 3426	75	45	119	70	40	110	80	e
[Ne V] 14.3 μm	179	107	286	18	13	31	19.6	d
[Ne V] 24.3 μm	156	64	220	30	19	49	23.1	d
[Ne VI] 7.6 μm	49	22	70	11	4.9	15.8	-	-
Mg I] 4565	0.00	0.73	0.73	0.00	0.28	0.28	0.13	a
Mg II 2800*	0.26	78	78	0.01	43	43	$\leq$1	e
[Mg IV] 4.49 μm	0.42	3.1	3.5	0.96	4.4	5.4	-	-
[Mg V] 2783	2.2	2.4	4.6	3.2	2.6	5.8	5.6	e
[Mg V] 5.6 μm	4.5	6.3	10.9	4.9	5.4	10.3	-	-
Si III] 1887	0.97	15	16	1.2	12.5	13.7	8	e
Si IV 1399*	2.7	7.9	11	2.8	5.4	8.2	9	e
[S II] 4070	0.0	2.1	2.1	0.0	2.8	2.8	2.693	a
[S III] 18.7 μm	0.03	38	38	0.31	38	38	8.7	d
[S III] 33.6 μm	0.02	16	16	0.2	15.6	16	-	-
[S III] 6312	0.006	3.7	3.7	0.005	3.4	3.4	2.27	a
[S IV] 10.5μm	7.23	207	214	24	210	234	35.0	d

* Attenuated by dust absorption (see Section 4.2.1.2).

[a] Tsamis *et al.* (2002); [b] Cahn *et al.* (1992); [c] Liu *et al.* (2001); [d] Bower (2001); [e] Clegg *et al.* (1987);[f] Pottasch *et al.* (1986).

is only applicable to spherical geometry and, therefore, in this work the definition given by Ferland *et al.* (1995) and expressed in Equation 2.21 was used instead. The fractional ionic abundances and the mean temperatures weighted by ionic species were also presented by Clegg *et al.* (1987), these are of great use in this work as they provide important parameters for the comparison of the Mocassin model to theirs. The observed value of the integrated $H\beta$ flux was obtained from Cahn *et al.* (1992) and it was dereddened by adopting an interstellar reddening constant, $c(H\beta)$, equal to 0.40. This value, which is within the error bars of the value estimated by Clegg *et al.* (1987), $c(H\beta) = 0.43 \pm 0.5$, was derived by Tsamis *et al.* (2002) and has been adopted in this work because it is consistent with observations of the optical Balmer emission lines, also published in Tsamis *et al.* (2002) and listed in Table 4.2 (reference *a*). It was not necessary to adjust the infrared line fluxes as these are not affected significantly by interstellar reddening. The optical observations presented by Tsamis *et al.* (2002) were obtained by uniformly scanning a long slit across the nebula, which method, when combined with the total Hβ flux measured with a large entrance aperture (e.g. Cahn *et al.*, 1992), yields the total fluxes for the whole nebula for all emission lines detected in the optical spectra. These fluxes are thus be directly comparable to those measured with spaceborne facilities using large apertures, such as the *IUE* in the ultraviolet and *ISO* in the infrared.

Most of the results shown in Table 4.2 are in reasonable agreement with the results published by Clegg *et al.* (1987), also reported in the same table. For both models, however, the doubly ionized helium recombination line at 4686 Å is too strong, while the singly ionized helium triplet line at 5876 Å is too weak, when compared with the observations. This result is consistent with the ionic fractions listed in tables 4.4 and 4.5 for these ions. It is worth noting, however, that the values of the relative fluxes that Clegg *et al.* (1987) observed for these lines are 45.0 for He II 4686Å and 9.5 for He I 5876Å on a scale where $H\beta = 100$. These values are closer to their model values of 48.0 and 7.8 than the more recent observations of 41.7 and 10.8 by Tsamis *et al.* (2002) quoted in Table 4.2 (reference a), the former being the values they had tried to reproduce in their model. A better agreement with the more recent observations can be obtained by using a different model atmosphere for the ionizing source. As has already been mentioned at the start of this chapter, a non-LTE model atmosphere for a central star with an effective temperature of $140,000\ K$, $log\ g = 6.5$ and photospheric $He/H = 0.10$ by number was used by Clegg *et al.* (1987) and in this work; however by increasing the value of $log\ g$, the depth

of the doubly ionized helium jump is decreased. This will result in fewer He^+ ionizing photons and, therefore, a lower He^{2+} and a higher He^+ nebular ionic fractions. The values obtained by using a non-LTE model for a central star of the same luminosity, effective temperature and He/H ratio, but with $log\ g = 7.5$, are 48 and 9.2 for the He II 4686Å and He I 5876Å line fluxes (relative to Hβ, on a scale where Hβ = 100), respectively. These values are closer to the observations than those obtained previously, with $log\ g = 6.5$ and reported in Table 4.2. One final point to be made about the nebular helium results is that, as it was mentioned at the start of this section, the nebular helium abundance used in this work is the empirical value calculated by Clegg *et al.* (1987), $He/H = 0.107$ by number, which is slightly higher than the value they used in their model, $He/H = 0.10$; this also contributes to the difference between the current model results obtained for the He II 4686 Å and the He I 5876 Å line fluxes and those presented by Clegg *et al.* (1987).

With regard to the other emission line fluxes listed in Table 4.2, some discrepancies between the two models do exist, but they are, in the majority of cases within 30% and the overall ionization structure of the nebula coincides. In particular, large discrepancies were found between the current work and that of Clegg *et al.* (1987) in the predictions of the [Ne V] fine-structure line fluxes, which will be discussed in Sections 4.2.1.1 and 4.4. Considering the significant progress in atomic physics in the past fifteen years, on the one hand, and the completely different treatment of the radiative transfer adopted in the two codes, on the other, that there are some differences in the results obtained is hardly surprising. Neither the Opacity Project (Verner *et al.*, 1996) nor the Iron Project (Hummer *et al.*, 1993) existed in 1987 and also other important processes' rates have changed since then.

Mocassin's predictions for electron density and temperature diagnostic line ratios can be compared to those obtained by Clegg *et al.* (1987), and to the observed ratios in Table 4.3. There is very good agreement between the two models' predictions of line ratios, which is to be expected, since the density distributions used were the same. The small differences observed are reflected in the emission line fluxes predictions, listed in Table 4.2, and, as has already been discussed, can probably be mostly assigned to differences in the atomic data sets. The diffuse radiation field, however, might also have some effect on the ionization structure, especially near the edges between the two sectors and in the outer regions of the nebula.

4.2.1.1 The [Ne V] fine-structure lines

The largest discrepancies are observed for the infrared fine-structure line fluxes of Ne^{4+}, namely [Ne V] 14.3 μm and [Ne V] 24.3 μm, which disagree by factors of almost 10 and 5, respectively with Clegg *et al.* (1987) predictions and indeed with the observations. This discrepancy between the models is due to differences in the collision strengths used for these lines. The collision strengths for these transitions used by Mocassin are the calculations by Lennon and Burke (1991) based on the R-matrix method described by Berrington *et al.* (1987). These collision strengths are much larger than the rates given by Mendoza (1983) based on the results from Saraph *et al.* (1970), which were used by Clegg *et al.* (1987) in their model. In 1987, however, the collision strengths of Aggarwal (1983) were already available for [Ne V], and these were also much higher than those given by Mendoza (1983), since they took into account the large resonances existing at energies just above the threshold for excitation of the fine-structure lines. Clegg *et al.* (1987) decided against using those results as they were not in agreement with the observed ratios of [Ne V] 3426 Å/ 14.3 μm. However, van Hoof *et al.* (2000) later argued that the collision strengths calculated by Lennon and Burke (1991), which were similar to the Aggarwal (1983) values, are reliable, and that the discrepancies found by Clegg *et al.* (1987) can be explained by the inaccuracy of the [Ne V] 3426 Å flux that they adopted. Moreover, Berrington (2001) in his contribution to the November 2000 Lexington workshop, discussed near threshold resonances in the calculation of collision strengths for fine-structure transitions, taking [Ne V] as a case study. He compared the effective collision strengths obtained using different methods, showing that they all largely agree with the Lennon and Burke (1991) results. During the same Lexington meeting, a new R-matrix calculation of [Ne V] was independently published by Griffin and Badnell (2000) who also obtained similar results. In this work the decision to use the collision strengths of Lennon and Burke (1991), although producing results which are in disagreement with Clegg *et al.* (1987) observations, was finally taken, since the benchmarking carried out for the Lexington optically thick, high excitation planetary nebula, which has a central star with effective temperature, $T_{eff} = 150,000\,K$ (similar to the central star of NGC 3918; see chapter 3), clearly showed that most photoionization codes (all but Sutherland's *Mappings*) use the new collision strengths. The likely cause of the large discrepancy between the predicted and the observed [Ne V] fine-structure line fluxes will be addressed in Sections 4.2.1.3 and

Section 4.4.

4.2.1.2 The resonance lines

There are some large discrepancies between the predictions of both Mocassin and Clegg *et al.* (1987) and the observations for the fluxes of the C IV 1550 Å and Mg II 2800 Å resonance lines. The reason for this is that these lines are attenuated by nebular dust absorption, which was not accounted for in this work, or in Clegg *et al.* (1987). Moreover, Mg II 2800 Å also suffers from absorption by interstellar Mg^+ and this is probably the main reason for the almost total absence of this line in the observed spectrum. Resonance lines must travel a much longer distance to escape from a nebula than do forbidden lines or the continuum radiation, because of the high optical depth in them; this translates into an enhanced probability of absorption by dust. The N V 1240 Å resonance line is also affected by this process, although in a minor way. The Si IV resonance line doublet at 1393 Å and 1401 Å can also be subject to attenuation by dust absorption, however this line appears to be only slightly overestimated by the Mocassin model and it is in agreement with the observations in Clegg *et al.* (1987). Harrington *et al.* (1988) published a dust model for NGC 3918 which confirms that the intensities of the resonance lines are indeed reduced. In their dust model Harrington, Monk and Clegg followed the same method as in the photoionization model for this object (Clegg *et al.*, 1987), treating the thin and the thick sector as two separate, spherically symmetric objects and then combined the results, weighted by the respective volume of each sector, i.e. 29% for the thick sector and 71% for the thin sector. In their model they found that the total flux of the C IV 1550 Å doublet, relative to $H\beta = 100$, was attenuated from 1435 to 950, with 45% of photons destroyed in the optically thick sector and 21% in the optically thin sector. This is still 85% too strong compared to the observed value they used (F(1550) = 512) and 107% too strong compared to the more recently re-calibrated and extracted *IUE* archive spectra presented by Tsamis *et al.* (2002) (F(1550) = 458). Harrington, Monk and Clegg do not give a final answer to whether the cause of this discrepancy lies in the photoionization model producing too much radiation or in the dust model being too ineffective in destroying it, however they speculate that if the grain opacity near 1550 Å were greater in their dust model, more line photons would be destroyed hence improving the fit. The flux of N V 1240 Å, relative to $H\beta = 100$, is reduced from 66 to 52, with 25% of photons being destroyed in the thick sector and 20% in the thin sector. The value measured by Tsamis *et al.* (2002) for this line

is 41.4. In the case of Si IV 1400 Å dust actually makes the fit worse, by attenuating the flux, relative to Hβ = 100, from 8.2 to 5.7, whereas the observed value is 9 (Clegg *et al.*, 1987). This is, however, a weak line and the observed flux might not be accurate. Finally, Harrington *et al.* (1988) predicted that the flux of Mg II 2800Å is also reduced by dust attenuation from 43 to 29. However, as mentioned above and in Clegg *et al.* (1987) this line shows evidence of interstellar absorption, so it cannot be measured properly. Aside from this, the dusty photoionization model is nearly identical to the one presented by Clegg *et al.* (1987).

4.2.1.3 The infrared fine-structure lines

Most of the infrared fine-structure line fluxes measurements reported in Table 4.2 are taken from Bower (2001) (reference *d*), measured from spectra taken with *ISO* Short-Wavelength Spectrometer (*SWS*) between 1996 and 1998. The fluxes measured by Bower (2001) for the infrared fine-structure lines of NGC 3918 are systematically smaller, by approximately a factor of two, than those measured by Pottasch *et al.* (1986), who used IRAS Low-Resolution Spectrometer (LRS) observations, and are smaller by factors of 3 to 6 for most lines, apart from the [Ne V] fine-structure lines, which are between 10-15 times smaller, compared to both Mocassin and Clegg *et al.* (1987) predictions. The reason for the [Ne V] fine-structure line discrepancy between the Mocassin results and Clegg *et al.* (1987) results has already been discussed above. This *ISO SWS* discrepancy is also evident in the spindle-like models of NGC 3918 (see Section 4.3.1) and is believed to be due to the combined effects of incorrect object coordinates used for the *ISO* observations and the small size of the *ISO SWS* aperture. The *ISO LWS* fluxes for [N III] 57.3 μm and [O III] 51.8 μm and 88.4 μm lines (Liu *et al.*, 2001) are in good agreement with the models' predictions. Although the same pointing error occurred, the much larger LWS aperture minimised the effects on the observed fluxes. Corrections for the *ISO SWS* line fluxes are calculated and discussed in detail in Section 4.4. The *ISO LWS* fluxes for the two [O I] infrared fine-structure lines, [O I] 63.12 μm and [O I] 145.5 μm, are much bigger than Mocassin's predictions; the reason for this discrepancy is that these lines are mostly emitted in the photodissociation regions (PDRs) of nebulae (Liu *et al.*, 2001), which is not treated in the current version of the code.

Table 4.3: Diagnostic ratios for electron temperature, T_e, and electron density, N_e. Ratios predicted by Mocassin's biconical model (column 3), Clegg *et al.* (1987) model (column 4) and observed ratio (column 5).

Ion[a]	Lines (Å)	Ratio (Mocassin)	Ratio (C87)	Ratio (observed)	ref
		N_e			
Mg I	4562/4571	0.54	0.42:	0.28	1
S II	6716/6731	0.72	0.70	0.57	1
O II	3726/3729	1.63	1.61	1.98	2
O II	7325/3727[b]	0.071	-	0.078	1
C III	1906/1909	1.34	1.36	1.31	2
Si III	1883/1892	1.28	1.30	1.37	2
Ne IV	2421/2424	0.94	0.93	1.00	2
N IV	1483/1486	1.50	1.87	1.85	2
O IV	1401/1404	1.21	1.14	1.50	2
		T_e			
N II	5755/6584	0.022	0.025	0.021	1
S II	4073/6724[c]	0.17	-	0.34	1
C^{2+}	4267/1908	0.0005	0.0005	0.0008	2
S III	6312/9532	0.032	0.029	0.032	2
O III	4363/5007	0.013	0.013	0.013	1
Ne IV	1602/2423	0.049	0.049	0.047	2
Ne V	1575/3426	0.0104	0.012	0.007:	2

C87 = Clegg *et al.* (1987)

[a] In order of increasing ionization potential.

[b] (7321+7332)/(3726+3729)

[c] (4068+4076)/(6717+6731)

ref: 1: Tsamis *et al.* (2002); 2: Clegg *et al.* (1987)

Table 4.4: Nebular-averaged fractional ionic abundances for the biconical model of NGC 3918 by Clegg *et al.* (1987).

	Ion						
Element	I	II	III	IV	V	VI	VII
H	0.92(-2)	0.991					
	0.53(-3)	0.999					
He	0.20(-2)	0.683	0.315				
	0.73(-5)	0.026	0.974				
C	0.19(-3)	0.066	0.512	0.289	0.134		
	0.27(-6)	0.60(-3)	0.044	0.244	0.712		
N	0.63(-3)	0.071	0.511	0.333	0.059	0.025	
	0.10(-6)	0.36(-3)	0.074	0.405	0.324	0.196	
O	0.14(-2)	0.053	0.708	0.174	0.047	0.014	0.024
	0.36(-7)	0.15(-3)	0.057	0.517	0.300	0.107	0.018
Ne	0.73(-5)	0.78(-2)	0.682	0.183	0.111	0.015	0.51(-3)
	0.18(-8)	0.24(-4)	0.019	0.325	0.541	0.112	0.37(-2)
S	0.75(-5)	0.024	0.301	0.483	0.095	0.072	0.024
	0.24(-8)	0.27(-4)	0.76(-2)	0.171	0.205	0.426	0.191
Si	0.30(-3)	0.285	0.189	0.213	0.251	0.060	
	0.12(-5)	0.77(-3)	0.016	0.076	0.578	0.328	
Mg	0.40(-3)	0.058	0.566	0.142	0.164	0.069	
	0.86(-7)	0.11(-4)	0.48(-2)	0.105	0.499	0.391	

For each element the upper row is for the optically thick phase and the lower row for the optically thin phase.

Table 4.5: Nebular averaged fractional ionic abundances for NGC 3918 (Mocassin: C87 biconical model)

	Ion						
Element	I	II	III	IV	V	VI	VII
H	0.14(-1)	0.986					
	0.51(-3)	0.999					
He	0.44(-2)	0.671	0.325				
	0.95(-5)	0.028	0.972				
C	0.12(-3)	0.053	0.487	0.333	0.128		
	0.46(-7)	0.21(-3)	0.028	0.260	0.711		
N	0.15(-2)	0.065	0.464	0.365	0.071	0.033	
	0.12(-7)	0.12(-3)	0.039	0.342	0.365	0.254	
O	0.80(-2)	0.067	0.674	0.156	0.070	0.021	0.43(-2)
	0.21(-7)	0.83(-4)	0.039	0.368	0.395	0.164	0.034
Ne	0.54(-4)	0.11(-1)	0.733	0.133	0.102	0.021	0.65(-3)
	0.32(-8)	0.55(-4)	0.038	0.258	0.536	0.162	0.48(-2)
S	0.17(-4)	0.027	0.294	0.362	0.214	0.081	0.022
	0.30(-9)	0.27(-5)	0.84(-3)	0.039	0.348	0.438	0.173
Si	0.21(-3)	0.325	0.195	0.256	0.127	0.078	0.019
	0.14(-6)	0.62(-3)	0.015	0.092	0.322	0.425	0.144
Mg	0.32(-2)	0.112	0.532	0.119	0.118	0.098	0.018
	0.61(-6)	0.59(-4)	0.34(-2)	0.056	0.298	0.507	0.136

For each element the upper row is for the optically thick phase and the lower row is for the optically thin phase.

Table 4.6: Mean temperatures (K) weighted by ionic species for the biconical model of NGC 3918 by Clegg *et al.* (1987).

	Ion						
Element	I	II	III	IV	V	VI	VII
H	12,100	12,920					
	16,330	16,770					
He	12,030	12,070	14,750				
	16100	16,270	16,780				
C	12,070	12,070	12,200	13,050	15,760		
	16,030	16,060	16,160	16,330	16,950		
N	12,060	12,070	12,280	13,220	15,620	17,610	
	16,000	16,050	16,150	16,350	16,760	17,870	
O	12,060	12,060	12,210	14,690	16,030	17,620	21,040
	15,950	16,020	16,130	16,400	16,900	17,830	20,730
Ne	12,030	12,010	12,070	14,130	15,450	17,550	22,610
	15,940	16,000	16,090	16,320	16,770	17,980	22,290
S	12,090	12,070	12,090	12,600	13,970	15,710	17,640
	15,960	15,980	16,060	16,170	16,380	16,730	17,830
Si	12,090	12,040	12,170	12,570	14,040	15,940	
	16,030	16,030	16,100	12,210	16,540	17,330	
Mg	12,060	12,000	11,990	13,480	14,750	16,180	
	15,910	15,940	16,010	16,180	16,510	17,250	

For each element the upper row is for the optically thick phase and the lower row for the optically thin phase.

Table 4.7: Mean temperatures (K) weighted by ionic species for NGC 3918 (Mocassin: biconical model).

	Ion						
Element	I	II	III	IV	V	VI	VII
H	11,386	12,925					
	15,881	16,326					
He	11,247	12,044	14,703				
	15,495	15,722	16,344				
C	11,582	11,585	12,116	13,133	15,858		
	15,300	15,459	15,603	15,861	16,526		
N	10,339	11,522	12,182	13,186	15,435	17,312	
	15,348	15,506	15,631	15,842	16,234	17,217	
O	10,834	11,618	12,221	14,507	15,680	17,081	20,296
	14,874	15,298	15,509	15,887	16,260	17,020	19,477
Ne	10,136	11,636	12,156	14,340	15,561	17,360	22,911
	14,990	15,243	15,467	15,859	16,269	17,301	21,769
S	11,549	11,412	11,845	12,409	13,887	15,5584	17,637
	15,016	15,115	15,353	15,603	15,910	16,285	17,437
Si	11,817	11,794	12,349	12,875	14,333	15,543	17,684
	15,362	15,398	15,561	15,677	15,949	16,364	17,563
Mg	11,747	11,690	12,013	13,491	14,605	15,547	17,563
	14,517	15,530	14,963	15,632	15,919	16,329	17,526

For each element the upper row is for the optically thick phase and the lower row for the optically thin phase.

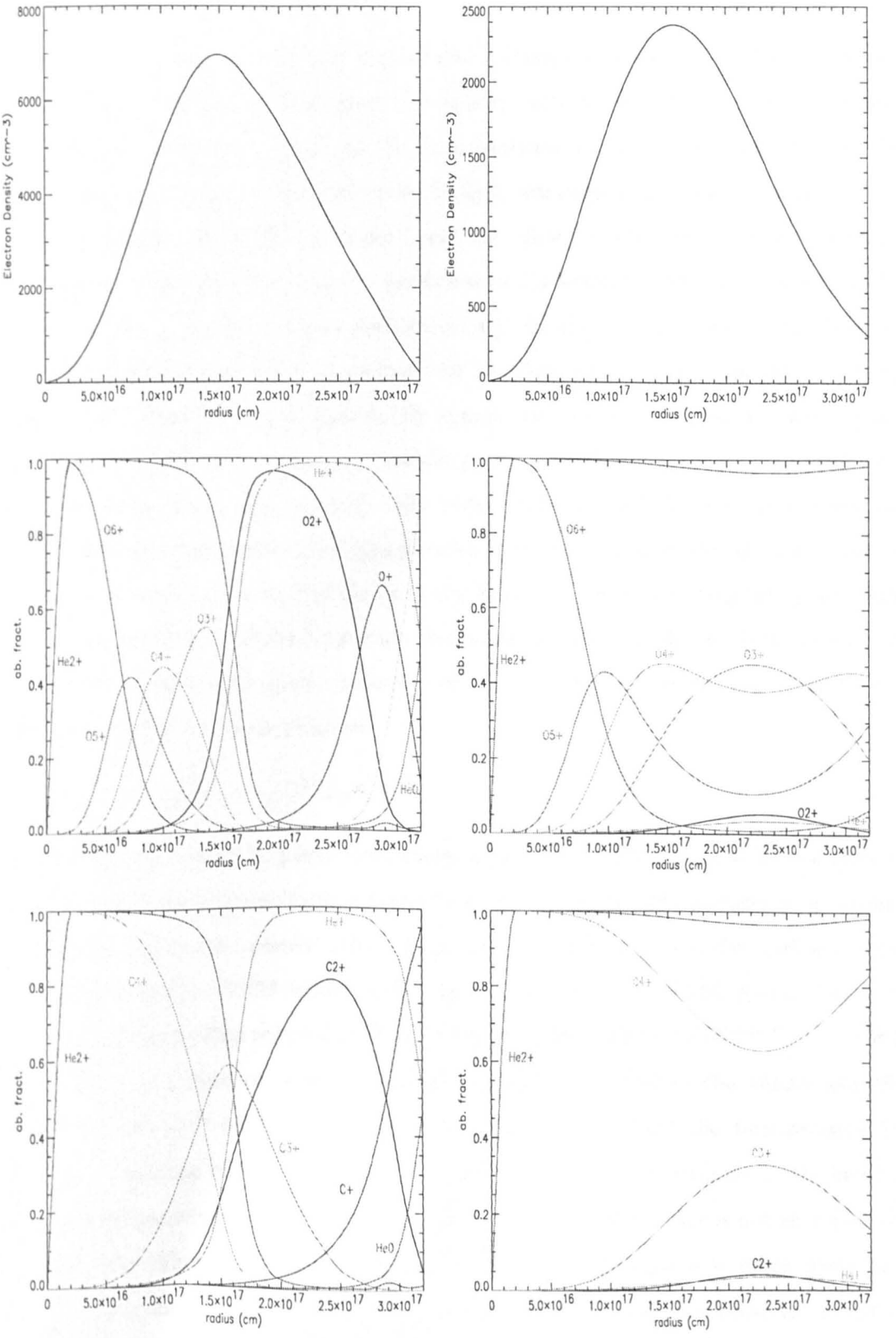

Figure 4.1: Mocassin ionic fractions for oxygen (middle panels) and carbon (bottom panels) along the polar (left panels) and equatorial (right panels) directions for the Clegg *et al.* (1987) biconical model of NGC 3918. The ionization structure of helium is also plotted in each panel. The top panels show the electron density plotted as a function of radius along the polar (top left panel) and equatorial (top right panel) directions.

4.2.1.4 The ionization structure

The general ionization structures of the nebula, calculated by the two codes and shown in tables 4.4 and 4.5, are in satisfactory agreement, with small differences which, again, can probably be attributed mainly to the improvements in the atomic data set and the different treatment of the radiative transfer. In fact, although both codes treat the diffuse field exactly, Clegg *et al.* (1987)'s model could not allow for transfer of diffuse radiation between the thin and the thick sectors. As shown by the scatter of values obtained for the benchmark problems, even amongst one-dimensional classical codes, it is usual for different codes to return slightly different predictions for the same problem, even in the extremely simplified case of homogeneous, spherically symmetric nebulae. Figure 4.1 shows plots of the ionization structure of oxygen (middle panels) and carbon (bottom panels) as a function of radius along the optically thin polar direction (left panels) and along the optically thick equatorial direction (right panels). The electron density distribution is also plotted as a function of radius for the optically thin polar direction (top-left panel) and for the optically thick equatorial direction (top-right panel). As discussed by Harrington *et al.* (1982), since the ionization potential of O^{2+} is very similar to that of He^{2+} one usually assumes the following relation

$$f(He^{2+}) = f(O^{3+}) + f(O^{4+}) + f(O^{5+}) + ... \tag{4.2}$$

where the definition of $f(X^i)$, taken from Harrington *et al.* (1982), is given in this work in Equation 2.19. However from Table 4.5 and from Figure 4.1 (middle panels), it is obvious that Equation 4.2 is not strictly valid. This is particularly true for the optically thick region, where $f(He^{2+}) = 0.329$ while $f(O^{3+})+f(O^{4+})+f(O^{5+})+... = 0.294$, giving a ratio of 1.12. For the optically thin region $f(He^{2+}) = 0.973$ and $f(O^{3+})+f(O^{4+})+f(O^{5+})+... = 0.965$, corresponding to a ratio of only 1.01. The discrepancy is due to the charge transfer rate for $O^{3+}+H^0 \rightarrow O^{2+}+H^+$, which is very large at the typical nebular temperatures for NGC 3918. The rate of the reaction is, of course, directly proportional to the neutral hydrogen abundance (see Section 1.2.2) and, therefore, charge exchange is not as important in the optically thin region where the neutral hydrogen abundance is much lower (see Table 4.5), and this is the main reason why the deviation from Equation 4.2 is not as pronounced there. Also, since in the optically thin region the radiation field is more intense at higher frequencies, a larger fraction of oxygen is in the form of O^{4+}, further decreasing the importance of the reaction $O^{3+}+H^0 \rightarrow O^{2+}+H^+$. Charge exchange reactions

were also included in the version of the Harrington code used by Clegg *et al.* (1987) for the modelling of NGC 3918, and, in fact, it is clear from Table 4.4 that their results are also discrepant from the prediction of Equation 4.2.

4.2.1.5 The temperature structure

The mean temperatures weighted by ionic species calculated by Mocassin for this model are listed in Table 4.7; these can be compared to those calculated by Clegg *et al.* (1987) and listed in Table 4.6. The most obvious difference between the two sets of results is that Mocassin's mean temperatures are systematically lower than Clegg et al.'s. This effect is even more pronounced for the optically thin region. As already predicted by Clegg *et al.* (1987), higher collision strengths for the [Ne V] fine-structure lines, as calculated by Aggarwal (1983) and by Lennon and Burke (1991)), and used in the current work, will make [Ne V] an important coolant. Furthermore, the fact that in the optically thin region the fractional ionic abundance of Ne^{4+} is higher could also explain why this region seems to be more affected by the cooling. It is also worth noticing that the mean ionic temperatures predicted by Clegg *et al.* (1987) show very little variation for the neutral species in each sector. These temperatures are all concentrated around $12,065 \pm 35\,K$ for the neutral species in the optically thick sector, and around $16,120 \pm 210\,K$ for the optically thin sector (if $T_e(H^0) = 16,330\,K$ is excluded then the rest of the neutral ion temperatures in the optically thin sector are grouped around the value 16,005±95 K). The scatter gets larger for the higher ionization species. Mocassin's results, on the other hand, show a larger scatter, even for the mean temperatures of the neutral species, with their temperatures grouped around $10960 \pm 896\,K$ for the optically thick region and 15105 ± 682 for the optically thin region. One probable explanation for this effect is the fact that, in Clegg *et al.* (1987) work, the biconical geometry is reproduced by combining two separate spherically symmetric models, hence taking no account of the interaction between the diffuse fields coming from the two phases, which could lead to fluctuations in local temperatures, particularly near the boundaries between the two regions. This is discussed in more detail in the next subsection.

4.2.2 Diffuse Field Transfer Consistency Test

Clegg *et al.* (1987) combined two appropriately weighted, spherically symmetric models to reproduce the biconical geometry. A consequence of this approach was that the diffuse

Table 4.8: Predicted emission lines fluxes for NGC 3918 (Composite versus self-consistent model.)

Line	Composite			Self-Consistent		
	Thin	Thick	Total	Thin	Thick	Total
$H_\beta/10^{-10}$ erg cm^{-2} s^{-1}	0.45	1.90	2.35	0.45	1.88	2.33
H_β 4861	100	100	100	100	100	100
He I 5876	0.07	8.7	8.8	0.08	8.5	8.5
He II 4686	23	28	51	24	30	54
C II] 2326	0.22	34	34	0.21	57	57
C II 4267	0.004	0.31	0.31	0.004	0.32	0.32
[C II] 157.74μm	.0005	.12	.12	0.0	0.35	0.35
C III] 1908	33	551	584	33	577	610
C III 4648	0.10	0.56	0.66	0.10	0.50	0.61
C III] 2297	1.05	6.6	7.7	1.11	5.9	7.0
C IV 1550	607	968	1575	596	964	1560
C IV 4658	0.24	0.16	0.40	0.25	0.16	0.40
[N I] 5199	0.0	0.006	0.006	0.0	0.21	0.21
[N II] 6584	0.06	27	28	0.06	73	73
N III] 1751	2.0	22	22	2.0	22	24
[N III] 57.3 μm	0.60	14	15	0.64	12	13
N IV] 1486	19	26	45	19	26	45
N V 1240	44	21	65	42	22	64
[O I] 6300	0.0	0.18	0.18	0.0	2.7	2.7
[O I] 63.12 μm	0.0	0.011	0.012	0.0	0.23	0.23
[O I] 145.5 μm	0.0	.0008	.0008	0.0	0.018	0.018
[O II] 3727	0.08	47.5	48	0.08	104	104
[O III] 51.8 μm	2.4	101	103	2.8	90	93
[O III] 88.4 μm	0.75	19.	20	0.91	16	17
[O III] 5007	35	1624	1659	40	1543	1583
[O III] 4363	0.78	20	21	0.85	20	20
[O IV] 25.9 μm	186	157	143	190	161	352
O IV] 1402	16	14	29	16	14	30
O IV 1342	1.3	0.84	2.1	1.4	0.83	2.2
[Ne II] 12.8 μm	0.001	0.62	0.64	0.001	0.94	0.94
[Ne III] 15.6 μm	1.6	130	133	1.8	130	132
[Ne III] 3869	3.7	161	165	4.1	161	165
[Ne IV] 2423	36	41	77	35	42	77
[Ne V] 3426	76	44	120	75	45	119
[Ne V] 14.3 μm	176	110	286	179	107	286
[Ne V] 24.3 μm	154	65	219	156	64	220
[Ne VI] 7.6 μm	49	21	70	49	22	70
Mg I] 4565	0.0	0.34	0.38	0.0	0.73	0.73
Mg II 2800	0.20	57	57	0.26	78	78
[Mg IV] 4.49 μm	0.39	3.1	3.5	0.42	3.1	3.5
[Mg V] 2783	2.2	2.4	4.6	2.2	2.4	4.6
[Mg V] 5.6 μm	4.4	6.6	11	4.5	6.3	11
Si III] 1887	1.1	14	15	0.97	15	16
Si IV 1399	2.9	7.6	11	2.7	7.9	11
[S II] 4070	0.	1.3	1.3	0.0	2.1	2.1
[S III] 18.7 μm	0.03	32	32	0.03	38	38
[S III] 33.6 μm	0.020	14	14	0.02	16	16
[S III] 6312	0.006	3.2	3.2	0.006	3.7	3.7
[S IV] 10.5μm	6.8	223	235	7.23	207	214

Table 4.9: Fractional ionic abundances for NGC 3918 (Mocassin: composite biconical model)

	Ion						
Element	I	II	III	IV	V	VI	VII
H	0.61(-2)	0.994					
	0.54(-3)	0.999					
He	0.19(-2)	0.697	0.301				
	0.88(-5)	0.025	0.975				
C	0.61(-4)	0.029	0.481	0.366	0.124		
	0.56(-7)	0.20(-3)	0.027	0.254	0.718		
N	0.97(-4)	0.025	0.476	0.399	0.068	0.032	
	0.26(-7)	0.12(-3)	0.037	0.334	0.369	0.259	
O	0.49(-3)	0.031	0.730	0.149	0.066	0.020	0.42(-2)
	0.16(-7)	0.72(-4)	0.034	0.360	0.403	0.167	0.035
Ne	0.38(-5)	0.76(-2)	0.747	0.126	0.098	0.020	0.61(-3)
	0.24(-8)	0.45(-4)	0.033	0.257	0.539	0.165	0.49(-2)
S	0.32(-5)	0.036	0.368	0.387	0.127	0.061	0.019
	0.16(-7)	0.14(-3)	0.015	0.126	0.275	0.413	0.170
Si	0.13(-3)	0.268	0.207	0.282	0.143	0.080	0.019
	0.19(-6)	0.66(-3)	0.016	0.094	0.319	0.425	0.144
Mg	0.17(-2)	0.082	0.638	0.133	0.066	0.065	0.014
	0.40(-5)	0.34(-3)	0.024	0.162	0.248	0.441	0.123

For each element the upper row is for the optically thick phase and the lower row is for the optically thin phase.

Table 4.10: Mean temperatures (K) weighted by ionic species for NGC 3918 (Mocassin, composite model).

	Ion						
Element	I	II	III	IV	V	VI	VII
H	12,060	12,880					
	16,061	16,486					
He	11,965	12,052	14,770				
	15,844	16,001	16,498				
C	11,964	11,985	12,108	12,931	15,661		
	15,702	15,757	15,842	16,039	16,667		
N	12,022	12,002	12,147	12,992	15,279	17,065	
	15,704	15,761	15,842	16,006	16,369	17,360	
O	12,032	11,989	12,155	14,481	15,507	16,862	20,001
	15,678	15,749	15,838	16,036	16,388	17,153	19,615
Ne	11,958	11,990	12,146	14,301	15,394	17,122	22,502
	15,686	15,736	15,817	16,010	16,406	17,449	21,943
S	11,986	11,982	12,946	12,233	13,638	15,402	17,367
	15,675	15,689	15,742	15,850	16,075	16,419	17,573
Si	11,919	11,947	12,169	12,624	14,066	15,293	17,397
	15,674	15,704	15,773	15,858	16,100	16,518	17,744
Mg	11,919	11,929	11,957	13,408	14,490	15,372	17,322
	15,650	15,671	15,717	15,841	16,066	16,473	17,680

For each element the upper row is for the optically thick phase and the lower row for the optically thin phase.

radiation field was not treated self-consistently, especially near the boundaries of the two zones. The effects of the diffuse radiation field are expected to be small, but they could account for some of the differences between Moccassin's results and those obtained with the spherically symmetric Harrington code. In order to investigate the magnitude of these effects, the biconical distribution was modelled again using Moccassin, but this time each sector was treated as if it were spherically symmetric. The results from each sector were then weighted by the volume of the same sector and added together to form the total flux relative to the total Hβ flux from the whole nebula. From now on this model will be referred to as the *composite model.*

Table 4.8 contains the fluxes of the emission lines relative to $H\beta$, on a scale where $H\beta$ is equal to 100, for each sector. For ease of comparison, the results from the previous, self-consistent model are also given in the same table. Tables 4.9 and 4.10 list the fractional ionic abundances and the weighted mean electron temperatures for individual ionic species for the composite model. It becomes apparent from inspection of Table 4.8 that all of the collisional lines coming from lower ionization species are much weaker in the optically thick region of the composite model than in the same region of the self-consistent model. This is consistent with the fractional ionic abundances of low ionization species being lower in the optically thick region of the composite model (Table 4.9), hence yielding lower line fluxes. The helium recombination line intensities calculated for the optically thick region of the composite model also indicate lower abundances of He^0 and He^{2+}, but a higher He^+ abundance, which is confirmed by the results in Table 4.9. The optically thin region results do not seem to be affected as much and they are almost identical for the composite and for the self-consistent model. There are two main causes for the discrepancies observed between the results of the optically thick regions of the composite and of the self-consistent model. First of all, the diffuse radiation field coming from the optically thin region of the self-consistent model is weaker than the diffuse field coming from the same region in the optically thick spherically symmetric nebula of the composite-model, since the diffuse field is approximately proportional to the square of the density, and the densities in the two regions of the spherically symmetric optically thick composite model are, obviously, the same everywhere and are higher than the density in the optically thin region of the self-consistent model. This means that more diffuse photons are available to ionize the low ionization potential species in the composite model than there are in the self-consistent one. Secondly, the shape of the diffuse continuum at the edges between the two regions

is different in the two models. In the self-consistent model the diffuse photons coming from the optically thin region will have higher frequencies, on average, than those coming from the same region in the optically thick spherically symmetric nebula of the composite model; this is due to the fact that in the optically thin medium the gas is in a higher ionization state. The photoionization cross-sections of the lower ionization species in the optically thick region of the self-consistent model will be, in general, quite small at the higher frequencies of the diffuse photons coming from the optically thin region and those species will not therefore be ionized by them. In the composite model, however, since the density distribution is spherically symmetric, the ionization structure is also the same in every radial direction; this means that the diffuse photons coming from adjacent regions will have frequencies close to the ionization thresholds of the lower ionization species which will, therefore, be ionized more than in the self-consistent model. On the other hand, the optically thin region of the self-consistent model will not be affected by the lower energy diffuse photons coming from the optically thick region since the gas in the optically thin region is already in a higher ionization stage. The combination of the two effects discussed above explains why the abundances of lower ionization species are lower in the optically thick region of the composite model than in the same region of the self-consistent one.

Another striking feature which emerges from running the composite spherically symmetric model is in the prediction of mean temperatures weighted by ionic species shown in Table 4.10. As mentioned in the previous subsection, the mean ionic temperatures predicted by Clegg *et al.* (1987) show very little variations for the neutral species in each sector, whereas the scatter of the results from Mocassin's self-consistent model is much larger. It was anticipated that a possible explanation for this effect could be the fact that in Clegg et al.'s work the diffuse radiation field transfer was not self-consistent, particularly near the boundaries between the two density regions and that the interaction between the two phases' diffuse radiation fields could lead to the fluctuations in the kinetic temperatures obtained in Mocassin's self-consistent model. The results obtained from Mocassin's composite model indeed confirm this hypothesis – within each sector the fluctuations in the mean ionic temperatures weighted by ionic abundances for neutral species disappear and their distribution resembles that obtained by Clegg *et al.* (1987), although the Mocassin temperatures are still slightly lower, particularly in the optically thin sector.

In conclusion, it is clear that the effects of the diffuse radiation field near the boundaries between the two phases are not negligible, even for the simple biconical distribution used in

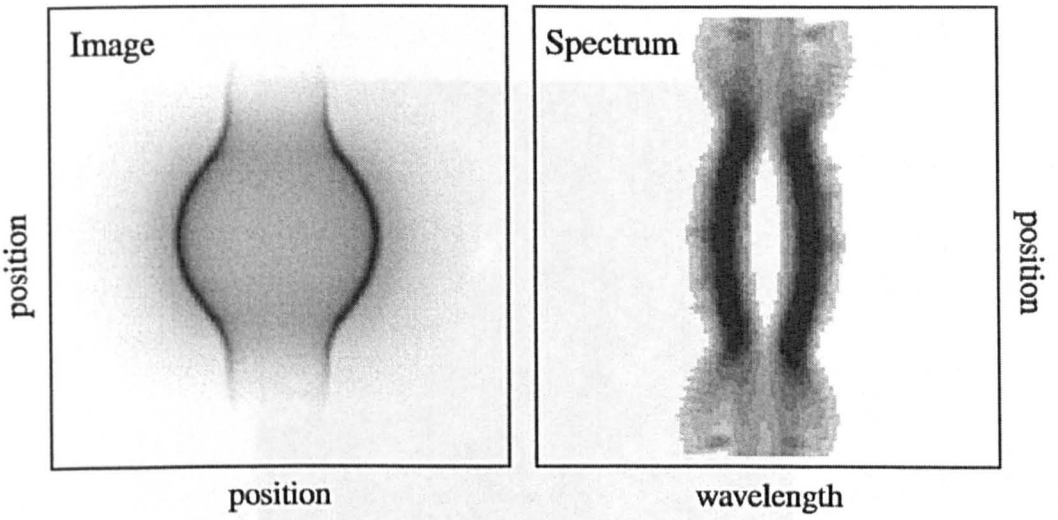

Figure 4.2: Model image (right) and long axis synthetic slit spectrum (left) from the hydrodynamical models of Mellema (1996). Figure adapted by Corradi *et al.* (1999) from Mellema's original thesis work.

this case. These effects are especially important for the abundances of the lower ionization species. It is not clear, however, why the ionization structure calculated by Clegg *et al.* (1987) (see Table 4.4), who used a composite model, bears more resemblance to Mocassin's self-consistent model results (see Table 4.5), than to Mocassin's composite model results (see Table 4.9). Unfortunately, due to the completely different approach to the radiative transfer used by the two codes and the fact that fifteen years have passed since Clegg *et al.* (1987) work was carried out, and, during this period, the atomic database has evolved considerably, any further comparison between the two codes becomes difficult.

4.3 A Spindle-like Density Distribution Model for NGC 3918

Figure 4.2 (from Corradi *et al.*, 1999) shows a qualitative representation of a density distribution obtained from a hydrodynamical model by Mellema (1996) that was adopted by Corradi *et al.* (1999) in their observational study of the spatio-kinematical properties of NGC 3918. The model chosen was one from a set that Dr. G. Mellema computed for his original thesis work (parameters $B = 6$ and $A = 0.9$ in his calculations, page 126).

The exact density distribution for the hydrodynamical model used in the Corradi *et al.* (1999) paper, was kindly provided by G. Mellema, and a first attempt to construct a photoionization model for this distribution was carried out. The density distribution,

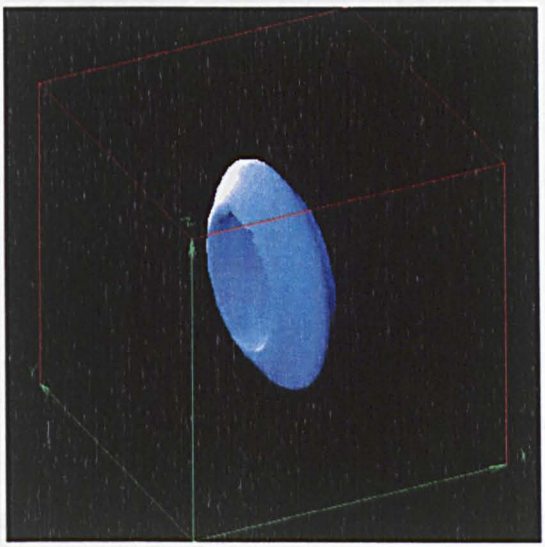

Figure 4.3: Three-dimensional iso-density plot of the spindle-like density distribution for model A of NGC 3918.

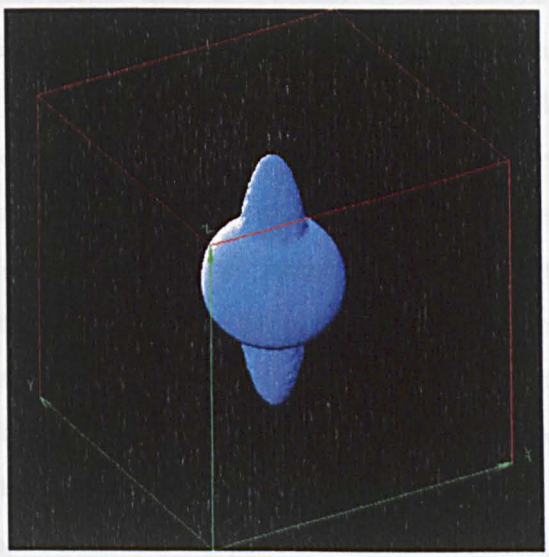

Figure 4.4: Three-dimensional iso-density plot of the spindle-like density distribution for model B of NGC 3918.

Table 4.11: Input shape and thickness parameters for the analytical fit to the density distribution of spindle-like model B (see Appendix A).

n_1 [cm^{-3}]	18000	$\Delta\theta$ [deg]	10
θ_1 [deg]	25	Δr_{eq}^{in}	0.06
r_{eq}	0.3	Δr_{eq}^{out}	0.2
r_{po}^{*}	0.2	Δr_{po}^{in}	0.0032
e	0.25	Δr_{po}^{out}	0.5

* normalized to the outer radius of the nebula

however, had to be scaled up by a factor of 1.6 in order to match the observed $H\beta$ flux. However, the integrated emission line spectrum still did not match the observations, as the emission line strengths from the lower ionization species were heavily underestimated. From the images, however, it is evident that NGC 3918 has an inner shell of denser material which *screens* the gas behind it from direct starlight, thus allowing the existence of a lower ionization region. In Mellema's simulations such *shells* can only be made by considering an evolving central star and having a slow H ionization front. This, however, was not the case for the model used in Corradi *et al.* (1999)'s analysis. In order to simulate such a dense inner shell, the density was artificially enhanced in the equatorial region to form a thick torus between the two lobes. The torus had to be thick enough to effectively screen the material behind it, and the latitudinal extension of the density enhancement was determined such that the model would return the observed Hβ flux. This trade-off between the density enhancement factor and its spatial extension resulted in the creation of a thick equatorial waist. The three-dimensional iso-density plot (obtained for a high density threshold) of the final density distribution used for this model is shown in Figure 4.3. Throughout this work this model will be referred to as *model A*.

A second attempt to reconstruct the density distribution of this object was to seek an analytical expression which could reproduce the structure shown in Figure 4.2 and in the *HST* and *NTT* images published by Corradi *et al.* (1999) (see Figure 4.12). The parameters of the central star and the adopted nebular abundances were the same as in the biconical model. The density distribution was obtained by combining a sphere with

an ellipsoid, using a combination of cut-off functions, C_{01} and C_{10}, defined as

$$\begin{aligned} C_{01}(x, x_0, \Delta x) &= 0.5 + \frac{1}{\pi} tan^{-1}\left(\frac{x - x_0}{\Delta x}\right) \\ C_{10}(x, x_0, \Delta x) &= 0.5 - \frac{1}{\pi} tan^{-1}\left(\frac{x - x_0}{\Delta x}\right) \end{aligned} \tag{4.3}$$

The functions above can be used to describe a smooth transition from 0 to 1 and from 1 to zero, respectively, about the value x_0, with a typical size for the transition of Δx.

The equatorial spherical shell can then be described as follows:

$$equat(r, \theta) = C_{01}(\theta, \theta_1, \Delta\theta) \cdot C_{01}(r, r_{eq}, \Delta r_{eq}^{in}) \cdot C_{10}(r, r_{eq}, \Delta r_{eq}^{out}) \tag{4.4}$$

where r is the radial distance and θ the polar angle ($\theta = 90°$ at the equator and $\theta = 0°$ at the two poles). Values for θ_1, $\Delta\theta$, r_{eq}, Δr_{eq}^{in} and Δr_{eq}^{out} are given in Table 4.11.

We then define r_e, the radius of the ellipsoid, as $r_e = \sqrt{x^2 + y^2 + (e \cdot z)^2}$, where e is the eccentricity (given in Table 4.11), then the polar protrusions can be created using the following expression

$$pole(r, \theta) = C_{10}(\theta, \theta_1, \Delta\theta) \cdot C_{01}(r_e, r_{po}, \Delta r_{po}^{in}) \cdot C_{10}(r_e, r_{po}, \Delta r_{po}^{out}) \tag{4.5}$$

where r_{po}, Δr_{po}^{in} and Δr_{po}^{out} are also given in Table 4.11. Finally, the density distribution at any point in the grid can be obtained by combining Equations 4.4 and 4.5, as follows

$$N_H(r, \theta) = n_1 \times (equator(r, \theta) + pole(r, \theta)). \tag{4.6}$$

The best fit to the observed integrated spectrum and to the images of NGC 3918 was obtained using the parameters listed in Table 4.11. Figure 4.4 shows the three-dimensional iso-density plot corresponding to this combination. In this work the spindle-like model constructed by using Equation ?? will be referred to as *model B*.

Corradi *et al.* (1999) study primarily focused on the kinematics of NGC 3918 and therefore they did not propose any new values for the central star parameters or for the nebular elemental abundances. Although derived for a different density distribution, the parameters given by Clegg *et al.* (1987), being the only ones available, had to be used for these models too. As given by Clegg *et al.* (1987), the dereddened stellar flux at 1300 Å is equal to 2.4×10^{-12} ergs cm^{-2}s^{-1}Å^{-1}. For an assumed distance of 1.5 kpc and a stellar effective temperature of T_{eff}=150,000 K, this flux corresponds to a stellar luminosity, L_*, of 5780 $L_\odot$.

Table 4.12: Input parameters for the spindle-like models.

L_*(A)	$6900 L_\odot$	N/H	1.5×10^{-4}
L_*(B)	$5780 L_\odot$	O/H	5.0×10^{-4}
R_{in}	0.	Ne/H	1.2×10^{-4}
R_{out}	0.106 pc	Mg/H	1.4×10^{-5}
T_{eff}	140,000 K	Si/H	1.0×10^{-5}
log g	7.5	S/H	1.6×10^{-5}
He	0.107	Ar/H	2.0×10^{-6}
C	8.0×10^{-4}	Fe/H	3.7×10^{-7}

The abundances are given by number, relative to H

The stellar luminosity in Clegg *et al.* (1987) model, however, was finally adjusted by them to a slightly higher value of $F_\oplus$(1300Å), 2.9×10^{-12}ergs cm^{-2}s^{-1}Å^{-1}, corresponding to $L_* = 6900\,L_\odot$. In this work both values for $F_\oplus$(1300Å) were used, in turn, for both models A and B. Finally, $F_\oplus$(1300Å)=2.9×10^{-12}ergs cm^{-2}s^{-1}Å^{-1} (L_*=6900$L_\odot$) was chosen for model A and $F_\oplus$(1300Å)=2.4×10^{-12}ergs cm^{-2}s^{-1}Å^{-1} (L_*=5780$L_\odot$) was chosen for model B, as these produced the best results. Table 4.12 summarises the nebular and stellar parameters used for the models described in this section.

4.3.1 Spindle-like Density Distribution Model: Results

Table 4.13 lists the predicted emission line fluxes integrated over the nebular volume for the spindle-like models A and B of NGC 3918; for comparison, the observed values are also reported in the last column of this table. The observed spectrum is reasonably reproduced by both models. The Hβ fluxes predicted by models A and B are slightly different, but they are both within 10% of the observed value. The emission line predictions for helium seem to indicate that in both models the abundance of He^{2+} is slightly overestimated, hence leaving too little He^+. However both results are comparable to those obtained using the biconical model and indeed to Clegg *et al.* (1987) results presented in Section 4.2.1. The major discrepancies between the two models and the observations are the same as for the biconical model case. The C IV 1550 Å and the Mg II 2800 Å resonance lines, are overestimated by large factors by the Mocassin models, which do not take dust absorption into account.

Table 4.13: Observed and predicted emission lines fluxes for the spindle-like models of NGC 3918.

	Predicted			
Line	A	B	Observed	ref
$H_\beta/10^{-10}$ erg cm−2 s−1	2.19	2.58	2.34	b
H_β 4861	100	100	100	-
He I 5876	8.15	7.56	10.81	a
He II 4686	57.2	53.6	41.65	a
C II] 2326	34.6	27.8	31.24	a
C II 4267	0.23	0.21	0.50	a
[C II] 157.74μm	0.22	0.10	0.21	c
C III] 1908	543	480	492.5	a
C III 4648	0.89	0.98	0.42	a
C III] 2297	10.2	11.3	5:	e
C IV 1550*	2267	2220	457.6	a
C IV 4658	0.37	0.37	0.35	a
[N I] 5199	1.03	0.46	0.63	a
[N II] 6584	41.8	33.9	84	a
N III] 1751	22.9	20.2	26.7	a
[N III] 57.3 μm	7.41	9.16	13.5	c
N IV] 1486	61.4	59.3	46.4	a
N V 1240*	45.6	38.7	41.4	a
[O I] 63.12 μm	0.40	0.26	6.72	c
[O I] 145.5 μm	.029	.014	0.23	c
[O I] 6300	3.95	2.57	5.24	a
[O II] 3727	42.7	37.9	94.5	a
[O III] 51.8 μm	79.4	112	88.6	c
[O III] 88.4 μm	14.2	22.2	27.5	c
[O III] 5007	1760	1789	1657	a
[O III] 4363	25.0	24.8	21.6	a
[O IV] 25.9 μm	352	365	89	d
O IV] 1402	34.9	31.8	48.9	a
O IV 1342	1.87	1.72	2:	e
[Ne II] 12.8 μm	1.61	0.75	12:	f
[Ne III] 15.6 μm	123	127	46.3	d
[Ne III] 3869	174	173	135.5	a
[Ne IV] 2423	89.2	87.5	132	e
[Ne V] 3426	108	99.1	80	e
[Ne V] 14.3 μm	267	256	19.6	d
[Ne V] 24.3 μm	170	146	23.1	d
[Ne VI] 7.6 μm	62.0	54.4	-	-
Mg I] 4565	0.32	0.33	0.13	a
Mg II 2800*	47.2	36.7	$\leq$1	e
[Mg IV] 4.49 μm	4.25	5.10	-	-
[Mg V] 2783	4.84	5.02	5.6	e
[Mg V] 5.6 μm	12.5	14.1	-	-
Si III] 1887	13.9	11.2	8	e
Si IV 1399*	11.5	10.2	9	e
[S II] 4070	1.90	1.42	2.69	a
[S III] 18.7 μm	16.6	14.3	8.7	d
[S III] 33.6 μm	5.21	4.68	-	-
[S III] 6312 1.98	1.55	2.27	a	
[S IV] 10.5μm	198	213	35.0	d

* Attenuated by dust absorption.
[a] Tsamis *et al.* (2002); [b] Cahn *et al.* (1992); [c] Liu *et al.* (2001); [d] Bower (2001); [e] Clegg *et al.* (1987);[f] Pottasch *et al.* (1986).

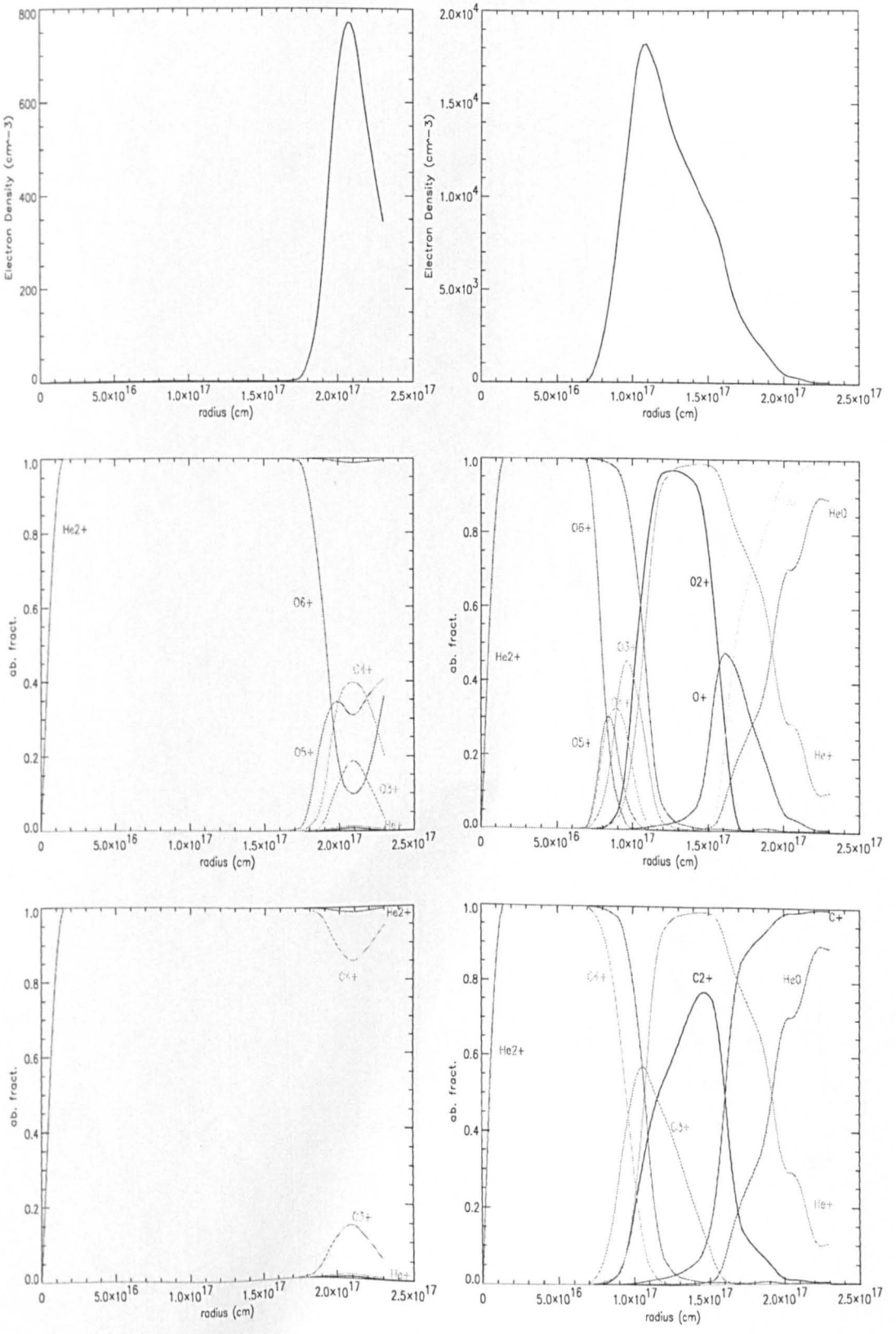

Figure 4.5: Ionic fractions of oxygen (middle panels) and carbon (bottom panels) along the polar (left panels) and equatorial (right panels) directions. The ionization structure of helium is also plotted in each panel. The top panels show the electron density plotted as a function of radius along the polar (top left) and equatorial (top right) directions. Spindle-like model A for NGC 3918.

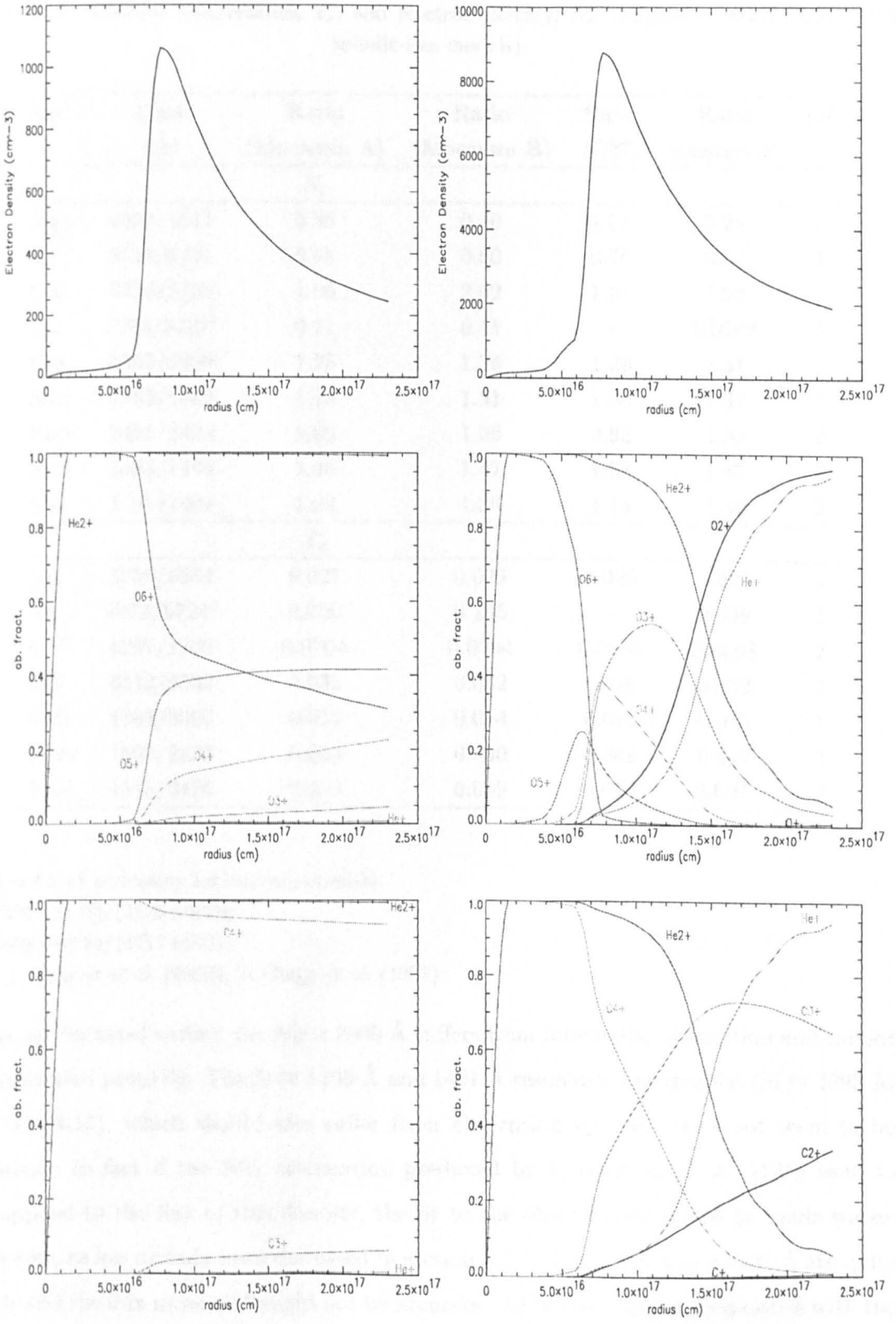

Figure 4.6: Ionic fractions of oxygen (middle panels) and carbon (bottom panels) along the polar (left panels) and equatorial (right panels) directions. The ionization structure of helium so also plotted in each panel. The top panels show the electron density plotted as a function of radius along the polar (top left) and equatorial (top right) directions. Spindle-like model B for NGC 3918.

Table 4.14: Electron temperature, T_e, and electron density, N_e, diagnostic ratios (NGC 3918 spindle-like models).

Ion[a]	Lines (Å)	Ratio (Mocassin A)	Ratio (Mocassin B)	Ratio (C87)	Ratio (observed)	ref
		N_e				
MgI	4562/4571	0.38	0.40	0.42:	0.28	1
SII	6716/6731	0.65	0.60	0.70	0.57	1
OII	3726/3729	1.96	2.02	1.61	1.98	2
OII	7325/3727[b]	0.11	0.11	-	0.0783	1
CIII	1906/1909	1.25	1.34	1.36	1.31	2
SiIII	1883/1892	1.15	1.31	1.30	1.37	2
NeIV	2421/2424	1.09	1.06	0.93	1.00	2
NIV	1483/1486	1.45	1.47	1.87	1.85	2
OIV	1401/1404	1.32	1.36	1.14	1.50	2
		T_e				
NII	5755/6584	0.021	0.023	0.025	0.021	1
SII	4073/6724[c]	0.200	0.245	-	0.339	1
C^{2+}	4267/1908	0.0004	0.0004	0.0005	0.0008	2
SIII	6312/9532	0.032	0.032	0.029	0.032	2
OIII	4363/5007	0.014	0.014	0.013	0.013	1
NeIV	1602/2423	0.053	0.050	0.049	0.047	2
NeV	1575/3426	0.009	0.009	0.012	0.007:	2

[a] In order of increasing ionization potential.
[b] (7321+7332)/(3726+3729)
[c] (4068+4076)/(6717+6731)
ref: 1: Tsamis *et al.* (2002); 2: Clegg *et al.* (1987)

Also, as discussed earlier, the Mg II 2800 Å suffers from interstellar absorption and cannot be measured properly. The Si IV 1393 Å and 1401 Å resonance line doublet (Si IV 1393 Å, in Table4.13), which should also suffer from absorption by dust, does not seem to be affected. In fact if the 30% attenuation predicted by Harrington *et al.* (1988) were to be applied to the flux of this doublet, the fit to the observations would be made worse. However, as has already been discussed in section 4.2.1, Si IV 1393 Å and 1401 Å are quite weak and the flux measured might not be accurate. As before, large discrepancies with the observations, of factors of about ten, are also observed for the [Ne V] fine-structure lines, namely [Ne V] 14.3 μm and [Ne V] 24.3μm, due to the collision strengths used (Lennon

Table 4.15: Fractional ionic abundances for NGC 3918 (Spindle-like models of NGC 3918)

	Ion						
Element	I	II	III	IV	V	VI	VII
H	0.14(-1)	0.986					
	0.85(-2)	0.991					
He	0.64(-2)	0.509	0.485				
	0.32(-2)	0.513	0.483				
C	0.73(-4)	0.33(-1)	0.284	0.462	0.221		
	0.96(-4)	0.23(-1)	0.258	0.509	0.210		
N	0.53(-2)	0.32(-1)	0.279	0.501	0.129	0.053	
	0.23(-2)	0.25(-1)	0.256	0.544	0.125	0.047	
O	0.13(-1)	0.28(-1)	0.544	0.250	0.120	0.038	0.62(-2)
	0.71(-2)	0.24(-1)	0.562	0.257	0.112	0.033	0.52(-2)
Ne	0.68(-3)	0.14(-1)	0.553	0.195	0.192	0.045	0.99(-3)
	0.12(-3)	0.66(-2)	0.560	0.207	0.186	0.039	0.92(-3)
S	0.11(-4)	0.21(-1)	0.116	0.295	0.386	0.149	0.032
	0.15(-4)	0.13(-1)	0.094	0.276	0.445	0.144	0.028
Si	0.81(-4)	0.133	0.128	0.247	0.211	0.211	0.070
	0.84(-4)	0.101	0.110	0.243	0.249	0.230	0.068
Mg	0.15(-2)	0.59(-1)	0.351	0.123	0.179	0.225	0.060
	0.15(-2)	0.44(-1)	0.313	0.149	0.203	0.233	0.056

For each element the upper row is for model A and the lower row is for model B

Table 4.16: Mean temperatures (K) weighted by ionic species for NGC 3918 spindle-like models.

	Ion						
Element	I	II	III	IV	V	VI	VII
H	10,142	13,739					
	10,763	13,593					
He	9,795	12,430	15,061				
	10,519	12,457	14,770				
C	10,683	10,715	12,521	13,733	15,539		
	10,945	11,193	12,484	13,518	15,278		
N	9,254	10,853	12,653	13,805	15,381	16,088	
	9,805	11,239	12,606	13,594	15,085	15,924	
O	9,606	11,256	12,729	14,939	15,524	16,020	17,278
	10,188	11,518	12,689	14,656	15,288	15,792	17,839
Ne	9,093	10,202	12,603	14,771	15,422	16,004	17,881
	9,663	11,186	12,574	14,464	15,149	15,785	19,909
S	10,487	10,207	11,871	12,801	14,221	15,434	16,218
	10,872	10,796	11,840	12,712	13,875	15,133	16,117
Si	11,636	11,557	12,579	13,117	14,308	15,081	15,736
	11,628	11,652	12,443	12,968	13,935	14,655	15,381
Mg	11,403	11,189	12,197	13,730	14,759	15,250	15,812
	11,446	11,456	12,106	13,338	14,384	14,902	15,529

For each element the upper row is for model A and the lower row for model B

and Burke, 1991); this has already been discussed in Section 4.2.1. Finally, the large discrepancies between the spindle-like models predictions for the infrared line fluxes and the *ISO* SWS observations measured by Bower (2001) and reported in Table 4.13 are most probably due, as for the biconical model, to the *ISO SWS* aperture being offset from the centre of the nebula. This will be discussed in more detail in Section 4.4. In general, the integrated spectra obtained from the spindle-like models are in good agreement with those obtained from Mocassin's biconical model, and, therefore, comments made during the discussion of the latter (Section 4.2.1) largely apply to the models A and B discussed in this section. The diagnostic line ratios calculated for models A and B are given in Table 4.14. They are in satisfactory agreement with the observed ratios, also reported in the same table, with model B providing the slightly better fit.

Tables 4.15 and 4.16 list, respectively, the fractional ionic abundances, $f(X^i)$, and the mean electron temperatures weighted by ionic species, for the spindle-like distribution models of NGC 3918. In each row of the two tables the upper entry is for model A and the lower entry for model B. It is difficult to make a comparison with Mocassin's biconical model results or with those of Clegg *et al.* (1987), since both of the spindle-like models consist of a continuously varying gas density distribution, where clear edges do not exist. The values of the ionic fractions reported in Table 4.15 were obtained from Equation 2.19, and represent an average over the whole ionized volume of the local ionic fractions weighted by the local density. Figures 4.5 and 4.6 show the ionic fractions of oxygen (top panels) and carbon (bottom panels) as a function of radius along the polar (left panels) and equatorial (right panels) directions for the spindle-like models A and B, respectively. It is clear from the figures that the oxygen and carbon radial ion distributions are very different along the two directions of each model, according to the gas density structure. The integrated ionic fractions, $f(X^i)$, such as those listed in Table 4.15, are very useful when discussing the large-scale ionization structure of models with density variations, however plots of the type shown in Figures 4.5 and 4.6 can provide a better insight into the actual ionization topography of and models. Following the discussion in Section 4.2.1, it is also worth noticing that in the spindle-like model the effects of the charge exchange reaction $O^{3+}+H^0 \rightarrow O^{2+}+H^+$ are clearly appreciable when comparing the ratio of the ionic fraction, $f(He^{2+})$ to those of $f(O^{3+})+f(O^{4+})+f(O^{5+})+....$ For both models the ratio deviates from the value of unity predicted by Equation 4.2, yielding a ratio of 1.16 for model A and 1.19 for model B, respectively.

	Band	λ_{key} (μm)	Grating order	Aperture nr.	Aperture area (")	Detector type	Detector area (pixels)	Wavelength range (μm)	Sensitivity ratio $\frac{\text{in-orbit}}{\text{ground}}$
SW section	1A	2.5	SW 4	1	14 × 20	InSb	1 × 12	2.38 - 2.60	0.6
	1B	2.9	SW 3	1	14 × 20	InSb	1 × 12	2.60 - 3.02	0.6
	1D	3.1	SW 3	2	14 × 20	InSb	1 × 12	3.02 - 3.52	1.1
	1E	3.8	SW 2	2	14 × 20	InSb	1 × 12	3.52 - 4.08	1.1
	2A	4.5	SW 2	2	14 × 20	Si:Ga	1 × 12	4.08 - 5.30	4.5
	2B	5.9	SW 1	2	14 × 20	Si:Ga	1 × 12	5.30 - 7.00	4.5
	2C	7.7	SW 1	3	14 × 20	Si:Ga	1 × 12	7.00 - 12.0	4.5
LW section	3A	14.0	LW 2	1	14 × 27	Si:As	1 × 12	12.0 - 16.5	6.5
	3C	17.0	LW 2	2	14 × 27	Si:As	1 × 12	16.5 - 19.5	6.5
	3D	24.0	LW 1	2	14 × 27	Si:As	1 × 12	19.5 - 27.5	6.5
	3E	28.5	LW 1	3	20 × 27	Si:As	1 × 12	27.5 - 29.0	6.5
	4	32.0	LW 1	3	20 × 33	Ge:Be	1 × 12	29.0 - 45.2	5.5

Figure 4.7: Definition of the SWS AOT bands (de Graaw and et al., 1996)

As shown in Table 4.16, the weighted mean temperatures calculated by Mocassin for model B (lower entries) are consistently lower than those calculated for model A (upper entries), apart from the third and fourth column values (for doubly and triply ionized species), which are, on the contrary, higher for model B. It is also evident that the scatter of values for the same column ionic stages is more accentuated for model B even for the lower ionization stages, while the scatter is very small for model A. The effects of density distributions on the final values obtained for the mean weighted temperatures have already been discussed in Section 4.2.2. It is clear that in this case the behaviour of the two models depends heavily on their density distributions.

4.4 The Infrared Fine-Structure Lines

The main reason for the discrepancy observed between the models' predictions of the infrared line fluxes and the Bower (2001) measurements from the *ISO* SWS data for NGC 3918 is that the nebular coordinates used for the *ISO* observations were incorrect by approximately 14 arcsec. The position given by the Strasbourg-CDS Simbad database for NGC 3918, in the J2000 FK5 reference frame, is $\alpha(2000)$ = 11 50 17.2 and $\delta(2000)$ = -57 10 53, while the position used for the *ISO* SWS and LWS observations of NGC 3918 was that measured by Milne (1976), namely $\alpha(1950)$ = 11 47 50.1 and $\delta(1950)$ = -56 54 10, or, equivalently, $\alpha(2000)$ = 11 50 18.9 and $\delta(2000)$ = -57 10 51. This resulted in the SWS apertures being offset from the nebular centre by 1.8 arcsec north in declination and by 13.6 arcsec (= 1.68 sec) east in right ascension, giving a total diagonal offset of 13.8 arcsec. In this section it is shown that the effects of this SWS aperture offset, together

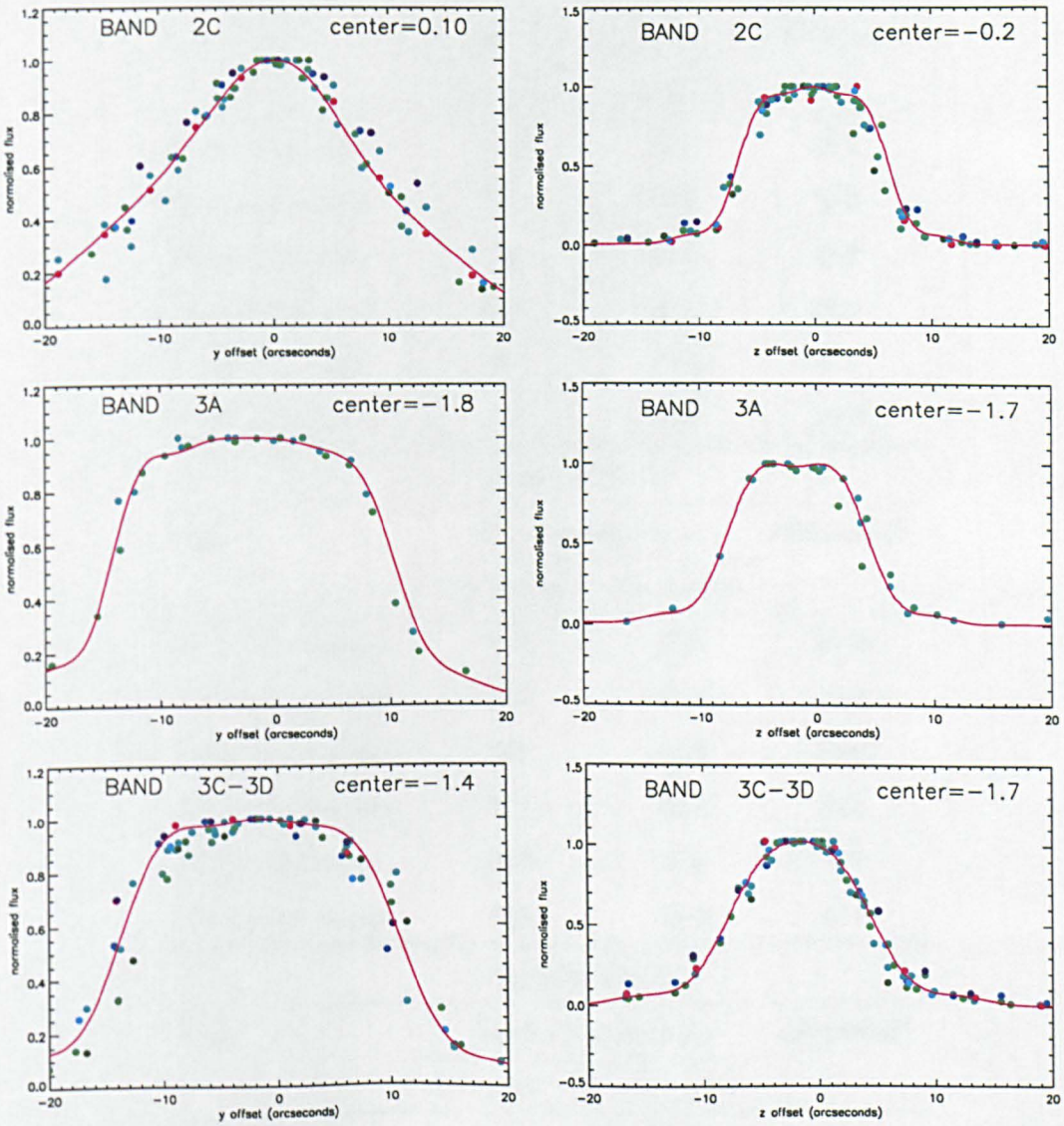

Figure 4.8: Observations (dots) and calibration file (curves) for the beam profile for three different SWS bands, in the y-axis (cross-dispersion, left panels) and z-axis (in-dispersion, right panels) directions. Dots with the same colour correspond to the same observation. Profiles compiled from Leech et al. (2002).

Table 4.17: Infrared line fluxes of NGC 3918 corrected for the *ISO SWS* beam sizes, profiles and offset.

Biconical Model[a]			
Line	Model predictions		Observed[d]
	Uncorrected	Corrected	
[O IV] 25.9 μm	352	96.1	89.0
[Ne III] 15.6 μm	131	33.8	46.3
[Ne V] 14.3 μm	286	69.7	19.6
[Ne V] 24.3 μm	220	60.1	23.1
[S III] 18.7 μm	38	11.3	8.7
[S IV] 10.5 μm	214	85.0	35.0
Spindle-like A[b]			
Line	Model predictions		Observed[d]
	Uncorrected	Corrected	
[O IV] 25.9 *mum*	352	100	89.0
[Ne III] 15.6 *mum*	174	31.1	46.3
[Ne V] 14.3 *mum*	267	68.6	19.6
[Ne V] 24.3 *mum*	170	49.4	23.1
[S III] 18.7 *mum*	16.6	3.4	8.7
[S IV] 10.5 *mum*	198	68.9	35.0
Spindle-like B[c]			
Line	Model predictions		Observed[d]
	Uncorrected	Corrected	
[O IV] 25.9 *mum*	365	105	89.0
[Ne III] 15.6 *mum*	173	56.1	46.3
[Ne V] 14.3 *mum*	256	58.0	19.6
[Ne V] 24.3 *mum*	146	40.9	23.1
[S III] 18.7 *mum*	14.3	6.01	8.7
[S IV] 10.5 *mum*	213	80.1	35.0

[a] The fluxes are given relative to $H\beta = 2.33 \times 10^{-10}$ erg cm^{-2} s.

[b] The fluxes are given relative to $H\beta = 2.20 \times 10^{-10}$ erg cm^{-2} s.

[c] The fluxes are given relative to $H\beta = 2.56 \times 10^{-10}$ erg cm^{-2} s.

[d] The fluxes are given relative to $H\beta = 2.34 \times 10^{-10}$ erg cm^{-2} s.

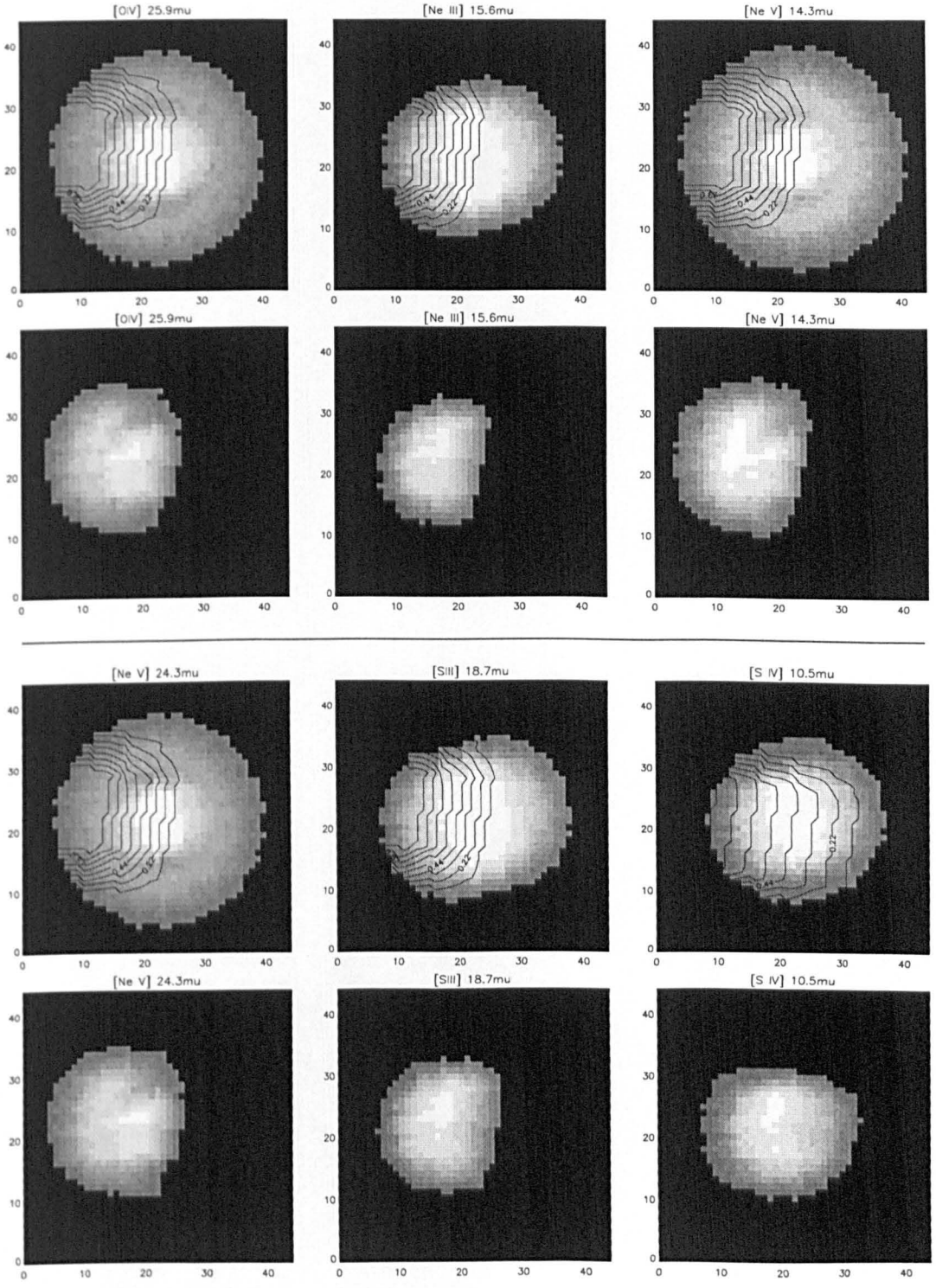

Figure 4.9: Predicted projected images of NGC 3918 in the six infrared lines observed by the *ISO SWS* for the biconical model. The upper panels show contour plots of the ISO-SWS apertures superimposed on the map in the given emission line. The lower panels contain the projected maps of the nebula in each line after convolution with the aperture response maps. All the images are oriented such that north is up and east is left.

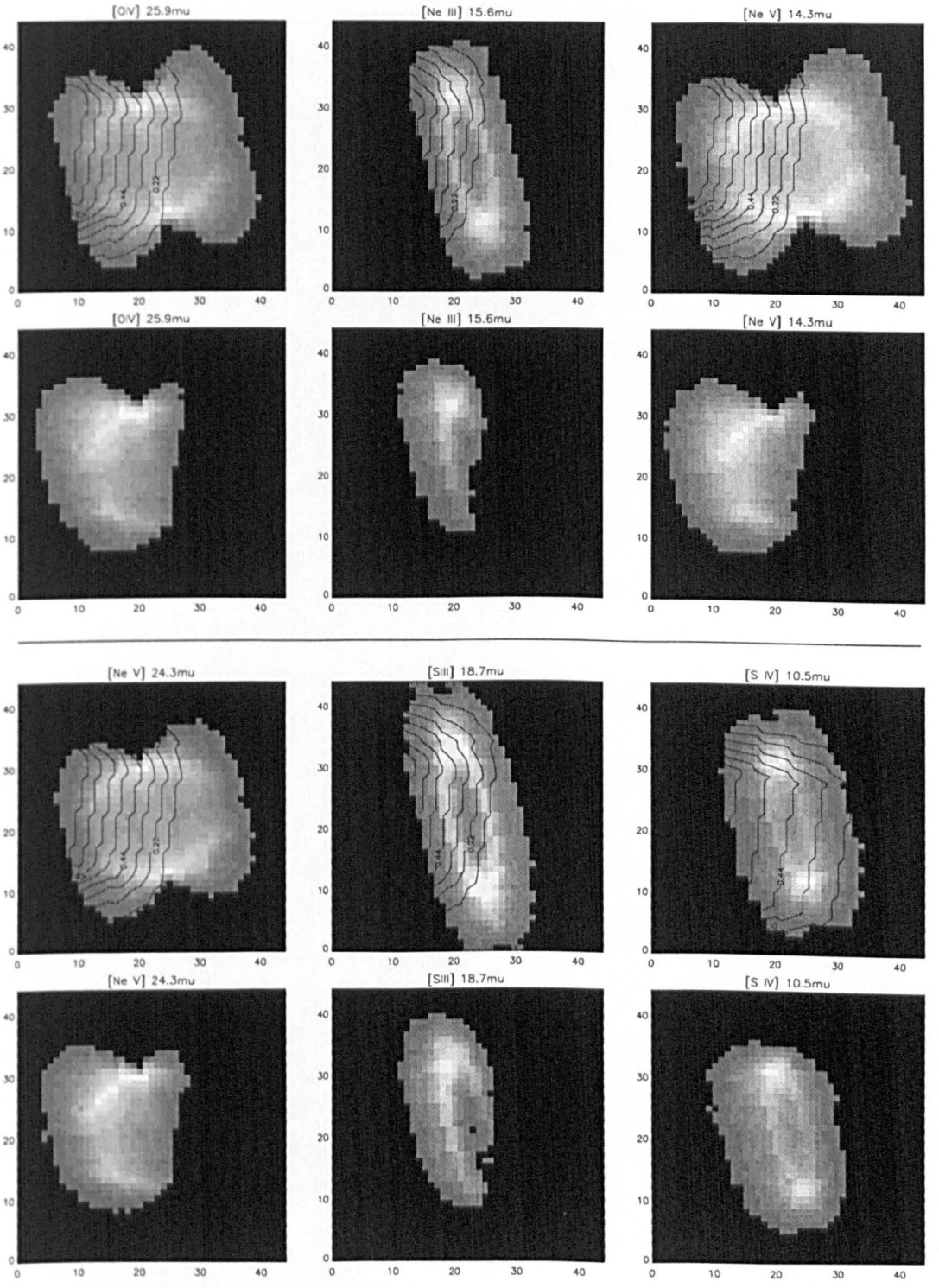

Figure 4.10: Predicted projected images of NGC 3918 in the six infrared lines observed by the *ISO SWS* for the spindle-like model A. The upper panels show contour plots of the ISO-SWS apertures superimposed on the map in the given emission line. The lower panels contain the projected maps of the nebula in each line after convolution with the aperture response maps. All the images are oriented such that north is up and east is left.

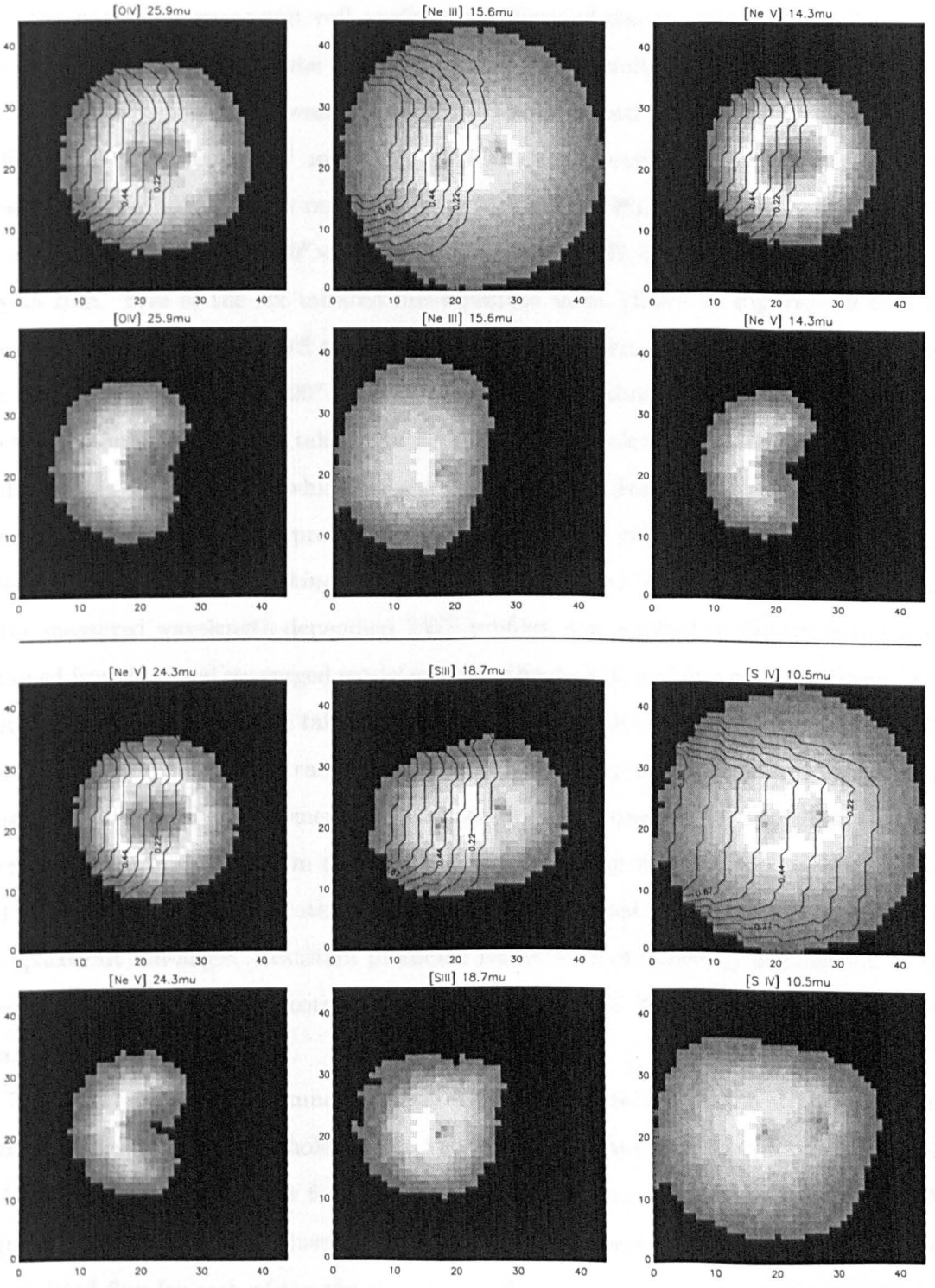

Figure 4.11: Predicted projected images of NGC 3918 in the six infrared lines observed by the *ISO SWS* for the spindle-like model B. The upper panels show contour plots of the ISO-SWS apertures superimposed on the map in the given emission line. The lower panels contain the projected maps of the nebula in each line after convolution with the aperture response maps. All the images are oriented such that north is up and east is left.

with the particular spacecraft roll angle at the time of the the observations (retrieved from the *ISO* archives) and the SWS subspectra beam profiles, are sufficient to largely explain the discrepancies between the model predictions and the observations. The table in figure 4.7 (from de Graaw and et al., 1996) lists the wavelength dependent aperture sizes of the *ISO* SWS. These range from $14''\times20''$, for $2.38\mu\text{m} \leq \lambda \leq 12.0\mu\text{m}$, $14''\times27''$ for $12.0\mu\text{m} \leq \lambda \leq 27.5\mu\text{m}$, $20''\times27''$ for $27.5\mu m \leq \lambda \leq 29.0\mu\text{m}$, $20''\times33''$ for $29.0\mu\text{m} \leq \lambda \leq 45.2\mu\text{m}$. Five of the six infrared fine-structure lines, shown in Figures 4.9 to 4.11, were observed by the *ISO* SWS through a $14''\times27''$ aperture, while the [S IV] 10.5μm line was observed through a $14''\times20''$ aperture. As mentioned above, the aperture dimensions, are not the only factor to be taken into account, there is also the transmission efficiency profile across the aperture, which, in some cases, is far from flat (Leech et al., 2002). Figure 4.8 shows the beam profiles for the three bands relevant to the infrared lines listed in Table 4.17. A *masking* IDL routine (Morisset *et al.*, 2002), which makes use of the measured wavelength-dependent SWS profiles, was applied to the projected maps obtained from the final converged model grids, in the six infrared fine-structure lines. This routine returns a *mask* which takes into account the wavelength-dependent aperture size and beam profile, and which can then be applied to a map of the object in the required emission line to predict the emergent flux that would be measured. The position of the aperture centre was offset from the centre of the nebula by the amounts specified above, and the mask obtained was rotated by an angle of 80° East of North[1] to correspond to the spacecraft roll-angle. Resultant predicted fluxes were obtained by convolution of the offset, rotated mask with the correctly oriented map of NGC 3918 in the required emission line.

Table 4.17 provides a summary of the line fluxes predicted for the six infrared fine-structure lines, first for the whole nebula, i.e. without the aperture corrections (column 2) and then after the corrections for the aperture profile, offset and orientation (column 3). Figures 4.9, 4.10 and 4.11 illustrate the effects of the aperture corrections on the final transmitted flux for each of the the six infrared lines for the biconical model nebula, and for spindle-like models A and B, respectively. The upper panel of each pair shows a map of NGC 3918 in a particular infrared fine-structure emission line, oriented such that the

[1]From the *ISO* archive, CINSTROLL = 350°, where CINSTROLL is the instrument's roll angle, defined as the angle anticlockwise between north and the spacecraft z-axis. Since the long axis of the apertures is in the y-direction and the short axis is in the z-direction, then P.A. = CINSTROLL + 90°.

north is up and east to the left; a contour map of the appropriate wavelength-dependent aperture transmission profile is superimposed on each map. The lower panel of each pair in the three figures shows the map from the corresponding upper panel *after* convolution with the appropriate *ISO SWS* aperture profile.

It is clear from the images and from the corrected line fluxes reported in Table 4.17 that the SWS aperture offset is indeed the main reason for the SWS infrared line flux discrepancy. However, even after these corrections the fluxes for the predicted [Ne V] fine-structure lines are still a factor of two to three too strong compared to the observed values; this is mainly due to the collision strengths used in the Mocassin code, which are much larger than those used in the Harrington code by C87. This has already been discussed in Section 4.2.1. A discrepancy also remains between the SWS flux in the [S IV] 10.5 μm line measured by Bower (2001) and the corrected fluxes predicted by Mocassin, which are a factor of 2 to 3 stronger. Clegg *et al.* (1987) also predicted a flux for this line which was a factor of 3.6 stronger than the IRAS LRS measurements of Pottasch *et al.* (1986). The origin of this discrepancy still remains unclear.

It is worth noting that although the aperture offset of 14 arcsec also applied to the LWS observations made with *ISO* (Liu *et al.*, 2001), this would not affect the integral flux measurements, due to the much larger aperture size of the LWS ($\approx$80 arcsec FWHM).

4.5 Visualization of the Models' Results

A large amount of observational data has been obtained for NGC 3918 over the years. Some of the most recent data published include the optical images and the high resolution, long slit spectra presented by Corradi *et al.* (1999). Figure 4.12 (Corradi *et al.*, 1999), shows Hubble Space Telescope (*HST*) and NTT images of NGC 3918. The images, which were retrieved from the *HST* archives (top two panels in Figure 4.12), were obtained in 1995 with the Wide Field Planetary Camera 2 (WFPC2) in the F555W filter. Corradi *et al.* (1999) claimed that the emission in this image (central wavelength = 5252 Å; FWHM = 1223 Å) is dominated by [OIII] 4959+5007Å, however many other nebular lines, including Hβ, He I 5876 Å, He II 4686Å, [Ar IV] 4711,4740 Å and [N II] 5755 Å fall within the transmission range of this filter and, although weaker than the [O III] lines, can be important at particular positions in the nebula.

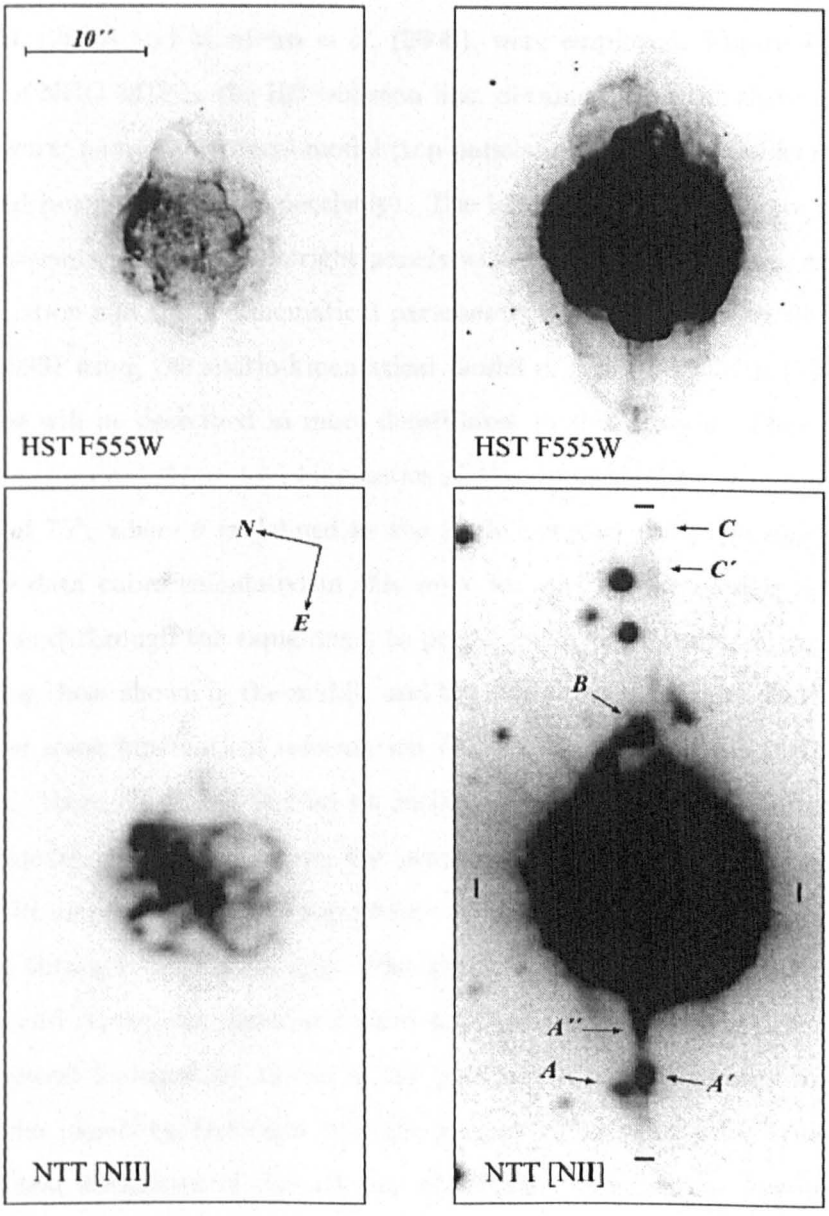

Figure 4.12: *HST* and NTT images of NGC 3918 on the same scale, rotated so as to have the main jetlike feature oriented along the vertical direction. Both images are shown using two different intensity cuts. *Left:* Showing the highest intensity levels on a linear scale. *Right:* Showing the faintest structures on a logarithmic scale. (Corradi *et al.*, 1999)

4.5.1 Projected Images

In order to compare the final model results for the biconical distribution and the spindle-like distribution models, the IDL visualization routines described in Section 2.4 and in Morisset *et al.* (2000) and Monteiro *et al.* (2000), were employed. Figure 4.13 show predicted maps of NGC 3918 in the Hβ emission line, obtained from the three models developed in this work; namely, biconical model (top panels) and the spindle-like models A and B (middle and bottom panels, respectively). The left panels in each figure are displayed with linear intensity scales and the right panels with logarithmic intensity scales.

The inclination and spatio-kinematical parameters of NGC 3918 were derived by Corradi *et al.* (1999) using the spatio-kinematical model of Solf and Ulrich (1985) (see Figure 4.14); this will be described in more detail later in this section. They obtained the best fit to the observed shape and kinematics of the inner shell by assuming an inclination angle θ of 75°, where θ is defined as the angle between the polar axis and the line of sight. The data cubes calculated in this work for spindle-like models A and B were, therefore, rotated through the same angle to produce projected maps in various emission lines (including those shown in the middle and bottom panels of Figure 4.13). Clegg *et al.* (1987) derived some kinematical information from a Coudé spectrum in [O II] $\lambda\lambda$3726, 3729 doublet. From this they derived an inclination angle, θ, for the biconical density distribution model, of 15°. Therefore, the projected images for the biconical model (including the Hβ maps shown in the top panels of Figure 4.13) were obtained by rotating the final grid through the same angle. The images of NGC 3918 published by Corradi *et al.* (1999) and reproduced here in Figure 4.12 are displayed using different intensity cuts; the brightest features are shown in the panels on the left, using a linear intensity scale, while the panels on the right plot the images on a logarithmic scale in order to show the faintest structures of the nebula, which also include some low-intensity small scale features. In this work no attempt was made to reproduce the small scale features of NGC 3918. These were discussed in more detail by Corradi *et al.* (1999) and include several low-ionization structures located roughly along the major axis of the nebula and clearly visible in the logarithmic [N II] image (Figure 4.12, bottom right), where they are labeled with the letters A, A′, A″, B, C and C″. The shape of the inner shell, described in Section 4.1, is more clearly visible in the *HST* images (Figure 4.12, top panels), while the lower angular resolution linear NTT image in [N II] (Figure 4.12, bottom left) shows

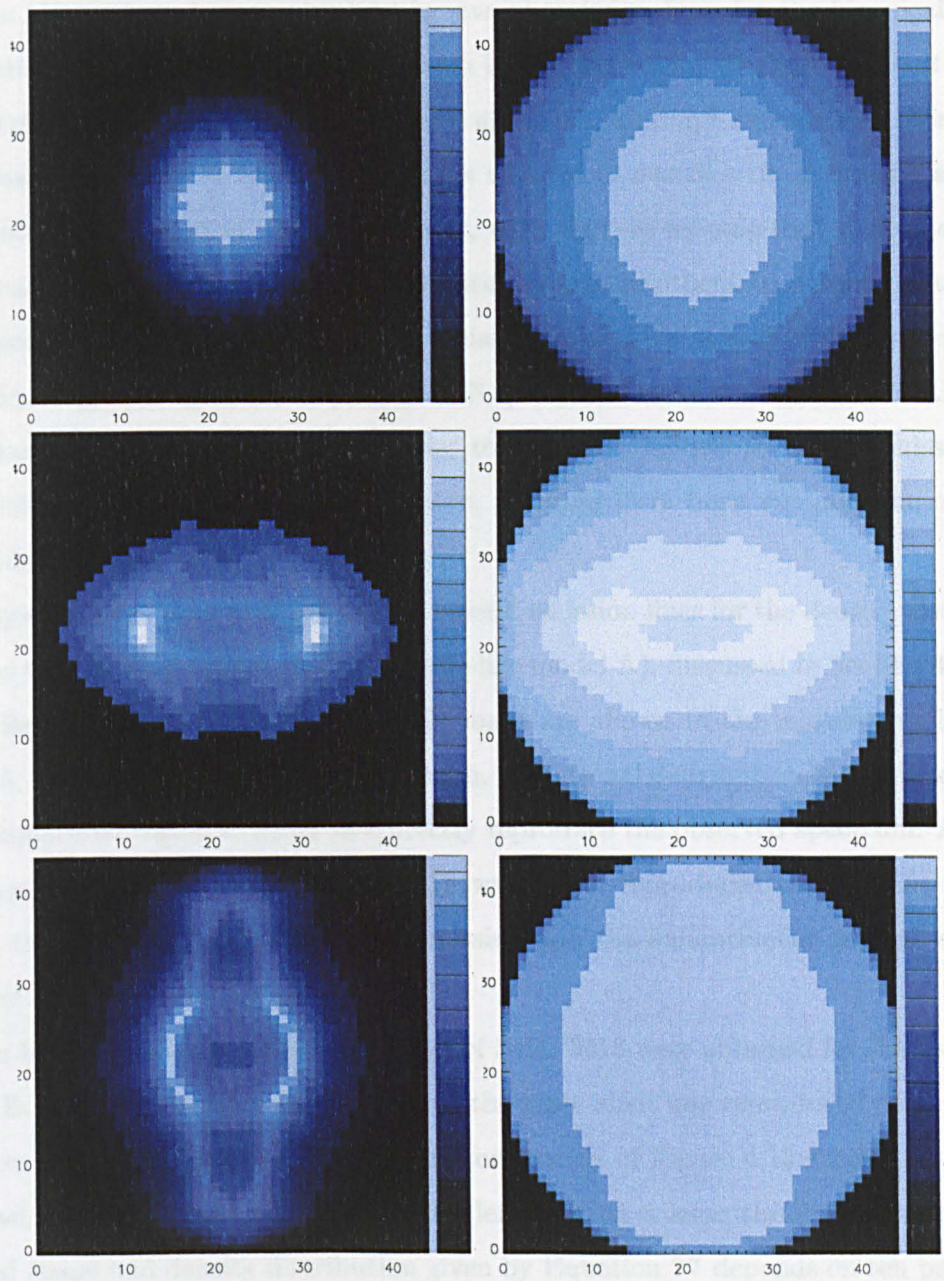

Figure 4.13: .

Predicted projected maps of NGC 3918 in Hβ for the biconical model (top panels), the spindle-like model A (middle panels) and the spindle-like model B (bottom panels). The left-had panels are displayed with linear intensity scales and the right-hand panels are displayed in logarithmic scales. The spatial units are pixels and the intensity range is in arbitrary units.

an almost filamentary distribution.

From the projected maps obtained in several emission lines for the biconical density distribution model (the Hβ maps are shown in the top panels of Figure 4.13) it became obvious that the model proposed by Clegg *et al.* (1987), although successful in reproducing the emission spectrum of NGC 3918, cannot be used to describe the geometric structure of this object. Clegg *et al.* (1987), however, were right to assume that this object must be optically thick in some directions and optically thin in others, in order to obtain such a complex spectrum, exhibiting strong emission lines from a wide range of ionization stage, from e.g. [Ne V], He II to [O I] and [N I]. A number of combinations of thick and thin phases could possibly have been used to construct models to fit the emission lines and, without additional spatial information, it would have been virtually impossible to distinguish between them.

Projected maps were also obtained in several emission lines for the density distribution given by the Mellema (1996) model (spindle-like model A), discussed in Section 4.3. Once again, for the sake of space, only the Hβ maps are shown in the middle panels of Figure 4.13. As discussed in the previous section, the original distribution had to be enhanced in the equatorial region in order to correctly reproduce the observed spectrum. Although the shape of the inner shell of NGC 3918 was better reproduced than by the biconical model, the polar protrusions were still missing and the enhancement seemed to be too localised in a small equatorial torus.

The best match to the observed images of NGC 3918 were obtained for the spindle-like model B, where the density distribution of the inner shell was reproduced using the analytical expression in Equation ??. The bottom panels of Figure 4.13 shows the Hβ maps obtained for this model, on a linear scale (left) and on a logarithmic scale (right). The detailed shape and density distribution given by Equation ?? depends on ten parameters and it is possible that a number of combinations of these could be used to reproduce the observations. However the combination used in this model (see Table 4.11) produces images (Figure 4.13, bottom panels) and spectroscopic results (see below) which are in agreement with the observations. It might be possible to obtain even better fits by further adjusting the density distribution parameters and, possibly, also the central star parameters, considering that those obtained by Clegg *et al.* (1987) were based on a completely different geometrical model. The central star parameters, however, were based on global nebular properties which shouldn't change as much.

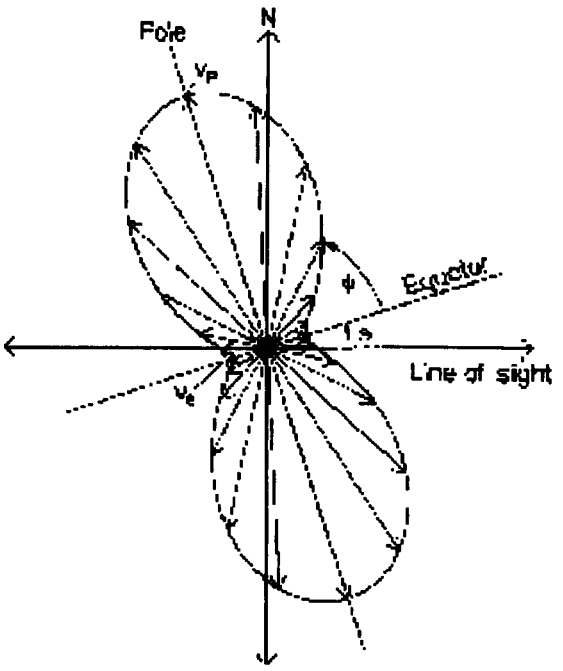

Figure 4.14: The bipolar mass flow model of Solf and Ulrich (1985). The polar axis is inclined by an angle θ with respect to the plane of the sky. The expansion velocity is a function of the latitude angle ϕ of the flow vectors, increasing from a minimum rate v_e in the equatorial plane to a maximum rate v_p in the direction of the poles.

4.5.2 Position-Velocity Diagrams and Line Profiles

As mentioned above, Corradi *et al.* (1999) used the spatio-kinematical empirical model of Solf and Ulrich (1985) to describe the nebular expansion velocity, V_{exp}, in order to fit their observations of position velocity plots of Hα and the shape of the inner shell of NGC 3918. In this model V_{exp} increases from the equatorial plane towards the polar axis, as shown in Figure 4.14, according to the following equation (Solf and Ulrich, 1985)

$$V_{exp}(\phi) = V_e + (V_p - V_e) sin^{\gamma} \mid \phi \mid \tag{4.7}$$

where ϕ is the latitude angle, defined such as ϕ=0° in the equatorial plane and ϕ=90° in the polar direction; V_p and V_e are the equatorial and polar velocity components, respectively (V_p = 50 km s^{-1} and V_e = 23 km s^{-1}, in their work); γ is a shape parameter (γ=12, in their work). Here the velocity field described above was also used for the spindle-like density distribution model A in order to produce position-velocity diagrams (echellograms) along slits positioned at P.A.=–76° and P.A.=+13°, in order to compare with Corradi et al.'s observations, shown in Figure 4.15. Position-velocity diagrams were obtained for

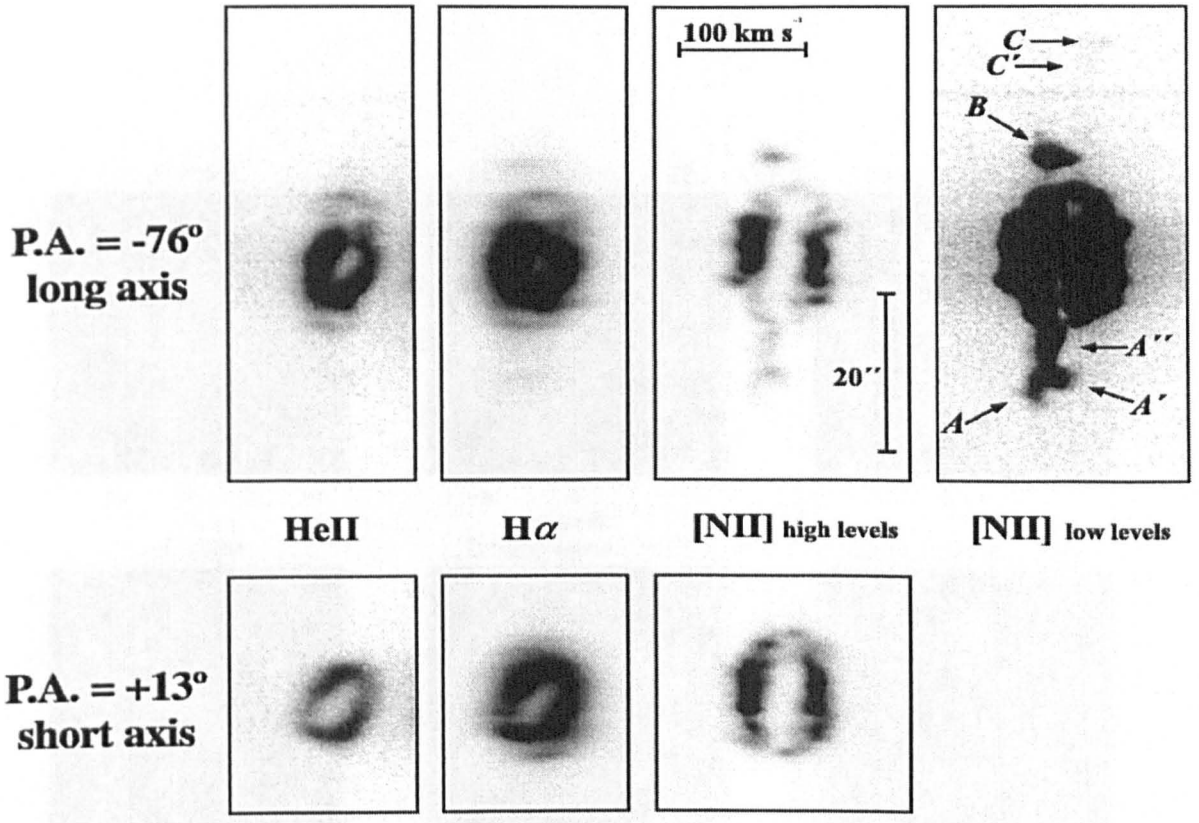

Figure 4.15: NTT long-slit spectra of NGC 3918. Images are in a logarithmic intensity scale with different cuts for the He II 6560Å, Hα, and [N II] 6583Å (Corradi *et al.*, 1999)

each of the lines with the long slit spectra presented by Corradi *et al.* (1999), and include He II λ4686, Hα and [N II] λ6584. These are shown in Figure 4.17 (the middle and the right-hand panels in each figure represent P.A.=–76° and P.A.=+13°, respectively), together with the projected images of the nebula in the given lines (left-hand panel in each figure). All the synthetic position-velocity diagrams shown in this section are plotted on a logarithmic intensity scale. It is worth noting, at this point that all minor axis position-velocity diagrams (bottom left panel in all figures) are plotted such that the ordinate is the velocity, in [km s^{-1}], and the abscissa is the spatial variable in pixels; this has to be taken into account when comparing the synthetic spectra to the observations in Figure 4.15, where the abscissa and the ordinate are reversed.

Position-velocity maps were also produced for the biconical density distribution model (Figure 4.16) and spindle-like model B (Figure 4.18) using the same slit positions as above.

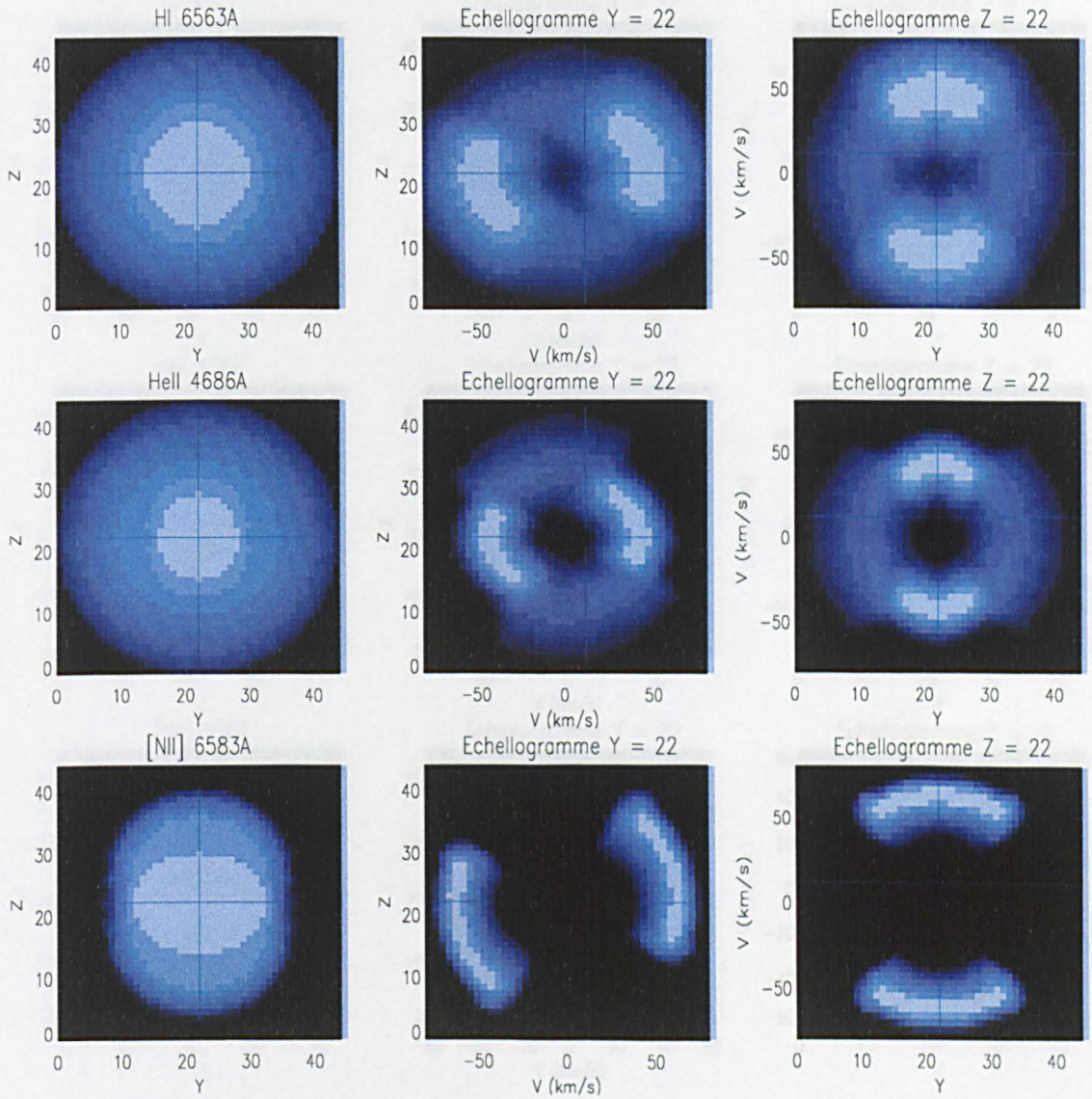

Figure 4.16: Predicted line images (left-hand panels) and position-velocity diagrams (central and right-hand panels) from Mocassin's biconical model of NGC 3918. The images and the position-velocity diagrams shown were obtained for the Hα line (top panels), the He II 4686 Å line (middle panels) and the [N II] 6584 Å line (bottom panels). For each line the position velocity diagrams were obtained with slits oriented at PA = –76° (central panels) and PA=+13° (right-hand panels).

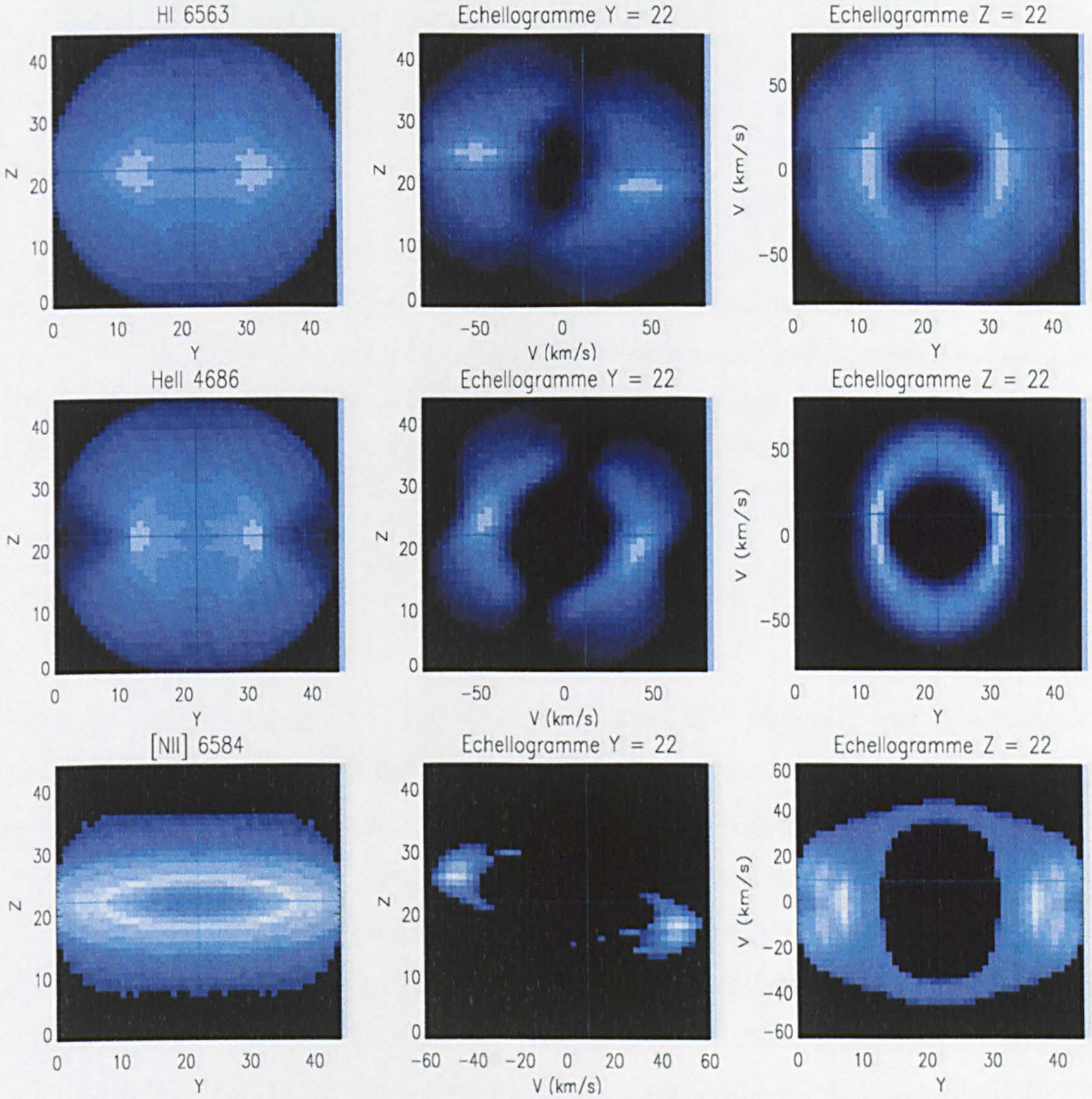

Figure 4.17: Predicted line images (left-hand panels) and position-velocity diagrams (central and right-hand panels) from Mocassin's spindle-like model A of NGC 3918. The images and the position-velocity diagrams shown were obtained for the Hα line (top panels), the He II 4686 Å line (middle panels) and the [N II] 6584 Å line (bottom panels). For each line the position velocity diagrams were obtained with slits oriented at PA = $-76°$ (central panels) and PA=$+13°$ (right-hand panels).

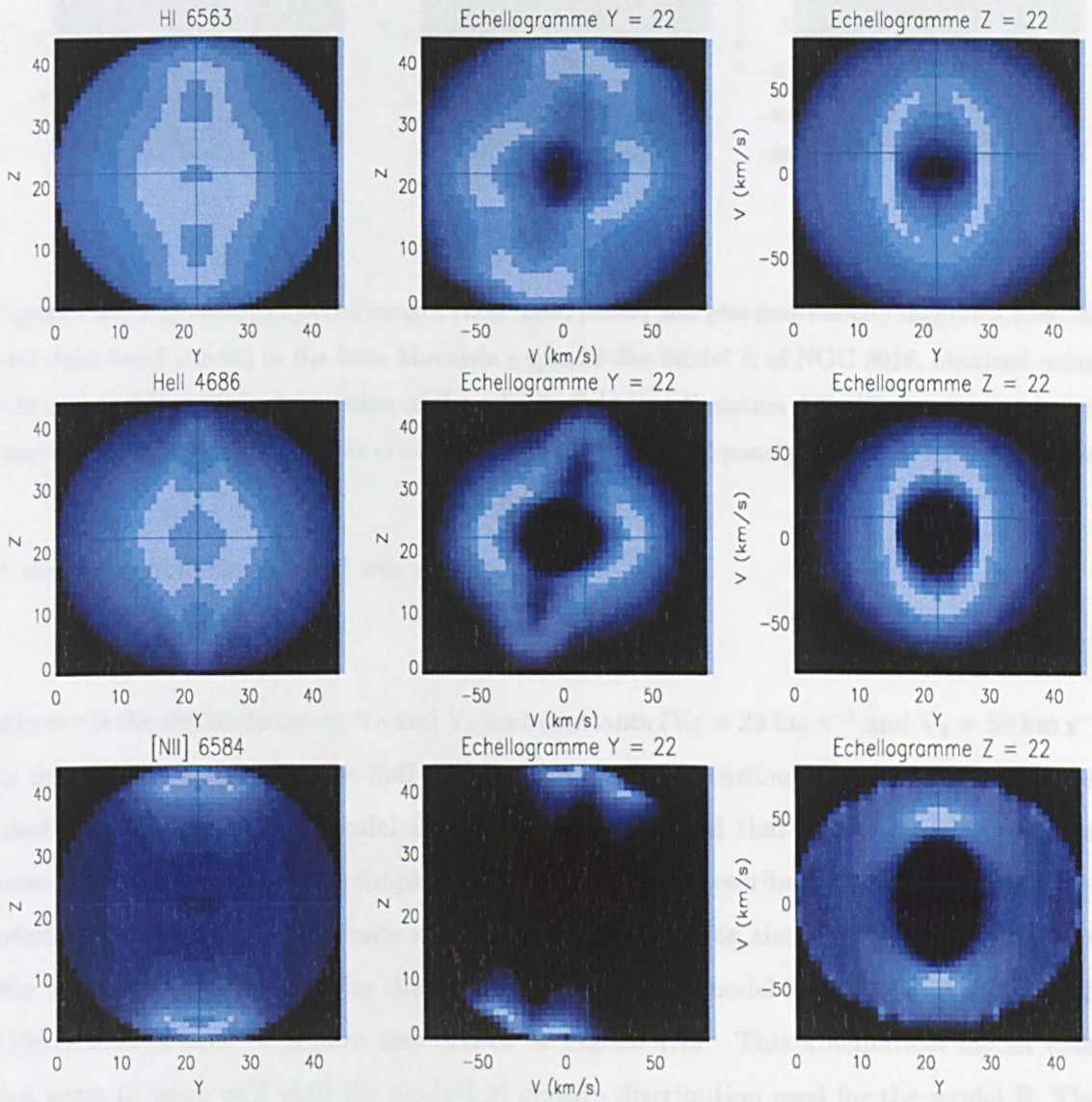

Figure 4.18: Predicted line images (left-hand panels) and position-velocity diagrams (central and right-hand panels) from Mocassin's spindle-like model B of NGC 3918. The images and the position-velocity diagrams shown were obtained for the Hα line (top panels), the He II 4686 Å line (middle panels) and the [N II] 6584 Å line (bottom panels). For each line the position velocity diagrams were obtained with slits oriented at PA = −76° (central panels) and PA=+13° (right-hand panels).

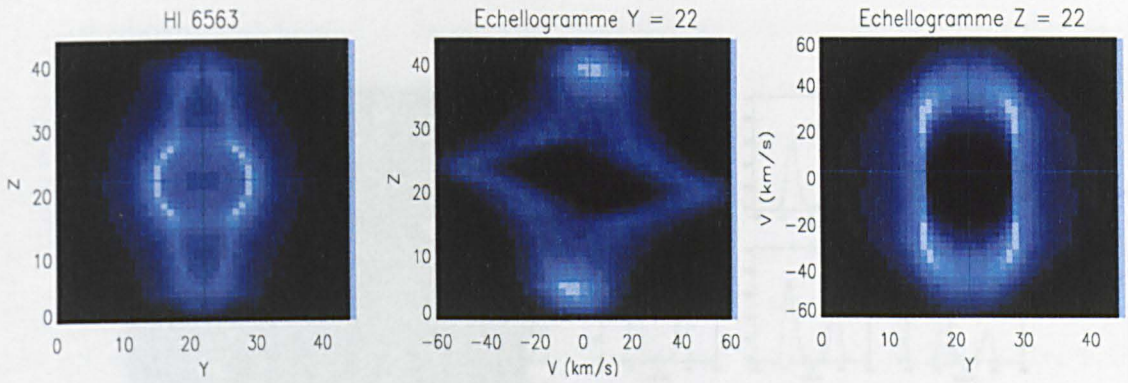

Figure 4.19: Predicted projected images (Left-hand panel) and position-velocity diagrams (central and right-hand panels) in Hα from Mocassin's spindle-like model A of NGC 3918, obtained using Solf and Ulrich (1985)'s description of the velocity field (see Equation 4.7). The position velocity diagrams were obtained with slits oriented at PA = −76° (central panel) and PA=+13° (right-hand panel).

A simple radial velocity field was adopted, namely

$$V(r) = V_0 + V_1 \cdot r \tag{4.8}$$

where r is the radial distance; V_0 and V_1 and constants ($V_0 = 23$ km s^{-1} and $V_1 = 50$ km s^{-1} in this work). Originally, the Solf and Ulrich (1985) description of the velocity field was used also for spindle-like model B; however it was found that better matching results were obtained by using the simple radial velocity field described above, which was applied to obtain the echellograms shown in Figure 4.18. For the sake of comparison, the Hα synthetic position-velocity diagrams obtained from model B, using Solf and Ulrich (1985) kinematical model are also shown in Figure 4.19. This kinematical model does not seem to work well with the analytical density distribution used for the model B. The disagreement is particularly evident in the major axis position-velocity diagrams, where the polar enhancement of the velocity field creates two bright spots which have not been observed. The same does not happen when Solf and Ulrich (1985) velocity field is applied to the spindle-like model A, since the two polar protrusions (which are created in model B by embedding an elliptical shell within a spheroid) are *not closed* at the poles (see Figure 4.2). However, from the *HST* images in Figure 4.12 it seems that the polar protrusions are indeed *closed*, although not very dense, and therefore the density distribution used in model B seems more appropriate.

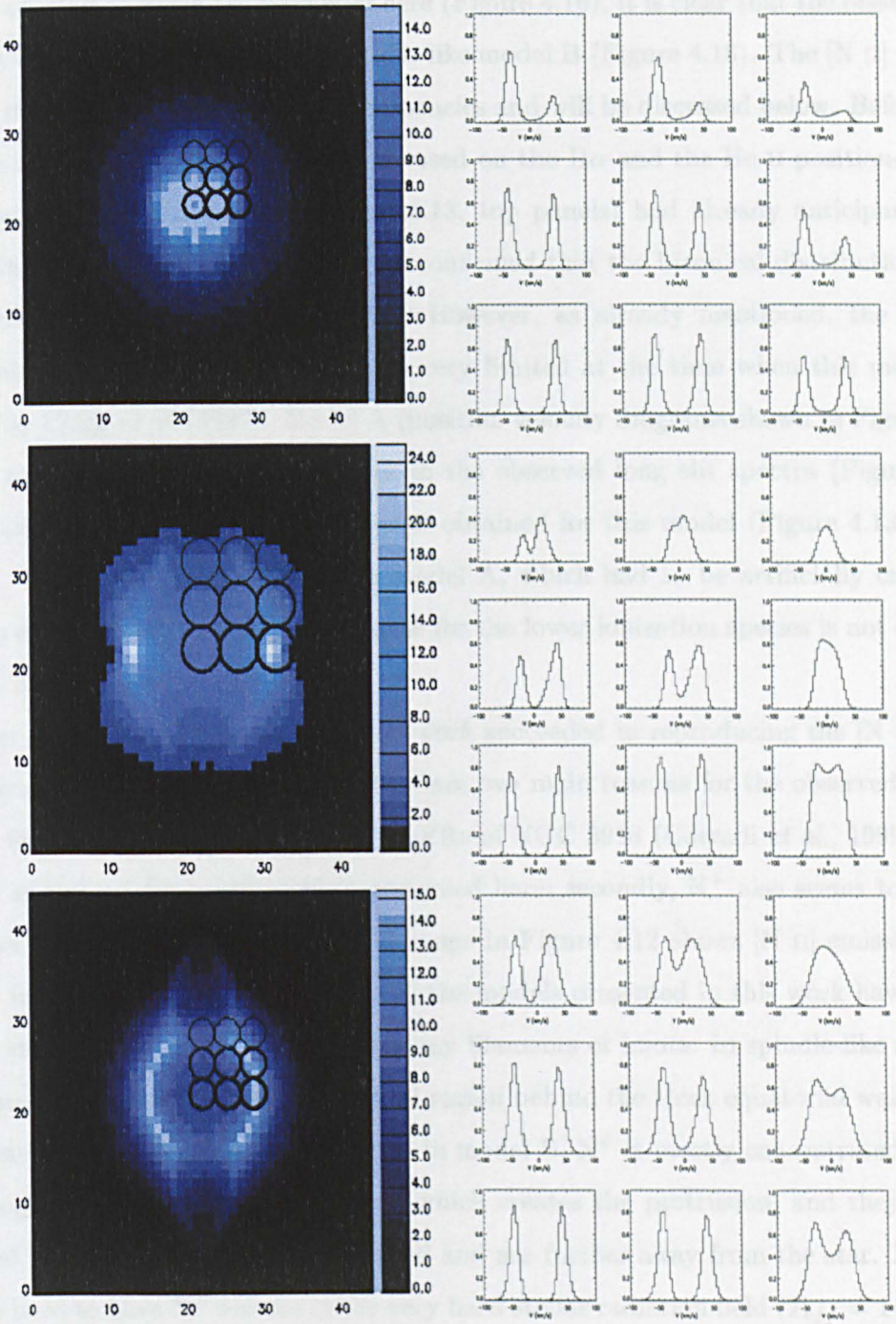

Figure 4.20: Predicted He II 4686 Å line profiles (right-hand panels) for the biconical model (top panels) and the spindle-like models A (middle panels) and B (bottom panels). The aperture sizes and positions are shown on the He II 4686 Å projected maps (left-hand panel). The line intensities are in arbitrary units.

After inspection of all the position-velocity diagrams obtained for the three models, a selected number of which are presented here (Figure 4.16), it is clear that the observations are most closely reproduced by the spindle-like model B (Figure 4.18). The [N II] position velocity diagrams show the largest discrepancies and will be discussed below. Before that, however the discussion will mainly be focused on the Hα and the He II position-velocity diagrams. The projected maps (Figure 4.13, top panels) had already anticipated, and the synthetic echellograms in Figure 4.16 confirmed that the biconical distribution is not a realistic representation of NGC 3918. However, as already mentioned, the imaging information available for this object was very limited at the time when this model was devised by Clegg *et al.* (1987). Model A (position velocity diagrams shown in Figure 4.17) fails to reproduce the polar protrusions in the observed long slit spectra (Figure 4.15), as was also clear from the projected maps obtained for this model (Figure 4.13, middle panels). Moreover, the thick waist in model A, which had to be artificially created in order to obtain the observed line strengths for the lower ionization species is not observed in NGC 3918.

None of the models presented in this work succeeded in reproducing the [N II] λ6584 echellograms shown in Figure 4.15. There are two main reasons for the observed discrepancies: firstly, N^+ is abundant in the FLIERs of NGC 3918 (Corradi *et al.*, 1999), which are not accounted for in the models presented here; secondly, N^+ also seems to exist in the inner regions of the shell; the NTT image in Figure 4.12 shows [N II] emission to be present in almost a *filamentary* form. All the models presented in this work have *smooth* density distributions and do not include any filaments or knots. In spindle-like model A, N^+ is mainly concentrated in the toroidal region behind the thick equatorial waist, which is screened from direct starlight, whereas in model B, N^+ is mostly concentrated in small polar regions beyond the elliptical shell which creates the protrusion, and they are also screened from direct starlight by this shell and are further away from the star. In fact, it is quite hard to have N^+ *survive* in the very hard stellar radiation field (T_{eff} = 140,000 K) in the inner shell unless some sort of density enhancement is postulated. This shows that, although spindle-like model B appears to be quite successful in reproducing the main spectroscopic and kinematic characteristics of NGC 3918, there is still scope for improvement.

Figure 4.20 show HeII λ4686 line profiles calculated at various locations on the nebula, for the biconical model (top panels) and for spindle-like models A (middle panels) and B (bottom panels), respectively. Aperture sizes and positions can be selected and are shown

on the projected maps in the lefthand panels of Figure 4.20. Unfortunately, no observations of this kind are yet available for comparison; however, the images are included here to demonstrate the code's capabilities.

4.6 Conclusions

In this chapter three photoionization models were constructed for the planetary nebula NGC 3918, a biconical model and two spindle-like models. The first spindle-like model (A) used the density distribution of the Mellema (1996) model already applied to this object by Corradi *et al.* (1999). The second spindle-like model (B) instead used an analytical expression for the density distribution, which aimed to mimic, by means of an ellipsoid embedded in a sphere, the shape of the inner shell of NGC 3918. The aim was to find a model which could not only reproduce the main spectroscopic features observed for this object, but also the spatio-kinematical properties of the nebula which recent observations (Corradi *et al.*, 1999) have uncovered.

The integrated emission line spectra obtained from the three different models were all in fair agreement with the observations. Discrepancies exist between the observed line fluxes of the C IV $\lambda\lambda$1548,1550 and Mg II$\lambda\lambda$2796,2803 resonance doublets, which can largely be explained by dust absorption in the nebula (Harrington *et al.*, 1988). Large discrepancies were also found between the models' predictions for the fluxes of the infrared fine-structure lines and the measurements of the *ISO SWS* spectra. The most likely cause for this discrepancy is a pointing error which affected *ISO* observations of NGC 3918, causing an offset of approximately 14 arcsec from the centre of the nebula. The corrected predicted line fluxes, obtained by convolving the *ISO SWS* aperture profiles with projected nebular maps in the relevant emission lines, confirmed that most of the discrepancy between the observed and model fluxes could be attributed to the pointing error, although there is still a factor of three discrepancy for the [S IV] 10.5 μm line.

A diffuse radiation field consistency test was also carried out in this work, which showed that the interaction of the diffuse radiation fields from two adjacent regions of different densities is not negligible, even in the relatively uncomplicated case of the biconical density distribution used by Clegg *et al.* (1987). We found that the low ionization species in the optically thick cones were particularly affected by the diffuse radiation field coming from the optically thin sector.

Although the volume-integrated emission line spectra obtained by the three models of NGC 3918 were in agreement with each other, the projected maps and the synthetic long-slit spectra obtained in several emission lines were, however, very different from one model to the other. Spindle-like model B produced the best fits to the observations, although some discrepancies still exist, particularly in the [N II] maps and long slit spectra, as discussed in Section 4.5.2.

This work has indicated that a detailed model of a nebula cannot be verified just by comparison of the observed integrated spectrum with model predictions. In fact, in the case of NGC 3918 approximately the same spectrum can be obtained with a number of different geometries and density distributions. For this reason, three-dimensional models are necessary in order to allow a spatio-kinematical analysis to be carried out by comparing predicted images and position-velocity diagrams in several lines to available observational data. Mocassin provides all the tools needed for such simulations and for the visualization of the final results.

CHAPTER 5

Modelling of Abell 30

5.1 Introduction

The large angular diameter planetary nebula Abell 30 belongs to the very peculiar class of planetary nebulae with hydrogen-rich envelopes surrounding hydrogen-deficient inner knots. Such characteristics are generally interpreted using the *born-again* scenario proposed by Iben *et al.* (1983) and discussed in Section 1.1.4.

The outer envelope of Abell 30 has a radius of 64″ and an almost perfectly round shape, showing a high excitation and a very low surface brightness. Given the size of the outer envelope and the fact that it appears to be very diffuse, Abell 30 is believed to be quite old (~10,000 yr, if a distance of 1.3 kpc is assumed; Harrington and Feibelman, 1984). Its hydrogen-deficient central star, however, still appears to be quite bright (V=14.3). These characteristics, and, in particular, the presence of four symmetrically placed hydrogen-deficient inner knots led Iben *et al.* (1983) to classify this object as a planetary nebula with a *born-again* nucleus. The central knots were identified simultaneously by Jacoby (1979) and Hazard *et al.* (1980); according to *born-again* scenario, these knots consist of material whose abundance distribution has been altered by complete hydrogen burning and later ejected when the star returned to a brief red-giant phase after a final He-shell flash. However, more recently, Livio (1995) proposed that the strongly axial symmetric structure of Abell 30 is suggestive that tidal interaction of the central star with a companion may actually be a more plausible mechanism. Following Jacoby's discovery, the knots were named J1 to J4, clockwise, starting from the southernmost one; they are marked on the HST image of Abell 30 shown in Figure 5.1 (Borkowski *et al.*, 1993).

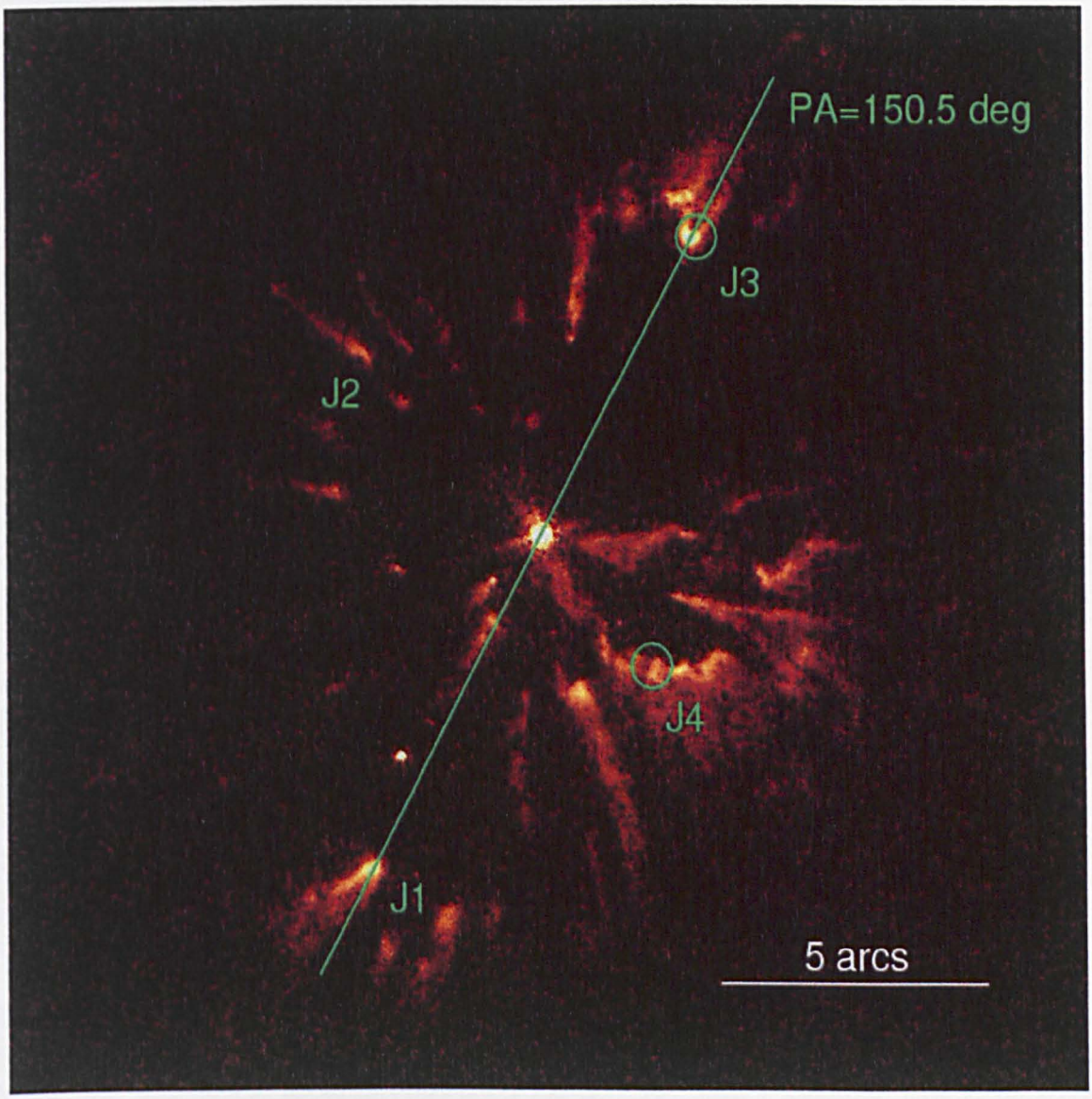

Figure 5.1: Abell 30. HST WFPC2 image Borkowski *et al.* (1995). The four hydrogen-deficient knots are labelled J1-J4. This nebula, believed to be quite old, has a very low surface brightness and it is not visible in this image (Borkowski *et al.*, 1993).

Since the discovery of the hydrogen-deficient knots in Abell 30, this object has been widely studied. Harrington and Feibelman (1984) obtained IUE spectra of the nebulosity near the nucleus, in proximity to one of the knots, and carried out a study of the chemical abundances from the observed emission lines. More recently, Guerrero and Manchado (1996) published a study of the chemical abundances of hydrogen-poor planetary nebulae, including Abell 30, based on long-slit data obtained in 1986 at the 3.6 m telescope at La Silla Observatory (Chile). Wesson *et al.* (2002) have analysed new observational data, including optical spectra of the polar knots J1 and J3 and of the central star of Abell 30, obtained on February 20th 2000 with the ISIS spectrograph mounted on the 4.2 m WHT at the Observatorio del Roque de los Muchachos, on La Palma, Spain, as well as archive ultraviolet spectra of knots J3 and J4 obtained on December 8th 1994 by the Faint Object Spectrograph aboard the Hubble Space Telescope. They found a large discrepancy between the ionic abundances measured from optical recombination lines (ORLs) and those measured from collisionally excited lines (CELs). This had already been noticed by Jacoby and Ford (1983) who found a very high carbon abundance (almost half that of hydrogen) from ORLs, far higher than that derived from CELs. Subsequently, Harrington and Feibelman (1984) proposed that this discrepancy could be explained if very large temperature variations were present within the knots of Abell 30. A high concentration of heavy elements in the core of the knots could create a very cool ($\approx$1000 K) but still ionized region emitting the observed ORLs. This could be surrounded by a hotter region consisting of material with more typical nebular abundances emitting the observed CELs. The analysis of Wesson *et al.* (2002) seems to be in agreement with this interpretation.

5.1.1 The Photoionization Model

In this work a model of knot J3 of Abell 30 is constructed using the observational data of Wesson *et al.* (2002), in order to investigate the temperature and ionic structures which could give rise to the observed ORLs and CELs. Given the very low surface brightness of the main extended nebula, and hence the very low density of material there, the effects of contamination of the spectra of the knots from this region are expected to be very small. Nevertheless a background nebular spectrum was subtracted from the spectra of the knots by Wesson *et al.* (2002) in order to correct for any contamination. The photoionization model consists of a three-dimensional Cartesian grid with the ionizing radiation source in one corner. The spatial sampling varies throughout the grid with most of the grid

Table 5.1: Model elemental abundances in the two assumed regions (dense, cold core and thin hotter outer region) of the knot J3 in Abell 30. Also listed, in columns 3 and 6, respectively, are empirical elemental abundances from the whole knot, derived from ORLs and from CELs Wesson *et al.* (2002)

	Core	ORLs		Outer	CELs*
H/He	0.0286	.0850	H/He	0.025	0.085
C/He	0.0143	.0390	C/He	9.00×10^{-4}	1.41×10^{-4}
N/He	0.0314	.0220	N/He	1.30×10^{-3}	6.76×10^{-5}
O/He	0.0325	.1080	O/He	2.47×10^{-3}	2.09×10^{-3}
Ne/He	0.0183	.0830	Ne/He	3.12×10^{-3}	5.13×10^{-4}

* No estimate for the helium abundance was available to Wesson *et al.* (2002) from CELs, H/He was assumed to be equal to the value obtained by Wesson *et al.* (2002) from the ORL analysis.

cells being in the knot region; the rest of the nebular region is assumed to be empty. The centre of the knot is placed on the x axis of the grid, at 1.68×10^{17} cm from the central star, meaning that only half of the spherical knot needs to be modelled, and the full picture is reconstructed, as usual, at the end of the simulation (the knot is assumed to be symmetric about a plane through its centre).

In the first model constructed, the density and abundances in the knot were assumed to be homogeneous. This approach did not succeed since the heating, which, in the virtual absence of hydrogen, mainly comes from helium photoelectrons, was not adequate. This model resulted in the knot being too cold (~300 K) to collisionally excite the optical and ultraviolet heavy element forbidden lines observed (Table 5.3). A similar problem was encountered by Harrington and Feibelman (1984) when they tried to construct photoionization models of the hydrogen deficient knots in Abell 30. This led them to hypothesise a chemical inhomogeneity in the knot, as mentioned in Section 5.1, with a central region where the ratio of C, N and O relative to He is very high (~10%). However, as it was difficult to construct a one-dimensional photoionization model capable of adequately reproducing the postulated chemical inhomogeneity, Harrington & Fiebelman could not test their hypothesis.

With their result in mind, a second model was constructed in this work, consisting of

Table 5.2: Adopted parameters for Abell 30 photoionization model

L_*	4974 $L_\odot$	R_{core}	$0.45 \times R_{knot}$
T_*	100,000 K	N_{He}(core)	10,710 cm^{-3}
log g	5.5	N_{He}(outer)	1800 cm^{-3}
D_{knot}	1.68×10^{17}cm	ρ_d/ρ_g	0.05
R_{knot}	4.80×10^{15}cm	a_d	1.0×10^{-6}cm

D_{knot}: distance of the centre of the knot from the ionizing source

R_{knot}: radius of the hydrogen-deficient knot

R_{core}: the radius of the thick, cold inner core of the knot

N_{He}(core): hydrogen density by number [cm^{-3}] in the inner core of the knot

N_{He}(outer): hydrogen density by number [cm^{-3}] in the outer region of the knot

ρ_d/ρ_g: dust-to-gas ratio by mass

a_d: radius of the dust grains

a two phase spherical blob, where the nucleus is assumed to be more metal-rich then the surrounding layer. A two-dimensional representation of the model is shown in figure 5.3. The abundances derived by Wesson *et al.* (2002) from the CELs were taken as a starting point for the model abundances in the outer regions of the knot and the abundances from the ORLs were taken as a starting point for the abundances in the nucleus. However, the He/H abundance ratio cannot be derived from CELs , and therefore this was set to a starting value of 0.5 by number, i.e. enhanced by a factor of 5 with respect to typical nebular values He/H, this is the same factor by which the C/H abundance appeared to be enhanced from Wesson *et al.* (2002)'s CEL analysis. However it should be noted that, in Wesson et al.'s analysis, the abundances were derived without taking into account the possibility of chemical and density inhomogeneities within the knot, which would give rise to regions with different ionization structures. This implies a certain degree of freedom in the choice of abundances for the photoionization model, which, as will be seen later, requires two sets of abundances for the two regions of the knot which are quite different from those of Wesson et al.. However, this second model also failed to produce enough heating for the knot, which, according to Wesson et al.'s analysis, has an electron temperature of T_e[OIII] = 16680 K.

The first two models described above showed that photoionization of He and other elements cannot provide enough heating to account for the collisionally excited emission

observed; Harrington and Feibelman (1984) proposed that the extra heating might be provided by electron conduction from the shocked stellar wind. However, Harrington (1996) later argued that, while this is a possibility, the presence of even a weak magnetic field could prevent such conduction and that a better candidate for the additional energy source needed to produce the extra heating is photoelectric emission from dust grains. This was first proposed by Borkowski and Harrington (1991) in their analysis of the hydrogen-deficient planetary nebula IRAS 18333-2357. Evidence for the presence of dust in Abell 30 is provided by the fact that Cohen and Barlow (1974) detected 10- and 20-μm emission from warm dust located within a radius of 5.5 arcsec of the central star, while Cohen *et al.* (1977) detected 1.6-3.5-μm emission from hot dust grains located in the same region. In addition, the central star appears to be reddened, and, as discussed by Harrington and Feibelman (1984), given the high galactic latitude of this object, the reddening is likely to be intrinsic. A study by Borkowski *et al.* (1994), based on optical and near infrared images, confirmed the presence of dust in an expanding equatorial ring of H-poor gas around Abell 30; they detected no emission from the H-poor polar knots, concluding that there must be a dust deficiency there relative to the equatorial ring. In the recent analysis of Wesson *et al.* (2002), it was found that the extinction coefficients, $c(H\beta)$, derived from the spectrum of the central star ($c(H\beta) = 0.60$) and derived for the knot J3 ($c(H\beta) = 0.55$) are in good agreement. It is hard, however, to estimate the amount of dust actually locked into the knots, and, therefore, in this work, the dust-to-gas ratio is treated as a free parameter. A proper radiative transfer treatment including dust has not been implemented in Mocassin yet; the heating provided by the grains, however, was estimated by using a simplification of the approach used by Borkowski and Harrington (1991) for the modelling of the grain-heated, dusty planetary nebula in M22. An outline of this method is given in the next section.

The final model consisted of a spherical knot composed of two phases: a dense inner nucleus (Ne $\approx$ 13,000 cm^{-3}), with a radius equal to 0.45 of the total radius of the knot, $R_{\rm knot}$, surrounded by a less dense outer region (Ne $\approx$ 3200 cm^{-3}), occupying the remaining volume of the knot. The elemental abundances adopted for the two regions are summarised in Table 5.1, together with the empirical abundances derived by Wesson *et al.* (2002). The abundances for the outer region and for the cold dense core, where most of the ORL emission is produced, are given by number with respect to helium (columns 5 and 2, respectively, in Table 5.1), since this is the most abundant element. The abundances in the

core are compared to the empirical ORL abundances of Wesson *et al.* (2002), also given by number with respect to helium (column 3, Table 5.1). Most of the CEL emission is believed to be produced in the hotter outer layer and therefore the model abundances in this region (column 5 of Table 5.1) are compared with the empirical CEL abundances (column 6 of Table 5.1). Note that an empirical value for the abundance of helium could not be obtained from CELs in the analysis of Wesson *et al.* (2002). The value of the He/H ratio given in Table 5.1 was assumed to be equal to the value obtained by Wesson *et al.* (2002) from ORLs. Table 5.2 lists all the other parameters used for the final simulation. The central star parameters, $L_* = 4974\ L_\odot$, $T_* = 100{,}000$ K, log g = 5.5, are in fair agreement with the values of $T_{eff} = 110{,}000$ K, log g = 6.0 and $L_* = 5000\ L_\odot$ derived by Harrington and Feibelman (1984) using the Zanstra method. The non-LTE stellar atmosphere used in this work was calculated by Clegg *et al.* (1987) using the program of Mihalas and Auer (1975). It is worth noting at this point that this set of stellar atmospheres were calculated for normal abundances; a hydrogen-deficient stellar atmosphere would have provided a more realistic representation of the central star of Abell 30. The other parameters listed in Table 5.2 include D_{knot}, the distance of the centre of the knot from the ionizing source, R_{knot}, the radius of the hydrogen-deficient knot, R_{core}, the radius of the thick, cold inner core of the knot, N_H(core) and N_H(outer), which are the hydrogen density by number [cm^{-3}] in the inner core and in the outer layer of the knot, respectively, and, finally, ρ_d/ρ_g and a_d in [cm] which are the dust-to-gas ratio and the radius of the dust grains (both assumed to be constant throughout the knot).

5.1.1.1 Grain Photoemission

Photoelectric emission from dust grains occurs when the electrons in the dust material are ejected from a grain following the absorption of a photon. The ratio between the number of photoelectrons emitted and the number of absorbed photons defines the photoelectric yield, Y. This of course depends on the grain species and size, since the photoelectron could be excited by a photon several layers from the surface on the grain, and, therefore, in small grains the probability of this occurring near the surface, and hence the photoelectron escaping, is higher. Experimental data exist for several materials (e.g. the data for graphite and vitreous carbon by Feuerbacher and Fitton, 1972), but for the present calculations

the following approximation for the photoelectric yield is used (Draine, 1978)

$$Y(h\nu) = Y_\infty \left(1 - \frac{B}{h\nu}\right) \tag{5.1}$$

where B is a parameter which is chosen to be some energy above the photoelectric emission threshold energy, or work function,E_w, at which the yield becomes negligible, and Y_∞ is another parameter which depends on the material used and is determined experimentally. Based on the results of Feuerbacher and Fitton (1972) and Feuerbacher *et al.* (1972) Draine (1978) defines a *standard model*, appropriate for organic, metallic and silicate grains where $Y_\infty = 0.5$ and B = 8 eV.

Another important quantity which must be considered in estimating of the grain heating is the energy distribution of the photoelectrons ejected from the dust grains. In this calculation the photoelectron distribution function, $f(h\nu, E)$, where E is the photoelectron energy, is approximated using the formulation of Borkowski and Harrington (1991), valid for photon energies above 11 eV,

$$f(h\nu, E) \propto \begin{cases} E & : \quad E < 2.7 \text{ ev} \\ [E - 1.7 + \alpha^3 (E - 2.7)^3]^{-1} & : \quad E > 2.7 \text{ eV} \end{cases} \tag{5.2}$$

where $\alpha = 0.059\,(26.4 - h\nu)$ for $h\nu < 26.4$ eV and $\alpha = 0$ for higher photon energies. For a particular photon energy, $h\nu$, this photoelectron energy distribution is truncated at an electron energy of $h\nu - E_w$, where $E_w = 5$ eV (Feuerbacher and Fitton, 1972). For photon energies below 11 eV, equation 5.2 is scaled by substituting E by $(11 - E_w)\,E\,/\,(h\nu - E_w)$. This scaling is necessary because, from the experimental data, is apparent that there is a shift of the maximum in the distribution function f, from ~2.7 eV at high incident photon energies to lower electron energies for $h\nu < 11$ eV. In practice, $f(h\nu, E)$ is the fraction of all electrons ejected by a photon of frequency ν which emerge with kinetic energies between E and $E + dE$.

In this work only a qualitative description of the role of dust in the energy balance of the nebula is investigated. A simplified approach is used, where grain charge and other factors are not taken into account, and the frequency-dependent contribution of the dust grains to the heating of the nebula, $G_d(\nu)$, is estimated at each grid cell according to

$$G_d(\nu) = n_d \cdot (\pi\, a_d^2) \cdot F(\nu) \cdot Y(\nu) \cdot < E_\nu > \tag{5.3}$$

where n_d is the local dust density by number, a_d is the radius of the dust grains assumed to be constant throughout the ionized region, and $F(\nu)$ is the photon flux. The

quantity $< E_\nu >$ is the mean photoelectron energy, weighted by the photoelectron energy distribution function, $f(h\nu, E)$, namely,

$$< E_\nu > \; = \; \frac{\int_0^{h\nu - E_w} f(h\nu, E)\, E\, dE}{\int_0^{h\nu - E_w} f(h\nu, E)\, dE} \tag{5.4}$$

The total dust contribution to the heating is then obtained by integration of equation 5.3 over all photon energies above the work function, $E_w = h\nu_{th}$,

$$G_d \; = \; \int_{\nu_{th}}^{\nu_{max}} G_d(\nu)\, d\nu \tag{5.5}$$

where ν_{max} is the higher limit of the frequency range considered; in the Mocassin models of Abell 30, ν_{max} was set to 24 Ryd ($\approx$ 326.4 eV). The integrals $\int_0^{h\nu - E_w} f(h\nu, E)\, E\, dE$ and $\int_0^{h\nu - E_w} f(h\nu, E)\, dE$ must be evaluated numerically; it is therefore advantageous to compute them in advance and store them in two frequency-dependent arrays for all photon energies above E_w.

Finally, the total dust contribution to the heating, calculated at each grid cell is added to the local thermal balance equations as an extra heating channel, so that equation 1.16 simply becomes

$$G_{phot} + G_d = L_c + L_r + L_{ff} \tag{5.6}$$

where G_{phot} is the heating due to the photoionization of the gas, L_c is the contribution due to collisional excited radiative cooling and L_r and L_{ff} are the contributions due recombination and free-free radiation, respectively.

5.2 Modification to the Mocassin code

Some modifications to the original version of Mocassin had to be made in order to allow the simplified dust treatment used here. They mainly consisted of the addition of the dust heating term (Equation 5.5) to the thermal balance equation (Equation 1.16). However, these modifications will not be included in the public release version of Mocassin, since it is intended to enhance the code in the future by implementing a proper treatment of the radiative transfer including dust. The analysis carried out in this chapter can be considered to be a qualitative investigation of the effects of dust photoelectric heating in an hydrogen deficient environment.

An external density file was used to describe the density discontinuity within the knot and the *composition_mod* module (Chapter 2) was expanded, in order to treat the assumed chemical inhomogeneity. As the composition of the nebula is defined at each grid cell, it is indeed very simple to simulate any type of chemical composition distribution.

An extra driver was also implemented, *mocassinHeat*, which writes out to a file (*thermChannels*) the breakdown of all the heating and cooling contributions in each grid cell.

5.3 Abell 30 model results

The fluxes of some important emission lines predicted by Mocassin for the final model of Abell 30 are listed in Table 5.3, together with the corresponding observed values (Wesson *et al.*, 2002). The fluxes are given relative to He I 5876 Å, since helium is the most abundant element in this object. The contributions from each of the two assumed regions of the knot are given separately in the table, and, as expected, it is clear that the ORLs are mainly emitted in the cold inner core of the knot, while the CELs are emitted in the hotter outer layer surrounding it. The predicted line fluxes mostly agree with the observed values within a factor of about two; however, at this stage, a close match to the observed spectrum is not really required, since, given the simplistic approach used for the treatment of the dust grain heating, a quantitative analysis is not attempted.

The largest discrepancies are observed for the [O II] 3727 Å and [N II] 6584 Å lines. Both of these lines, however, may have a recombination component (Rubin, 1986), which is not accounted for in the fluxes listed in Table 5.3. An estimate of the radiative recombination component was made for [O II] λ3727 and is equal to 0.703 of the He I 5876 Å flux, raising the total [O II] λ3727 flux from 0.136 to 0.839, which is then within a factor of two of the observed flux (= 1.66 relative to He I 5876 Å). It must be noted, however, that this estimate was obtained without taking into account collisional de-excitation of the upper levels of the 3727,3729 Å doublet. Moreover, recombination coefficients for O^{2+} have not yet been calculated for the very low electron temperatures (500 K-2000 K) occurring in the inner core of the model of J3. A power law was fitted to the coefficients calculated by Storey (1994) (valid in the range 5,000 K$< T_e <$20,000 K), in order to extrapolate to the required temperatures. In any case, the estimate obtained, although not exact, is sufficient to show that the contribution from recombinations to the total flux of O II 3727 Å is probably dominant and is likely to be the cause of the discrepancy

Table 5.3: Observed and predicted emission lines fluxes for knot J3 of Abell 30

Line	Predicted			Observed[a]
	Core	Outer	Total	
He I 5876/$10^{-15}\frac{erg}{cm^2 s}$	6.57	0.47	7.04	7.37
He I 5876	0.933	0.067	1.	1.
He II 4686	0.765	0.806	1.58	2.50
Hβ 4861	0.067	0.003	0.070	0.080
C II 4267	0.226	.0003	0.227	0.452
C III] 1908	0.	1.46	1.46	2.8
C III 4648	0.024	.0001	0.024	0.030
C III] 2297	0.815	0.015	0.830	0.960
C IV 1550*	0.	11.2	11.2	9.2
[N II] 6584	0.	0.182	0.182	0.829
N IV] 1486	0.	2.45	2.45	2.56
[O II] 3727	0.	0.136	0.136	1.66
O II 4303	0.022	0.	0.022	0.094
O II 4097	0.028	0.	0.028	0.174
O II 4089	0.054	0.	0.054	0.06
O II 4075	0.119	0.	0.119	0.149
[O III] 5007	0.	12.6	12.6	14.2
[O III] 4363	0.	0.305	0.305	0.349
[Ne III] 3869	0.	8.66	8.66	2.85
[Ne IV] 2423	0.	8.77	8.77	15.2
[Ne V] 3426	0.	1.16	1.16	1.20

* Attenuated by dust absorption.

[a] Wesson *et al.* (2002).

between the observations and the model predictions for this doublet listed in Table 5.3. The same argument may also apply to the [N II] 6584 Å, which is underestimated in the Mocassin models and also has a component due to recombination (Rubin, 1986), although an estimate for the latter was not calculated in this work.

There are also discrepancies between the Mocassin predictions of the optical recombination lines of O II and the observations. However, O II 4303 Å, 4097 Å and 4089 Å all come from the $3d\,^4F$ level and therefore their relative strengths are only determined by the branching ratios, which are well known (e.g., see Liu *et al.*, 1995). The observed relative intensities of these lines do not conform to the theoretical branching ratios. As indicated in Table 5.3, the O II 4097 Å line should not be taken into account, since this may be blended with one of the secondary Bowen fluorescence lines of N III. Nevertheless, the relative fluxes of O II 4303 Å and O II 4089 Å are also in disagreement with the theoretical branching ratios. Tsamis *et al.* (2002) also noticed a similar effect in the spectra of five H II regions, namely, M 17, NGC 3576, 30 Doradus, LMC N11B and SMC N66. They suggested that at the low electron densities characteristic of those nebulae, a breakdown of the statistical equilibrium may occur among the fine-structure levels of the parent $^3P_{0,1,2}$, ground term of recombining O^{2+}, causing the observed behaviour. However, in the case of the high electron density (N_e ~13,000 cm^{-3}) core region of the knot J3 of Abell 30, this is not expected to occur.

A discrepancy is also evident between the observed flux of [Ne III] 3869 Å and Mocassin's prediction. The emission line spectrum of neon is, in general, very sensitive to the shape of the ionizing spectrum, and, as has already been mentioned, the stellar atmosphere model used in this work was one obtained for a star with a normal hydrogen abundance, instead of a hydrogen-deficient one, which would have probably been more suitable in this case.

Table 5.4 lists the diagnostic ratios for electron density and temperature predicted by Mocassin and those observed by Wesson *et al.* (2002). Good agreement is obtained for most line ratios; the prediction for the [O II] 3726/3729 ratio is ~10% lower than the observed value, however as mentioned above, the contribution due to recombinations could be dominant in the case of this line. A slightly lower ratio was also obtained for O II 4075 Å/4089 Å, indicating that the Mocassin model predicts a slightly lower temperature for the inner core of the knot.

Table 5.5 lists mean temperatures, weighted by the ionic abundances, for the two re-

Table 5.4: Diagnostic ratios for electron temperature, T_e, and electron density, N_e. Ratios predicted by Mocassin (column 3) and observed ratios (column 5).

Ion	Lines (Å)	Ratio (Mocassin)	Ratio (Observed)
N_e			
[O II]	3726/3729	1.554	1.725
T_e			
He I	5876/4471	2.66	2.76
He I	6678/4471	0.761	0.777
O II	4075/4089	2.18	2.47
[O III]	(5007+4959)/4363	55.5	54.5

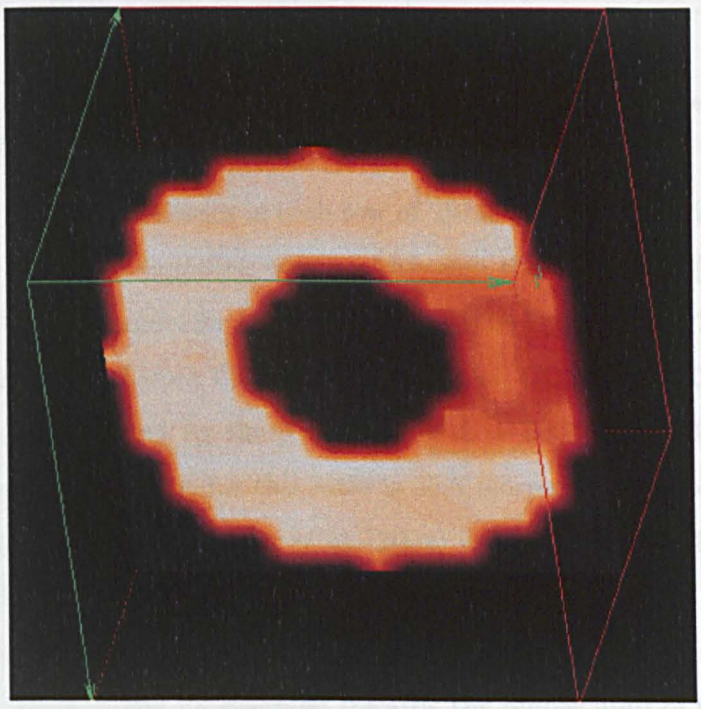

Figure 5.2: Cross-section map of the electron temperature distribution in the Mocassin model of knot J3 of Abell 30.

Table 5.5: Mean temperatures (K) weighted by ionic species for knot J3 of Abell 30.

	Ion						
Element	I	II	III	IV	V	VI	VII
H	851	961					
	11,687	15,664					
He	465	951	1,386				
	10,211	13,132	16,965				
C	559	688	987	1,203	1,486		
	6,279	8,426	12,994	16,665	17,118		
N	506	605	983	1,198	1,475	1,578	
	6,982	9,582	13,522	16,630	17,112	17,131	
O	505	644	1,036	1,447	1,514	1,551	1,602
	6,911	9,271	14,520	17,019	17,137	17,162	17,161
Ne	467	659	1,054	1,467	1,540	1,570	1,597
	8,026	10,143	14,863	17,066	17,100	17,100	17,102

For each element the upper row is for the optically thick inner core and the lower row for the optically thin outer layer of the knot.

gions of the knot. The upper entries in each row of Table 5.5 are for the inner core and the lower entries are for the surrounding region. Although the value of T_e[O III] = 14520 K obtained by the Mocassin model for the outer region of the knot is about 2000 K lower than the empirical value derived from CELs by Wesson *et al.* (2002) of T_e[O III] = 16,680 K, this difference is not reflected by the [O III] (4959 Å + 5007 Å)/4363 Å ratios; in fact the value predicted by Mocassin for this ratio is 55.5 (corresponding to a temperature of 16,500 K) and that derived by Wesson *et al.* (2002) is 54.5 (corresponding to a temperature of 16,680 K). This can be explained by the fact that there could be fluctuations in temperature in the O^{2+} region, in which case the empirical temperature derived by the [O III] diagnostic ratios would be weighted towards the higher limit of the range.

The volume-averaged fractional ionic abundances for the two regions of the knot are listed in Table 5.6, where, once again, the upper entries for each element are for the inner

Table 5.6: Fractional ionic abundances for knot J3 of Abell 30

	Ion						
Element	I	II	III	IV	V	VI	VII
H	0.18(-1)	0.982					
	0.12(-2)	0.999					
He	0.65(-1)	0.913	0.22(-1)				
	0.38(-2)	0.338	0.658				
C	0.86(-3)	0.140	0.788	0.71(-01)	0.98(-4)		
	0.27(-4)	0.21(-1)	0.245	0.574	0.160		
N	0.98(-3)	0.180	0.605	0.213	0.30(-3)	0.23(-6)	
	0.18(-4)	0.16(-1)	0.283	0.649	0.50(-1)	0.17(-2)	
O	0.12(-2)	0.202	0.788	0.90(-2)	0.10(-4)	0.11(-7)	
	0.10(-4)	0.16(-1)	0.494	0.452	0.37(-1)	0.66(-3)	
Ne	0.51(-2)	0.237	0.756	0.13(-2)	0.55(-5)	0.26(-8)	
	0.22(-4)	0.21(-1)	0.572	0.356	0.50(-1)	0.68(-3)	

For each element the upper row is for the optically thick inner core and the lower row for the optically thin outer layer of the knot.

core and the lower entries are for the surrounding knot region.

It is obvious from the Tables 5.5 and 5.6 that the model predicts very different temperature and ionization structures for the two regions of the knot. This has important implications for empirical determinations of abundances from spectroscopic observations, which generally assume constant ionization fractions throughout a region. In this light it is possible to account for the large differences between the elemental abundances inferred using Mocassin models and those obtained by Wesson *et al.* (2002) using empirical methods.

From an analysis of the thermal equilibrium channels stored by the *mocassinHeat* driver in the *thermChannels.out* file, it appears that dust grains play the leading role in the heating of the knot in the outer regions, dominating over the heating produced by photoionization of helium and other elements (including the small quantity of hydrogen

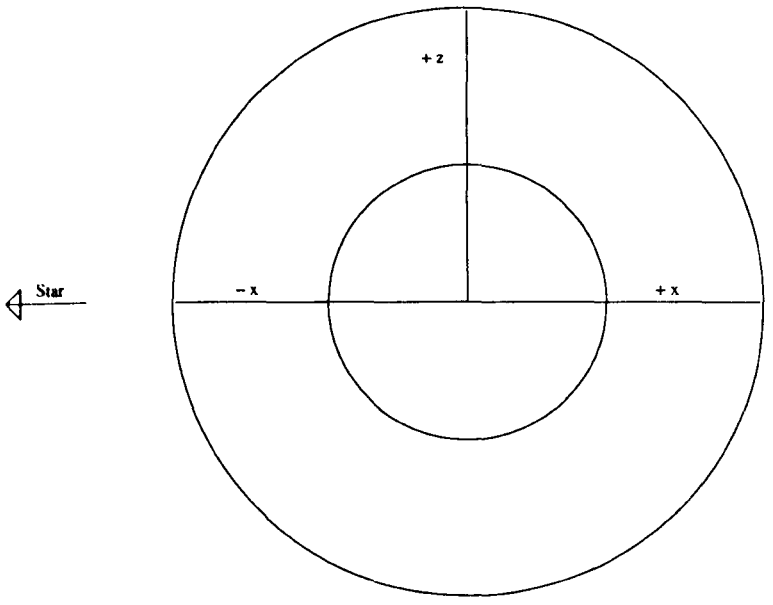

Figure 5.3: Two-dimensional schematic representation of knot J3 of Abell 30.

in the knot). This is very clearly visible in the left-hand panels of Figure 5.4, where the heating and cooling contributions due to the various components are plotted as a function of radial distance from the centre of the star. The helium ionic fractions are plotted on the right-hand panels of Figure 5.4 also as a function of radial distance from the centre of the knot. The plots are produced along three directions in the frame of reference of the knot; these are indicated in Figure 5.3. The top panels of Figure 5.4 show the plots along the negative x-axis (see Figure 5.3: $-x$), the middle panels show the plots along the positive z-axis (see Figure 5.3: $+z$); finally, the bottom panels show the plots along the negative x-axis (see Figure 5.3: $+x$).

Heating from the photoionization of atoms and ions is higher in the inner regions of the knot since the abundance of singly ionized helium (or neutral helium, in the case of the positive x-axis direction; $+x$ in Figure 5.3) is higher there. In the top and middle panels of Figure 5.5 there is, in fact, an exact correspondence between the shift of the dominant source of heating from photoionization to dust photo-electron emission and the shift of the most abundant species from He^{+} to He^{++}. The plots in the positive x-direction (Bottom panels) are slightly different, since they include the shadow region of the knot and, therefore, heating by photoionization has decreased sharply already within the inner region of the knot, due to the screening effect of the thick core.

On the contrary, heating by photoelectron emission of dust grain is higher in the

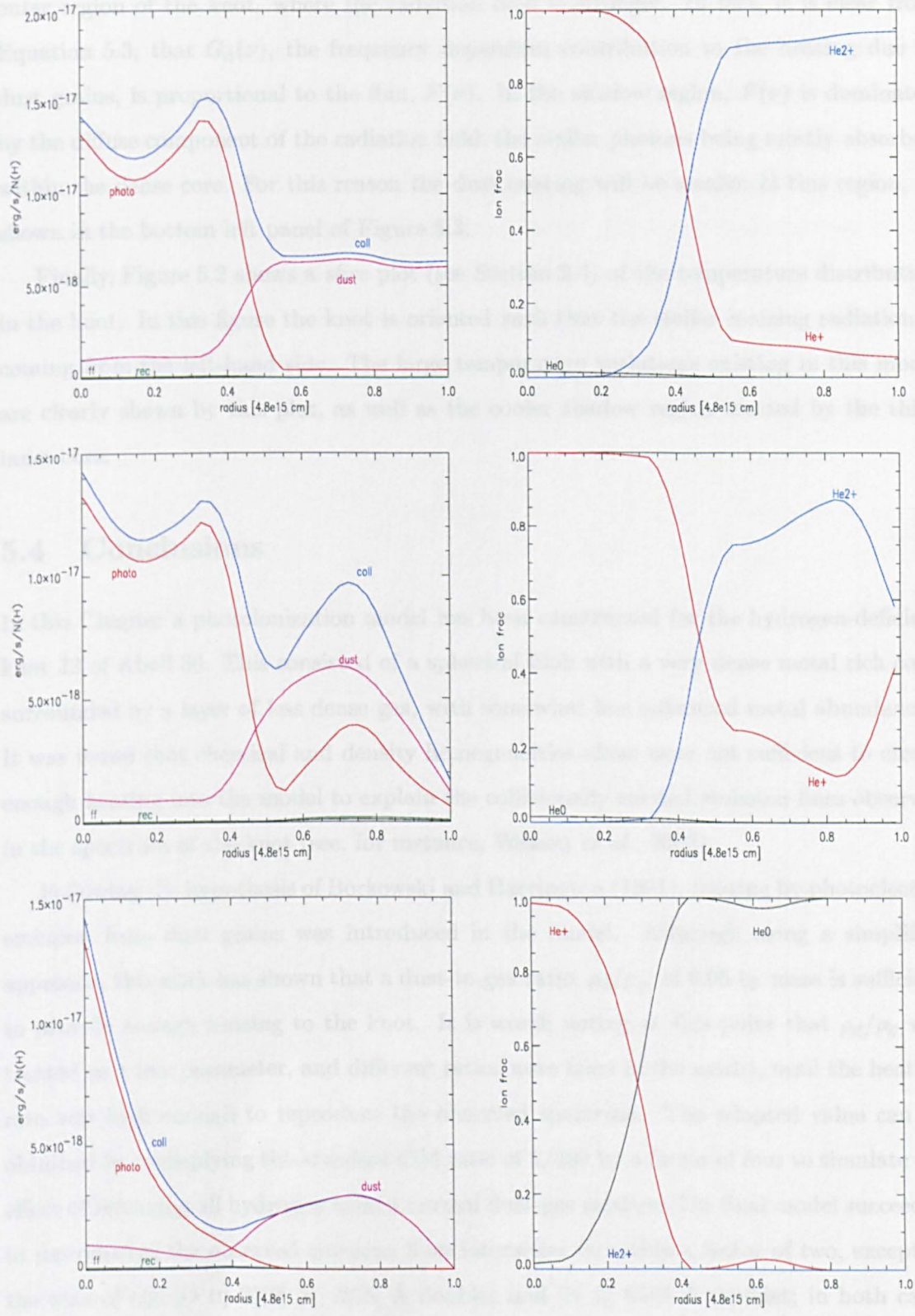

Figure 5.4: *Left panels:* Heating and cooling contributions in knot J3 of Abell 30, plotted as a function of radial distance from the centre of the knot (*photo*: photoelectric heating by atoms and ions; *dust* photoelectric heating by dust grains; *coll*: collisional cooling by ions; *ff*: cooling by free-free radiation; *rec*: cooling by recombination). *Right panels:* Fractional ionic abundances for helium. *Top panels:* plotted along the negative x-axis ($-x$ in Figure 5.3).*Middle panels:* plotted along the positive z-axis ($+z$ in Figure 5.3).*Bottom panel:* plotted along the positive x-axis ($+x$ in Figure 5.3)

outer region of the knot, where the radiation field is stronger. In fact, it is clear from Equation 5.3, that $G_d(\nu)$, the frequency dependent contribution to the heating due to dust grains, is proportional to the flux, $F(\nu)$. In the shadow region, $F(\nu)$ is dominated by the diffuse component of the radiation field, the stellar photons being mostly absorbed within the dense core. For this reason the dust heating will be smaller in this region, as shown in the bottom left panel of Figure 5.3.

Finally, Figure 5.2 shows a *slice* plot (see Section 2.4) of the temperature distribution in the knot. In this figure the knot is oriented such that the stellar ionizing radiation is coming from the left-hand side. The large temperature variations existing in this model are clearly shown by this plot, as well as the cooler shadow region created by the thick inner core.

5.4 Conclusions

In this Chapter a photoionization model has been constructed for the hydrogen-deficient knot J3 of Abell 30. This consisted of a spherical blob with a very dense metal rich core, surrounded by a layer of less dense gas, with somewhat less enhanced metal abundances. It was found that chemical and density homogeneities alone were not sufficient to create enough heating into the model to explain the collisionally excited emission lines observed in the spectrum of the knot (see, for instance, Wesson *et al.*, 2002).

Following the hypothesis of Borkowski and Harrington (1991), heating by photoelectric emission from dust grains was introduced in the model. Although using a simplified approach, this work has shown that a dust-to-gas ratio, ρ_d/ρ_g, of 0.05 by mass is sufficient to provide enough heating to the knot. It is worth noting at this point that ρ_d/ρ_g was treated as a free parameter, and different ratios were tried in the model, until the heating rate was high enough to reproduce the observed spectrum. The adopted value can be obtained by multiplying the *standard* ISM ratio of 1/200 by a factor of four to simulate the effect of removing all hydrogen from a normal dust-gas mixture.The final model succeeded in reproducing the observed emission lines intensities to within a factor of two, except in the case of the [O II] 3726 Å, 3729 Å doublet and [N II] 6584 Å doublet; in both cases contributions to the line fluxes due to recombinations are believed to be the cause of the discrepancy.

The observed relative intensities measured for the O II recombination lines at 4303 Å,

4097 Å and 4089 Å, all originating from the same upper level ($3d^4F$) do not agree with the theoretical branching ratio and are in disagreement with Mocassin's predictions. The O II 4097 Å line may be blended with one of the secondary Bowen fluorescence lines of N III and, therefore, should not be taken into account.

It was shown that in the optically thin outer layer of the model of knot J3 photoelectric heating by dust grains is the dominant source of energy. The analysis carried out in this work is, however, only qualitative as a proper treatment of the dust radiative transfer has not yet been implemented, although, as will be discussed in Chapter 6, it is intended to extend the code in this direction in the near future.

CHAPTER 6

Conclusions and future work

A fully three-dimensional photoionization code, Mocassin, has been developed for the study of photoionized nebulae, using Monte Carlo techniques. The stellar and the diffuse radiation fields are treated self-consistently; moreover, Mocassin is completely independent of the assumed nebular geometry and it is therefore ideal for the study of aspherical and/or inhomogeneous nebulae, or nebulae having one or more exciting stars located at non-central positions.

The code is fully parallel and has been extensively tested and tuned to run on a Silicon Graphic Origin 2000 machine with 24 processors and 6 Gb of memory and on a SUN Microsystem Sunfire V880 machine with 16 processors and 64 Gb of memory.

In Chapter 2 of this thesis a description of the Monte Carlo techniques applied to photoionization problems was given, together with a detailed description of all the procedures developed in the code, including computational methods, input commands and output files. Chapter 2 constitutes a basic user manual for the code and will be distributed with the source code once Mocassin is made publicly available.

The code was successfully benchmarked against established one-dimensional photoionization codes for standard spherically symmetric model nebulae (see Péquignot, 1986; Ferland *et al.*, 1995; Péquignot *et al.*, 2001). The results of the benchmarking were discussed in Chapter 3, where a performance analysis was also carried out. The outcome of this analysis was very positive, demonstrating Mocassin's suitability for modelling astrophysical nebulae.

A detailed three-dimensional photoionization study of the planetary nebula NGC 3918 was carried out, using Mocassin, in Chapter 4. Three models were developed for this

object: a biconical model based on the description given by Clegg *et al.* (1987) and two spindle-like models, of which one, model A, used a density distribution from one of Mellema's (1996) hydrodynamical models (already used by Corradi *et al.* (1999) in their observational study of NGC 3918), while the other, model B, used an analytical expression for an ellipsoid embedded in a sphere to simulate the shape of the inner shell of NGC 3918. From a comparison with observations of predicted projected maps and position-velocity diagrams in various emission lines, produced for the three models constructed for this object, it emerged that the biconical model used by Clegg *et al.* (1987) is not a realistic representation of NGC 3918. The shape of the inner-shell of NGC 3918, visible in the *HST* images of this object, and the long-slit spectra of Corradi *et al.* (1999) were best reproduced by the spindle-like model B. Nevertheless, all three models developed here succeeded in reproducing the general characteristics of the integrated emission line spectrum of this nebula. From this, the conclusion can be made that the reproduction of the integrated emission line spectrum of a nebula is not sufficient alone to demonstrate the validity of a given model; when spatio-kinematical information is available, it is crucial to be able to produce projected emission line maps and position-velocity diagrams in order to constrain the geometry of the object studied. This is only possible if a three-dimensional approach to the modelling is used.

A consistency test was also carried out in Chapter 4, in order to investigate the effects of the interaction of the diffuse radiation fields coming from two adjacent regions of different densities. Such effects were found to be non-negligible even in the case of an uncomplicated biconical distribution, hence emphasizing the limitations of the technique employed by one-dimensional codes, where a number of spherically symmetric models are combined in order to simulate inhomogeneous nebulae.

A discrepancy arose between the model predictions for the infrared fine-structure line fluxes and the ISO SWS observations (Bower, 2001). The main reason of this discrepancy was found to be a pointing error during the ISO observations, which used incorrect coordinates for this object. This, together with the small ISO SWS aperture and the beam transmission profiles not being flat, was shown to be the main cause of the discrepancy found between the uncorrelated predicted fluxes and the observations.

In Chapter 5 a photoionization model was constructed for one of the hydrogen-deficient knots (J3) in the born-again planetary nebula Abell 30. The model consisted of a spherical blob with a dense metal-rich core, surrounded by an optically thin layer of slightly more

normal abundances (but still metal-rich and severely hydrogen deficient). A source of extra heating energy proved to be necessary and this was posited to be provided by photoelectron emission from dust grains. Using a simplified approach in order to estimate the heating produced by the hypothetical grains, it was found that a dust-to-gas ratio of 0.05 by mass was sufficient to provide enough heating to the model. It was shown that, in this model, the dust heating was the dominant energy input in the optically thin outer layer of the knot, where the radiation field is more intense. On the contrary, heating by photoionization of helium and other heavy elements dominated in the dense inner region, due to the large amount of singly ionized helium available there.

Mocassin is currently set up to handle photon energies up to 24 Rydbergs ($\approx$326 eV), however the extension of its photon energy coverage into the X-ray spectral domain should be straightforward. This would allow the modelling of non-spherically symmetric nebulae around high energy radiation sources. The code can already handle arbitrary spectral energy distributions, including power laws. In addition, the input radiation field does not need to be situated at the centre of the three-dimensional grid and can be spatially extended. Once the code incorporates the X-ray domain, an obvious application would be to the modelling of clumped tori around high energy AGN nuclei. Other potential applications include the treatment of X-ray photoionized disks and clouds around T Tauri stars. Although several new processes will have to be incorporated (e.g. Auger ionization) this upgrade to the code is expected to be straightforward to implement, since the necessary atomic data are already being used in a number of well known one-dimensional codes (e.g. the Cloudy code of Ferland, 1994).

It is clear that dust grains can play an important part in the energy balance of a photoionized nebula, providing an extra heating channel, which can in some cases become the dominant one. A proper treatment of dust radiative transfer is not yet included in the current version of Mocassin, with only a very simplified dust heating function being used for the modelling of knot J3 of Abell 30 in Chapter 5. A number of dust radiative transfer codes already exist, e.g. that of Bjorkman and Wood (2001), including the fully three-dimensional Monte Carlo code of Gordon *et al.* (2001) and Misselt *et al.* (2001). However, no Monte Carlo code currently treats dust radiative transfer within a photoionized nebula. It is hoped to implement such a treatment in Mocassin in the near future, by incorporating the scattering, absorption and emission of radiation by dust particles which are mixed with gas. This will allow the competition between gas and dust for ionizing photons to

be dealt with correctly, as well as the heating of dust particles by nebular resonance line photons (and the reduction of such resonance lines due to dust absorption). Initially, grain size distributions for a representative silicate and for amorphous carbon would be incorporated, and the code tested by benchmarking it against the results from a number of standard dust transfer codes (by switching off atomic processes within Mocassin). A wider range of particle species (crystalline silicates, PAH) can subsequently be tested. As well as equilibrium grain emission, the non-equilibrium emission by small particles, due to temperature-spiking, following the absorption of energetic photons, will also be treated. Grain photoelectric heating of nebular gas will also be incorporated, which as already mentioned, is of particular significance for clumps in which the normally dominant heating by photoelectrons ejected from hydrogen is reduced due to H-deficiency (e.g. Borkowski and Harrington, 1991).

Most current photoionization codes, including Mocassin, stop the calculation at a point in the ionization front beyond which the neutral fraction rises above some pre-specified value, with the result that processes in the neutral zone beyond the ionization front are not treated. Many of the far-infrared fine structure lines observed from nebulae (e.g. [C II] 158 μm and [O I] 63.2 and 145.4 μm) originate predominantly from the neutral photodissociation region surrounding the ionized gas (Liu *et al.*, 2001), so the accurate prediction of their intensities demands a self-consistent treatment of both the neutral and ionized zones of the nebula. The processes that dominate the heating and cooling within the neutral zone should, therefore, be incorporated, as well as the formation and destruction processes for all the main species.

It is hoped to publicly release the pure ionization version of Mocassin by the end of 2002; any subsequently enhanced versions would also be made publicly available.

APPENDIX A

Atomic Data References

Free-bound emission for hydrogenic ions (H I and He II): Ferland (1980)

Free-bound emission for He I: Brown and Matthews (1970)

Two-photon emission for hydrogenic ions (H I and He II): Nussbaumer and Schmutz (1984)

Two-photon emission for He I: Drake *et al.* (1969)

Free-free emission for interaction between ions of nucleus Z and electrons: Allen (1973)

Effective recombination coefficient to H I 2^2S: Pengelly (1964)

Effective recombination coefficient to He I 2^1S: Almog and Netzer (1989)

H I and He II recombination line emissivities: Storey and Hummer (1995)

He I recombination line emissivities: Benjamin *et al.* (1999)

Collision transition rates for H I 2^2S - 2^2P: Osterbrock (1989, page94)

Cooling due to free-free radiation from hydrogenic ions (H I and He II): Hummer (1994)

Cooling due to free-free radiation from He I: Hummer and Storey (1998)

Cooling due to recombination of hydrogenic ions (H I and He II): Hummer (1994)

Cooling due to He I recombination: Hummer and Storey (1998)

Collision Ionization of hydrogen: Drake and Ulrich (1980)

Charge exchange with hydrogen: Kingdon and Ferland (1996)

Fits to radiative recombination for H-like, He-like, Li-like, Ne-like ions: Verner *et al.* (1996). Other ions of C, N, O, Ne: Péquignot *et al.* (1991) Fe XVII-XXIII: Arnaud and Raymond (1992) Other ions of Mg, Si, S, Ar, Ca, Fe, Ni: Shull and van Steenberg (1982*b*) Other ions of Na, Al: Landini and Monsignori Fossi (1990) Other ions of F, P, Cl, K, Ti, Cr, Mn, Co (excluding Ti I-II and Cr I-IV): Landini and Monsignori Fossi (1991)

Dielectronic recombination coefficients: Nussbaumer and Storey (1983, 1986, 1987)

Non relativistic free-free Gaunt factor for hydrogenic ions: Hummer (1988)

Fits to opacity project data for the photoionization cross-sections (outer shell): Verner *et al.* (1996)

Collision strengths, and transition probabilities to calculate collisionally excited line strengths from ions:

C I Collision strengths from Péquignot and Aldrovandi (1976); ^{5}S-^{3}P from Thomas and Nesbit (1975). Transition probabilities from Nussbaumer and Rusca (1979).

C II Collision strengths from Hayes and Nussbaumer (1984). Transition probabilities from Nussbaumer and Storey (1981).

C III collision strengths and transition probabilities from Keenan *et al.* (1992) and Fleming *et al.* (1996).

C IV collision strengths from Gau and Henry (1977). Transition probabilities from Wiese *et al.* (1966).

Mg I Collision Strengths from Saraph (1986) JAJOM calculations. Transition probabilities from Mendoza (1983).

Mg II collision strengths and transition probabilities from Mendoza (1983).

Mg IV Collision strengths from Butler and Zeippen (1994). Transition probabilities from Mendoza and Zeippen (1983).

Mg V Collision strengths from Butler and Zeippen (1994). Transition probabilities from Mendoza (1983).

Mg VI Collision strengths from Bhatia and Mason (1980). Transition probabilities from Eidelsberg *et al.* (1981).

Mg VII Collision strengths from Aggarwal (1984*a*) and Aggarwal (1984*b*). Transition probabilities from Nussbaumer and Rusca (1979).

Ne II Collision strength from Bayes *et al.* (1985). Transition probabilities from Mendoza and Zeippen (1983).

Ne III Collision strengths from Butler and Zeippen (1994). Transition probabilities from Mendoza and Zeippen (1983).

Ne IV Collision strengths from Giles (1981). Transition probabilities from Zeippen (1982).

Ne V Collision strengths from Lennon and Burke (1991). Transition probabilities from Nussbaumer and Rusca (1979).

Ne VI Collision strengths from Butler & Storey (unpublished). Transition probabilities from Wiese *et al.* (1966).

N I Collision strengths from Berrington *et al.* (1981). Transition probabilities from Zeippen (1982).

N II Collision strengths from Stafford *et al.* (1994). Transition probabilities from Nussbaumer and Rusca (1979).

N III Collision strengths from Nussbaumer and Rusca (1979), rescaled to Nussbaumer and Storey (1982), fine-structure terms from Butler & Storey (unpublished). Transition probabilities from Fang *et al.* (1993).

N IV Collision strengths from Mendoza and Zeippen (1983). Transition probabilities from Nussbaumer and Rusca (1979) and Fleming *et al.* (1995).

N V Collision strengths from Osterbrock and Wallace (1977). Transition probabilities from Wiese *et al.* (1966).

O I Collision strengths from Berrington *et al.* (1981) and Berrington (1988). Transition probabilities from Baluja and Zeippen (1988).

O II Collision strengths from Pradhan (1976). Transition probabilities from Zeippen (1982).

O III Collision strengths from Aggarwal (1983). Transition probabilities from Nussbaumer and Storey (1981).

O IV Collision strengths from Zhang *et al.* (1994) and from Hayes and Nussbaumer (1984). Transition probabilities from Nussbaumer and Storey (1982).

O V Collision strengths and transition probabilities from Mendoza (1983).

O VI Collision strengths and transition probabilities from Mendoza (1983).

Si II Collision strengths from Dufton and Kingston (1991). Transition probabilities from Mendoza and Zeippen (1983) and from Dufton *et al.* (1991).

Si III Collision strengths from Dufton and Kingston (1989). Transition probabilities from Mendoza and Zeippen (1983)

Si IV Collision strengths and transition probabilities from Mendoza (1983).

Si VII Fine structure collision strengths from Butler (unpublished). Transition probabilities from Bhatia *et al.* (1979).

S II Collision strengths from Mendoza and Zeippen (1983). Transition probabilities from Mendoza (1983).

S III Collision strengths from Mendoza and Zeippen (1983). Transition probabilities from Mendoza (1983)

S IV Collision strengths from Saraph and Storey (1996). Transition probabilities from Storey (unpublished)

Bibliography

Abbott, D. C. and Lucy, L. B., 1985, *ApJ*, **288**, 679

Aggarwal, K. M., 1983, *J.Phys.B.*, **16**, 2405

Aggarwal, K. M., 1984*a*, *SoPh*, **94**, 75

Aggarwal, K. M., 1984*b*, *ApJS*, **56**, 303

Aldrovandi, S. M. and Péquignot, D., 1973, *A&A*, **25**, 137

Allen, C. W., 1973, *Astrophysical Quantities* (The Athlone Press, University of London, 4 Gower st., London)

Almog, Y. and Netzer, H., 1989, *MNRAS*, **238**, 57

Arnaud, M. and Raymond, J., 1992, *ApJ*, **398**, 394

Arnaud, M. and Rothenflug, R., 1985, *A&ASS*, **60**, 425

Badnell, N. R., 2001, in *Spectroscopic Challanges of Photoionized Plasmas*, volume 247 of *ASP Conference Series*, p. 37

Balick, B., Hajian, A. R., Terzian, Y., Perinotto, M. and Patriarchi, P., 1998, *AJ*, **116**, 360

Balick, B., Perinotto, M., Maccioni, A., Terzian, Y. and Hajian, A. R., 1994, *ApJ*, **424**, 800

Balick, B., Rugers, M., Terzian, Y. and Chengalur, J. N., 1993, *ApJ*, **411**, 778

Baluja, K. L. and Zeippen, C. J., 1988, *J.Phys.B.*, **21**, 1455

Bayes, F. A., Saraph, H. E. and Seaton, M. J., 1985, *MNRAS*, **215**, 85

Benjamin, R. A., Skillman, E. D. and Smits, D. P., 1999, *ApJ*, **514**, 307

Berrington, K. A., 1988, *J.Phys.B.*, **21**, 1083

Berrington, K. A., 2001, in *Spectroscopic Challanges of Photoionized Plasmas*, volume 247 of *ASP Conference Series*, p. 137

Berrington, K. A., Burke, P. G., Butler, K., Seaton, M. J., Storey, P., Taylor, K. T. and Yan, Y., 1987, *J.Phys.B.*, **20**, 6379

Berrington, K. A., Burke, P. G., Dufton, P. L. and Kingston, A. E., 1981, *ADNDT*, **26**, 1

Bhatia, A. K., Feldman, U. and Doscheck, G. A., 1979, *A&A*, **80**, 22

Bhatia, A. K. and Mason, H. E., 1980, *MNRAS*, **190**, 925

Bjorkman, J. E. and Wood, K., 2001, *ApJ*, **554**, 615

Bloecker, T., 1995a, *A&A*, **297**, 727

Bloecker, T., 1995b, *A&A*, **299**, 755

Bloecker, T., 2001, *ApSS*, **275**, 1

Boissé, P., 1990, *A&A*, **228**, 483

Borkowski, K. J. and Harrington, J. P., 1991, *ApJ*, **379**, 168

Borkowski, K. J., Harrington, J. P., Blair, W. P. and Bregman, J. D., 1994, *ApJ*, **435**, 722

Borkowski, K. J., Harrington, J. P., Tsvetanov, Z. and Clegg, R. E. S., 1993, *ApJ*, **415**, 47

Borkowski, K. J., Harrington, J. P. and Tsvetanov, Z. I., 1995, *ApJ*, **449**, 143

Boroson, B., Blair, W. P., Davidsen, A. F., Urtilek, S. D., Raymond, J. C., Long, K. S. and McCray, R., 1997, *ApJ*, **491**, 903

Bowen, I. S., 1934, *Publs astr.Soc. Pacif.*, **46**, 146

Bower, K., 2001, *Final Year Astronomy Project, University College London*

Brocklehurst, M., 1972, *MNRAS*, **157**, 211

Brown, R. L. and Matthews, W. G., 1970, *ApJ*, **160**, 939

Burgess, A., 1964, *ApJ*, **139**, 776

Butler, S. E. and Dalgarno, A., 1980, *ApJ*, **241**, 838

Butler, S. E., Heil, T. G. and Dalgarno, A., 1980, *ApJ*, **241**, 442

Butler, S. E. and Zeippen, C. J., 1994, *A&AS*, **108**, 1

Cahn, J. H., Kaler, J. B. and Stanghellini, L., 1992, *A&AS*, **94**, 399

Castor, J. I., 1974, *ApJ*, **189**, 273

Clegg, R. E. S., Harrington, J. P., Barlow, M. J. and Walsh, J. R., 1987, *ApJ*, **314**, 551

Cohen, M. and Barlow, M. J., 1974, *ApJ*, **193**, 401

Cohen, M., Hudson, H. S., Odell, S. L. and Stein, W. A., 1977, *MNRAS*, **181**, 233

Corradi, R. L. M., Perinotto, M., Villaver, E., Mampaso, A. and Gonçalves, D. R., 1999, *ApJ*, **523**, 721

de Graaw, T. and et al., 1996, *A&A*, **315**, L49

Draine, B. T., 1978, *ApJS*, **36**, 595

Drake, G. W. F. and Ulrich, H., 1980, *ApJS*, **42**, 351

Drake, G. W. F., Victor, G. A. and Dalgarno, A., 1969, *Phys.Rev.*, **180**, 25

Dufton, P. L., Keenan, F. P., Hibbert, A., Stafford, R. P., Byrne, P. B. and Agnew, D., 1991, *MNRAS*, **253**, 474

Dufton, P. L. and Kingston, A. E., 1989, *MNRAS*, **241**, 209

Dufton, P. L. and Kingston, A. E., 1991, *MNRAS*, **248**, 827

Eidelsberg, M., Crifo-Magnant, F. and Zeippen, C. J., 1981, *A&AS*, **43**, 455

Ellis, T. M. R., Philips, I. R. and Lahey, T. M., 1994, *Fortran 90 Programming* (Addisno-Wesley, Edinburgh Gate, Harlow, Essex, CM20 2JE, England)

Ercolano, B., 2001, *Spectroscopic Challanges of Photoionized Plasmas, ASP Conf. Ser.*, **247**, 281

Fang, Z., Kwong, V. H. S. and Parkinson, W. H., 1993, *ApJ*, **413**, 141

Ferland, G., Binette, L., Contini, M., Harrington, J., Kallman, T., Netzer, H., Péquignot, D., Raymond, J., Rubin, R., Shields, G., Sutherland, R. and Viegas, S., 1995, *The Analysis of Emission Lines, STScI Symposium*, **8**, 83

Ferland, G. J., 1980, *PASP*, **92**, 596

Ferland, G. J., 1994, *Hazy* (Department of Physics and Astronomy Internal Report, university of Kentucky, Lexington, USA)

Feuerbacher, B., Anderegg, M., Fitton, B., Laude, L. D., Willis, R. F. and Grard, R. J. L., 1972, *Geochim. Cosmochim. Acta Suppl. 2*, **3**, 2655

Feuerbacher, B. and Fitton, B., 1972, *Appl. Phys.*, **43**, 1563

Fischer, O., Henning, T. and Yorke, H. W., 1994, *A&A*, **284**, 187

Fleming, J., Bell, K. L., Hibbert, A., Vaeck, N. and Godefroid, M. R., 1996, *MNRAS*, **279**, 1289

Fleming, J., Brage, T., Bell, K. L., Vaeck, N., Hibbert, A., Godefroid, M. R. and Fischer, C. F., 1995, *ApJ*, **455**, 758

Flower, D. R., 1968, *ApJL*, **2**, 205

García-Segura, G., 1997, *ApJ*, **489**, 189

Gau, J. N. and Henry, R. J. W., 1977, *PhRvA*, **16**, 986

Giles, K., 1981, *MNRAS*, **195**, 63

Gorczyca, T. W. and Korista, K. T., 2001, in *Spectroscopic Challanges of Photoionized Plasma*, volume 247 of *ASP Conference Series*, p. 79

Gordon, K. D., Misselt, K. A., Witt, A. N. and Clayton, G. C., 2001, *ApJ*, **551**, 269

Griffin, D. C. and Badnell, N. R., 2000, *J.Phys.B.*, **33**, 4389

Guerrero, M. A. and Manchado, A., 1996, *ApJ*, **472**, 711

Hammersley, J. M. and Handscomb, D. C., 1964, *Monte Carlo Methods* (J. Wiley, New York)

Harries, T. J. and Howarth, I. D., 1997, *A&AS*, **121**, 15

Harrington, J. P., 1968, *ApJ*, **152**, 943

Harrington, J. P., 1996, in *Hydrogen-deficient stars*, volume 96 of *ASP Conf. Ser.*, p. 193

Harrington, J. P. and Feibelman, W. A., 1983, *ApJ*, **265**, 258

Harrington, J. P. and Feibelman, W. A., 1984, *ApJ*, **277**, 716

Harrington, J. P., Monk, D. J. and Clegg, R. E. S., 1988, *MNRAS*, **231**, 577

Harrington, J. P., Seaton, M. J., Adams, S. and Lutz, J. H., 1982, *MNRAS*, **199**, 517

Hayes, M. A. and Nussbaumer, H., 1984, *A&A*, **134**, 193

Hazard, C., Terlevich, R., Ferland, G., Morton, D. C. and Sargent, W. L. W., 1980, *Natur*, **285**, 463

Herwig, F., 2000, *A&A*, **360**, 952

Herwig, F., Bloecker, T., Langer, N. and Driebe, T., 1999, *A&A*, **349**, L5

Hummer, D. G., 1988, *ApJ*, **327**, 477

Hummer, D. G., 1994, *MNRAS*, **268**, 109

Hummer, D. G., Berrington, K. A., Eissner, W., Pradhan, A. K., Saraph, H. E. and Tully, J. A., 1993, *A&A*, **279**, 298

Hummer, D. G. and Storey, P. J., 1998, *MNRAS*, **297**, 1073

Hyung, S., Aller, L. H. and Feibelman, W. A., 1997, *ApJS*, **108**, 503

Iben, I. J., 1984, *ApJ*, **277**, 333

Iben, I. J., Kaler, J. B., Truran, J. W. and Renzini, A., 1983, *ApJ*, **264**, 605

Iben, I. J. and Renzini, A., 1983, *ARA&A*, **21**, 271

Jacoby, G. H., 1979, *PASP*, **91**, 754

Jacoby, G. H. and Ford, H. C., 1983, *ApJ*, **266**, 298

Kahn, F. D., 1989, in *Planetary Nebulae*, volume 131 of *IAU Symp.*, p. 411

Kallman, T. R. and McCray, R., 1982, *ApJS*, **50**, 263

Kastner, S. O. and Bhatia, A. K., 1996, *MNRAS*, **279**, 1137

Keenan, F. P., Feibelman, W. A. and Berrington, K. A., 1992, *ApJ*, **389**, 443

Kingdon, J. B. and Ferland, G. J., 1996, *ApJS*, **106**, 205

Knigge, C., Woods, J. and Drew, J., 1995, *MNRAS*, **273**, 225

Kwok, S., 1994, in *Astronomical Society of the Pacific*, volume 106 of *Publications*, p. 344

Kwok, S., Purton, C. R. and Fitzgerald, P. M., 1978, *ApJ*, **219**, L125

Landini, M. and Monsignori Fossi, B. C., 1990, *A&AS*, **82**, 229

Landini, M. and Monsignori Fossi, B. C., 1991, *A&AS*, **91**, 183

Leech, K. et al., 2002, *The ISO handbook. Volume V: SWS- The Short Wavelength Spectrometer* (ESA)

Lefevre, J., Bergeat, J. and Daniel, J. V., 1982, *A&A*, **114**, 341

Lefevre, J., Daniel, J. V. and Bergeat, J., 1983, *A&A*, **121**, 51

Lennon, D. J. and Burke, V. M., 1991, *MNRAS*, **251**, 628

Liu, X. W., 1993, *MNRAS*, **261**, 465

Liu, X. W., Barlow, M. J., Cohen, M., Danziger, I. J., Luo, S.-G., Baluteau, J. P., Cox, P., Emery, R. J., Lim, T. and Péquignot, D., 2001, *MNRAS*, **323**, 343

Liu, X. W., Storey, P. J., Barlow, M. J. and Clegg, R. E. S., 1995, *MNRAS*, **272**, 369

Livio, M., 1995, in *Asymmetric Planetary Nebulae*, eds. A.Harpaz and N. Soker, p. 51

Lopez, J. A., Meaburn, J., Bryce, M. and Rodríguez, L. F., 1997, *ApJ*, **475**, 705

Lucy, L. B., 1999, *A&A*, **344**, 282

Lucy, L. B., 2001, *MNRAS*, **326**, 95L

Lucy, L. B., 2002, *A&A*, **384**, 725L

McLaughlin, B. M. and Bell, K. L., 1998, *J.Phys.B.*, **31**, 4317

Mellema, G., 1996, *Numerical Models for the formation of aspherical planetary nebulae* (PhD Thesis, Univ. Leiden)

Mendez, R. H., 1991, in *Evolution of stars: The Photospheric Abundance Connection*, volume 145 of *IAU Symposium*, p. 375

Mendoza, C., 1983, *Planetary Nebulae, IAU Symposium, ed. D.R. Flower*, **103**, 143

Mendoza, C. and Zeippen, C. J., 1983, *MNRAS*, **202**, 981

Metropolis, N. and Ulam, S., 1949, *J.Amer.Statistical. Assoc.*, **44**, 247

Mihalas, D. and Auer, L. H., 1975, *NCAR-TN/STR-104*

Milne, D. K., 1976, *AJ*, **81**, 753

Misselt, K. A., Gordon, K. D., Clayton, G. C. and Wolff, M. J., 2001, *ApJ*, **551**, 277

Monteiro, H., Morisset, C., Gruenwald, R. and Viegas, S. M., 2000, *ApJ*, **537**, 853

Morisset, C., Gruenwald, R. and Viegas, S. M., 2000, *ApJ*, **533**, 931

Morisset, C., Schaerer, D., Martn-Hernndez, N. L., Peeters, E., Damour, F., Baluteau, J.-P., Cox, P. and Roelfsema, P., 2002, *A&A*, **386**, 558

Nahar, S. N., 2000, *A&AS*, **147**, 549

Nahar, S. N. and Pradhan, A. K., 1999, *A&AS*, **135**, 347

Netzer, H., 1993, *ApJ*, **411**, 445

Nussbaumer, H. and Rusca, C., 1979, *A&A*, **72**, 129

Nussbaumer, H. and Schmutz, W., 1984, *A&A*, **138**, 495

Nussbaumer, H. and Storey, P., 1981, *A&A*, **96**, 91

Nussbaumer, H. and Storey, P. J., 1982, *A&A*, **115**, 205

Nussbaumer, H. and Storey, P. J., 1983, *A&A*, **126**, 75

Nussbaumer, H. and Storey, P. J., 1986, *A&AS*, **64**, 545

Nussbaumer, H. and Storey, P. J., 1987, *A&AS*, **69**, 123

Och, S. R., Lucy, L. B. and Rosa, M. B., 1998, *A&A*, **336**, 301

Osterbrock, D. E., 1989, *Astrophysics of Gaseous Nebulae and Active Galactic Nuclei* (University Science Books, Mill Valley, CA)

Osterbrock, D. E. and Wallace, R. K., 1977, *ApL*, **19**, 110

Pagel, B. E. J., 1997, *Nucleosynthesis and Chemical Evolution of Galaxies* (Cambridge University Press, Cambridge, UK)

Pengelly, R. M., 1964, *MNRAS*, **127**, 145

Péquignot, D., 1986, in *Workshop on model nebulae*, Publication de l'Observatoire de Meudon, Paris, ed. D. Pequignot

Péquignot, D. and Aldrovandi, S. M., 1976, *A&A*, **50**, 141

Péquignot, D., Ferland, G., Netzer, H., Kallman, T., Ballantyne, D., Dumont, A.-M., Ercolano, B., Harrington, P., Kraemer, S., Morisset, C., Nayakshin, S., Rubin, R. and Sutherland, R., 2001, *Spectroscopic Challanges of Photoionized Plasmas, ASP Conference Series*, **247**, 533

Péquignot, D., Petitjean, P. and Boisson, C., 1991, *A&A*, **251**, 680

Péquignot, D., Stasinska, G. and Aldrovandi, S. M. V., 1978, *A&A*, **63**, 313

Perinotto, M., 2000, *ApSS*, **274**, 205

Petitjean, P., Boisson, C. and Péquignot, D., 1990, *A&A*, **240**, 433

Pottasch, S. R., Preite-Martinez, A., Olnon, F. N., Jing-Er, M. and Kingma, S., 1986, *Astr.Ap*, **161**, 363

Pradhan, A. K., 1976, *MNRAS*, **177**, 31

Ramsbottom, C. A., Bell, K. L. and Keenan, F. P., 1998, *MNRAS*, **293**, 233

Reilman, R. F. and Manson, S. T., 1979, *ApJS*, **40**, 815

Robbins, R. R., 1968, *ApJ*, **151**, 497

Rubin, R. H., 1968, *ApJ*, **153**, 761

Rubin, R. H., 1986, *ApJ*, **309**, 334

Sahai, R., 2000, *ApJ*, **537**, L43

Saraph, H. E. and Seaton, M. J., 1980, *MNRAS*, **193**, 617

Saraph, H. E., Seaton, M. J. and Shemming, J., 1970, *Phil. Trans. Roy. Soc. London*, **A264**, 77

Saraph, H. E. and Storey, P. J., 1996, *A&AS*, **115**, 151

Shreider, Y. A., 1964, *Method of Statistical Testing: Mote Carlo Method* (Elsevier Publishing Company, 335 Jan Van Galenstraat, P.O. Box 211, Amsterdam)

Shull, J. M. and van Steenberg, M., 1982*a*, *ApJS*, **48**, 95

Shull, J. M. and van Steenberg, M., 1982*b*, *ApJS*, **49**, 351

Soker, N., 1997, *ApJS*, **112**, 487

Soker, N., 2001, *MNRAS*, **324**, 699

Soker, N. and Harpaz, A., 1999, *MNRAS*, **310**, 1158

Solf, J. and Ulrich, H., 1985, *A&A*, **148**, 274

Stafford, R. P., Bell, K. L., Hibbert, A. and Wijesundera, W. P., 1994, *MNRAS*, **268**, 816

Stancil, P. C., 2001, in *Spectroscopic challanges of photoionized plasmas*, volume 247 of *ASP Conference Series*, p. 3

Stancil, P. C., Schultz, D. R., Kimura, M., Gu, J.-P., G., H. and Buenker, R. J., 1999, *A&AS*, **140**, 225

Storey, P. J., 1981, *MNRAS*, **195**, 27

Storey, P. J., 1994, *A&A*, **282**, 999

Storey, P. J. and Hummer, D. G., 1995, *MNRAS*, **272**, 41

Sutherland, R. and Dopita, M., 1993, *ApJS*, **88**, 253

Swartz, D. A., 1994, *ApJ*, **428**, 267

Tarter, C. B., Tucker, W. and E., S., 1969, *ApJ*, **156**, 943

Thomas and Nesbit, 1975, *PhRvA*, **12**, 2378

Tsamis, Y. G., X.-W., L., Barlow, M. J., Danziger, I. J. and Storey, P. J., 2002, *MNRAS*, **submitted**

van Hoof, P. A. M., Beintema, D. A., Verner, D. A. and Ferland, G. J., 2000, *A&A*, **354**, 41

Verner, D. A., Ferland, G. J., Korista, K. T. and Yakovlev, D. G., 1996, *ApJ*, **465**, 487

Verner, D. A. and Yakovlev, D. G., 1995, *A&AS*, **109**, 125

Wesson, R., Liu, X.-W. and Barlow, M. J., 2002, *MNRAS*, **in preparation**

Wiese, W. L., Smith, M. W. and Glennon, B. M., 1966, *Atomic transition probabilities: Hydrogen through Neon. A critical data compilation* (NSRDS-NBS 4, Washington, D.C.: US Department of Commerce, National Buereau of Standards)

Wolf, S., Henning, T. and Secklum, B., 1999, *A&A*, **349**, 839

Zeippen, C. J., 1982, *MNRAS*, **198**, 111

Zhang, H. L., Graziani, M. and Pradhan, A. K., 1994, *A&A*, **283**, 319

List of Publications

Three-dimensional Monte Carlo Simulations of Ionized Nebulae B. Ercolano, 2001, PASP, 247, 281

Photoionization Model Nebulae Péquignot, D., Ferland, G., Netzer, H., Kallman, T., Ballantyne, D., Dumont, A.-M., Ercolano, B., Harrington, P., Kraemer, S, Morisset, C., Nayakshin, S., Rubin, R.H. and Sutherland, R., 2001, PASP, 247, 533

Mocassin: A fully three-dimensional Monte Carlo photoionization code Ercolano, B., Barlow, M. J., Storey, P. J. and Liu, X.-W., 2002, MNRAS, submitted, astro-ph#:0209378

Three-Dimensional Monte Carlo Simulations of Ionized Nebulae Ercolano, B., Morisset, C., Barlow, M. J., Liu, X.-W. and Storey, P. J., 2002, proc. IAU 209, ed. R. Sutherland, S. Kwok and M. Dopita, in press

Three-dimensional photoionization modelling of the planetary nebula NGC 3918 Ercolano, B., Morisset C., Barlow, M. J., Storey, P. J. and Liu, X.-W., 2002, MNRAS, submitted, astro-ph#:0209417

ACKNOWLEDGMENTS

First of all I'd like to say that the past three years have undoubtedly been the happiest and most fulfilling three years of my life (so far..) and for this I have to thank all the people who have made them such. The list is very long and it would be impossible to thank everybody here.. but to those of you I have missed out from this list, please forgive me.

I THANK Mike Barlow for many many things, but most importantly for being there all the time, he's been like a rock for me during the past three year and I know I would have never made it without his support. *Second* only to Mike for the time he dedicated to my many *quick questions* is Pete Storey, who I will always be grateful to and I apologize for my *tic-toc-tic-toc* messages. I thank Xiao-Wei for all the energy levels diagrams he drew for me (from the top of his head!). I thank deeply Christophe Morisset, first of all for being so nice and also for giving me so many good ideas for the code and for sharing his IDL routines with me. I also thank Daniel Péquignot for suggesting to carry out the diffuse field consistency test and also for all the other suggestions he gave me during the development of Mocassin. I thank Bob Rubin for sending me the diffuse field distribution output from his own photoionization code to help me test mine. I also want to thank Professor Wilkin for answering all the random maths questions I nagged him with over the past three years (including those ones I should have known the answer to from 1B21.. sorry!). I thank Garrelt Mellema for sending me the density distribution file I used for the spindle-like model A of NGC 3918. I also thank Jeremy Yates and Callum Wright for all the help they gave me with Miracle and for protecting me from fastidious furniture. I also thank John Deacon for his help with the Starlink (and non-Starlink) machines. A big thank-you (and a kiss) to Richard Price for keeping his side of the office tidy and having to suffer in silence for my mess. Although he subsequently abandoned me.. fortunately Roger Wesson came to the rescue with endless bags of green tea and big smiles.

I also want to thank all my friends for all the times they had to listen to my incessant moaning, but most importantly thanks for all the good time we've had in the past three (or more) years! Thanks (not in any order) to Pia, Jay & Tamsin, Claire & Dave, Tosh & Leanne, Lloyd & Gill, Mr. Sterne, Barry Shaw, Harry Monk, James & Elaine, the Whites, Jenkins Jackson etc..

I also thank Kevin's mum and dad and Barry and Sian and everybody else on the Wirral Peninsula who have made me feel so welcome there.

E adesso voglio ringraziare Mamma, Papa', Giorgio, i Nonni, Zio Franco e tutte le persone della mia famiglia che mi hanno tenuta sempre nel loro cuore e mi hanno sostenuta nei momenti a dir poco *di stanca.* Senza il vostro affetto e supporto non credo proprio che ce l'avrei fatta!!

Last but certainly not least a very soppy thank you goes to the boy (man?!?) with the longest eyelashes in the world. He's incredibly gorgeous and he's made me very happy and certainly a more balanced person. I truly believe that without his love and support the past three years would not have been as amazing as they have.